Experimental and Numerical Investigation of Three-Dimensional Laminar Wall Jet of Newtonian and Non-Newtonian Fluids

by

Kofi Freeman Krobea Adane

A Thesis Submitted to the Faculty of Graduate Studies of
The University of Manitoba
In Partial Fulfillment of the Requirements of the Degree of

Doctor of Philosophy
In
Mechanical Engineering

Department of Mechanical and Manufacturing Engineering
University of Manitoba
Winnipeg, Manitoba
Canada

ABSTRACT

A research program was designed to investigate the characteristics of three-dimensional laminar wall jet flow of both Newtonian and two shear-thinning non-Newtonian fluids. The non-Newtonian fluids were prepared from xanthan gum solutions of various concentrations. Both experimental and numerical methodologies were employed in this study. The wall jet was created using a circular pipe of diameter 7 mm and flows into an open fluid tank. The initial Reynolds numbers based on the pipe diameter and jet exit velocity ranged from 250 to 800. The velocity measurements were conducted using a particle image velocimetry technique. The measurements were conducted at several streamwise locations to cover both the developing and self-similar regions. For the numerical study, the complete nonlinear Navier-Stokes equation was solved using an in-house colocated finite volume based CFD code. A Carreau model was employed for the non-Newtonian fluids. The viscosity in the governing equations was obtained explicitly.

From the PIV measurements and CFD results, velocity profiles and jet half-widths were extracted at selected downstream locations to study the effects of Reynolds number and specific fluid type on the jet characteristics. It was observed that the numerical results are in reasonable agreement with the experimental data. The decay of maximum velocity, jet spread rates, skin friction coefficient, streamwise velocity profiles, and secondary flows depend strongly on the initial Reynolds number irrespective of the fluid. The results also show that the jet spreads more in the spanwise direction than in the transverse direction in the early flow development whereas the reverse is true in the downstream region. Important differences were observed when the results for the non-Newtonian fluids were compared with those for Newtonian fluid.

ACKNOWLEDGEMENT

My profound appreciation and gratitude goes to my advisor, Prof Mark Francis Tachie for his splendid professional guidance and impressive help with all aspects of this dissertation. I would like to thank Profs S. J. Ormiston and S. Cenkowski for serving on this work committee. My appreciation also goes to Dr Xiaochen Gu and Tao Wang in Faculty of Pharmacy for their assistance with fluid rheology.

Also, I would like to thank my three loving sisters and my uncle for their invaluable support. I am grateful to Martin Agelin-Chaab and Paul Krueger for their co-operation during the course of experimentation. Thanks to Robyn Tully, Dr S. S. Paul, Gerald Brown and everyone who directly or indirectly contributed to the success of this dissertation. Special thanks to Him through whom all things are completed.

To

Myself and all those who took the challenge to pursue this advance degree.

TABLE OF CONTENTS

LIST OF FIGURES

LIST OF TABLES

NOMENCLATURE

English

$C_{f\,j}$	:	Skin friction coefficient based on u_j ($= 2\tau_w/\rho u_j^2$)
$C_{f\,m}$	:	Skin friction coefficient based on u_m ($= 2\tau_w/\rho u_m^2$)
d	:	Inlet pipe diameter [m]
h, b, l	:	Dimension of channel [m]
H, L, B	:	Dimension of lid cavity [m]
M_o	:	Momentum flux at the pipe exit [kg•m/s]
M_x	:	Local momentum flux at x locations [kg•m/s]
$M_{x,o}$	:	Normalised local momentum flux at x locations ($= M_x/M_o$)
n	:	Power-law index
p	:	Pressure [Pa]
r	:	Local radius [m]
Re	:	Reynolds number based on bulk velocity or lid velocity and channel height ($= \rho\, U_b^{2-n}\, h^n / \mu_0\, \theta^{n-1}$)
Re_j	:	Reynolds number based on maximum streamwise velocity and pipe diameter ($= \rho\, u_j^{2-n}\, d^n / \mu_0\, \theta^{n-1}$)
Re_m	:	Local Reynolds number based on local maximum velocity and $z_{0.5}$ ($=\rho\, u_m\, z_{0.5} / \mu_{0.5}$)
t	:	Time [s]
t_r	:	Response time [s]
S_r	:	Spread rates ratio
S_y	:	Spanwise spread rate ($= dy_{0.5}/dx$)

S_z	:	Transverse spread rate (= $dz_{0.5}/dx$)
u	:	Streamwise component of velocity [m/s]
u_b or U_b	:	Bulk velocity [m/s]
u_c	:	Maximum centreline velocity [m/s]
u_j	:	Maximum streamwise velocity at the jet inlet [m/s]
u_j^m	:	Measured maximum streamwise velocity at the jet inlet [m/s]
u_m	:	Local maximum streamwise velocity [m/s]
U	:	Normalised streamwise velocity (= u/u_m)
U_c	:	Normalised maximum centreline velocity (= u_c/u_b)
U_{lid}	:	Lid velocity [m/s]
U_m	:	Normalised local maximum streamwise velocity (= u_m/u_j)
v	:	Spanwise component of velocity [m/s]
v_s	:	Settling velocity [m/s]
v	:	Velocity vector [m/s]
v_m	:	Local maximum spanwise velocity [m/s]
V	:	Normalised spanwise velocity (= v/v_m)
V_u	:	Normalised spanwise velocity (= v/u_m)
w	:	Transverse component of velocity [m/s]
W	:	Normalised transverse velocity (= w/w_m)
W_u	:	Normalised transverse velocity (= w/u_m)
x	:	Streamwise coordinate [m]
X	:	Normalised streamwise distance (= x/d)
y	:	Spanwise coordinate [m]

Y	:	Normalised spanwise distance (= y/d)
$y_{0.5}$	:	Jet half-width in spanwise direction [m]
$Y_{0.5}$	:	Normalised spanwise jet half-width (= $y_{0.5}/d$)
Y '	:	Normalised spanwise distance (= $y/y_{0.5}$)
z	:	Transverse coordinate [m]
Z	:	Normalised transverse distance (= z/d)
$z_{0.5}$	:	Jet half-width in transverse direction [m]
$Z_{0.5}$	:	Normalised transverse jet half-width (= $z_{0.5}/d$)
z_m	:	Jet thickness in transverse direction [m]
Z '	:	Normalised transverse distance (= $z/z_{0.5}$)

Greek Symbols

λ	:	Consistency index [Pa•s^n]
Λ	:	Second invariant of the shear rate tensor
μ	:	Dynamic viscosity [N•s/m^2]
μ_0	:	The limit viscosity at low shear rate [N•s/m^2]
μ_∞	:	The limit viscosity at high shear rate [N•s/m^2]
ω_x	:	Streamwise vorticity [s^{-1}]
ω_y	:	Spanwise vorticity [s^{-1}]
ω_z	:	Transverse vorticity [s^{-1}]
Ω_x	:	Normalised streamwise vorticity (= $1000\,\omega_x\, d / u_j$)
ρ	:	Density [kg/m^3]
θ	:	Time constant [s]

τ_w : Wall shear stress [N/m^2]

ACRONYMS

2D	:	Two-dimensional
3D	:	Three-dimensional
CFD	:	Computational fluid dynamics
CV	:	Control volume
CDS	:	Central difference scheme
DNS	:	Direct numerical simulation
FFT	:	Fast Fourier transform
IWs	:	Interrogation windows
LDA	:	Laser Doppler anemometry
Nd: YAG	:	Neodymium: Yttrium Aluminum Garnet
PIV	:	Particle image velocimetry
SIMPLE	:	Semi-implicit method for pressure-linked equation
SIMPLEC	:	Semi-implicit method for pressure-linked equation consistent
SIP	:	Strongly implicit procedure
UDS	:	Upwind differencing scheme
XG	:	Xanthan gum
XG005	:	Aqueous solution of 0.005 *wt*% of xanthan gum
XG010	:	Aqueous solution of 0.010 *wt*% of xanthan gum

Chapter 1

INTRODUCTION

1.1 Overview

This work pertains to the experimental and numerical study of three-dimensional laminar wall jet flow of both Newtonian and non-Newtonian fluids. The first section of this chapter provides an overview of wall jet flows. This is followed by a brief discussion on non-Newtonian fluids and their behavioural characteristics. The techniques employed to study fluid flows are then highlighted. The motivation and objectives, and the structure of the present work are also presented.

1.2 The Wall Jet

"The wall jet flow can be defined as a shear flow directed along a wall where, by virtue of the initially supplied momentum, at any station, the streamwise velocity over some region within the flow exceeds that in the external stream" (Launder and Rodi, 1983). A typical production of this flow is a discharged of a fluid from a tube directed parallel to the bottom plane wall of a tank of the same medium. In a wall jet flow, the surrounding ambient medium can be quiescent, co-flowing or counter-flowing. Also, depending on the specific application, the ambient medium may be decelerating or accelerating.

Figure 1.1 shows a sketch of a typical three-dimensional (3D) wall jet flow, and also defines the Cartesian coordinate system and some of the flow nomenclature, employed in this study. A jet is released from a circular orifice into a similar infinite quiescent medium. The velocity increases transversely from zero at the wall to a maximum, u_m, at distance z_m from the wall and then decreases progressively to zero (Fig. 1.1b). The

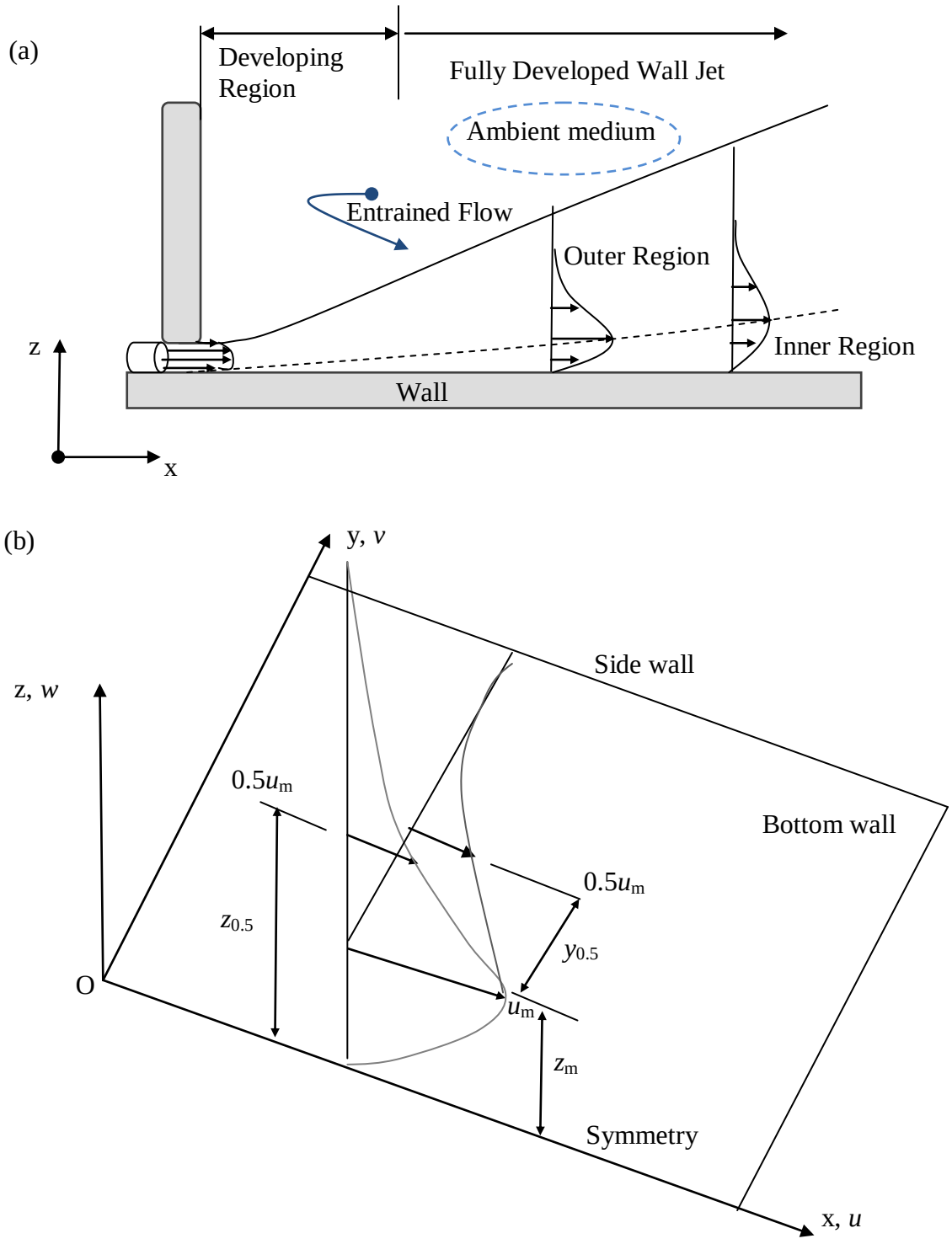

Figure 1.1: Schematic diagram of a 3D wall jet flow.

region extending from the wall to z_m (i.e., $z_m \leq 0$) is often referred to as the inner region while the flow region from z_m to the outer edge of the flow ($z_m > 0$) is the outer region. The characteristics of the inner region of a wall jet resemble those of a viscous boundary layer whereas the outer region is akin to a free jet flow. The free jet has its initial momentum gradually carried over to the ambient fluid (entrainment) which in turn leads to an ever widening jet. Meanwhile, in the case of the flat plate or classical boundary layer flows, the wall friction diminishes the initial momentum as the flows evolved downstream. Since these two flows, boundary layer and a free jet, have quite different characteristics, the interaction between the inner and outer regions of a wall jet produces a flow field that is relatively more complex than the classical boundary layer or the free jet. In fact, the wall jet flow sustains a momentum loss on the bottom plane wall and spreads in all the non-wall bounded direction into the ambient fluid like the free jet. It is therefore not surprisingly that the wall jet has been used as a prototypical flow to conduct fundamental research on complex shear flows

The jet half-widths ($z_{0.5}$ and $y_{0.5}$) are defined as the distance measured from the origin to the respective location at which u is one-half of u_m (Fig. 1.1b). As the jet develops downstream, it entrains more ambient fluid. As a result, the local maximum velocity decays with increasing downstream location, and the jet half-widths in both the transverse and spanwise directions increase. These wall jet flow parameters are very useful for the description of flow behaviour. For example, the variation of u_m with streamwise distance from the jet exit provides an insight into the decay of the velocity field. The jet half-widths ($y_{0.5}$ and $z_{0.5}$), on the other hand, represent the spread of the jet

in the spanwise and transverse directions while z_m indicates the thickness of the inner region.

As shown in Fig. 1.1a, the flow passes through two basic stages as it evolves in the streamwise direction. These stages are the developing region which is immediately downstream of the efflux section, and the fully developed wall jet flow which occurs further downstream. In the fully developed wall jet region, the flow has evolved to achieve a self-preserved state or self-similar condition with the downstream direction (Glauert, 1956; Gorla and Jeng, 1971; Hari, 1973). This implies that the velocity profiles normalised by the corresponding local streamwise maximum velocity (u/u_m) and transverse distance from the wall normalised by the jet half-width ($z/z_{0.5}$) become universal and independent of streamwise location for two-dimensional (2D) flows. In the case of three-dimensional (3D) flow, the normalised velocity (u/u_m) plotted against the normalised spanwise distance from the origin ($y/y_{0.5}$) is also universal and independent of streamwise location.

1.3 Non-Newtonian Fluid

Fluids come in so many forms ranging from gaseous state to semi-solid state. Examples include air, water, mud, ice, lava, and painting oil. These fluids can be classified as Newtonian or non-Newtonian. As is well known, the viscosity of a Newtonian fluid is constant at specific temperature and pressure, and independent of the shear rate. Examples of Newtonian fluids are air and water. On the other hand, the viscosity of a non-Newtonian fluid is not constant and is a function of the shear rate. Common examples of non-Newtonian fluids are mud, ice, lava, painting oil, toothpaste, drilling

mud, chocolate, blood, milk, clay, liquid cement, high molecular weight liquids such as polymer melts, and solutions of polymers (such as aqueous solution of xanthan gum), as well as liquids in which fine particles are suspended (slurries and pastes). Obviously, this unusual property of a non-Newtonian fluid makes it more complex compared with a Newtonian fluid.

Rheology is the study of deformation and flow of matter. Normally, rheology involves fluids such as non-Newtonian fluids that behave "unusually" or in a wide variety of ways. Today, there are a lot of industrial and domestic fluid flow applications in which rheology plays a key role. These include biological macromolecules behaviour in biotechnological industries, the transport of foams and yield-stress fluids in oil drilling and enhanced oil recovery (EOR), and the study of volcanism and convection through Earth's mantle and outer core. In all these problems, rheology helps in the understanding of the behaviour of the particular fluid.

Typically, for non-Newtonian fluids, the slope of the viscosity (shear stress) versus shear rate curve is not constant as the shear rate changes at a given temperature or pressure, or varying temperature or pressure or both temperature and pressure. This non-linearity and other behaviours such as inhibition of stretching, elastic or plastic effects are usually used to characterise non-Newtonian fluids. This work focuses on the non-linearity of the fluid.

In general, there are three types of the non-linear fluids (Tanner, 1985). These are:

- Time-independent fluids in which the shear rate is only a function of the shear stress. These are usually termed as non-Newtonian viscous fluids or generalised Newtonian fluids.

- Time-dependent fluids in which the relation between the shear rate and shear stress takes into account the time the fluid has been sheared.
- Viscoelastic fluids in which the fluid exhibits partial elastic recovery after deformation. This class of fluids usually have characteristics of both solid and fluids.

Both time-dependent (thixotropic and rheopectic) and viscoelastic fluids are beyond the scope of this study. The time-independent fluids may be sub-classified into three distinct categories. These are shear-thinning or pseudo-plastic, shear-thickening or dilatants, and yield stress or viscoplastic fluids. This classification is based on the nature of the relationship between the shear stress and the shear rate or flow rate and pressure drop.

As shown in Fig. 1.2, the viscosity of shear-thinning fluids decreases with increasing shear rate. Previous experimental studies have shown that this type of fluid displayed two "Newtonian" regions, namely a lower region and an upper region which correspond to the limits of very low and very high shear rates, respectively. Figure 1.2 also demonstrates that the viscosity in these two Newtonian regions is constant. Examples of this type of fluids include polymers such as aqueous solution of xanthan gum, molten polystyrene, polyethylene oxide in water, blood, synovial fluid, and some paints. For shear-thickening fluids, the viscosity increases as the fluid is subjected to a higher shear rate. Most of the shear-thickening fluids tend to show shear-thinning behaviour at very low shear rates. Examples of shear-thickening fluids include clay slurries, and solutions of certain surfactants. A viscoplastic fluid will not flow unless shear stress is applied. The shear stress must exceed a critical value known as the yield stress of the fluid.

Examples of viscoplastic fluids are toothpaste, drilling mud, nuclear fuel slurries, mayonnaise, greases, oil paints, and blood. This work will consider only shear-thinning fluids. Since rheology is a broad subject, only the basics that are relevant to the present study will be discussed. A more vivid and comprehensive discussion on rheology can be found, for example, in Barnes *et al* (1989), Tanner (1985), and Macosko (1994).

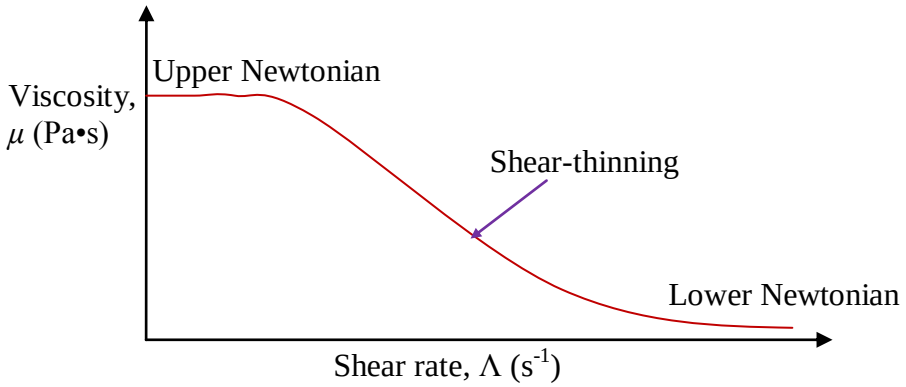

Figure 1.2: Viscosity versus shear rate of shear-thinning fluid.

1.4 Numerical and Experimental Analysis of Fluid Flow

Recent advances in computational resources with lower cost to computing power ratio have enabled computational fluid dynamics (CFD) to be applied to complex flow fields. In fact, the application of a CFD technique to study fluid flow is now very attractive and popular in the design of a wide range of fluid engineering processes. The reasons include low cost, less design time, and ease of geometric and other parametric variations. These advantages are based on the premise that the governing mathematical models of the flows are solved accurately. However, CFD results are always an approximation. This is because the discretised governing differential equations that are numerically solved are approximations, and the solution of these discretised equations is obtained by iterative methods. Therefore, there is a need for benchmark experimental data sets to validate the

numerical results. This is particularly true for a relatively complex flow such as a three-dimensional wall jet flow of a non-Newtonian fluid.

A number of measurement devices of varying sophistication are now available for conducting velocity measurements. Most of these devices, for example, hot-wire anemometer and laser Doppler anemometry (LDA) are point-wise measurement techniques. Although these measurement techniques have an excellent spatial resolution, the need for a technique that can provide instantaneous measurements of the flow velocity at several positions either in two-dimensional (2D) or three-dimensional (3D) domain is vital. The particle image velocimetry (PIV) method is a multi-point measuring technique that is capable of providing whole field instantaneous flow velocity measurements. Furthermore, the PIV technique is non-intrusive measurement. It is also well suited for estimating velocity gradients and derived quantities such as vorticity. These features have made the use of PIV in many fluid mechanics applications very attractive. In this study, the PIV technique is used to perform the experimental measurements.

1.5 Applications of Wall Jet Flows

Wall jet flows have diverse biomedical and engineering applications. In neurobiological and neural tissue engineering, for example, a wall jet flow is used as mass transport enhancement in a bioreactor perfusion system. This novel three-dimensional neural culture represents a more realistic approximation of the brain (Cullen *et al,* 2007). Recently, it has been shown by Mautner (2004) that the use of laminar wall jets in biosensor microfluidic systems for fluid mixing enhancement can be advantageous in the

deoxyribonucleic acid (DNA) hybridisation. This is because it requires no additional micromachining or flow channel wall coating to obtain the required flow channel properties.

Applications of wall-jet detector biosensor can be found in electrochemistry (Itagaki *et al*, 2000; Simison *et al*, 1999; Saad *et al*, 2000). Other applications include control of air contaminants in ecology and process hygiene (Curd, 1981; Saad *et al*, 2000; Settles *et al*, 1998), ceramic plasma actuator panels (Roth, 2003), and airless spray painting (Settles *et al*, 1998). It is worth mentioning that most of the aforementioned applications involved non-Newtonian fluids.

Traditionally, the wall jet has been applied in diverse fluid engineering and heat transfer applications such as film cooling on turbine blades, boundary-layer control over a wing in aerodynamics (Wang and Sun, 2000), cooling mechanism employed in Intel chip based Acer^{TM} Timeline systems (3810T, 4810T and 5810T) ultrathin laptops, fibre in headbox and black-liquid (tar) in gun in pulp and paper (Bibeau, 2007), flow in stirred tank (Bittorf and Kresta, 2004**)**, heating, condensate removal and ventilating, evaporation enhancement in defrosting of vehicle windscreens, gas turbine combustion chamber walls (Curd, 1981; Issa, 2006), petrochemical industries, liquid food processing industries (Gorla, 1984), window deicing, paper drying, metals annealing, heating of metal ingots (Gorla and Jeng, 1971).

1.6 Motivation and Objectives

As discussed in the previous sections, there are both practical and fundamental interests in understanding the characteristics of wall jet flows. A number of studies have been

conducted to investigate the characteristics of 2D laminar wall jet flows of Newtonian fluid. Admittedly, most practical wall jet flow applications are three-dimensional. It should be noted that the three-dimensional wall jet flow of non-Newtonian fluid is far more complicated than either free jet or classical near-wall flows such as fully developed channel flows and zero pressure gradient boundary layer. Yet, the 3D wall jet flow of non-Newtonian fluid has not received any research attention. There is a need, therefore, to conduct detailed research to advance understanding of 3D wall jet flow of non-Newtonian fluid. This would lead to the design of more efficient engineering systems and optimise wall jet applications.

The objectives of the present study are:

- Provide detailed velocity measurements in 3D laminar wall jet flows of both Newtonian and non-Newtonian fluids at various Reynolds numbers. These results will form the basis of the numerical results.
- To compute the 3D laminar wall jet flows studied experimentally using an in-house code, and to use these results to study the effects of Reynolds number and the specific fluid on the wall jet characteristics.

1.7 Methodology

To achieve the above mentioned objectives, three different types of fluids were used. These are a Newtonian fluid (water) and two shear-thinning non-Newtonian fluids prepared from aqueous solutions of xanthan gum. The experiments and numerical analyses are conducted over a wide range of Reynolds numbers in the laminar flow regime ($250 \leq Re_j \leq 800$, where Re_j is based on the maximum velocity at the pipe exit and

the pipe diameter). The velocity measurements are made using a planar PIV technique. An in-house numerical code based on colocated finite volume method was used to obtain the CFD results. The code solved the general governing equations of both non-Newtonian and Newtonian fluids. The SIMPLEC (Semi-Implicit Method for Pressure-Linked Equations Consistent) algorithm is used to solve pressure-velocity coupling equation. To take advantage of convergence without compromise of accuracy, deferred-correction method was employed. Deferred correction approach tends to promote numerical stability as it ensures that the coefficient matrix is more diagonal dominant. The benchmark experimental data sets are used to validate the CFD results.

1.8 The Structure of the Thesis

This thesis consists of five chapters and appendices. A comprehensive literature survey is presented in Chapter 2. The literature survey summarises the most relevant theoretical, numerical, and experimental investigations on laminar wall jet flows of both Newtonian and non-Newtonian fluids. The methodology used in the present work is reported in Chapter 3. Results and discussion are presented in Chapter 4, while conclusions and recommendations for future work are presented in Chapter 5. A detailed description of the PIV system and measurement uncertainties are provided in Appendix A while details on the mathematical models and numerical procedure are presented in Appendix B.

Chapter 2

LITERATURE SURVEY

2.1 Overview

The diverse applications of wall jet flow indicated in Section 1.5 necessitated extensive research on both laminar and turbulent wall jet flows in the past decades. These studies employed analytical, experimental and numerical methodologies. In this Chapter, a review of previous research on laminar wall jet flows of both Newtonian and non-Newtonian fluids is presented. Prior to the presentation of the review, a summary of prior works on rheological properties of shear-thinning non-Newtonian fluid is presented.

2.2 Shear-thinning Non-Newtonian Fluid

2.2.1 Introduction

As mentioned in Chapter 1, the apparent viscosities of most non-Newtonian fluids are a function of the velocity gradient (or shear rate). For shear-thinning fluids, the apparent viscosity decreases with increasing shear rate. This is due to the alignment of the fluid molecular particles in the flow field. Application of a shear rate to a resting fluid results in an instantaneous alignment of molecular particles in the direction of shear, thus providing a lower resistance to flow. This means that, for an advection dominant flow which is characterised by high shear rates, one would expect a lower participation of the viscosity on the flow dynamics.

Unlike Newtonian fluids for which the viscosity-shear rate relation is universal, the apparent viscosity for non-Newtonian fluids, specifically, shear-thinning is not uniquely described in all flows. It is therefore imperative that one has to develop a ‘new’ relation

for viscosity and shear rate that incorporate the unusual characteristics of the fluids. In this section, the various relations used to describe the apparent viscosity are summarised and their limitations for shear-thinning fluids are presented. This is followed by a description of the experimental approach used in previous works to obtain the viscosity-shear rate relationships.

2.2.2 Constitutive Equations

In Fig. 1.2, it was observed that shear-thinning non-Newtonian fluids may exhibit three distinct regions. These comprised of a lower Newtonian region where the apparent viscosity (μ) is independent of shear rate ($\dot{\gamma}$). In the second (intermediate) region, the apparent viscosity decreases with increasing shear rate. Mostly, the power-law equation which will be discussed later is used to describe the fluid characteristics in this region. The last region is the upper Newtonian region where the slope of the apparent viscosity is also independent of the shear rate. Both a minimum and a maximum effective viscosity (Newtonian regions) which every real non-Newtonian fluid has exhibited, depend on the physical chemistry at the molecular level. This notwithstanding, any model or relation describing the apparent viscosity should be able to fit at least the intermediate or second region. However, for flow problems involving high, low or zero shear rates, all the regions including the Newtonian regions are essential (Steffe, 1996; Denier and Dabrowski, 2004; Denier and Hewitt, 2004; Gutfinger and Shinnar, 1964).

Constitutive equations are used to describe the relationship between force and deformation in materials such as liquids. There are many variances of constitutive equation that have been proposed to mimic the behaviour of shear-thinning non-

Newtonian fluids. The most common of these models are shear-dependence power-law based, Bingham, and Herschel-Bulkley. This study will focus on shear-dependence power-law based models and a brief description of them will be given. A more in-depth description of these models and other non-Newtonian models can be found in Macosko (1994), Steffe (1996), Tanner (1985) and Bird *et al* (1987). Further, the analysis of shear-thinning fluid in this work will only involved the effect of steady shear rate. The rationale is that previous studies demonstrated that the extension and elongation effects are weak in aqueous solutions of xanthan gum and could be predicted on the basis of shear viscosity alone (Lindner *et al*, 2000). Also, the elastic property of xanthan gum based fluids is negligible (Lindner *et al*, 2000). Therefore, the fluid of interest is inelastic with negligible inertia effects.

For shear-thinning fluids, power-law model is the simplest and most commonly used viscous constitutive relation. The constitutive relation given by Bird *et al* (1987) is

$$\mu(\Lambda) = \lambda \Lambda^{n-1} \tag{2.1a}$$

$$\Lambda = [2\{(\partial u/\partial x)^2 + (\partial v/\partial y)^2 + (\partial w/\partial z)^2\} + (\partial u/\partial y + \partial v/\partial x)^2 + (\partial u/\partial z + \partial w/\partial x)^2 + (\partial v/\partial z + \partial w/\partial y)^2]^{1/2} \tag{2.1b}$$

where μ is the apparent viscosity, λ is a measure of the consistency of the fluid with higher values representative of more viscous materials, n is the power-law index, and Λ is the shear rate which is a function of the second invariant of the rate-of-strain tensor (Eqn. 2.1b). For shear-thinning fluids, n is less than unity while n is greater than unity for shear-thickening fluids. It should be remarked that Newtonian fluids can be considered as a special case of power-law non-Newtonian fluids with $n = 1$; in this case, λ becomes the dynamic viscosity.

Equation 2.1 is a good approximation to data from viscosity-shear rate relation for many polymeric liquids, and is well suited for a steady simple shear flow. This model accurately represents the shear-thinning region in the viscosity curve shown in Fig. 1.2. This model has unbounded viscosity function for both limits of shear rates. At both low and high shear rates, the apparent viscosity should approach a constant value instead of infinite and zero values, respectively, since *n* is usually less than unity. In view of these limitations, the validity of Eqn. (2.1) for shear-thinning fluids is restricted to a finite range of shear rate. In fact, it has been suggested that this model is not suitable for flows which possess a point of inflection in the velocity profiles (Denier and Dabrowski, 2004; Denier and Hewitt, 2004; Gutfinger and Shinnar, 1964). Since the velocity profiles for a wall jet has an inflection point, the simple model represented by Eqn. (2.1) is not suitable for wall jets. Obviously, any other model that accounts for these shortcomings associated with Eqn. (2.1) is implemented at the expense of simplicity.

To account for both the minimum and maximum effective apparent viscosities, Cross (1965) proposed the following model:

$$\mu(\Lambda) = \mu_\infty + (\mu_0 - \mu_\infty)[1 + (\lambda^2 \Lambda)^{1-n/2}]^{-1} \tag{2.2}$$

This four-parameter model also displays a nonzero bounded viscosity at both the upper and lower limits for some fluid flow applications. Therefore, Carreau (1972) proposed the following a power-law based model (Eqn. 2.3) to correct the singularities in the Cross model (Eqn. 2.2):

$$\mu(\Lambda) = \mu_\infty + (\mu_0 - \mu_\infty)\left[1 + (\theta\Lambda)^2\right]^{n-1/2} \tag{2.3}$$

where μ_0 and μ_∞ are the viscosities at the limits of low (zero) and high (infinity) shear

rate, respectively, for shear-thinning fluid and the converse is true for a shear-thickening fluid, θ is a characteristic time scale, which measures the scale at which shear-thinning effects becomes eminent, and all other parameters have their usual meaning. This model accurately models the shear-thinning region and Newtonian plateaus observed at low and sometimes high shear rates.

Subsequently, Yasuda *et al* (1981) proposed the following five-parameter model:

$$\mu(\Lambda) = \mu_\infty + (\mu_0 - \mu_\infty)/[1 + (\theta\,|\Lambda|^{1/2})^\beta]^{(1-n)/\beta} \tag{2.4}$$

where β describes the transition region between the zero-shear rate and the power-law region, and all other parameters have their usual meaning. For β = 2, Eqn. (2.4) becomes identical to Carreau model (Eqn. 2.3). There are also other models which tend to rectify the failure of the power-law model. For example, the Sisko (1958) model, which was originally proposed for lubricating grease, can describe the flow properties of shear-thinning materials at high shear-rate measurements such as yogurt for four to five decades of shear rate (Barnes *et al*, 1989). It should also be emphasised that the above mentioned models are only for steady shear flows, and do not describe normal-stress phenomena, unsteady shear flows, or flows which are not predominantly shear flows.

2.2.3 Fluid Characterisation

In the application of non-Newtonian fluids, one has no foreknowledge of the relation that describes the apparent viscosity and its dependence on the shear rate. Therefore, fluid characterisation has to be performed. During fluid characterisation, measurements are taken at several shear rates with corresponding viscosity values, and are extrapolated to

estimate the values. This method helps to detect rheological behaviour that may have an effect on processing, and also to estimate the viscosity-shear rate relation.

In the present work, an aqueous solution of xanthan gum (XG), which is one of the most common shear-thinning non-Newtonian fluids, is used. This high molecular weight extracellular polysaccharide produced by the bacterium *xanthomonus campestris* is used extensively in industry as a stabilising agent due to its unusual properties (Meyer *et al*, 1993; Zirnsak and Boger, 1998).

There are numerous studies on xanthan gum. Torrestiana *et al* (1989) obtained rheological behaviour for various concentrations of xanthan gum. The pseudoplastic behaviour of the xanthan gum solutions was in good agreement with the basic power-law model (Eqn. 2.1). Escudier and Smith (1999) used aqueous solution of xanthan gum as test fluids in their experimental study of turbulent flow in axisymmetric channels with sudden expansion. The relationship between the viscosity and shear rate for xanthan gum was well represented by the Cross model. Recently, Arzate *et al* (2004) performed fluid characterisations of three aqueous dispersions of xanthan gum. An inelastic shear-thinning fluid with the power-law curve was observed for all the solutions. In Table 2.1, a summary of xanthan gum based test fluids employed in previous studies are reported and most of them were described by the power-law model (Eqn. 2.1). The possible reason for this is that the operating shear rates were not low and high enough to predict the Newtonian regions of the fluid. It is worth commenting that most of the power-law model fluids were prepared from more than one solvent. Generally, the molecules of xanthan gum are sensitive to bacteriological degradation and therefore, for any long

period of experimentation a biocide agent is required (Escudier *et al*, 1995).

Table 2.1: Summary of previous test fluids (Xanthan Gum)

Authors	Grade	Solvent	XG	Biocide
Power law Model				
Torrestiana *et al* (1989)	Food	Water, Sucrose	0.5–10 kg/m^3	-
Stokes (1998)	Technical	Water, Sucrose	0.30 *wt*%	-
Bachmann *et al* (2000)	-	Glycerin, Sodium Iodide (NaI), Water	0.433g / litre	-
Arzate *et al* (2004)	-	Water	0.3-0.7 *wt*%	-.
Daugan *et al* (2004)	-	Water	750-3000 ppm	NaN_3
Dressler (2006)	Food	Wheat syrup, water	0.02 *wt*%	Na N_3
de Vicente *et al* (2006)	Food	Deionised Water	0.005-0.2 *wt*%	NaN_3
Smolka and Belmonte (2006)	Commercial	Water/KCL	0.039, 0.078 *wt*%	-
Cross Model				
Escudier and Smith (1999)	Food	Water	0.25 *wt*%	Kathon
Carreau–Yasuda Model				
Escudier *et al* (2001)	Food	Water	0.25 *wt*%	FD*
Sisko Model				
Escudier *et al* (1995)	Food	Purified water	0.15 *wt*%	FD*
Cavasada and Pinho (2004)	Food	Water	0.10-0.25 *wt*%	Kathon

* FD = formaldehyde

2.3 Wall Jet Flows

Wall jet flows are usually characterised by the decay of the local maximum streamwise velocity (u_m), the spread of the jet in both spanwise ($y_{0.5}$) and transverse ($z_{0.5}$) directions, and similarity of the streamwise velocity profiles. In addition, other quantities such as vorticity distributions, skin friction coefficient, and exterior momentum flux are useful in providing a better understanding of characteristics of wall jets.

2.3.1 Velocity Decay, Spread Rates, and Skin Friction Coefficient

Tetervin (1948) was one of the pioneers to conduct analytical studies on the two-dimensional (2D) laminar wall jet flow of a Newtonian fluid. In his analysis, it was assumed that both the velocity decay and the growth of the jet vary as a power of the downstream distance. The governing equations were solved using numerical integration. It was shown that the local maximum velocity decayed as one-half-power ($u_m \propto x^{-1/2}$) while the jet half-width increased as three-quarter-power of the downstream distance ($z_{0.5} \propto x^{3/4}$). Subsequently, Glauert (1956) carried out a similar analysis for both 2D laminar and turbulent wall jets of a Newtonian fluid in which he employed the boundary layer theory for the inner region and modeled the outer region as a free jet. Glauert showed that, in fact, the constant of proportionality in the expression of the velocity decay and the jet half-width given by Tetervin (1948) depends significantly on Reynolds number through the fluid viscosity and the jet exit velocity. In addition, he showed that the skin friction also depends strongly on the fluid viscosity. It is worth commenting that using the expressions $u_m \propto x^{-1/2}$ and $z_{0.5} \propto x^{3/4}$, it is easy to recognise that the local Reynolds number, Re_m ($= u_m \, z_{0.5} \, / \, \nu$) will increase as one-quarter-power of the downstream distance.

Subsequent to these early analytical works on 2D wall jets, several experimental (Bajura and Szewczyk, 1970; Tsuji *et al*, 1977; Cohen *et al*, 1992; Peters *et al*, 2008) and numerical (Issa, (2004, 2006); Gorla and Jeng, 1971) studies have been conducted to better understand the characteristics of wall jets of Newtonian fluid. The jet exit Reynolds number (Re_j), which is based on the maximum velocity at the jet exit and the slit height (d) was varied from 40 to 770. The results from these studies were consistent with the previous analytical studies by Glauert (1956) and Tetervin (1948). Issa (2006) who employed commercial CFD code (Fluent) also reported that the local skin friction coefficients ($C_{fj} = \tau_w / 0.5\rho u^2_j$, where τ_w is the wall shear stress, ρ is density and u_j is maximum velocity at the jet inlet) decreased with downstream distance. It should be noted that, with the exception of the PIV measurements by Peters *et al* (2008), all the experimental studies employed hot-wire anemometry.

Recently, Bhattacharjee and Loth (2004) investigated the effect of different inflow profiles (parabolic, ramp and uniform) and Reynolds numbers ($100 < Re_j < 10{,}000$) on the velocity and temperature distributions in 2D laminar and turbulent-transition co-flowing wall jet flows of a Newtonian fluid using a direct numerical simulation (DNS). The results show that the jet thickness which was defined as z value where $u = 0.25u_m$ tends to decrease as the Reynolds number increased for laminar flow ($Re_j < 550$). However, in the transitional regime (700-2,000), the jet grows with an increase in Reynolds number. This later trend was attributed to the significant level of instabilities of the wall jet as the Reynolds number increases. The entrainment of the ambient co-flow was also observed to be influenced by the inflow velocity profile, especially at higher Reynolds numbers. In general, the ramp profile consistently gave the lowest

entrainment, while the uniform profile gave the highest entrainment. This was attributed to the discontinuity of the uniform profile at the edge (the difference of the uniform velocities and the co-flow inflow velocities) which gave rise to a very high local gradient. It was argued that increased initial velocity gradients tend to create instabilities, and thus vortices which in turn increase momentum transport and scalar diffusion rates.

Since Glauert's (1956) work on a Newtonian fluid, a number of researchers have employed his approach to predict wall jet flows of non-Newtonian fluids. Unfortunately, only a few of these studies report the velocity decay, spread rates and skin friction coefficient. Filip *et al* (1991), for example, employed an analytical technique to investigate similarity conditions for laminar wall jets of power-law fluids past axisymmetric bodies. The functional dependence of the jet half-width and local maximum velocity decay on the power-law index, consistency and the streamwise distance was determined. It was reported that these wall jet characteristics are not only a function of streamwise distance but also the fluid properties such as the power-law index and consistency. On the other hand Gorla (1984) observed that, the skin friction coefficient decreases as the fluid becomes more shear-thinning or shear-thickening.

Krechetnikov and Lipatov (2002) theoretically analysed the self-similar solutions of 2D and 3D laminar wall jets of both Newtonian and shear-thickening non-Newtonian fluids. The similarity exponents for 2D laminar wall jet flow of the Newtonian fluid were in good agreement with those reported by Glauert (1956). For the 3D laminar wall jets of Newtonian fluids, it was established that the similarity exponent for both local maximum streamwise, u_m and spanwise, v_m velocities should be less than -0.5. Similarly, the

exponent of the jet half-width in the transverse direction ($z_{0.5}$) varies from 0.75 to 2.0 with the downstream distance. The corresponding exponent for the spanwise jet half-width ($y_{0.5}$) varies from 0.125 to 2.0. For the 3D laminar wall jets of shear-thickening non-Newtonian fluid, it was concluded that the similarity exponents for the three velocity components and jet half-widths were a function of the fluid behaviour index.

Craft and Launder (2001) numerically studied the spreading mechanisms in 3D laminar and turbulent wall jet flows. A computation of the laminar wall jet was performed in the similarity region of the flow. It was reported that the spread rates ($dy_{0.5}/dx$ and $dz_{0.5}/dx$) vary linearly with downstream distance. In addition, both spread rates depend on the local Reynolds number, Re_m. For the laminar wall jets the jet spreads more rapidly in the transverse direction than it does in the spanwise direction. In contrast, the turbulent wall jets spread more in the spanwise direction than in the transverse direction. They reported that the ratio of the spread rates ($dy_{0.5}$ / $dz_{0.5}$) for turbulent wall jets varies from 0.97 to 15.3 for various turbulence models. Based on these observations, it was concluded that there is insignificant streamwise vorticity and that viscous diffusion is principally responsible for the growth of 3D laminar wall jet.

Adane and Tachie (2008a, 2008b) numerically studied the effects of Reynolds number and power-law rheology on the characteristics of 3D laminar wall jet flows. The Reynolds number varies from 77 to 310 whereas the power-law index, n ranges from 0.4 to 1.0 with n = 1.0 being a Newtonian fluid. They reported that the wall jet characteristics such as the jet growth, jet half-widths, skin friction coefficient, and maximum velocity decays depend significantly on Reynolds number and fluid type,

specifically the power-law index.

2.3.2 Similarity of Velocity Profiles

As the wall jet evolves downstream, the dimensionless velocity profile also changes and then becomes universal in the similarity region. In fact, it has been shown that the velocity profile in the similarity region has no upstream memory effect (Issa, 2006; Glauert, 1956). However, the onset of the self-similar region may depend on both the inlet Reynolds number and the flow field. For instance, for 2D laminar wall jet flow of Newtonian fluid, it was found that the self-similar region begins at $x / d = 18$ for $Re_j = 377$ (Bajura and Szewczyk, 1970), $x / d = 10$ for $Re_j = 635$ (Tsuji *et al*, 1977), and $x / d = 30$ for $Re_j = 466\text{-}725$ (Cohen *et al*, 1992). For $Re_j = 500$, Kanna and Das (2005) reported that the flow becomes self-similar at $x / d = 18$. Adane and Tachie (2008a, 2008b), on the other hand, reported the onset of self-similarity for $Re_j = 77\text{-}310$ to be $x / d = 5$ irrespective of the fluid.

Glauert (1956) presented an analytical streamwise velocity profile for 2D wall jet flows. The results from subsequent experimental studies (Bajura and Szewczyk, 1970; Tsuji *et al*, 1977; Cohen *et al*, 1992; Peters *et al*, 2008) showed very good agreement with the analytical profile obtained by Glauert (1956). Bajura and Szewczyk (1970) performed experiment on a Newtonian fluid and for the Reynolds numbers in the ranges: $270 \leq Re_j \leq 770$. They reported a single velocity profile in the self-similar region for each Reynolds number studied. There was no distinguishable difference between the experimental and analytical profiles in the region $z/z_{0.5} \leq 1.25$. Similar observations were also made in other previous experimental works (Cohen *et al*, 1992; Tsuji *et al*, 1977). The agreement

between the measured velocity (Bajura and Szewczyk, 1970; Cohen *et al*, 1992; Tsuji *et al*, 1977) and the analytical profiles close to the outer edge ($z/z_{0.5} > 1.25$) is not particularly good. On the contrary, the PIV results presented by Peters *et al* (2008) collapsed onto the analytical profile even in the outer edge ($z/z_{0.5} > 1.25$) of the jet. It is not clear if the discrepancy between the experimental and analytical data in the outer region is due to the limitation of the hot-wire anemometer. It is also worth mentioning that none of these experimental works was able to make measurements in the immediate vicinity of the wall ($z/z_{0.5} < 0.08$). In general, irrespective of the technique employed, it was observed that the velocity profile does not depend on the inlet Reynolds number. Meanwhile, the numerical results (Issa, (2004, 2006); Kanna and Das, 2005) also showed a very good agreement with the analytical results by Glauert (1956).

Tsuji *et al* (1977) also reported that the velocity profiles at $Re_j = 635$ were in better agreement with laminar analytical profile (Glauert, 1956) up to approximately $x/d = 45$. On the contrary, the velocity profile at $x/d = 60$ was rather in a better agreement with the analytical profile reported for a turbulent wall jet (Glauert, 1956).

As indicated in the earlier paragraphs, wall jet flows of non-Newtonian fluids have not received significant research attention. Gorla (1984) analytically established the existence of the similarity condition for 2D laminar wall jet of a non-Newtonian fluid in plane, divergent and convergent surfaces. It was observed that in the inner region, the normalised velocities obtained on the convergent surface are higher than those in a plane and divergent surface. Meanwhile, in the outer region the reverse is true; that is, the normalised velocities are lower on a convergent surface and higher on a divergent

surface. Similar analysis was performed by Filip *et al* (1991) for laminar wall jet flows of power-law fluids past axisymmetric bodies. They consider shear-thinning, Newtonian and shear-thickening fluids. The similarity profile was observed to be fluid dependent. In the region $z/z_{0.5} > 0.3$, the shear-thinning fluid has higher normalised velocities whereas the shear-thickening fluid has lower normalised velocities. However, in the very near-wall region ($z/z_{0.5} \leq 0.3$), there was no difference among the profiles.

Craft and Launder (2001) presented the similarity profiles in both transverse and spanwise directions at various *x/d* locations for their 3D laminar wall jet. It should be noted that the *x/d* locations were defined in terms of local Reynolds number, Re_m which ranges from 38 to 308. They reported good agreement among profiles.

The numerical results presented by Adane and Tachie (2008a, 2008b) also showed a self-similar condition in both the transverse and spanwise directions and irrespective of the inlet Reynolds number for fluids with higher power law index (n = 0.7 and 1.0). At a lower value of n (i.e., n = 0.4), however, the profiles particularly those at a lower Reynolds number (Re_j = 77) failed to collapse onto a universal curve. It should be mentioned that all the previous works on non-Newtonian fluids are based on the power-law model (Eqn. 2.1).

2.3.3 Vorticity Distributions

One of the applications of the wall jet is in the area of mixing as mentioned in Chapter 1. This mixing is done through vortex generation, a phenomenon that influences the spreading of the jet. Previous studies (Craft and Launder, 2001; Bhattacharjee and Loth, 2004) argued that the spreading mechanism in laminar wall jet flows is dominated by

viscous diffusion. In fact, Craft and Launder (2001) attributed the higher spread rate observed in the spanwise direction than in the transverse direction to an intense streamwise vorticity generated in turbulent flow. Meanwhile, the relatively lower jet spread rate in the spanwise direction compared to the spread rate in the transverse direction was attributed to the insignificant streamwise vorticity generated in a laminar wall jet.

The governing equation of the flow is given as:

$$\rho\left(\mathbf{v}\nabla\mathbf{v}+\frac{\partial\mathbf{v}}{\partial t}\right)=\mu\nabla^2\mathbf{v}-\nabla p \qquad (2.5)$$

where **v** is a velocity vector, *t* is time, *p* is pressure and all other variables have their usual meanings. The above equation (Eqn. 2.5) can be rewritten in terms of the streamwise vorticity, ω_x as follows:

$$\frac{D\omega_x}{Dt}=\underbrace{\omega_x\frac{\partial u}{\partial x}}_{I}+\underbrace{\omega_y\frac{\partial u}{\partial y}+\omega_z\frac{\partial u}{\partial z}}_{II}+\underbrace{\frac{\mu}{\rho}\left(\frac{\partial^2\omega_x}{\partial y^2}+\frac{\partial^2\omega_z}{\partial z^2}\right)}_{III}$$

where the streamwise vorticity, $\omega_x=\partial v/\partial z-\partial w/\partial y$, spanwise vorticity, $\omega_y=\partial w/\partial x-\partial u/\partial z$, transverse vorticity, $\omega_z=\partial u/\partial y-\partial v/\partial x$, and all other variables have their usual meanings. Based on the coordinates system adopted in the present work, counter-clockwise rotation is taken as positive.

The vortex turning (ω_y and ω_z, term II) is responsible for the generation of the streamwise vortex whereas viscous diffusion (term III) basically diffused the vorticity (Launder and Rodi, 1981; Craft and Launder, 2001). In wall jet flows, the vortex stretching (term I) actually reduces the vorticity since $\partial u/\partial x$ is always less than zero. In the similarity

region of wall jet flows, the streamwise vorticity produces a laterally outward secondary flow and thereby intensifies the interaction between the jet and the ambient fluid which in turn increases the spread in the spanwise direction. Craft and Launder (2001) showed that the streamwise vorticity in the inner region is positive but negative in the outer region.

2.4 Closure

The review of previous studies led to the following observations:

- There are no experimental works conducted to study the characteristics of 3D laminar wall jet flows of both Newtonian and non-Newtonian fluids.
- There have been only analytical studies on the 2D laminar wall jet of non-Newtonian fluid.

Even the previous numerical studies on the non-Newtonian fluid are based on power-law model for which the apparent viscosity is unbounded. Thus, there is a need to provide benchmark experimental data sets to provide a better understanding of 3D laminar wall jets of both Newtonian and non-Newtonian fluids, and also for the purpose of validating both numerical and analytical results.

Chapter 3

EXPERIMENTAL AND NUMERICAL TECHNIQUES

This chapter provides an overview of both the experimental and numerical techniques used. Prior to the presentation of the techniques used, a description of the procedure employed for the preparation of the test fluids and their rheology is presented. The experimental test facility and measurement technique used are described. This is followed by the description of the numerical technique. A more thorough description of the techniques can also be found in Appendix A and Appendices B for the experiment and numerical methods, respectively.

3.1 Fluid Characterisations

3.1.1 Test Fluids

The non-Newtonian fluids were obtained by preparing aqueous solution of xanthan gum (commercial food-grade) with a filtered tap water as solvent. Two stock solutions were prepared by dissolving 0.005 *wt*% and 0.01 *wt*% of xanthan gum in the solvent. In the forthcoming sections, the fluids corresponding to 0.005 *wt*% and 0.01 *wt*% of xanthan gum will be denoted by XG005 and XG010, respectively. The tap water was only filtered to take out the debris and not the minerals.

The stock solution of the xanthan gum was prepared by thoroughly dispersing the required amount of gum in the solvent. The xanthan gum solution was continuously stirred at ambient temperature of 23°C until the gum was evenly dissolved (including the disappearance of all microgels). A typical stirring of the solution lasted for about 2-3 hours at a speed of 200-300 rpm. The aqueous solution was allowed to sit for at least 6

hours before use to allow a complete hydration of the molecules.

3.1.2 Rheology

All measurements of viscometric characteristics were carried out using a controlled shear-rate TA Instruments rheometer with stainless steel 0.04 m diameter parallel plate geometry. The measurements were performed at a temperature of 23°C. Temperature control of the TA rheometer was achieved via a plate that uses the Peltier effect to control the temperature of the sample to within ±0.1°C. The flow curves (i.e. shear viscosity versus shear rate) for the test fluids and the solvent are shown in Fig. 3.1. Figure 3.1 showed a shear-thinning behaviour with the two Newtonian plateaus for the xanthan gum based solutions (XG005 and XG010).

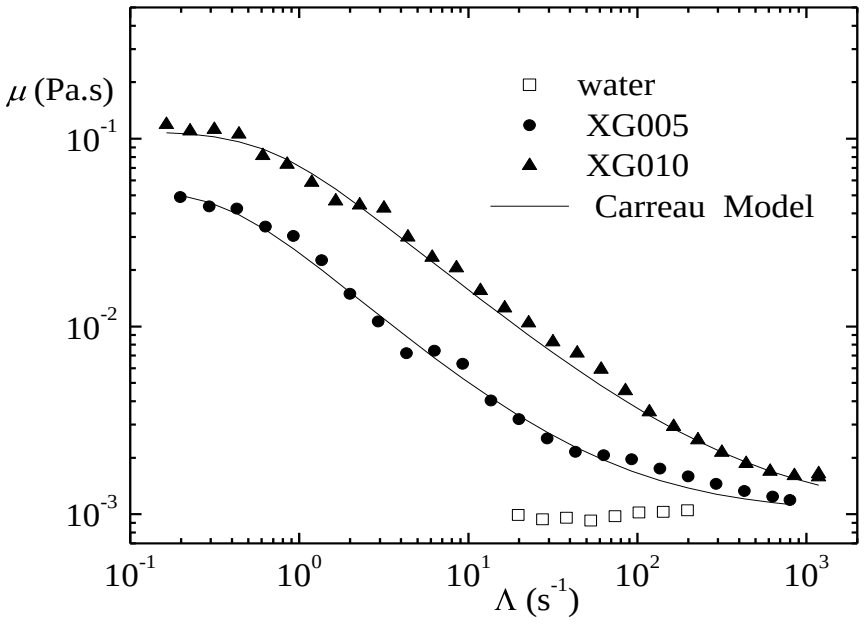

Figure 3.1: Shear viscosity data of the test fluids.

The relationship between the apparent viscosity and shear rate is well represented by the Carreau model (Eqn. 2.3) for both test fluids. Using a least-square method, a curve

fitting of this model to individual solutions (XG005 and XG010) was performed, and the model parameters are summarised in Table 3.1 for all the test fluids. From Table 3.1, the XG010 solution is regarded as the most viscous fluid with the zero shear rate viscosity being almost one hundred times the infinite shear rate viscosity. It is worth mentioning that the aqueous solutions of the xanthan gum are known to demonstrate weak extension and elongation effects and could be predicted on the basis of shear viscosity alone (Lindner *et al,* 2000). Also, the elastic property of these fluids is negligible (Lindner *et al,* 2000). In fact, for the present test fluids, the elasticity which is measured by the normal stress was below the measurable tolerance of the rheometer. Therefore, the fluids are considered inelastic with negligible inertia effects.

Table 3.1: Carreau model parameters

Fluids	μ_0 (Pa•s)	μ_∞ (Pa•s)	θ (s)	n
Water	1.0×10^{-3}	-	0	1.00
XG005	0.055	1.0×10^{-3}	2.66	0.21
XG010	0.110	9.98×10^{-4}	1.50	0.26

3.2 Experimental Procedure

3.2.1 The Wall Jet Facility

A schematic diagram of the set-up for the wall jet facility is shown in Fig. 3.2 while a picture of the experimental set-up during a typical measurement in the symmetry plane is shown in Fig. 3.3. As shown in these figures, the set-up consists of the test section, a variable speed centrifugal pump (model no. 75211-62) supplied by Cole-Parmer Canada Inc. (Montreal, Canada), tubing, and a storage tank. This variable speed centrifugal

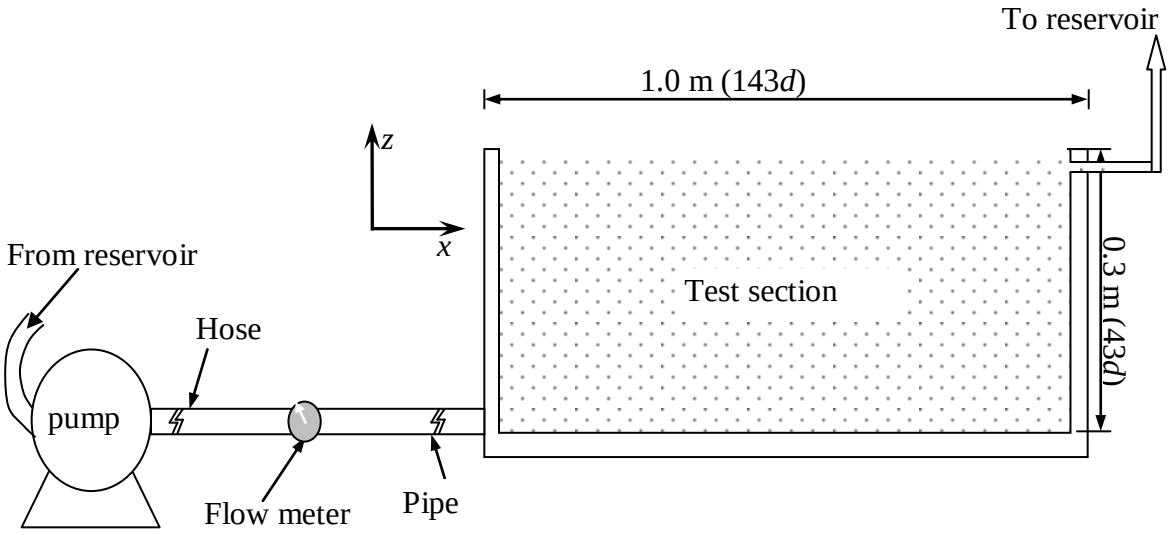

Figure 3.2: Schematic diagram of the wall jet facility.

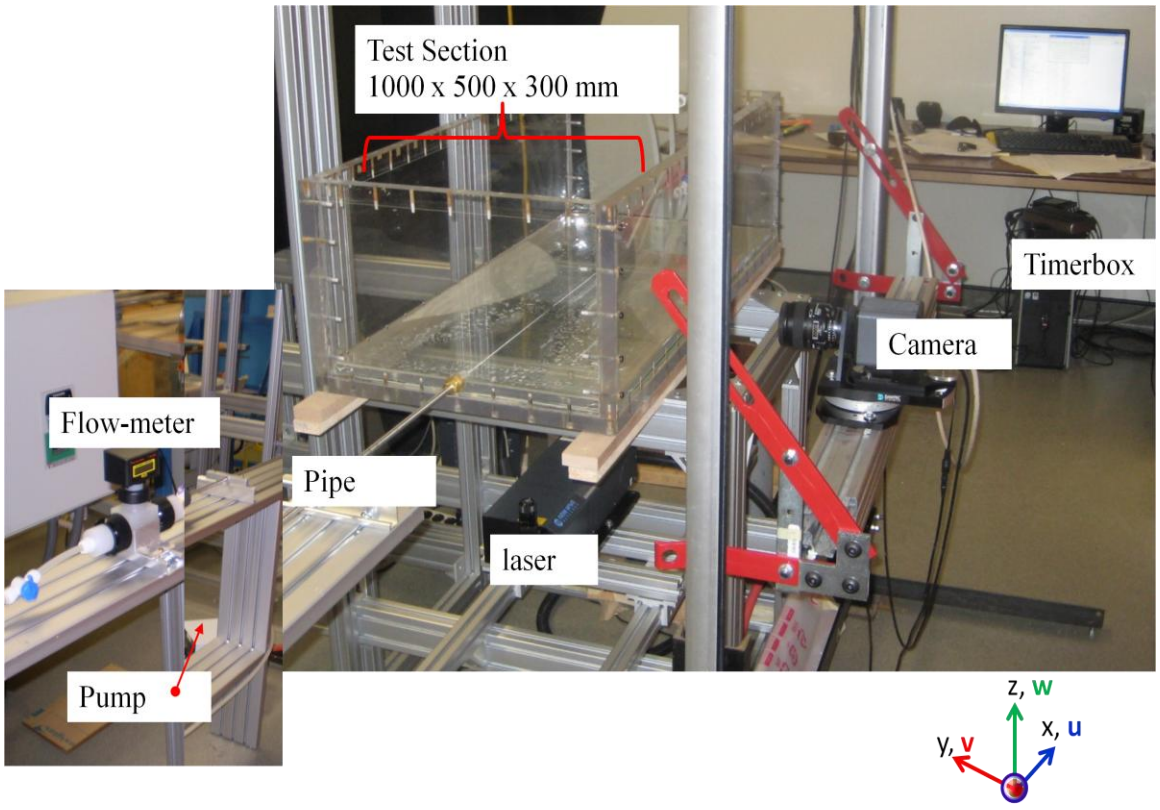

Figure 3.3: A picture showing an **e**xperimental set-up for measurements in the symmetry plane.

pump with maximum flow rate of 7 gallon/min was used for the higher flow rate experiments. For the lower flow rate experiments, it was not possible to generate the wall jet flow with a constant velocity using the centrifugal pump. Therefore, the flow was generated under gravity.

The inlet pipe has diameter, $d = 7 \pm 0.21 \times 10^{-3}$ m and is 1.10 m long (157d) to ensure a fully-developed flow at the exit section. The pipe is made from steel. To facilitate optical access and flow visualization, the walls of the test section were constructed from 0.025 m thick transparent acrylic plates having a refractive index of 1.47. The test section of the channel has a length of 1.00 m (143d), height of 0.30 m (43d), and width of 0.50 m (71d). The coordinate system used here is the same as that in Chapter 1.

3.2.2 Test Conditions

Measurements were made for the following three different fluids: Newtonian fluid (water), and two non-Newtonian fluids (XG005 and XG010). The wall jet flow was characterised by a generalised inlet or initial Reynolds number, Re_j at the pipe exit which is given as:

$$Re_j = \rho u_j^{2-n} d^n / \mu_o \theta^{n-1} \tag{3.1}$$

where u_j is the maximum velocity at pipe exit and all other parameters have their usual meanings. The Newtonian fluid can be considered as a special case of a power-law based non-Newtonian fluid. In this case, $n = 1.0$ whereas the viscosity at zero shear rate, μ_0 becomes the dynamic viscosity of the fluid with the characteristic time scale, θ taking a value of zero.

The Reynolds numbers for the measurements were in the range: $250 \leq Re_j \leq 800$. Due to

optical challenge at the inlet of the jet (x/d = 0), the measured inlet velocities were obtained at $x/d \approx 0.5$. Table 3.2 provides a summary of the expected exit jet velocity (u_j) which is obtained from Eqn. 3.1 and the measured jet velocity (u_j^m). It should be remarked that the more viscous fluid will have higher velocity at the same Reynolds number. It is clear from Table 3.2 that the expected velocity is approximately 0.0 to 6% higher than the corresponding measured values.

Table 3.2: Summary of inlet jet velocities, u_j (m/s) with Reynolds numbers

Re_j	Newtonian		XG005		XG010	
	u_j	u_j^m	u_j	u_j^m	u_j	u_j^m
250	-		0.106	0.100	0.224	0.214
310	0.044	0.042	-	-	-	-
420	-		0.142	0.135	0.302	0.300
800	0.114	0.110	0.203	0.203	0.438	0.425

For each test condition corresponding to a Reynolds number (Re_j), measurements were conducted in various x-z and x-y planes positioned either at the plane of symmetry (y = 0) or z_m. These measurements were performed over a streamwise distance that covers both the developing and self-similar regions. The experimental procedure is given in the next section.

3.2.3 Measurement Procedure

The velocity measurements were performed using a particle image velocimetry (PIV) technique. A detail description of the principle of PIV is presented in Appendix A. Therefore, only the various components of the specific PIV system, image acquisition

and post-processing are presented in this section.

The flow was seeded with 10 μm hollow glass spheres seeding particles having a specific gravity of 1.4. Based on the analysis and expressions provided in Section A.1.3 (Appendix A), the settling velocity and particle response time were estimated to be v_s = 2.18 x 10^{-11} m/s and t_r = 7.78 x 10^{-6} s, respectively for the Newtonian fluid. The corresponding values based on apparent viscosity at zero shear rate for XG005 and XG010 are 3.96 x 10^{-13} m/s and 1.41 x 10^{-7} s and 1.98 x 10^{-13} m/s and 7.07 x 10^{-8} s, respectively. An Nd-YAG dual pulsed-laser (120 mJ/pulse) of 532 nm wavelength was employed to illuminate the flow field. Measurements were performed in both the symmetry plane of the jet (y = 0) and the x-y plane at z_m. For the measurement in the symmetry plane, the laser sheet was positioned at the bottom of the channel and the camera at the side. A 12 bit HiSense 4M camera (2048 pixels × 2048 pixels CCD array size and a 7.4 μm pixel pitch) was used to image the flow field. Several planes of measurements were made in order to cover the region $0 \leq x/d \leq 70$. The measurement plane had a field of view of 90 mm × 90 mm. The time interval between pulses was chosen such that the maximum particle displacement was 25% of the interrogation window size. The particle image diameter was estimated to be d_p = 1.99. This value is very close to the recommended value of $d_p \approx 2$ pixels required to minimize peak locking (Raffel *et al,* 1998). In fact, histograms (Fig. A.3, Appendix A) of the raw velocity vectors confirmed that there was no observable peak locking.

The PIV images were post-processed using the adaptive-correlation option of FlowManger 4.50.17 (Dantec Dynamics, Ramsey, New Jersey, USA) to obtain the

instantaneous velocity vectors. Interrogation windows (IWs) of Δx = 16 pixels × Δz = 16 pixels with 50% overlap were used to process the images. The corresponding physical spacing between vectors was Δx = 0.35 mm × Δz = 0.35 mm in the symmetry planes. The adaptive correlation uses a multi-pass fast Fourier transform (FFT) cross-correlation algorithm to determine the average particle displacement within the IW. A three-point Gaussian curve fit was used to determine particle displacement with sub-pixel accuracy. Based on preliminary convergence test, for the Newtonian fluid, it was decided to use 450 and 700 instantaneous image pairs, respectively, to compute the velocities for Re_j = 310 and Re_j = 800 experiments. Meanwhile, 750 instantaneous image pairs were used to compute the velocity vectors for the non-Newtonian fluids.

A similar procedure was employed for the measurements in the $x - y$ plane. Here, the camera was positioned at the top of the channel and the laser sheet was shot from the side. The measurements were made at a field of view of 61 mm × 61 mm for several planes in the region $0 \leq x/d \leq 45$ for $x - y$ planes. The instantaneous images were post-processed with IW of 32 pixels x 32 pixels with 50% overlap, and the corresponding physical spacing between vectors was 0.48 mm.

3.2.4 Measurement Uncertainty

Measurement uncertainty analysis was performed following the methodologies proposed and explained by Coleman and Steele (1995) and Forliti *et al* (2000). A complete description of the uncertainty analysis is presented in Appendix A.2. In general, a complete uncertainty analysis involves identifying and quantifying both the bias and precision errors in each part of the measurement chain. In PIV technique, the accuracy of

velocity measurement is limited by the accuracy of the sub-pixel interpolation of the displacement correlation peak. Other sources of measurement uncertainties include particle response to fluid motion, light sheet positioning, light pulse timing, and size of interrogation window. Detailed analyses of bias and precision errors inherent in PIV technique are available in Prasad *et al* (1992) and Forliti *et al* (2000). Forliti *et al* (2000) showed that the Gaussian peak-fitting algorithm has the lowest bias and precision errors. On basis of the size of interrogation window and curve fitting algorithm used to calculate the instantaneous vector maps, and the large number of instantaneous images used to calculate the velocity, the uncertainty in the velocities at 95% confidence level is estimated to be ± 1.9% for the measurements in the Newtonian fluid. Close to the plane wall, uncertainties in velocities are estimated to be ± 2.7%. The corresponding values for the non-Newtonian fluids are ± 3.2% and ± 3.5%, respectively.

3.3 Numerical Procedure

3.3.1 Governing Equations and Boundary Conditions

The governing equations for an incompressible flow may be written in tensor form as follows:

Continuity equation:

$$\frac{\partial u_i}{\partial x_i} = 0 \tag{3.2}$$

Momentum equation:

$$\rho\left(u_j \frac{\partial u_i}{\partial x_j} + \frac{\partial u_i}{\partial t} \right) = \frac{\partial}{\partial x_j}\left[\mu\left(\frac{\partial u_i}{\partial x_j} + \frac{\partial u_j}{\partial x_i} \right) \right] - \frac{\partial p}{\partial x_i} \tag{3.3}$$

where u_i represents the velocity component corresponding to the Cartesian coordinate x_i, p is the pressure, and μ is either the dynamic or apparent viscosity depending on the fluid. Based on the fluids rheology given in Section 3.1.2, the apparent viscosity is computed using Eqn. 2.3.

The boundary conditions used for the computational domain shown in Fig. 3.4 are as follows:

i) Inlet ($x/d = 0$): a fully developed pipe flow profile in the region $0 < z/d < 1$ and $0 < y/d < 0.5$, specified; otherwise, $u = v = w = 0$. For the Newtonian fluid, the velocity profile is given as $u(r)/u_b = 2\,[1 - (2r/d)^2]$, where u_b is the bulk velocity, and r is the local radius which is a function of y and z. There is no analytical solution for Carreau fluid; therefore, a complete pipe flow was computed. The fully developed profiles will be presented and discussed subsequently (Section 3.3.2).

ii) Outlet ($x/d = 143$): pressure, $p_{spec} = 0$

iii) Symmetry plane ($y/d = 0$): $d(u, v, w, p)/dy = 0$. This was done to take advantage of the symmetric nature of the 3D wall jet flow field.

iv) Side wall ($y/d = 35.5$): $u = v = w = 0$.

v) Bottom wall ($z/d = 0$): $u = 0$, $v = 0$ and $w = 0$.

vi) Top surface ($z/d = 43$): $d(u, v)/dz = 0$, and $w = 0$.

It should be remarked that the computational domain is a replicate of the experimental domain including the coordinate system, i.e., streamwise, spanwise and transverse directions corresponding to x-, y- and z-axes, respectively; $x = 0$ at the pipe exit, $z = 0$ on the bottom wall and $y = 0$ in the symmetry plane of the jet. In the experimental set-up,

the top was open and therefore zero gradient was assumed with u and v at z/d = 43 obtained by using first-order approximation. At the outlet plane (x/d = 143) where pressure was specified, the normal velocity, u was obtained from the mass flux. Previous work (Adane and Tachie, 2008a) demonstrated that using zero-gradient at the outlet plane produced instability of the solver. It is therefore prudent to specify the pressure which is here taken as zero since one would expect nearly uniform distribution of the velocity at the outlet. Also, the outlet is far from the region of interest and therefore would not have a significant effect on the solution. The viscosity at the boundaries was obtained by first-order extrapolation. Meanwhile, the pressure at boundaries where pressure was not prescribed was obtained by a linear extrapolation from the two nearest neighbouring cells (Ferziger and Perić, 2002).

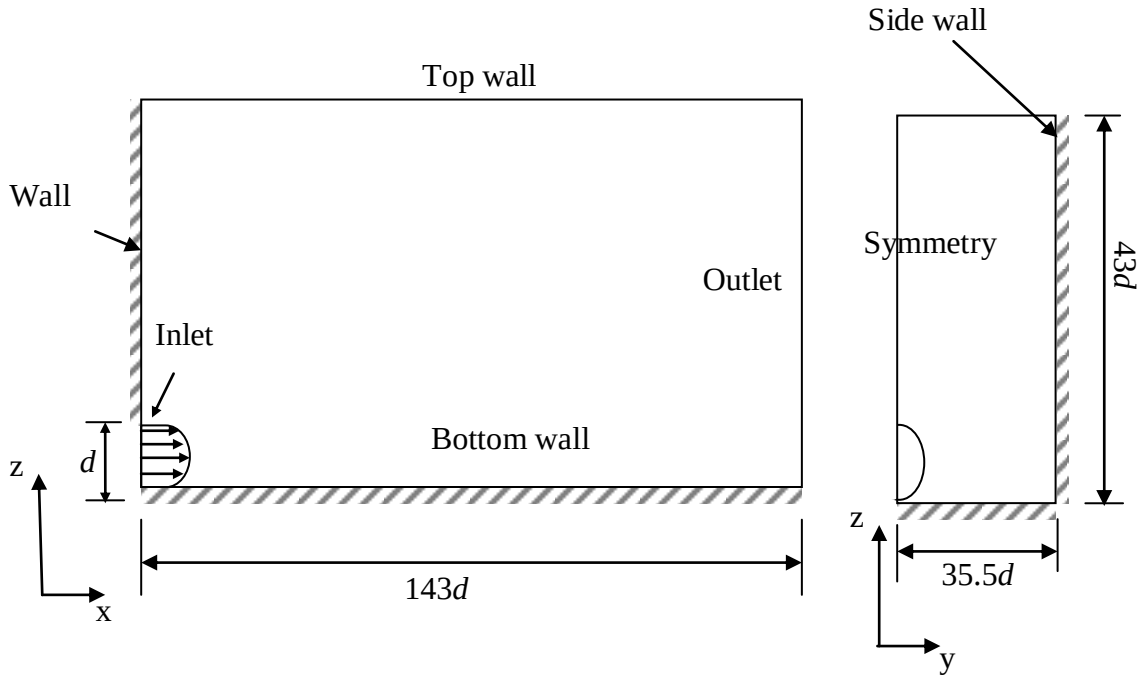

Figure 3.4: Schematic of the present computational flow domain with boundary conditions.

3.3.2 Fully Developed Velocity Profiles at Pipe Exit

The fully-developed velocity profiles normalised by the bulk velocity, U (= u/u_b) for the two non-Newtonian fluids (XG005 and XG010) at Re_j = 250, 420 and 800 are shown in Fig. 3.5. The transverse distance, z is normalised by d, i.e. Z = x/d. In each of the plots, a fully-developed profile for laminar flow of Newtonian fluid is shown for comparison.

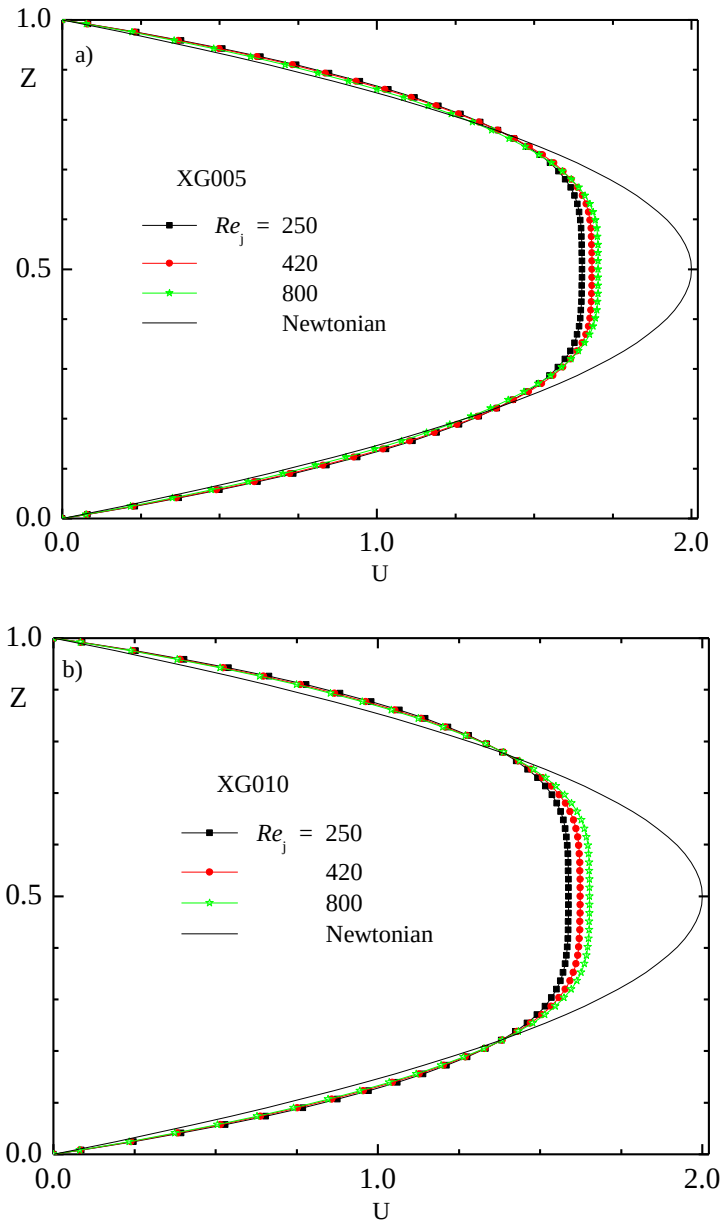

Figure 3.5: Comparison of the fully-developed velocity profiles at various Re_j: a) XG005 and b) XG010 with Newtonian fluid superimposed.

Unlike the parabolic velocity profile for the Newtonian fluid, the profiles for the two shear-thinning non-Newtonian fluids are typically 'plug-like' in the core region. For a given xanthan gum concentration, the profile becomes flatter as the inlet Reynolds number decreases. When the inlet Reynolds number is kept the same, the fluid with a higher concentration (XG010) becomes flatter. In the regions: $Z \geq 0.7$ and $Z \leq 0.3$, there is no significant difference among the various profiles for XG005 fluids. These profiles are also similar to the Newtonian velocity profile in the regions: $Z \geq 0.75$ and $Z \leq 0.25$. Although the various profiles for XG010 are also similar in the regions, $Z \geq 0.75$ and $Z \leq 0.25$, these profiles are distinctly different from the profile for the Newtonian fluid. It should be noted that the ratio of the maximum velocity to the bulk velocity (u_j/u_b) is 1.65, 1.68 and 1.73, respectively for Re_j = 250, 420 and 800 for XG005. The corresponding values for XG010 fluid are 1.58, 1.62 and 1.66 for Re_j = 250, 420 and 800, respectively. These values are significantly lower than $u_j/u_b = 2.0$ for the Newtonian fluid.

3.3.3 Numerical Solution Method

The conservation equations (3.2) and (3.3) were discretised using a colocated finite-volume method for general orthogonal grids which is described in detail in Ferziger and Perić (2002). Here, only a brief summary is provided, more details can be found in Appendix B. The standard central difference scheme (CDS) is used for the diffusion terms. In order to achieve a more accurate representation of the convective terms, the CDS was implemented in the form of a deferred correction (Khosla and Rubin, 1974) to the first-order upwind approximation (UDS). The main advantages of deferred correction are stability, simplicity, and computer-memory saving. The deferred correction approach tends to promote numerical stability as it ensures that the coefficient matrix is more

diagonal dominant. The discretisation of the equations (3.2) and (3.3) becomes:

$$\sum_f \dot{m}_f = 0 \tag{3.4}$$

$$C_P u_{i,P} + \sum_k C_k u_{i,k} = b_\phi \tag{3.5}$$

For a specific nodal point, 'P' index k runs over the six nearest neighbours, $\dot{m}_f$ and u_i (u, v and w) are the mass fluxes through the control volume faces and nodal velocity, respectively. Meanwhile, the coefficients C_k consists of contribution from the implicitly treated parts of both convection and diffusion fluxes, whereas b_φ contains the pressure term for the respective velocity component and the explicitly treated parts of convection and diffusion. It should be mentioned that at convergence the UDS terms are expected to cancel out leaving only CDS terms. Also, the deferred correction approach is implemented by using a blending factor ranging from 0.0 to 1.0 with 0.0 corresponding to UDS whereas 1.0 is for CDS. For results presented here, a blending factor of 1.0 was used. For the time integration, a three-time level implicit method scheme is employed via deferred correction with first order implicit Euler scheme. The time integration is formally O (Δt^2) accurate. The under-relaxation parameter was incorporated to account for the nonlinear nature of the equation systems and stability of the solver (Patankar, 1980).

Pressure-velocity coupling on the colocated grid was achieved with interpolation scheme suggested by Rhie and Chow (1983). A segregated solution approach using the SIMPLEC algorithm (Van Doormaal and Raithby, 1984) was used. A Poisson equation solved for the pressure-correction field by enforcing mass conservation is as follows:

$$C_P^m p_P + \sum_k C_k^m p_k = b_m \tag{3.6}$$

where b_m is an artificial mass source for each control volume left after mass conservation, and C_k^m is pressure-correction coefficients. The boundary velocities are assumed to be prescribed and are not corrected except at boundaries where pressure values are prescribed. This condition is equivalent to specifying a zero gradient on the pressure correction. The velocities on pressure prescribed boundaries are, however, corrected.

The resulting algebraic Eqns. (3.5 and 3.6) for nodal velocities and pressure correction, respectively, were solved using a 3D version of the strongly implicit procedure (SIP) solver (Stone, 1968). The solution algorithm consists of a sequential solution of the three discretised momentum equations and the pressure-correction equation. The velocities, mass fluxes and pressure are then corrected. These values are used to update the coefficients and to calculate the viscosity in the case of the non-Newtonian fluids for the next outer iteration. The viscosity is thus treated explicitly. For each SIMPLEC iteration (outer iteration), up to five and fifteen SIP iterations are performed for each of the velocity components and the pressure field, respectively. The SIP iterations are terminated if the residual level drops by a factor of five. A solution to a tighter tolerance yielded no advantage since the variables need to be updated in outer iterations. The convergence criterion, which is the residual norm (the sum of absolute residuals over all control volumes) for each equation, was set to 10^{-4}. It is noteworthy that pseudo-time marching algorithm was performed for the Newtonian fluid at Re_j = 800. Even for such flow conditions, only a steady-state condition was sought. All the simulations were performed on a Sun V20z machine with 4031MB memory. The longest computing time

for the Newtonian fluid is 3 days at Re_j = 800 for the medium grid which is 6.27 million cells. Preliminary results show that the velocities decrease to zero very early for the non-Newtonian fluids. Since these fluids required a very significant amount of computing time, the streamwise distance was reduced to x/d = 100. It should be noted that this region is still far from region of interest. Even with such a relatively small domain, a typical computation time was 3 days for the medium grid (6.68 million cells).

A thorough checked for internal consistency was performed on the code that implements the numerical model. As will be presented and discuss in Section 3.4, various benchmark problems including lid-driven cavity flows and fully-developed channel and pipe flows were used to validate the code. In addition, 3D laminar wall jet flows were computed using a commercial CFD code, Fluent. In all the test cases, very good agreement was obtained.

3.3.4 Mesh Independence

The goal of this section is to determine the grid structure that ensures acceptable numerical accuracy. Three grid meshes were used to investigate the mesh sensitivity of the computation. The computational domain shown in Fig. 3.4 was divided into a number of control volumes by assigning nodes on respective direction. The grid was uniformly spaced in the pipe region, and beyond that region clustered grids were used for both transverse and spanwise direction. In the streamwise direction, geometric expansion was used for grid spacing. The test was conducted using coarse, medium, and fine grids made up of coarse (3.47 million cells), medium (6.27 million cells) and fine (12.9 million cells) for the Newtonian fluid. The maximum and minimum grid sizes (Δx, Δy and Δz)

are given in Table 3.3. The streamwise nodes were kept constant for all the three meshes investigated. Preliminary tests were performed to assert that the chosen number of nodes showed no significance influence on the results. The corresponding meshes used for the two non-Newtonian fluids are coarse (2.85 million cells), medium (6.68 million cells) and fine (14.99 million cells), and the maximum and minimum grid sizes are also given in Table 3.3. A sample of the computational mesh is shown in Fig. 3.6.

Table 3.3: Mesh sizes in m

Mesh	**Δx (min, max)**	**Δy (min, max)**	**Δz (min, max)**
Newtonian Fluid			
Coarse	6.26×10^{-4}, 4.60×10^{-3}	1.40×10^{-4}, 2.39×10^{-2}	1.40×10^{-4}, 2.34×10^{-2}
Medium	6.26×10^{-4}, 4.60×10^{-3}	1.40×10^{-4}, 1.72×10^{-2}	1.40×10^{-4}; 2.00×10^{-3}
Fine	6.26×10^{-4}, 4.60×10^{-3}	1.13×10^{-4}, 1.16×10^{-2}	1.13×10^{-4}; 1.30×10^{-3}
Non-Newtonian Fluids (XG005 and XG010)			
Coarse	1.91×10^{-3}, 2.09×10^{-3}	9.46×10^{-5}, 2.40×10^{-3}	9.46×10^{-5}, 2.93×10^{-3}
Medium	1.91×10^{-3}, 2.09×10^{-3}	5.74×10^{-5}, 2.01×10^{-3}	5.74×10^{-5}, 2.45×10^{-3}
Fine	1.91×10^{-3}, 2.09×10^{-3}	3.85×10^{-5}, 1.06×10^{-3}	3.85×10^{-5}, 1.29×10^{-3}

Based on the jet half-widths in the similarity region, the maximum difference between the coarse and medium grids was 0.46% for the Newtonian fluid. In terms of local maximum velocity examined, the maximum percentage change was 0.21%. The corresponding differences between the medium and fine grids were 0.21% and -0.21%, respectively. For the non-Newtonian fluids the differences in jet half-widths are 2.30% and -0.90%, respectively, for the coarse and medium, and the medium and fine grids. Meanwhile, for

the local maximum velocity the corresponding differences were -2.50%, and -0.98%, respectively. Based on these tests, the medium grid for each fluid was used for the present work.

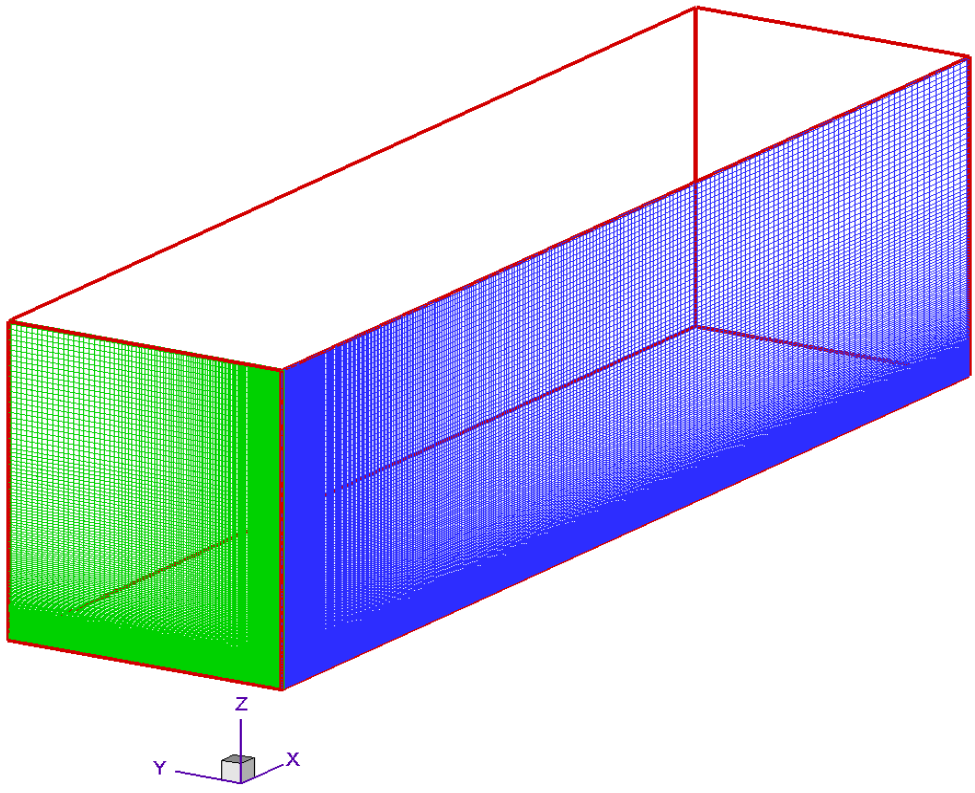

Figure 3.6: A sample of the computational mesh.

3.4 Validation of the Numerical Procedure

It is imperative that validation tests are performed for any numerical technique (CFD) employed for studying any fluid flow to assess its capability and accuracy. In the validation procedure, the numerical results are compared with either experimental results or other previous numerical or analytical results. The flow geometry for validation tests need not to be identical to that of the end application. However, the underlining flow physics and phenomena should be similar.

In the present work, various benchmark problems were used to assess the accuracy of the finite volume solver and validate its results. The benchmark problems selected for this study are: developing flow field in a channel and lid-driven cavity flows. These benchmark cases are carefully selected to investigate the ability of the code to accurately compute laminar, Newtonian, non-Newtonian, and incompressible flows. These test problems were also chosen because they are either similar to a wall jet which in the sense that they possess a point of inflection in the velocity profile or they have similar physical phenomena such as vortex dynamics. Moreover, they represent classical benchmark problems that have been carefully investigated by previous researchers and are well documented in the literature.

In the subsequent sections, individual test cases of the aforementioned flows are described and presented in detailed. The results from the present CFD code were compared with those from previous studies. The first part discussed the developing flow field in a channel, and then followed by the study of lid-driven cavity flows. The last section presents the work on mesh generation of circular pipe.

3.4.1 Developing Flow Field in a Channel

The fluid dynamics behaviour of flow through channels (non-circular ducts) has a wide application in heat transfer such as compact heat exchangers. Consequently, there have been extensive studies on such geometries analytically, numerically, and experimentally. Most of these studies involved Newtonian fluid and 2D channel flow. This is due to its simplistic analysis where the flow becomes one-dimensional in the fully developed region. In the non-circular ducts, however, the developing flows analysis is three-

dimensional. It is also not uncommon for one to encounter non-Newtonian fluids in many industries such as chemical, pharmaceutical, biological, and food. Since these fluids have their viscosities being a variant, the flow dynamics become complicated. This further increases the complexity of the analysis of flow in non-circular channels, especially those involving non-Newtonian fluids.

In addition to the above-mentioned practical applications, the availability of numerous analytical, numerical and experimental results has made these flows a suitable benchmark problem. Therefore, both 2D and 3D flows were computed for both Newtonian and non-Newtonian fluids.

3.4.1.1 Flow geometry and description

Most of the prior studies on 3D channel flows employed analytical (Han, 1960; Schechter, 1961), numerical (Curr *et al*, 1972; Gervang and Larsen, 1991) and experimental (Goldstein and Kried, 1967) techniques. The general observations from these studies are that there is a good agreement among the results in the fully developed region. For the Newtonian fluid, while, there is a better agreement between numerical and experimental results in the developing region, analytical techniques produced velocity and pressure in the developing region with significant variation (Curr *et al*, 1972). The obvious reason was the neglect of the cross-stream or transverse velocities and the non-linear terms in the streamwise momentum equation (Curr *et al*, 1972). Although some attempts have been made in the past to analytically predict channel flow of non-Newtonian fluids, it does appear that exact solution is still not available.

The present CFD code which has been fully described in Appendix B was used to

compute the flow in 2D channel shown in Fig. 3.7. The computations were performed for both Newtonian and non-Newtonian fluids. The generalised Reynolds number was defined as:

$$Re = \rho U_b^{2-n} h^n / \mu_o \theta^{n-1} \tag{3.7}$$

where ρ is density, U_b is the bulk velocity, h is the channel height, θ is a characteristic time scale, μ_o is the apparent viscosity at zero shear rate, and n is the power-law index. For a power-law fluid, λ which is the consistency index replaces μ_o and the characteristic time scale becomes 0. In the case of a Newtonian fluid which can be considered as a special case of the power-law non-Newtonian fluid; n = 1 and the consistency index, λ becomes the dynamic viscosity of the fluid. Three different power-law fluids (i.e. n = 1.0, 0.7 and 0.5) were used, and for each fluid the computation was performed at Reynolds number, Re = 245. The rheological data for the power-law non-Newtonian fluids from Li *et al* (2005) and Dressler (2006) were used for the two non-Newtonian fluids. These are: n = 0.5214, ρ = 1000 kg/m^3, λ = 3610.9 mPa•s^n and n = 0.702, ρ = 1090 kg/m^3, λ = 0.1803 Pa•s^n.

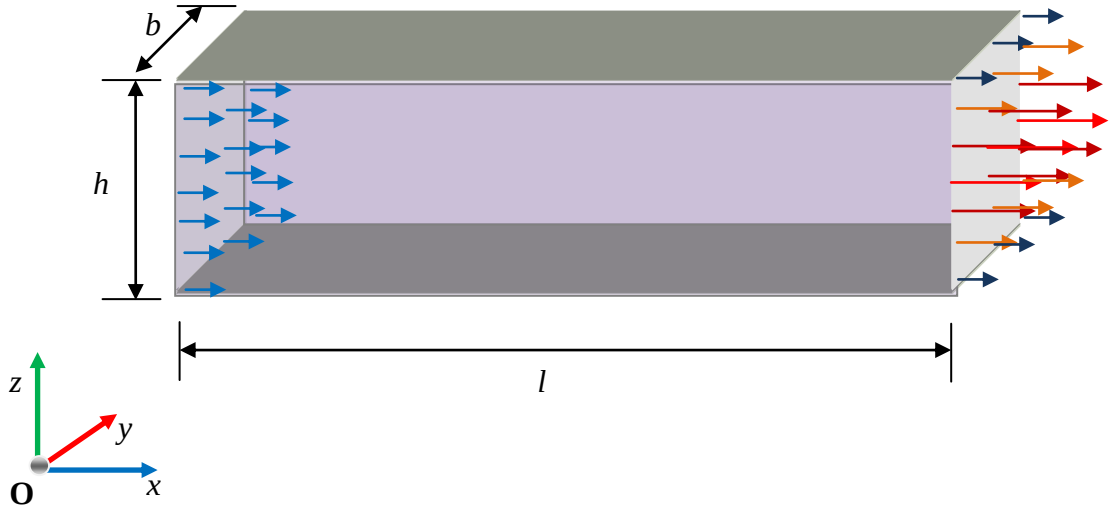

Figure 3.7: Schematic diagram of a square section channel.

The 2D case of Fig. 3.7 was achieved through the use of boundary conditions. The boundary conditions consist of the following:

$x = 0$: $u\,(0, z) = U_b$; $x = L$: $d\,(u, w, p) / dx = 0$; $z \in [0, h]$: $[u, w] = 0$

$y \in [0, b]$ = symmetry: $d\,(u, w, p) / dy = 0$

Three-dimensional flows through a square channel (Fig. 3.7) by Goldstein and Kried (1967) and Han (1960) were computed for a Newtonian fluid. The flow geometry shown in Fig. 3.7 consists of a 0.01 m square section (b x h) channel and 1.0 m (l) long. The Reynolds number based on the channel height and bulk velocity (Eqn. 3.7) is 387. It should be mentioned that for a square cross-section, the channel height is the same as the hydraulic diameter.

For the non-Newtonian fluid, the analytical (Schechter, 1961) and numerical (Gervang and Larsen, 1991; Lima *et al*, 2000) works were computed. Gervang and Larsen (1991) computed a non-Newtonian fluid through a rectangular cross-section channel. The channel cross-section is 0.001 m high and 0.016 m wide. Gervang and Larsen (1991) did not provide the length of the flow domain and therefore, 2.6 m was chosen for stability and better convergence of the present code. The Reynolds number of the flow is approximately 3 using Eqn. (3.7) with h being the channel height. The rheological data for the fluid are: $n = 0.37$, $\rho = 1000$ kg/m^3, $\lambda = 8.5$ Pa•s^n. Schechter (1961) and Lima *et al* (2000) studied various aspect ratios of the 3D channel flow with square cross-section as a special case. The works by Schechter (1961) and Lima *et al* (2000) were based on dimensionless form of the governing equations; therefore, the flow parameters including a well-defined Reynolds number were sketchy. Moreover, they studied various power-

law fluids which have power law index ranging from 0.4 to 1.5. For a comparison with the present study, a Reynolds number of 100 and power law index, n = 0.5 was selected. Also, a Carreau shear-thinning fluid (Carreau model) with similar power law index (n = 0.5) is investigated and to be compared with power-law fluid.

The rheological data for the power-law fluid was given by Barnes *et al* (1989) and they are: n = 0.5, λ = 50 Pa•s^n. This fluid is called molten chocolate which has density of ρ = 1500 kg/m^3 (Chhabra and Richardson, 1999). The corresponding data for Carreau fluid are: n = 0.49, θ = 11.0 s, μ_∞ = 0.001 Pa•s, ρ = 1003 kg/m^3, and μ_o = 8.20 Pa•s^n. This non-Newtonian fluid was prepared from 0.85 *wt*% Separan AP30 and water (Chhabra and Uhlherr, 1980).

The boundary conditions for the 3D Channel flows consist of the following:

$x = 0$: $u\,(0, y, z) = U_b$; $\quad x = L$: $d\,(u, w, p) / dx = 0$; $\quad z \in [0, h]$: $[u, v, w] = 0$

$y \in [0, b]$: $[u, v, w] = 0$

The viscosity at the boundaries was obtained by first-order extrapolation.

3.4.1.2 Results and discussion

Figure 3.8 shows the velocity profiles of the three power-law fluids for the 2D channel flow. The expression for the analytical solution is given as:

$$\frac{u(z)}{U_b} = \frac{2n+1}{n+1}\left[1-\left(\frac{2z}{h}-1\right)^{n+1/n}\right] \tag{3.8}$$

where all the symbols have their usual meaning. Equation 3.8 also indicates that the normalised maximum velocity is only a function of fluid behaviour. The grid used for this flow is 150 x 2 x 46 for streamwise, spanwise and transverse direction, respectively.

In Fig. 3.8, there is no distinction between the present and analytical results irrespective of the fluid. The velocity profile changed from a pure parabolic to the so-called "plug-like" nature as the degree of the shear-thinning, *n* increases. In a better sense, the sheared layer near the wall tends thinner as the fluid becomes more shear-thinning.

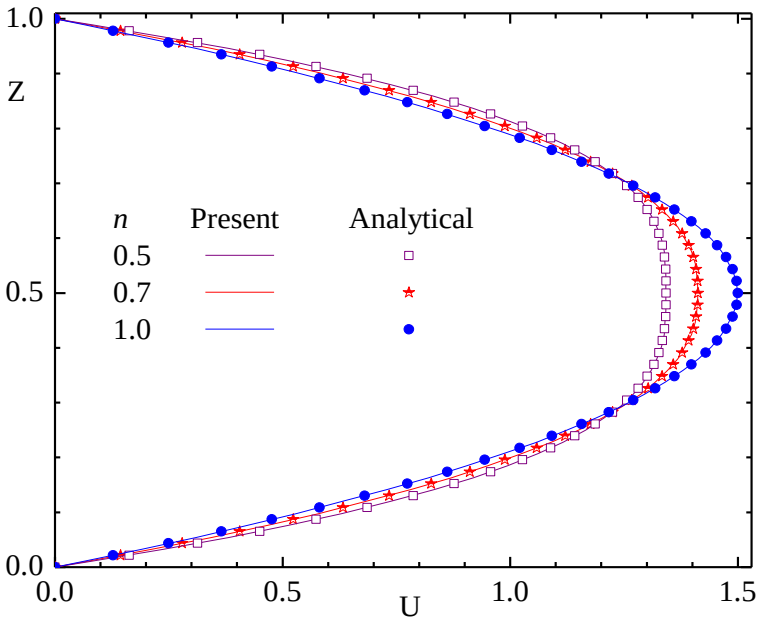

Figure 3.8: Normalised fully developed velocity profiles for various power-law fluids in a two-dimensional channel flow.

For Newtonian fluid, three meshes were employed to study 3D channel flows. These grids are coarse (32 x 32), medium (64 x 64), and fine (100 x 100) corresponding to the, spanwise and transverse direction, respectively. For each mesh, 200 node points were specified on the streamwise direction. This is because it is widely known that the channel flows are insensitive to the streamwise direction and any effect on the flow physics results from the cross-stream flows (Curr *et al*, 1972). The grid independent tests showed that the maximum difference between the coarse and medium for the maximum centreline velocity was 0.32%. The corresponding value for the medium and fine was 0.06%. Figure 3.9 shows the maximum centreline velocity, U_c (= u_c / U_b) along the

streamwise direction, X (= x / h) for various grids. In terms of pressure coefficient C_p (= (P_{in}-P_{out}) / 0.5ρU_b) the difference between coarse and medium, and medium and fine were -0.54% and 0.23%, respectively. Based on these tests, the medium grid was chosen and compared with previous works in the subsequent discussion.

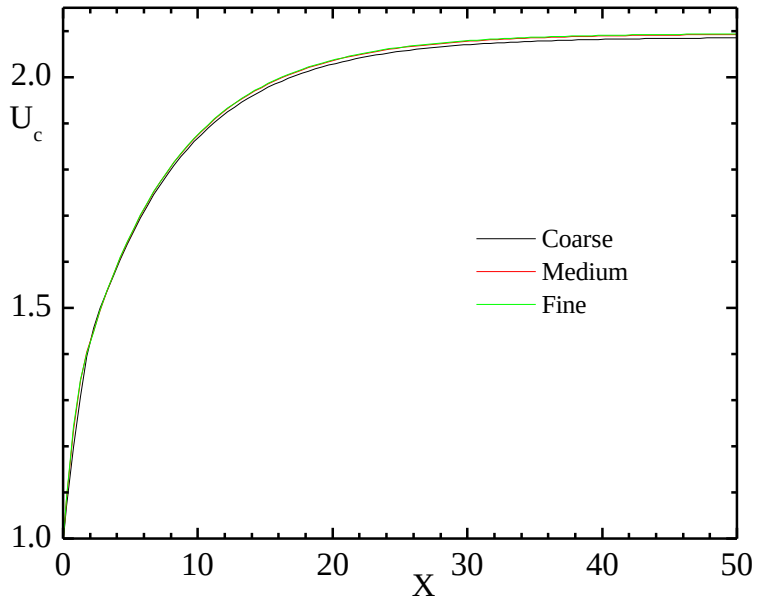

Figure 3.9: Centreline velocity development with streamwise direction 3D channel flow of Newtonian fluid.

The streamwise velocity profiles at two selected axial stations (X = 2.9 and fully-developed section) in the mid-plane, Y = 0.5 (where Y = y / h), are shown in Fig. 3.10a. There is no noticeable difference between the present results and the measurements by Goldstein and Kried (1967). Han's results over-predicted the velocities at X = 2.9 in the core region of the flow. This was also evident in the maximum centreline velocities along the channel (Fig. 3.10b). As noted in Section 3.4.1.1, the reason for the deviation of Han's analytical results is attributed to the neglect of the cross-stream velocities and the non-linear terms in the streamwise momentum equation.

Figure 3.10b shows that the flow becomes fully developed after X = 32.5. In the present

results, the maximum centreline velocity, U_c in the fully developed region was found to be 2.094. This value is in excellent agreement with 2.096±0.1% and 2.096 reported by Goldstein and Kried (1967) and Han (1960), respectively. The entrance length which is defined as X value at 99 percent of maximum U_c values was found to be 27.69 compared to 34.83 by Goldstein and Kried (1967) and 29.10 by Han (1960).

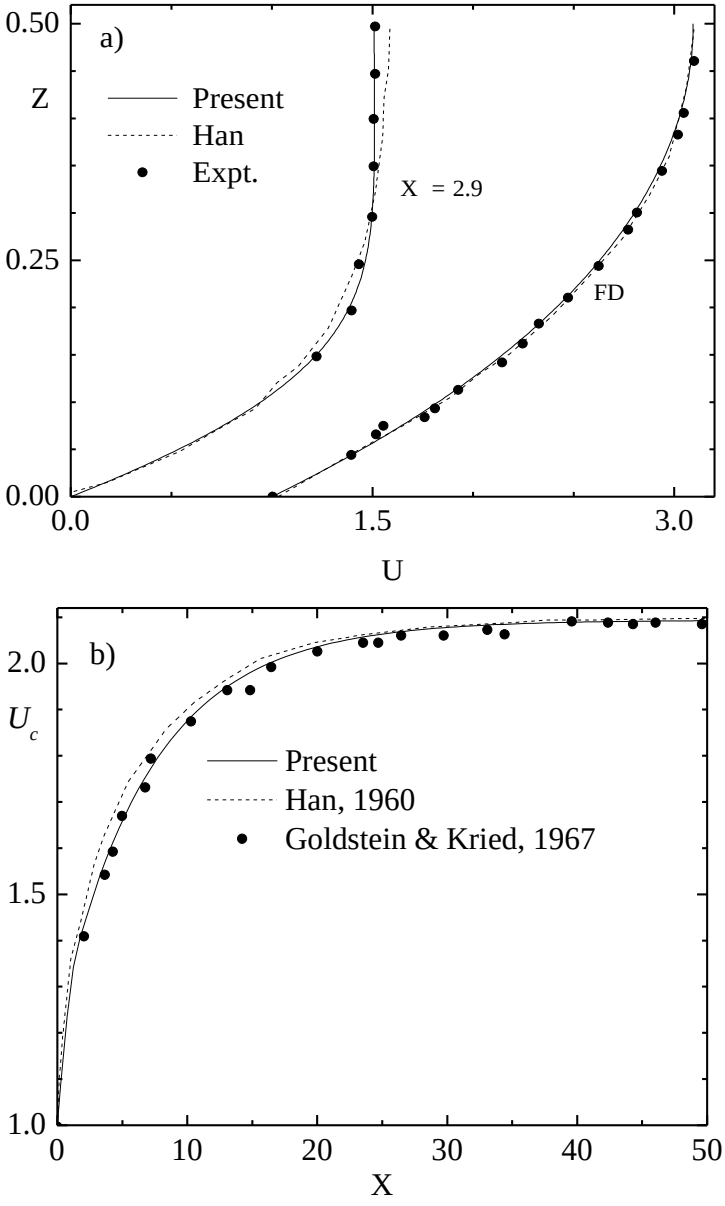

Figure 3.10: Comparison of the present and previous results: a) velocity profiles and b) centreline velocity for 3D channel flow of Newtonian fluid.

The velocity profiles for the non-Newtonian fluids are presented in Figs. 3.11 and 3.12. The vertical axes of these figures, the transverse and spanwise distances, are normalised by the height, h whereas the horizontal axes are normalised by the bulk velocity, U_b. That is, $Z = z / h$, $Y = y / h$ and $U = u / U_b$. In Fig. 3.11, the results at the mid-plane in transverse, $Z = 0.5$ and spanwise $Y = 8$ directions are compared with the previous study by Gervang and Larsen (1991). For the purpose of validation, the mesh (22^2) used by Gervang and Larsen (1991) were employed, and 100 grid points were specified in the streamwise direction. It should be mentioned that Gervang and Larsen (1991) provided no data on the streamwise direction. A very good agreement between the present and previous results is observed. Similar observation is made for Fig. 3.12, where there is no marked difference between the present and previous numerical results. Good agreement between the numerical and analytical (Schechter (1961) results is only observed in the region closed to the walls ($Z < 0.2$ and $Z > 0.8$). The analytical result over-estimated the normalised velocities in the core region including the maximum velocity. It should be remarked that, Fig. 3.12 shows no clear distinction between the power-law model profile and that of the Carreau model.

3.4.2 Lid-Driven Cavity Flows

3.4.2.1 Introduction

The lid-driven cavity is one of the simplest flow geometries with complex flow structure. For this reason, it is widely used as a benchmark for CFD code validations. For example, it exhibits numerous complex fluid dynamics phenomena such as eddies, recirculation zones, complex 3D patterns, and velocity singularities at the cavity corners. Some of these phenomena are found in wall jet flows. These flow dynamics pose a challenge for

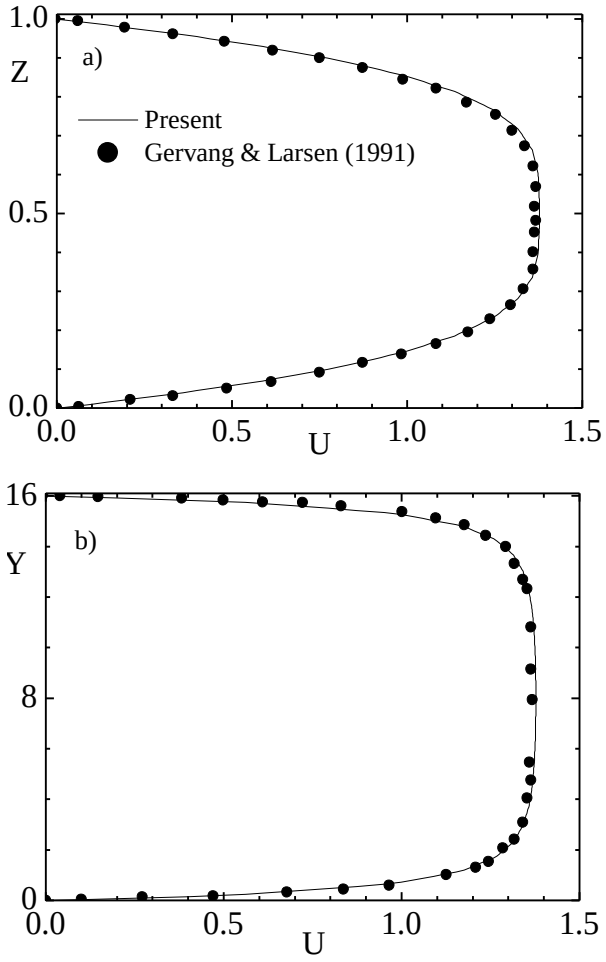

Figure 3.11: Fully developed streamwise velocity profiles: a) Y = 8 and b) Z = 0.5 for 3D channel flow of power-law non-Newtonian fluid.

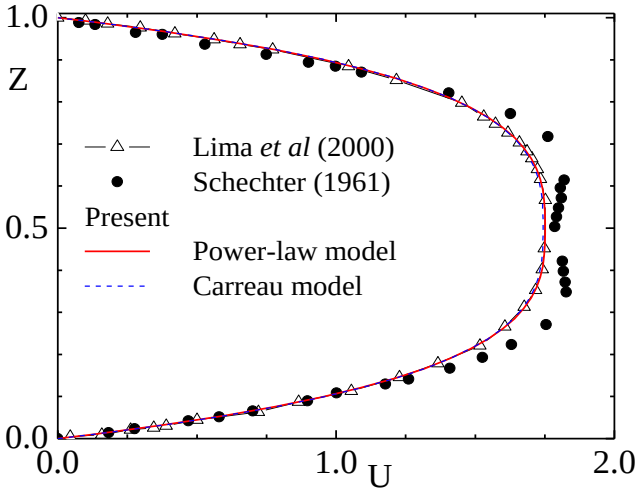

Figure 3.12: Fully developed streamwise velocity profiles for 3D channel flow of non-Newtonian fluid fluids.

any numerical methods especially if the fluid property is not constant as in the case of non-Newtonian fluids. The singularities will obviously be a challenge for the power-law model.

For the Newtonian fluids, Koseff and Street (1984) reported the existence of end wall effect in 3D cavity flow which was absent in 2D cavity flow. The end wall effect produces different flow patterns resulting in the formation of eddies and vortices. This effect also depends on the width to length ratio of the cavity (Koseff and Street, 1984). Recently, Shankar and Deshpande (2000) also reported that, at $Re \geq 1000$ the flow field becomes unsteady with loss of symmetry about the mid-plane.

In the case of power-law non-Newtonian fluids for the 2D cavity flows, the peak values of the velocities are influenced by both Reynolds number and power-law index (Neofytou, 2005). This observation was attributed to viscous effect.

In the subsequent sections, the discussion of present work on both 2D and 3D lid-driven flows is presented. The problem definitions and boundary conditions are first discussed, and the present results are compared with prior experimental and numerical works. The lid-driven flows of both Newtonian and non-Newtonian fluids were computed.

3.4.2.2 Problem definition

Most of the previous studies on this subject have been for 2D flows, especially those of the Newtonian fluid. The study of three-dimensional lid-driven flows has focused on Newtonian fluid (Koseff and Street, 1984; Shankar and Deshpande, 2000; Lilek *et al,* 1997; Lo *et al,* 2005). The 3D lid-driven flows computed for Newtonian fluid will be

compared with experimental studies by Koseff and Street (1984), and numerical works by Lilek *et al* (1997) and Lo *et al* (2005). Koseff and Street (1984) made laser Doppler anemometer (LDA) measurements of Reynolds numbers ranging from 1,000 to 10,000. The flow configuration is shown in Fig. 3.13. This figure showed a reproduction of Koseff and Street (1984) experimental setup. The flow geometry is of 0.150 m square section channel (H x L) and 0.450 m long (B). The computation is only performed for the Reynolds number of 3,200. At this Reynolds number one would expect unsteady flow field (Shankar and Deshpande, 2000). Thus, this problem will be used to validate the time-marching version (pseudo-transient) of the present code. The Cartesian reference frame described in Section 3.4.1 is utilised with the origin at the lower left corner of the cavity (see Fig. 3.13).

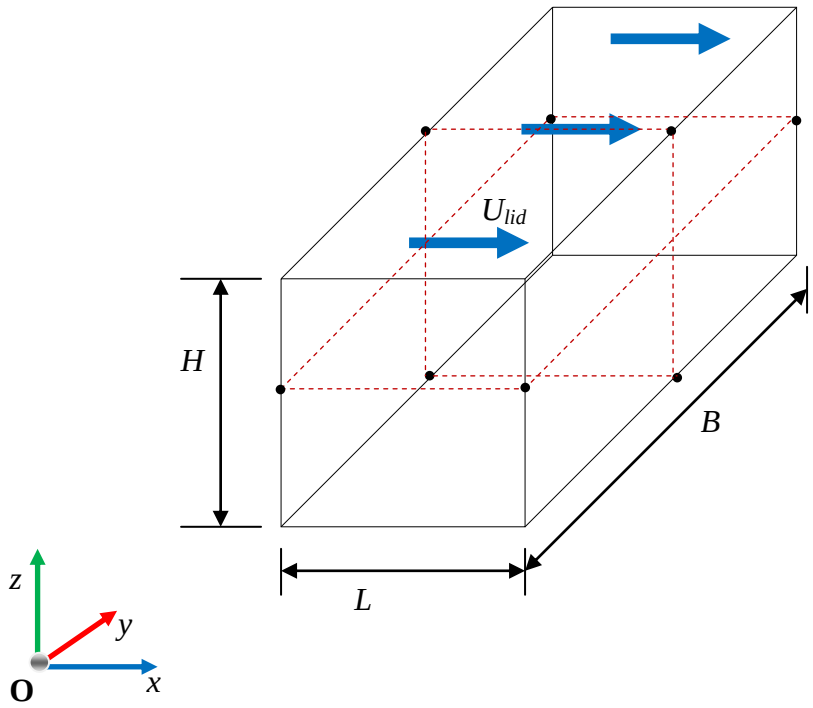

Figure 3.13: Schematic diagram of the lid-driven cavity.

Lilek *et al* (1997) solved the 3D lid-driven flow using a finite volume based colocated code by employing SIMPLE algorithm for velocity-pressure coupling. It should be mentioned that Lilek *et al* (1997) work was for code validation and they only compared results from various mesh sizes (8^3 - 128^3). Here, only the mesh (64^3) at Reynolds number of 1,000 was used for comparison. Lo *et al* (2005) on the other hand used a finite difference method to solve the vorticity transport equation for various Reynolds numbers (*Re*: 100 – 2,000) using a cubic cavity. Their computational results at *Re* = 1,000 will be compared with the present results. For both works (Lilek *et al*, 1997 and Lo *et al*, 2005), Fig. 3.13 was modified to a cuboid with a size of 1.0 m.

The two-dimensional lid-driven flow of non-Newtonian fluids by Neofytou (2005) was computed. Neofytou (2005) employed a finite volume colocated code based on SIMPLE algorithm to study the non-Newtonian effects on the lid-driven flows. The convective terms of the governing equations were discretised using QUICK whereas CDS was used for the diffusion terms. Various non-Newtonian constitutive equations including power-law model were implemented for the viscosity. The Reynolds number defined similar to Eqn. (3.7) was 100. In the present study, the 2D lid-driven flow was achieved through a smaller width (0.1 m) and boundary conditions. The present code will be used to solve a cubic cavity of *Re* = 1,000 for four power-law non-Newtonian fluids with water being a special case and one Carreau fluid.

The rheological data for the non-Newtonian fluids are:

(i) $n = 0.4$, $\lambda = 0.5$ Pa•s^n and $\rho = 1063$ kg/m^3. This fluid corresponds to synovial fluid

with its rheological data taken from Barnes *et al* (1989) and the density from Dai *et al* (1997).

(ii) The other two power-law fluids are n = 0.5 and 0.702, and the Carreau fluid, n = 0.49 whose rheological data are already given in Section 3.4.1.1.

3.4.2.3 Boundary conditions and numerical solution

The boundary conditions of the lid-driven cavity consist of the following:

2D Lid Cavity:

$x \in [0, L]$: $[u, w] = 0$; $z = 0$: $[u, w] = 0$; $z = h$: $u = U_{lid}$

$y \in [0, b]$ = symmetry: $d(u, v, w, p)/dy = 0$.

3D Lid Cavity:

$x \in [0, L]$: $[u, v, w] = 0$; $z = 0$: $[u, v, w] = 0$ $z = H$: $u\,(x, y) = U_{lid}$

$y \in [0, B]$: $[u, v, w] = 0$

The lid velocity, U_{lid} values are tabulated in Table 3.4. These values are based on Eqn. 3.7 and the fluid properties given in Sections 3.4.2.2 and 3.4.1.1. The viscosity at the boundaries was obtained by first-order extrapolation.

Table 3.4: The lid velocities, U_{lid} (m/s)

Re	**Newtonian**	**Power-law**			**Carreau**
2D		***n* = 0.50**			
100	-	2.232			
3D	***n* = 1.00**	***n* = 0.702**	***n* = 0.50**	***n* = 0.40**	***n* = 0.49**
1000	1.000	0.250	10.357	0.624	2.407
3200	3.200		-	-	

A grid independent study was only performed on the test cases whose meshes were not available in the previous works. The flow domain shown in Fig. 3.13 was computed

using structured grids. The mesh for 2D flows consists of 50 x 2 x 50 (coarse), 100 x 2 x 100 (medium) and 200 x 2 x 200 (fine) on the streamwise (x), spanwise (y), and transverse (z), respectively. Two nodes were specified in the spanwise direction in order to achieve the two-dimensionality of the flow.

For 3D flows, 64^3 mesh was used for Re = 1,000. The grids were geometrically expanded and contracted in all three directions in wall vicinities. A number of meshes were used to perform grid independence tests at the Re = 3,200. The grid independence tests were conducted using uniformly distributed grids made up of coarse (40^3), medium (60^3), and fine (90^3). A comparison of these meshes with previous works for Re = 3,200 will be discussed later.

A three level time-marching algorithm was used for Re = 3,200. A pure central differencing scheme (CDS) used for all the terms in all the governing equations produced several instabilities at this Reynolds number. Therefore, the results presented here are based on 20 % of UDS and 80 % of CDS. The convergence criterion was set to 10^{-5} and 10^{-4} for the Newtonian and non-Newtonian fluids, respectively.

3.4.2.4 Results and discussion

Table 3.5 summarised the results obtained for 3D lid driven flow of Newtonian fluid at Re = 3,200 for various grids used. In addition, the present results are compared with previous experimental (Koseff and Street, 1984) and numerical (Acosta, 2001) results. It is clear from Table 3.5 that the medium (60^3) mesh showed the least discrepancies. The percentage difference between the present result and measured data is: 3.5% for u_{min}, 7.5% for w_{min} and 31.5% for w_{max}. These discrepancies are, however, less than those

observed between previous numerical results (Acosta, 2001) and measurements. A comparison of normalised streamwise velocity (U) profiles taken at the symmetry plane (y = B /2) is shown in Fig. 3.14. From Fig. 3.14 and with 1 – 10 % measurement uncertainty reported by Koseff and Street (1984), the general inference is that, there is very good agreement between the present and previous results. Similarly, the velocity profiles plotted in Fig. 3.15 at Re = 1,000 show no noticeable difference and that all the results are in good agreement.

Table 3.5: Grid independent test and previous results

	Mesh	**[W_{max} , $W_{,min}$]**	**U_{min}**
present	40^3	0.21, -0.35	-0.23
	60^3	0.25, -0.43	-0.29
	90^3	0.29, -0.46	-0.33
Koseff and Street		0.19, -0.40	-0.28
Acosta		0.20, -0.35	-0.22

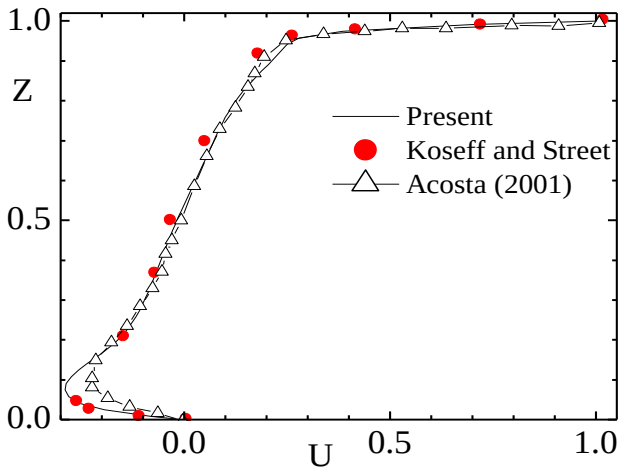

Figure 3.14: Normalised streamwise velocity profiles at symmetry plane.

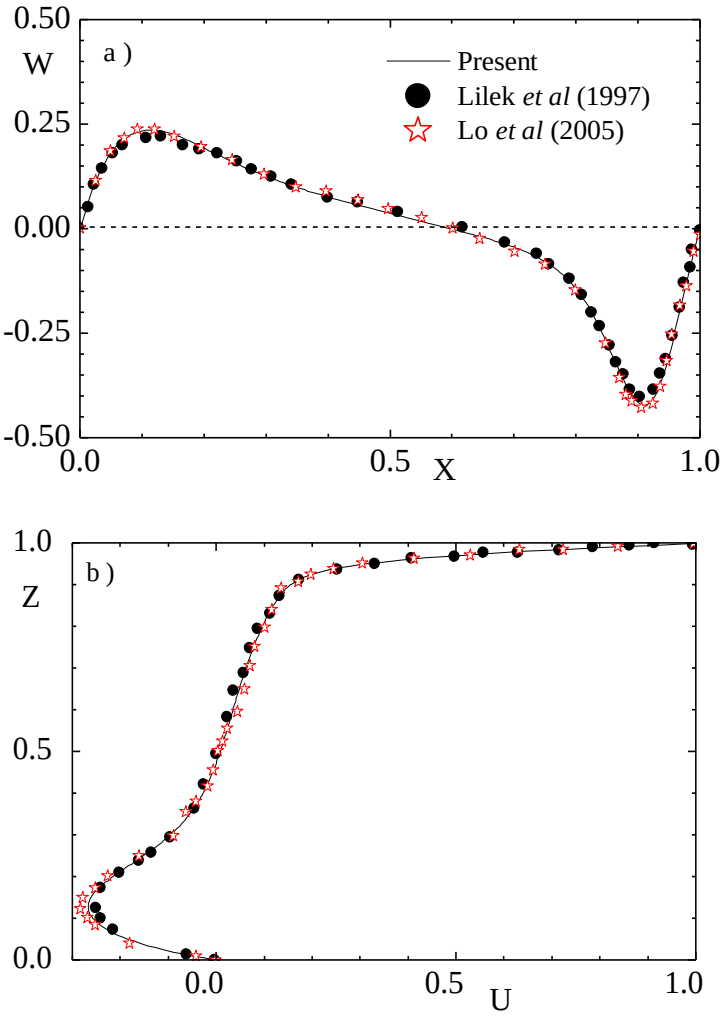

Figure 3.15: Comparison of normalised velocity profiles at symmetry planes.

The 3D flow structures which are presented in terms of the streamlines and velocity vectors are shown in Fig. 3.16. In this figure, three orthogonal central planes, *x*, *y* and *z* (see also Fig. 3.13) are shown for clarity. The axes are normalised by H, i.e, X = *x* / H, Y = *y* / H and Z = *z* / H. Figures 3.16a and 3.16b correspond to the *x*-*z* planes at Y = 1.5 (mid-plane) and 2.88 (end-wall), respectively which are shown by dash lines in Fig. 3.16c. Additionally, Figs. 3.16c and 3.16d, respectively show the flow patterns in the planes X = 0.5 and Z = 0.5. It should be recalled from Fig. 3.13 that Z = 0.5 plane is parallel to the moving lid. The figure clearly revealed that the flow is made up of one

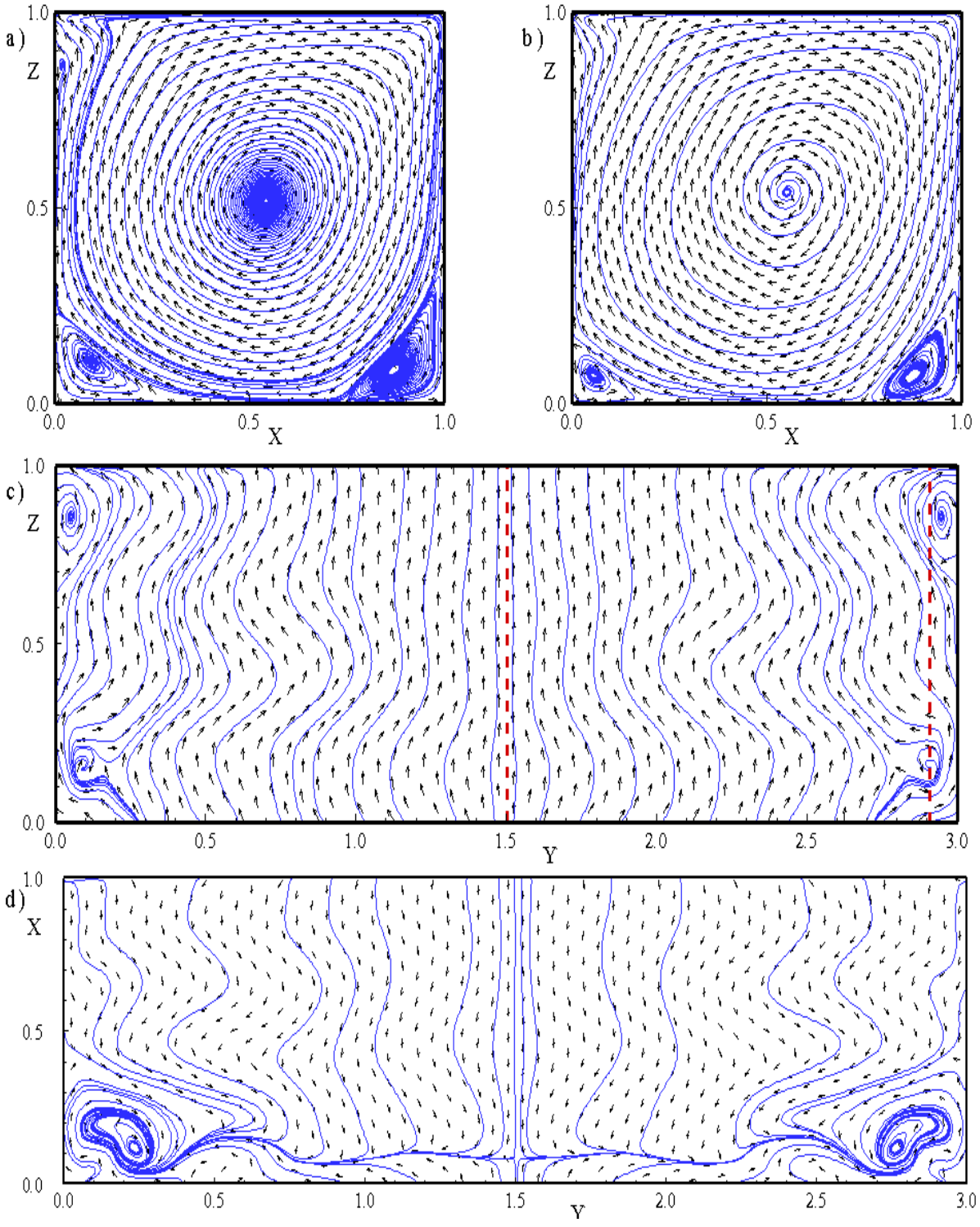

Figure 3.16: Flow visualisation of a 3D lid driven flow at planes: Y = 1.5(a) and 2.88 (b), X = 0. 5 (c) and Z = 0.5 (d).

core circulation cell and three secondary eddies (Figs. 3.16a and 3.16b). These features are more intense in the symmetry plane than the end-wall plane. Furthermore, Fig. 3.16 (c, d) also show the presence of corner vortex. As the top lid (wall) moves in the positive *x* direction, one would expect the fluid to take the opposite direction for the return flow. This is evidently seen in the velocity vectors shown in Fig. 3.16d. All these observations are similar to those reported by Koseff and Street (1984).

The *w*–*x* and *z*–*u* plots for the present and previous results for a 2D lid driven flow of non-Newtonian fluids are shown in Fig. 3.17. Except for the peak values of *w* where the difference between the present and previous results is about 11%, there is good agreement between them. It should be remarked that the fluids may be difference in terms of its consistency. This is because the previous work solved the dimensionless governing equations which obviously omit some of the fluid properties. This might affect the secondary velocity, *w*. Another factor that might have contributed to the discrepancy of the *w* values is the three-dimensionality of the present case. The 2D was achieved through the boundary condition.

The streamlines and the velocity vectors on the symmetry plane are shown in Fig. 3.18. There are one main and two bottom corner vortices. These observations are consistent with those made by Neofytou (2005). The location of the vortex eye shown in Fig. 3.18 by dash lines was (0.73, 0.80) which was the same as that reported by Neofytou (2005).

The results of the 3D lid driven flows of various power-law based fluids for *Re* = 1,000 is shown in Fig. 3.19. The plots shown in Fig. 3.19 were obtained at mid planes (X = 0.5 and Z = 0.5). It can be seen from Fig. 3.19 that, *n* = 0.4 has its normalised velocity

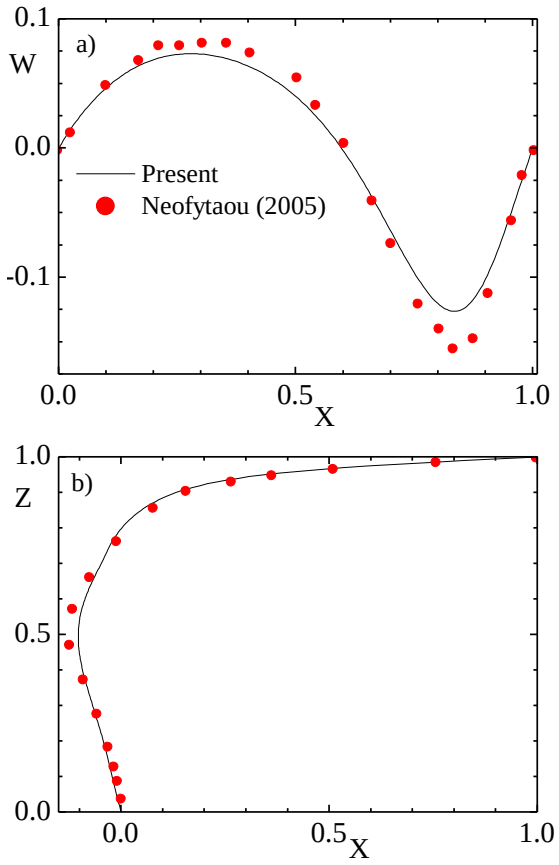

Figure 3.17: Comparison of normalised velocity profiles for 2D Lid driven flow.

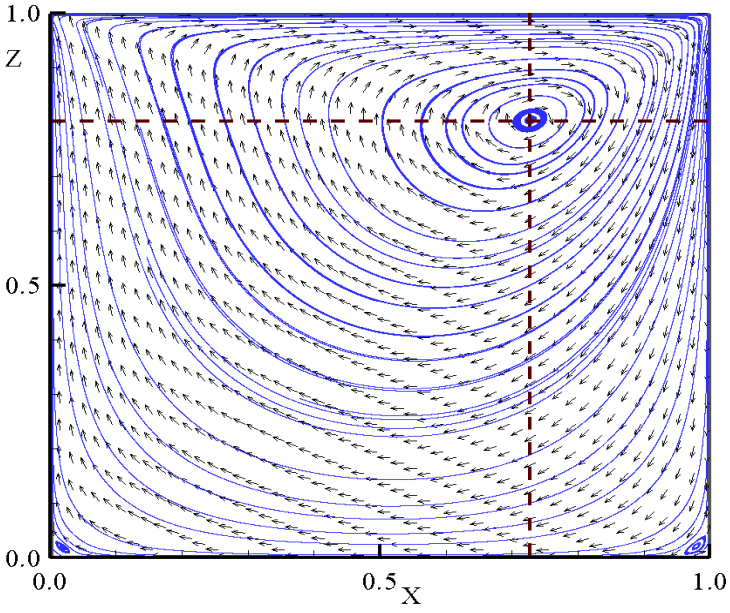

Figure 3.18: Flow visualisation of a 2D lid driven flow of power-law shear-thinning fluid, n = 0.5.

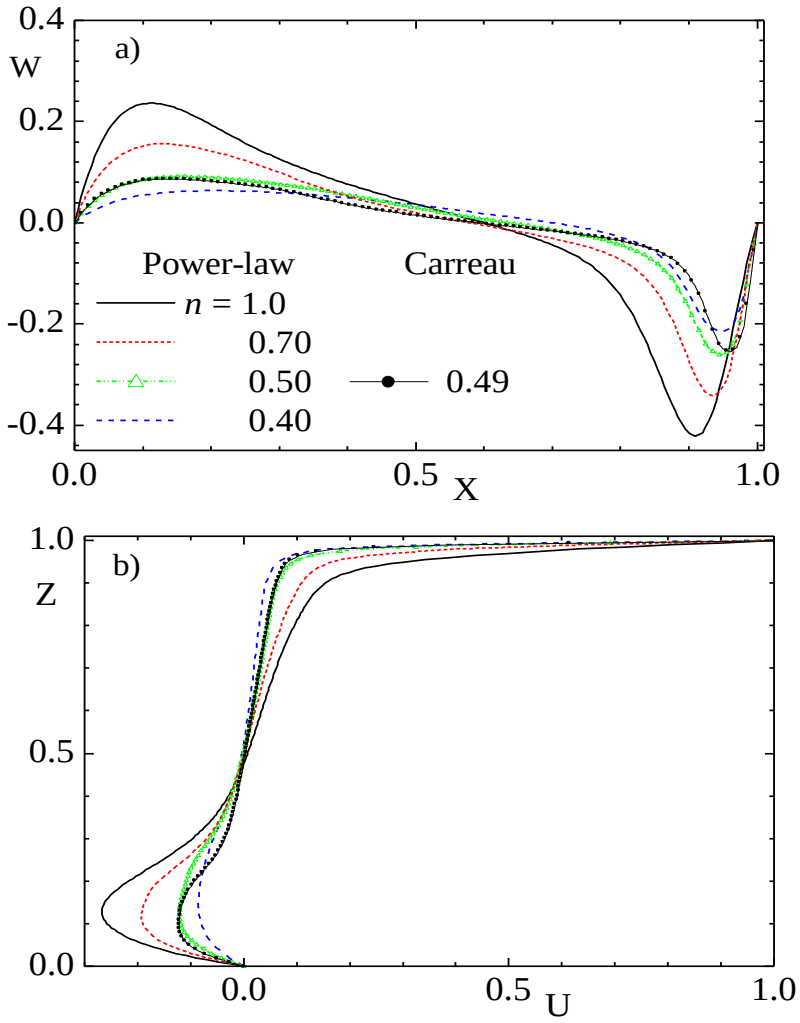

Figure 3.19: Comparison of normalised velocity profiles at symmetry planes for various power-law and Carreau shear-thinning fluids at *Re* = 1,000.

values substantially lower than those for n = 1.0. This is true for both u and w. Thus, decreasing n value resulted in a reduction of the velocities. This is due to the fact that the higher n values tend to exhibit lower apparent viscosities around the centre of the cavity which allows for higher velocity gradients to occur (Neofytou, 2005). In Fig. 3.19, the Carreau fluid that is close to power-law fluid with n = 0.50 is also shown. Although these fluids are completely different in reality since one is chocolate and the other is Separan AP30 based fluid, the rationale for this comparison is to qualitatively assess the limitation of the power-law model. The comparison (Fig. 3.19) shows that in the regions

(0.76 < X < 0.97) for W and (0.15 < Z < 0.49) for U, the velocities are higher for the Carreau fluid than the power-law fluid (n = 0.50). Meanwhile, in the region 0.13 < X < 0.67 for W, the values for Carreau fluid are lower than those for power-law fluid. Beside these discrepancies, there is no difference between the profiles of both fluids.

The flow patterns (Fig. 3.20) indicate that, by decreasing n the centre of the main vortex (vortex eye location) moves horizontally towards the right of the cavity. For instance, the vortex eye location for n = 1 was at (0.59, 0.47) whereas for n = 0.4, it was (0.7, 0.49). This is contrary to the observation made by Neofytou (2005) for his 2D case, where he reported that the centre of the main vortex moves towards the upper right corner of the cavity as n decreases. The probable reason might be due to the three-dimensionality. Another interesting observation is that the corner bottom vortices decreases in size with decreasing n. In fact, n = 0.4 has only one corner bottom vortex with the height almost 23.3% of that for n = 1 (Fig. 3.20a). In a typical shear-thinning fluid, the apparent viscosity is higher at those corners than other flow domain. These higher values prevented the secondary vortex structure thereby giving rise to a stagnant region in the lower region of the cavity. The vortex eye location was also different for the power-law fluid (n = 0.5) and the Carreau fluid. The vortex eye was located at (0.63, 0.48) for n = 0.50 and (0.59, 0.47) for Carreau fluid. In addition, only one corner bottom vortex (not shown here) was observed for n = 0.50 whereas Carreau fluid has two of the same strength corner vortices. These indicate that the power-law fluid (n = 0.50) may have overestimated the apparent viscosity in those regions where the velocity becomes singular due to its unbound nature of the model.

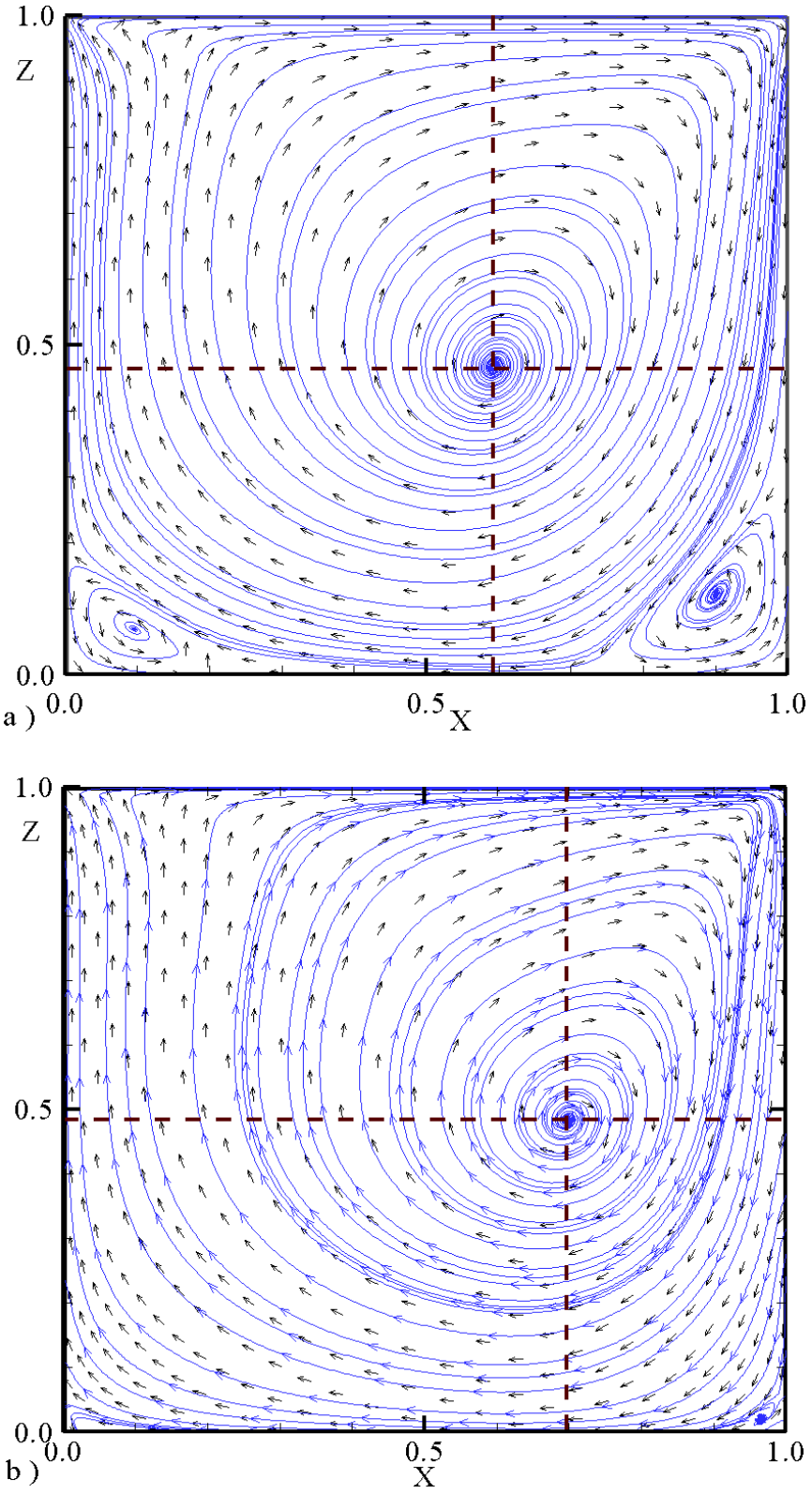

Figure 3.20: Flow visualisation of a 3D lid driven flow: a) Newtonian fluid, n = 1.0 and b) power-law shear-thinning fluid, n = 0.4.

3.4.3 Mesh Generation for the Circular Geometry

In the computations of the present work, a structure mesh was employed for the flow geometry including a circular section. While for the rectangular geometries this type of mesh will pose no problem, the converse may be true for the circular geometry. Figure 3.21a shows a typical 'stepwise' mesh used to approximate the circular pipe. This section will assess this approximation.

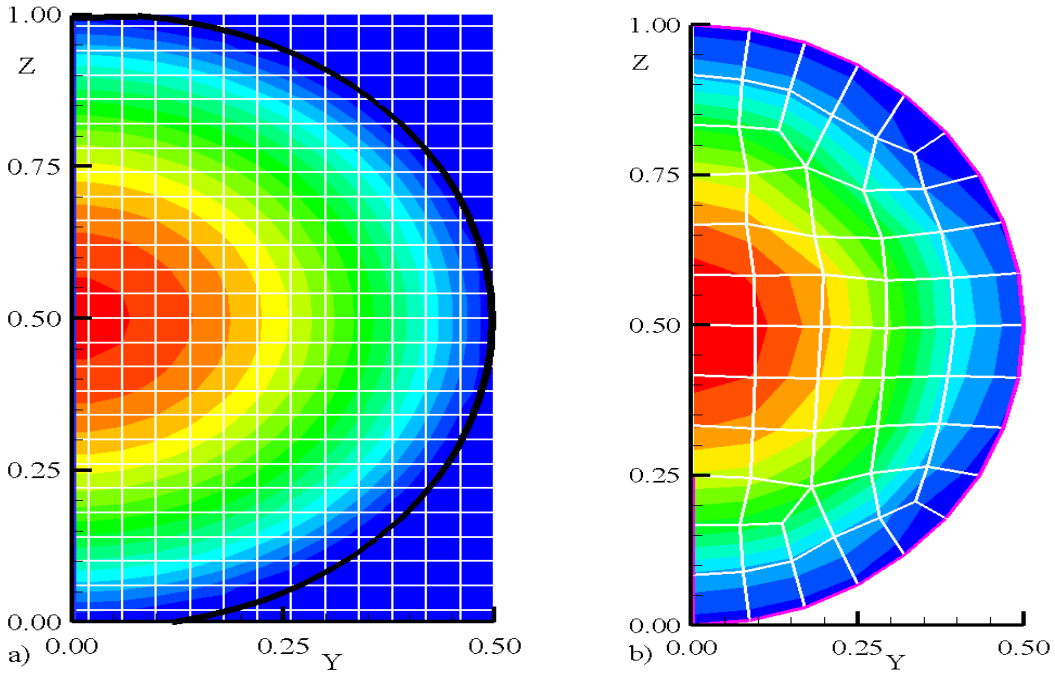

Figure 3.21: Sample mesh for the circular section: a) present code and b) Gambit (Fluent).

The present code was first used to compute a circular pipe flow of power-law fluid and the results compared with analytical solution. The power-law fluid is n = 0.5 of which rheological data have been given in the Section 3.4.2. Figure 3.22a shows that, there is no distinction between the present numerical and analytical results. The analytical result was obtained from $u(r) / U_b = (3n + 1) [1 - (2r/d)^{(n + 1)/n}] / (n + 1)$, where n = 0.5. The previous work by Pinho (2001) was also computed using the present code. Pinho (2001)

computed non-Newtonian fluid with n = 0.6, θ =1.0 s, and μ_0=1 Pa•s for a circular pipe. As shown in Fig. 3.22b an excellent agreement was observed between present result and Pinho (2001) with the exception of -1.14% difference in the peak values.

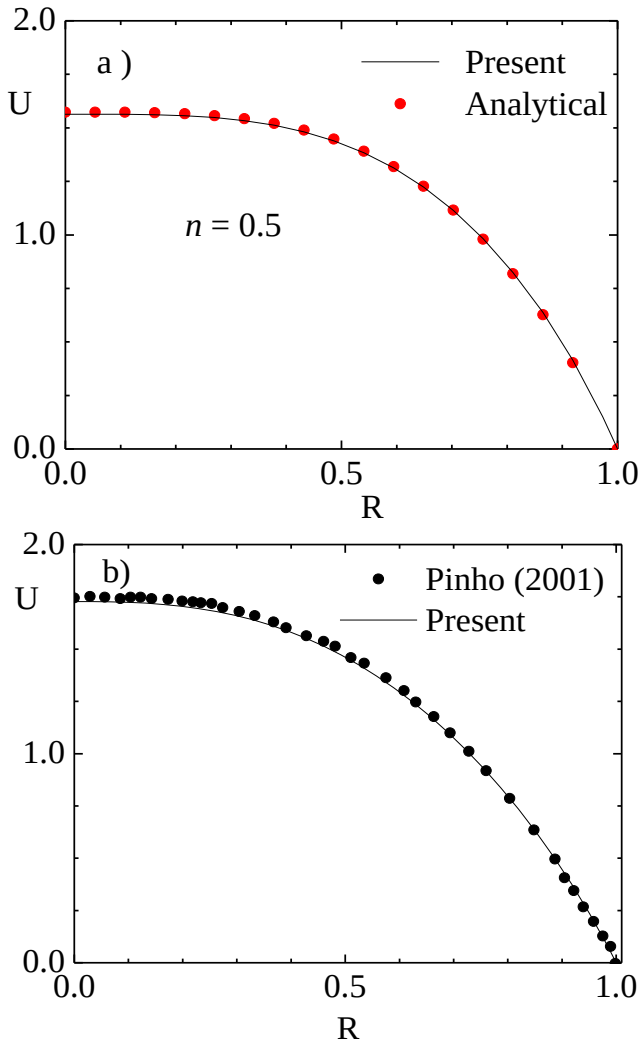

Figure 3.22: Comparison of a circular pipe flow between the present and: a) analytical at *Re* = 310, b) previous at *Re* = 5.261 results.

Both the present code and commercial CFD code (Fluent) were used to compute 3D laminar wall jet flows of Newtonian fluid at Re_j = 310 and 800. The Fluent unstructured mesh at the inlet is shown in Fig. 3.21b. The flow geometry was scale down to that reported by Adane and Tachie (2008a) due to computer memory for the Fluent code. This small geometry is denoted as SD in the subsequent discussion. It should be

mentioned that the same number of nodes were used for both codes. In addition, the present code recomputed the flow using geometry similar to the experimental geometry. Two grids (37 and 100) for the circular mesh were computed. Other grid distributions analyses were also performed but would not be shown here since no significant difference was observed.

Figure 3.23 shows variation of normalised streamwise maximum velocity, U_m (= u_m/u_j) with downstream distance, X. There is no significant difference between the numerical results. For instance in Fig. 3.23b, at X = 50 for the small domain (SD), U_m = 0.32 and 0.31, respectively for the present code and Fluent. Figure 3.23b shows that the numerical results underestimated the decay of U_m. A typical velocity profile in the similarity region from Fluent and present codes is also shown in Fig. 3.24. There is a reasonable agreement between the results.

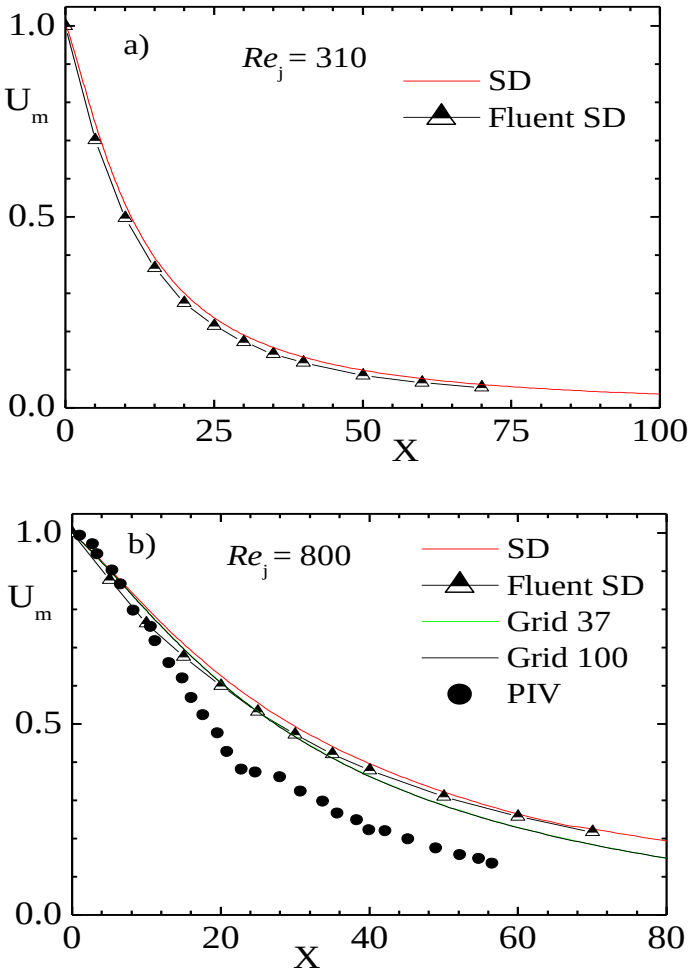

Figure 3.23: Comparison of the maximum velocity decay: a) Re_j = 310 and b) Re_j = 800.

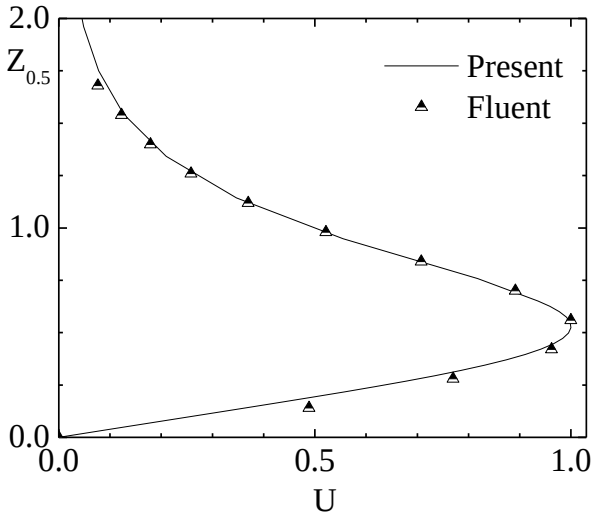

Figure 3.24: Comparison of the similarity profile at Re_j = 800.

Chapter 4

RESULTS AND DISCUSSION

This chapter presents discussion of the results from the present study. The first two sections (Section 4.1 and 4.2), respectively, focus on the experimental results for the Newtonian fluid and the non-Newtonian fluids. In the subsequent sections, numerical results are validated using the experimental data. Then additional quantities such as spread rates, momentum flux, skin friction coefficient, and streamwise vorticity that could not be evaluated from the measurements were obtained and presented in Section 4.3 to provide additional insight into the 3D laminar wall jet flows at various Reynolds numbers. The effects of the specific fluid on the wall jet characteristics are discussed in Section 4.4 by comparing the results from the non-Newtonian fluids with those from the Newtonian fluid.

4.1 Experimental Results of Wall Jet flow of the Newtonian Fluid

The flow development in the streamwise direction is often characterised by parameters such as the local maximum streamwise velocity (u_m), the location of u_m from the wall (z_m), and the jet half-width in the transverse ($z_{0.5}$) and spanwise ($y_{0.5}$) directions. In the discussion of the experimental results, the maximum streamwise velocity (u_m) is used to document the decay of the velocity in the streamwise direction. The jet half-widths ($z_{0.5}$ and $y_{0.5}$) are used to characterise the spread of the jet in the transverse and spanwise directions. As noted in Chapter 3, it was challenging to produce a high quality 3D wall jet flow at relatively low inlet or initial Reynolds numbers into a large amount of stagnant fluid.

4.1.1 Decay of Maximum Streamwise Velocity and Jet Half-widths

Figure 4.1a shows variation of the maximum local velocity ($U_m = u_m/u_j$) with streamwise distance ($X = x/d$) for two Reynolds numbers, Re_j = 310 and 800. As the jet evolves downstream, it entrains the stagnant ambient fluid and the jet velocity is slowed considerably. There is a modest difference between the decay of u_m at Re_j = 310 and 800 in the region $X \geq 15$. In this region of the flow, the values of U_m at Re_j =310 are marginally lower than the corresponding values at Re_j = 800. This observation is consistent with the notion that the jet with a lower exit momentum (Re_j = 310) should decay faster. As will be shown in subsequent figures, the momentum of the jet diminished with streamwise distance until the jet was no longer able to penetrate the relatively larger amount of stagnant Newtonian fluid in the tank. The approximate axial location where no meaningful penetration was possible and the jet began to disintegrate is demarcated by a solid line (Re_j = 310) and a dash line (Re_j = 800) in Fig. 4.1. It should be noted that the location for the jet with the lower Reynolds number is closer to the inlet plane of the jet.

The decay of u_m is accompanied by a spread in both the transverse and spanwise directions. As remarked earlier, the spread is often characterised by the jet half-widths in the transverse ($Z_{0.5} = z_{0.5} / d$) and spanwise ($Y_{0.5} = y_{0.5} / d$) directions. Figure 4.1(b, c) shows the variation of $Z_{0.5}$ and $Y_{0.5}$ with X. These figures demonstrate that the jet half-widths for Re_j = 310 are significantly larger than the corresponding values for Re_j = 800.

4.1.2 Velocity Vectors and Similarity Consideration

Figure 4.2 shows the vector plots of the velocity field in the symmetry plane in the

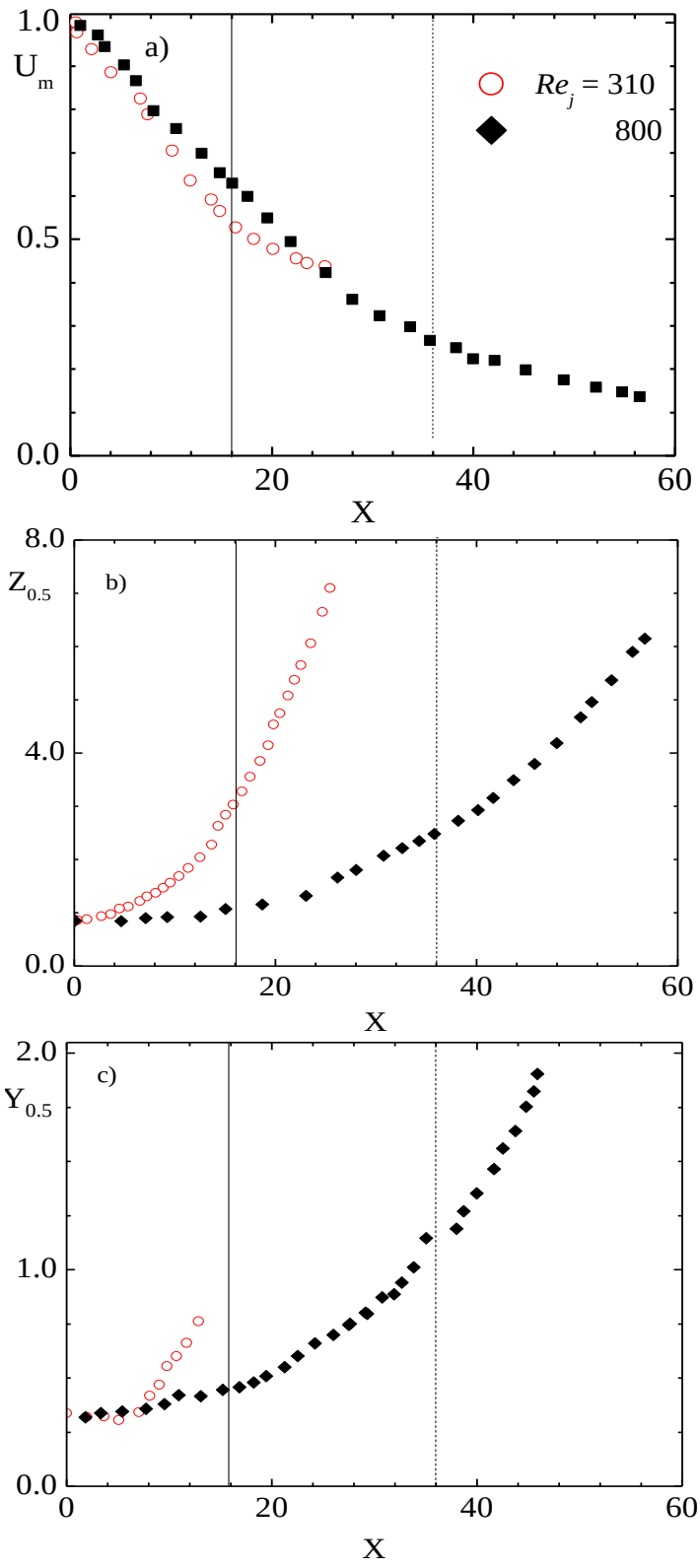

Figure 4.1: PIV results on variation: a) maximum velocity decay, U_m, b) and c) jet half-widths ($Z_{0.5}$ and $Y_{0.5}$) in downstream direction for Re_j = 310 and 800.

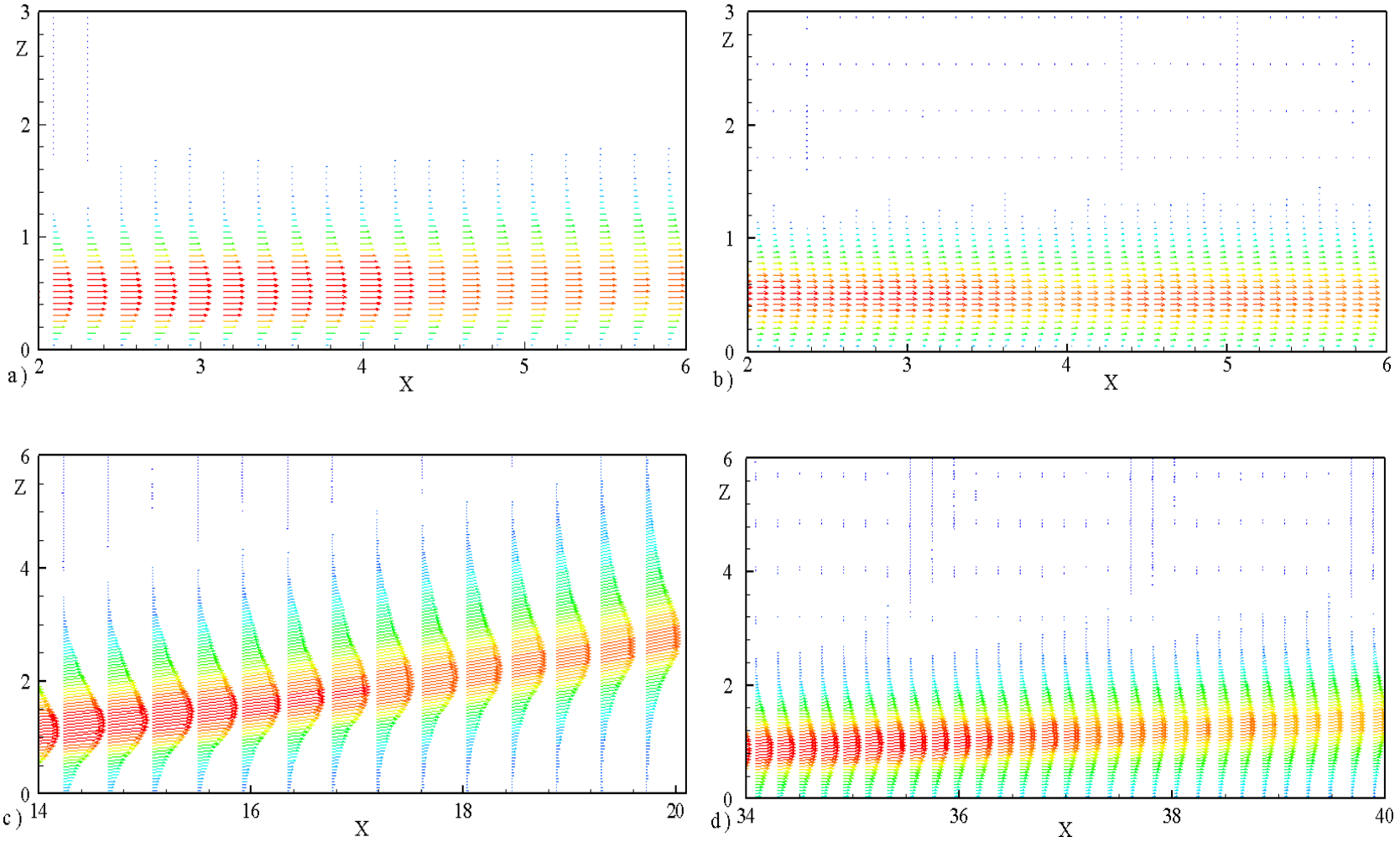

Figure 4.2: Velocity vectors in the regions: (a, b) $2 \leq X \leq 6$, (c) $14 \leq X \leq 20$ and (d) $34 \leq X \leq 40$. (a, c) at $Re_j = 310$ and (b, d) at $Re_j = 800$.

regions $2 \leq X \leq 6$ and $14 \leq X \leq 20$ for $Re_j = 310$ and $2 \leq X \leq 6$ and $34 \leq X \leq 40$ for $Re_j = 800$. The plots in the regions $2 \leq X \leq 6$ for $Re_j = 310$ and 800 are indicative of a classical wall jet. In these cases, the secondary (transverse) velocities are relatively low and the vectors in the inner region are parallel to the wall as should be expected (Fig. 4.2(a, b)). The velocity gradient (dU/dZ) also increases sharply. Further downstream ($14 \leq X \leq 20$) and ($34 \leq X \leq 40$) for $Re_j = 310$ and 800, respectively, the velocity vectors in the wall region are no longer parallel to the wall. Here, the streamwise component of velocity vectors close to the wall is small and the sharp increase in dU/dZ observed upstream is no longer evident. The jet appears to lift off from the wall and the location of the maximum velocity, Z_m, increases more dramatically with X than observed in Fig. 4.2(a, b).

In order to explore if the jet for the two Reynolds numbers achieves a self-similar condition, profiles of the streamwise velocity ($U = u / u_m$) in the symmetry plane (Fig. 4.3) were plotted at selected streamwise locations. For $Re_j = 310$ (Fig. 4.3a), it is clear that in the region $Z' (= z/z_{0.5}) \leq 1.2$ there is no significant difference between the profiles at X = 5 and 10. In this region, the normalised velocities at X = 2 are marginally lower. Based on this observation, it is reasonable to conclude that the jet for $Re_j = 310$ becomes self-similar at X = 5. Consistent with the observations made in Fig. 4.2c, the profiles at X = 15 and further downstream deviate significantly from the upstream profiles. The collapse among the profiles in the region $Z' \geq 1.2$ is not as good as in the inner region, even for X = 5 and 10. Such observations have been reported in previous 2D laminar wall jets (Bajura and Szewczyk, 1970; Cohen *et al*, 1992) and even 2D and 3D turbulent wall jets. Since the values of U are ordinarily small in this region, it is likely that the PIV

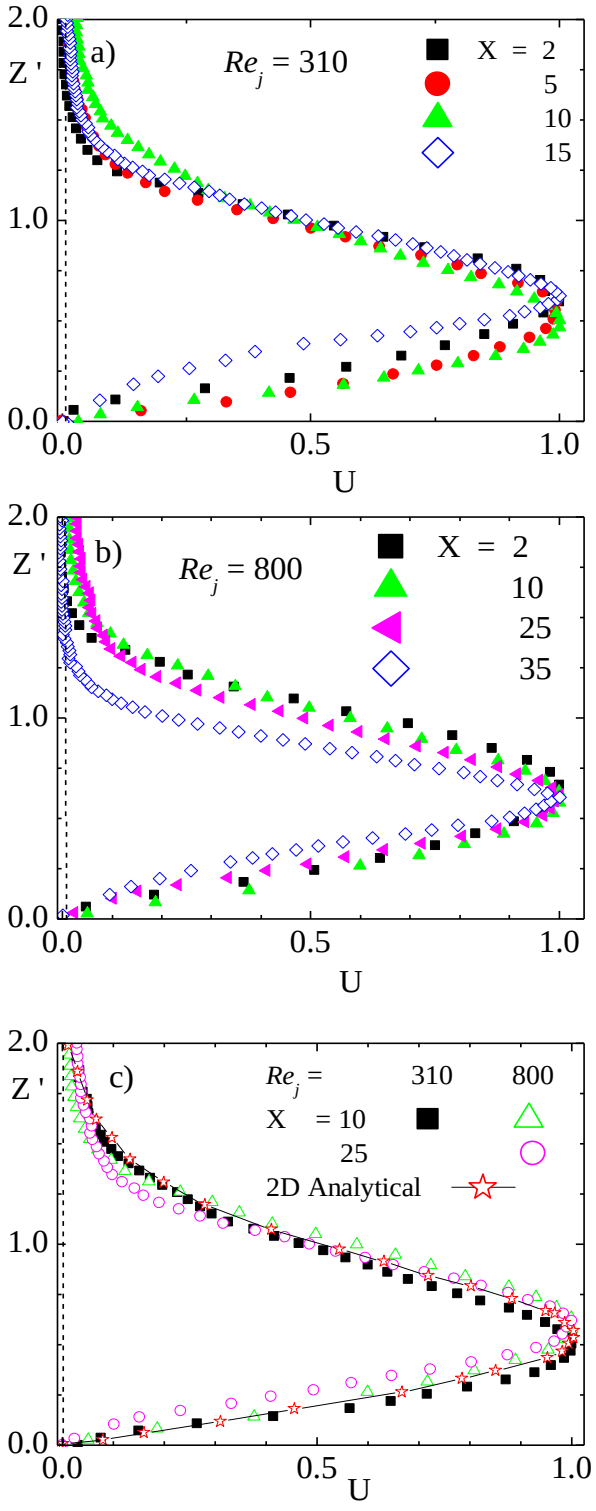

Figure 4.3: Normalised streamwise velocity profiles on transverse direction at various downstream locations.

is not able to resolve them accurately. Figure 4.3b shows profiles at Re_j = 800. Similar to what was observed for Re_j = 310, in the region Z ' $\leq$ 1.2, there are no significant differences among the various profiles except at X = 35. The deviation at 35 for Re_j = 800 should also be expected based on the velocity vectors shown in Fig. 4.2d. For Re_j = 800, it appears that similarity condition is achieved at X = 2. The locations of onset of similarity condition in the present study are in agreement with prior numerical results for 3D wall jets. For example, Adane and Tachie (2008a) reported that the velocity profiles for Re_j = 77 – 310 become self-similar at X = 5. For 2D wall jet flows, on the other hand, it has been shown that the onset of self-similarity is delayed until X = 18 (Bajura and Szewczyk, 1970) for Re_j = 377 and X = 18 (Cohen *et al*, 1992) for Re_j = 466-725.

Figure 4.3c shows a comparison among representative self-similar velocity profiles for Re_j = 310 and 800 from the present experiments and the analytical profile for a 2D laminar wall jet (Glauert, 1956). There is a modest difference between the location of the maximum velocity (Z ' = 0.56) for the 2D wall jet and the present data for Re_j = 800 and Z ' = 0.50 for the present data for Re_j = 310. Otherwise, the profiles for the 2D and 3D wall jets are similar, and are also independent of Reynolds number.

Consideration is now turned to the velocity profile in the spanwise plane located at z_m. It was observed the velocity profiles were symmetric with respect to the symmetry plane (y = 0). Therefore, only the velocity profiles for $y \geq 0$ will be reported in this work. The velocity distributions in the spanwise plane at selected streamwise locations are shown in Fig. 4.4. Although the quality of data in this plane (particularly in the region Y ' > 1) is not as good as those in the symmetry plane, it can be concluded that these profiles also

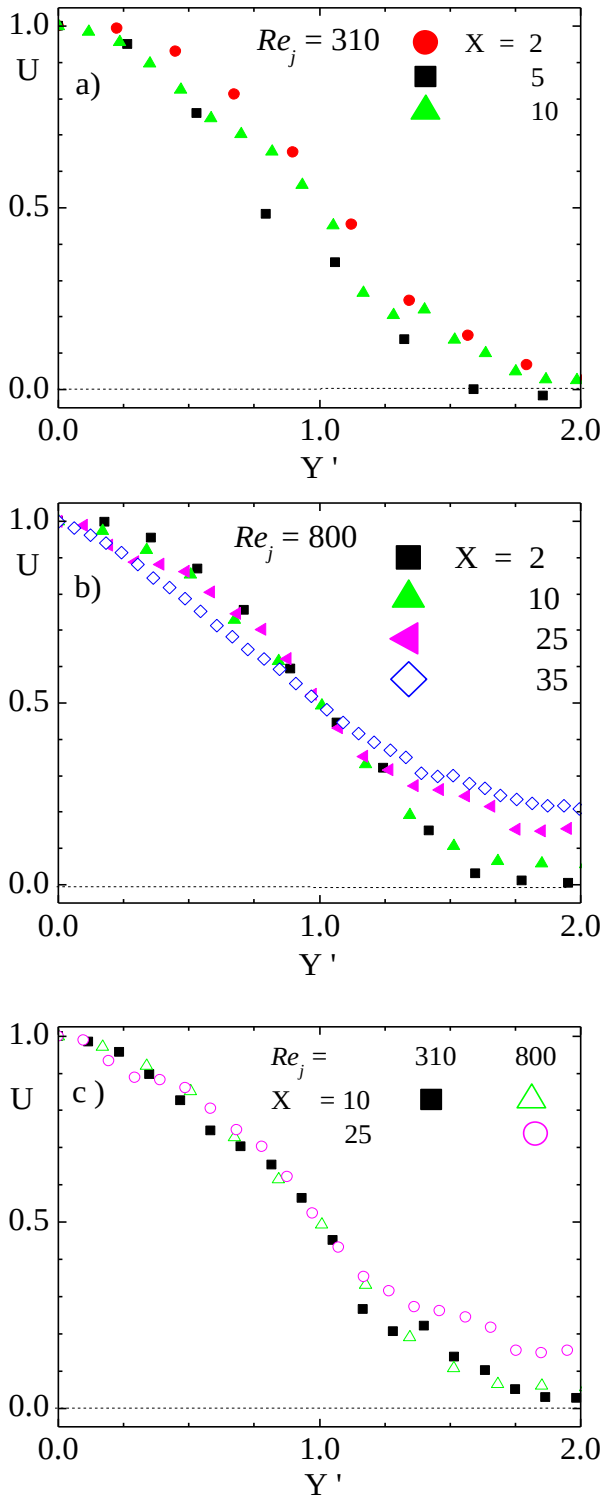

Figure 4.4: Normalised streamwise velocity profiles on spanwise direction at various downstream locations.

become self-similar at the axial locations where self-similarity was observed in the symmetry plane. Furthermore, the profiles in the region Y ' < 1 do not exhibit any Reynolds number effects. In summary, the profiles at the two Reynolds numbers studied in the present experimental study of a Newtonian fluid exhibit a self-similarity condition (albeit over a limited range of streamwise distance). Since the streamwise extent (X < 35) over which the velocity field for the higher Reynolds number (Re_j = 800) resemble a classical 3D laminar wall jet is relatively larger than that observed at the lower Reynolds number, the data sets at Re_j = 800 will be used for comparison with the numerical results in later sections.

4.2 Experimental Results of Wall Jet flow of non-Newtonian Fluids

As in Section 4.1, the jet half-width in the transverse direction ($z_{0.5}$) and spanwise direction ($y_{0.5}$) are used to document the spread of the jet in the respective directions whereas u_m is used to examine the velocity decay. Reference experimental results for 3D laminar wall jet of the Newtonian fluid at Re_j = 800 (Section 4.1) will be shown for comparison.

4.2.1 Decay of Maximum Streamwise Velocity and Jet Half-widths

Figure 4.5a shows the variation of the normalised maximum local velocity U_m with streamwise distance, for XG005 fluid at the three Reynolds numbers. The jet starts interacting with the ambient fluid immediately downstream of the efflux section. The entrainment of the stagnant ambient fluid by the jet in turn slowed the jet velocity. This is true for all the Reynolds numbers. This trend is similar to that reported by Filip *et al* (1991) and Adane and Tachie (2008a) for non-Newtonian fluids, and also in Section 4.1

and by Glauert (1956) for Newtonian fluids. There is no marked distinction of the decay of U_m among the various Re_j in the region $X \leq 6$. Similarly, in the region $X \leq 18$ for Re_j = 420 and 800, the figure shows no significant difference between the decay of U_m. However, at larger downstream locations, as expected, U_m decays most rapidly at the smallest inlet Reynolds number (Re_j = 250). For instance at X = 30, U_m is 0.30, 0.47 and 0.56, respectively, for Re_j = 250, 420 and 800.

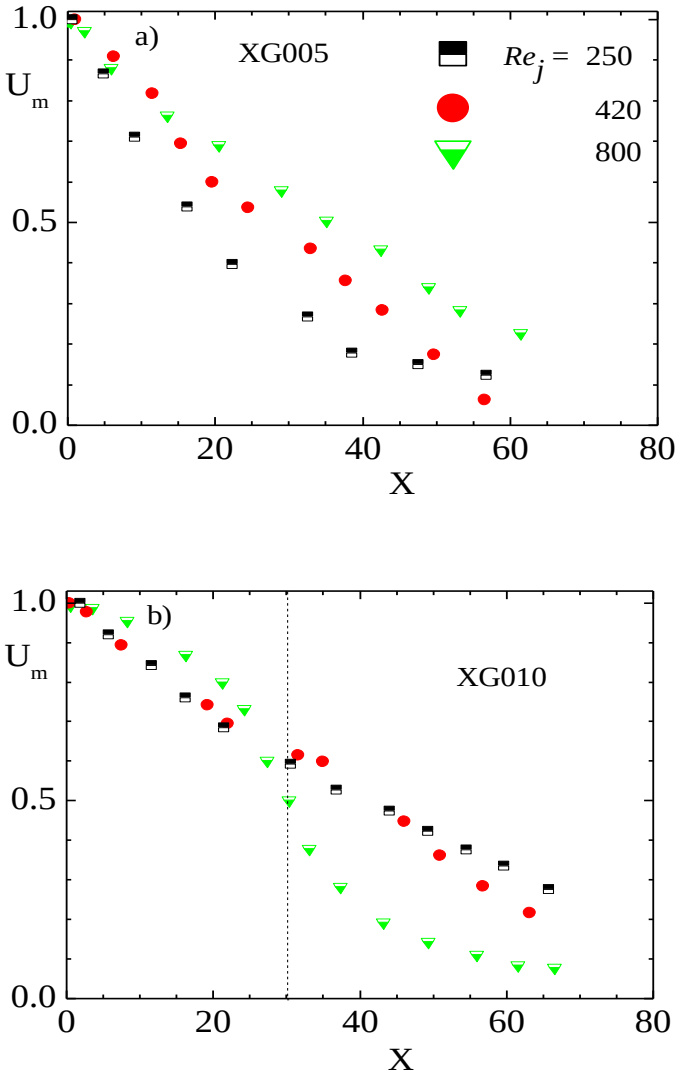

Figure 4.5: Variation of maximum velocity decay, U_m in the streamwise direction at various Re_j for (a) XG005 and (b) XG010.

In the region X < 8, the velocity decay for XG010 is also independent of Reynolds number (Fig. 4.5b). In fact, even in the region X < 52, the decay of U_m for Re_j = 250 and 420 showed no noticeable difference. Figure 4.5b shows that in the region X > 52, the decay of U_m for Re_j = 250 is slightly slower than at Re_j = 420. For example, at X = 60, U_m = 0.34 and 0.26 for Re_j = 250 and 420, respectively. It is clear from Fig. 4.5b that the flow development can be divided into two regions as demarcated by the dash vertical line. In the first region (X ≤ 30), U_m values for Re_j = 800 are relatively higher than those for Re_j = 250 and 420. Meanwhile, in the second region (X > 30) U_m values for Re_j = 250 and 420 are significantly higher than those for Re_j = 800. Further downstream (in the region X > 52), the U_m decreases consistently with increasing Re_j. This observation is contrary to those made for XG005 in the region X > 18 where the higher Re_j value has the slowest decay and also for measurements in 3D laminar wall jets of the Newtonian fluid (Section 4.1).

The spread of the jet in both transverse and spanwise directions are presented in Fig. 4.6. It is observed that the $Z_{0.5}$ values are independent of Reynolds number in the region X ≤ 25. Downstream of this region, the slower velocity decay observed for the higher Re_j produced a lower spread (Fig. 4.6a). Similarly, Fig. 4.6b demonstrates that the jet spreads fastest at Re_j = 800 and slower at Re_j = 250 and 420. Also, as observed earlier for U_m, there is a modest difference between the $Z_{0.5}$ values for Re_j = 250 and 420 in the region X ≥ 30.

The maximum percentage difference between the $Y_{0.5}$ values for XG005 fluid at Re_j = 420 and 800 is 13% whereas that between Re_j = 420 and 250 is approximately 61% in the

compared region (Fig. 4.6c). On the other hand, the values of $Y_{0.5}$ for both Re_j = 250 and 420 for XG010 fluid are similar and are significantly lower than those at Re_j = 800 in the region X > 20 (Fig. 4.6d). In the region X < 30, the ratio of $Y_{0.5}$ / $Z_{0.5}$ ranges from 0.38 to 1.0, whereas in the region X ≥ 30, it increases to 1.67. These ratios indicate that in the region X > 30 the jet spreads more in the spanwise direction than it does in the transverse direction. The corresponding values for Re_j = 420 ranges from 0.36 to 1.07.

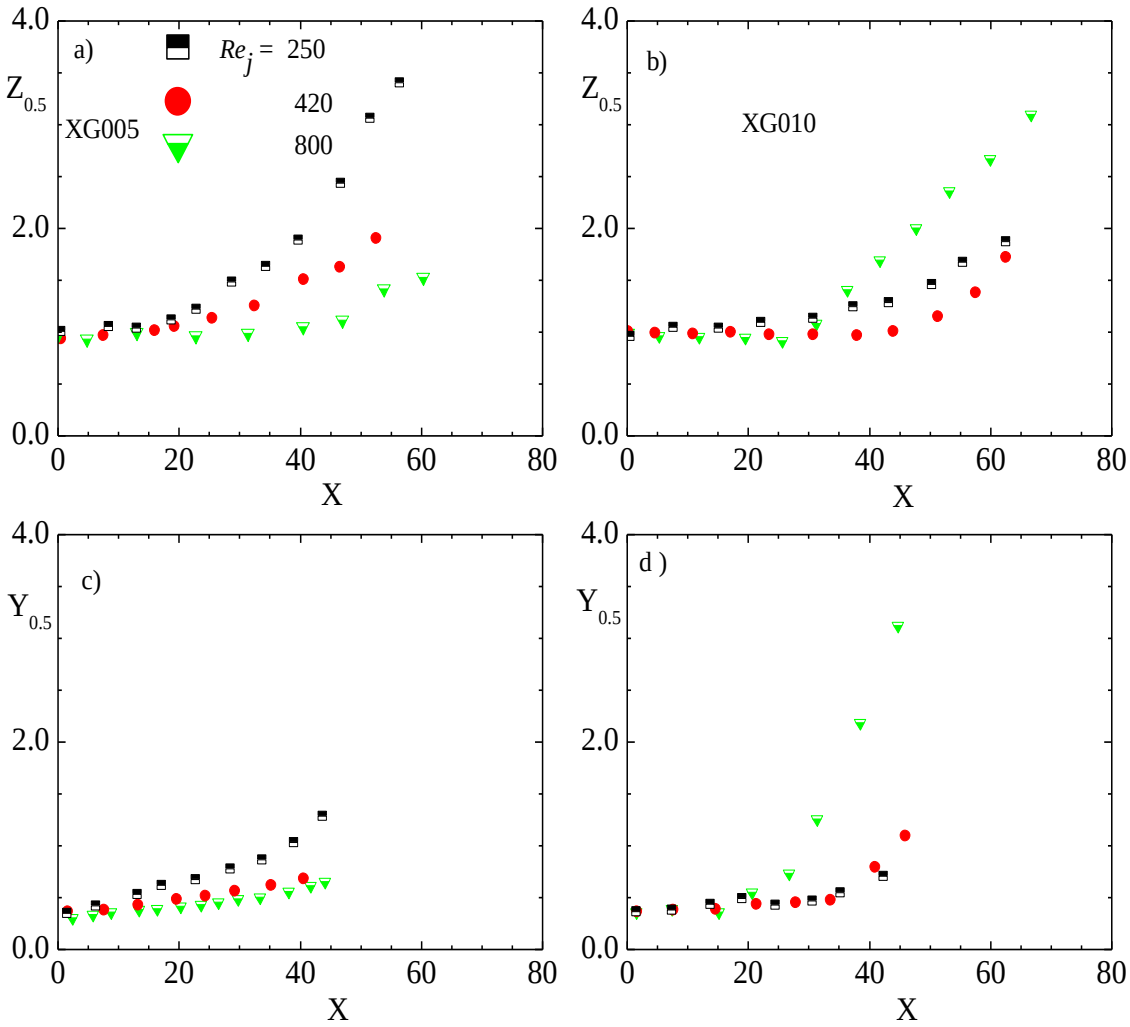

Figure 4.6: Variation of jet half-widths, $Z_{0.5}$ (a, b) and $Y_{0.5}$ (c, d) in the streamwise direction at various Re_j for XG005 (a, c) and XG010 (b, d).

On the contrary, it is obvious from Fig. 4.6 that irrespective of the Reynolds number for XG005 fluid as well as for the XG010 fluid at $Re_j = 250$, the jet rather spreads more in the transverse direction than it does in the spanwise direction. In fact, for these test cases, it was found that the ratio of $Y_{0.5} / Z_{0.5}$ is 0.45±0.11. This observation for the XG005 fluids and $Re_j = 250$ for XG010 fluid is consistent with that made in previous numerical study of 3D wall jet flows of power-law non-Newtonian fluids (Adane and Tachie, 2008a) as well as experimental (Section 4.1) and previous numerical (Craft and Launder, 2001) studies of 3D wall jet flow of a Newtonian fluid.

A comparison of the variation of decay of U_m and the jet half-widths with streamwise distance at various Reynolds number for the Newtonian and non-Newtonian fluids is shown in Fig. 4.7. In Fig. 4.7(a, b) irrespective of Re_j, the decay of U_m is consistently slower for XG010 than XG005. This is consistent with the observation made by Adane and Tachie (2008a) for power-law fluids where in the early region of the flow development, the lower power-law index has a slower decay.

Figure 4.7c shows that in the early region ($X \leq 30$), the XG010 fluid which has higher zero-shear apparent viscosity has the slowest decay rate. This is consistent with observations made earlier for the lower Reynolds numbers. On the contrary, the U_m values for XG010 are consistently lower than the measured values for the other two fluids in the region $X > 40$.

The comparison of the transverse jet half-width in Fig. 4.8a shows that the slower decay of U_m resulted in a slower spread of the jet. This is true for both Reynolds numbers (Fig.

4.8(a, c)). For instance at X = 40, $Z_{0.5}$ = 1.90 and 1.27 at Re_j = 250, respectively, for XG005 and XG010. At Re_j = 420, the corresponding values are 1.5 and 1.0, respectively.

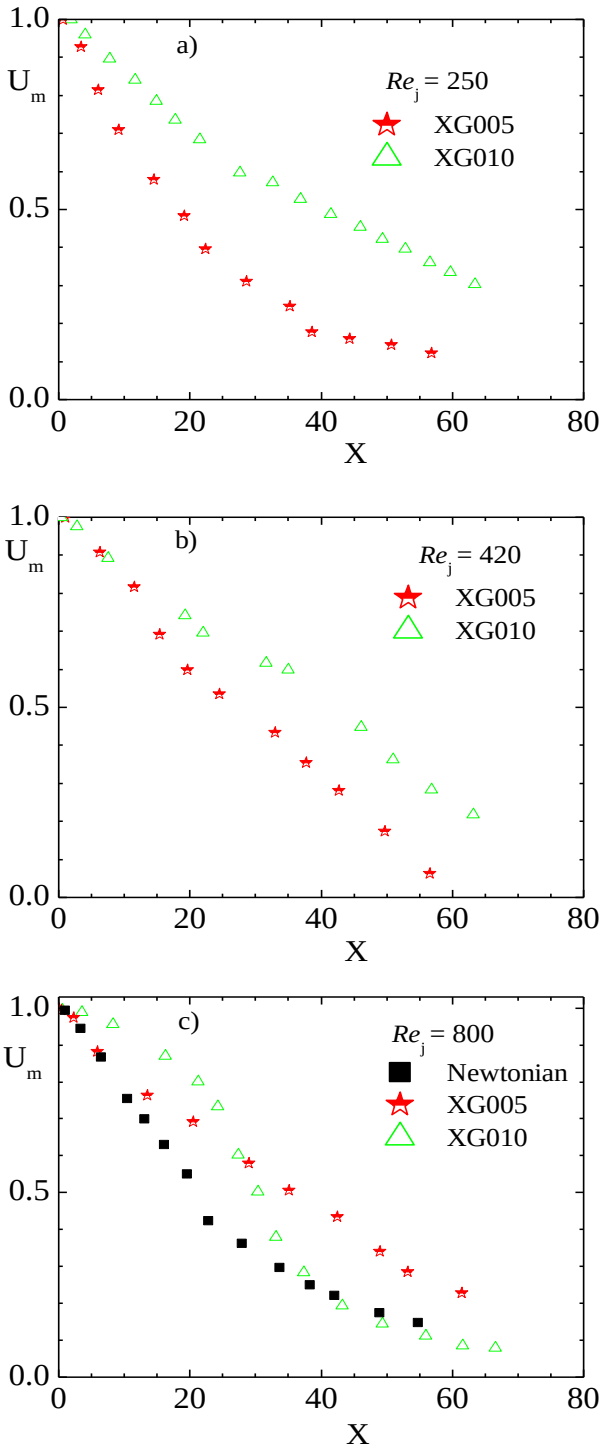

Figure 4.7: Comparison of maximum velocity decay, U_m for various fluids at Re_j = (a) 250, (b) 420 and (c) 800.

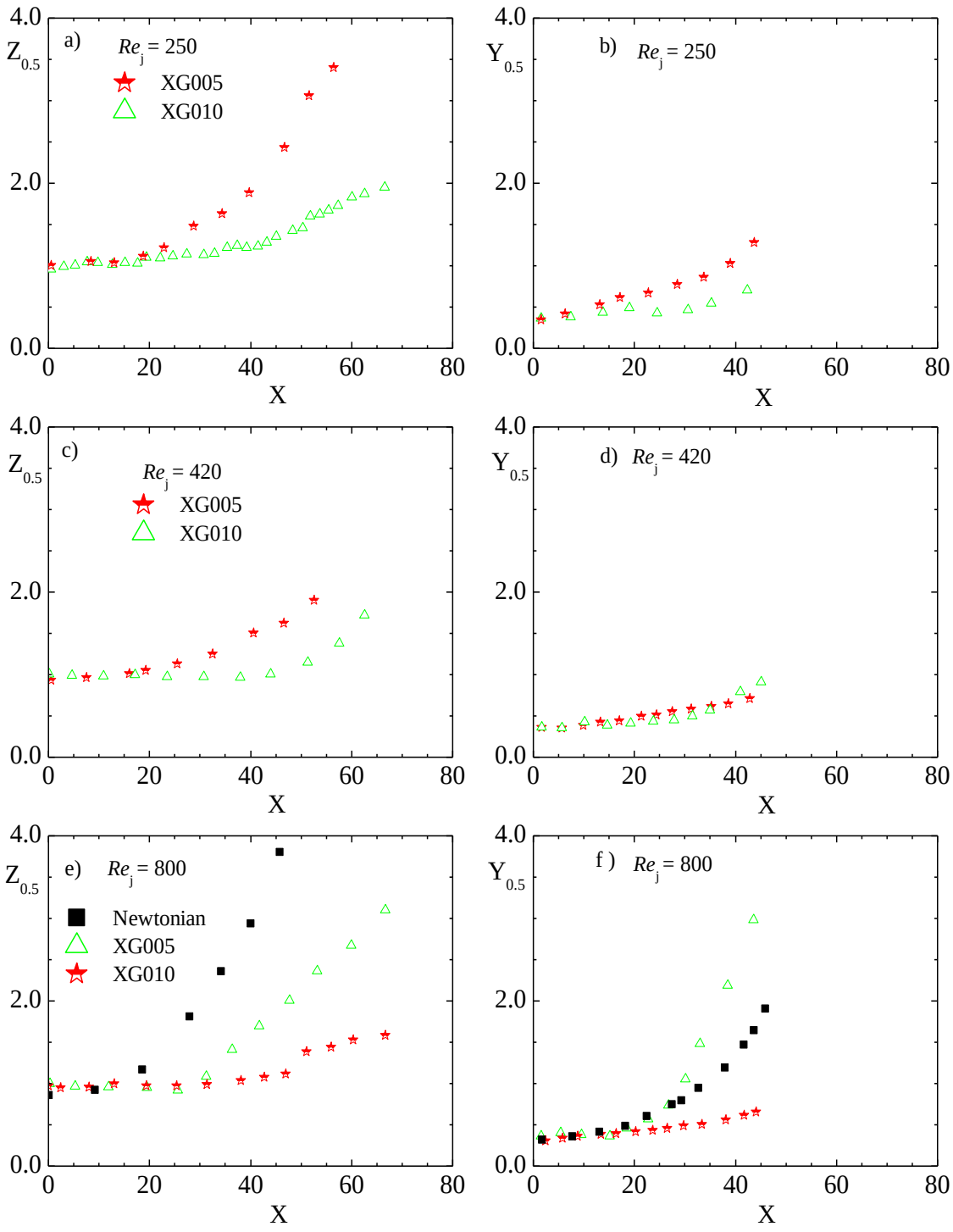

Figure 4.8: Comparison of: (a, c, e) $Z_{0.5}$ and (b, d, f) $Y_{0.5}$ for various fluids at Re_j = (a, b) 250, (c, d) 420, and (e, f) 800.

It is worth mentioning that, irrespective of Re_j, in the region $X \leq 25$ there is no difference between the $Z_{0.5}$ values for both XG005 and XG010 fluids. Similarly, in the region $X < 20$, the difference between the Newtonian fluid and non-Newtonian fluids is insignificant (Fig. 4.8e). Further downstream ($X > 30$), however, the jet spreads more for the Newtonian fluid and less for XG005.

Not surprisingly the growth of $Y_{0.5}$ is more rapid for XG005 than XG010 for the two lower Reynolds numbers (Fig. 4.8(b, d)). The fluid effect is only observed in the region $X > 20$ for the three fluids at $Re_j = 800$ (Fig. 4.8f). The spread is more rapid for XG010 than for XG005. Although this observation is different from those at the lower Reynolds numbers (Fig. 4.8(b, d)) and even that of $Z_{0.5}$ (Fig. 4.8e), it should be recalled that the spread was observed to be faster in the spanwise direction for XG010 than in transverse direction. Besides, the $Y_{0.5}$ values for XG005 are lower than those for the Newtonian fluid.

4.2.2 Velocity Profiles

Figures 4.9 shows the normalised streamwise velocity ($U = u / u_m$) profiles in the symmetry plane ($y = 0$) at various streamwise locations ($5 \leq X \leq 60$). The spanwise and transverse distances from their respective origin are normalized by the half-widths. That is, $Z' = z / z_{0.5}$ and $Y' = y / y_{0.5}$. For $Re_j = 250$ and the axial locations shown in Fig. 4.9a for XG005, it is observed that the location of the maximum velocity ($Z' = 0.56$) for profiles in the region $5 \leq X \leq 25$ is higher than $Z' = 0.46$ for $X > 25$. Otherwise, the velocity profiles in the transverse direction collapsed remarkably well onto a single curve in the region $Z' < 1.2$. As mentioned earlier, discrepancies among velocity profiles close

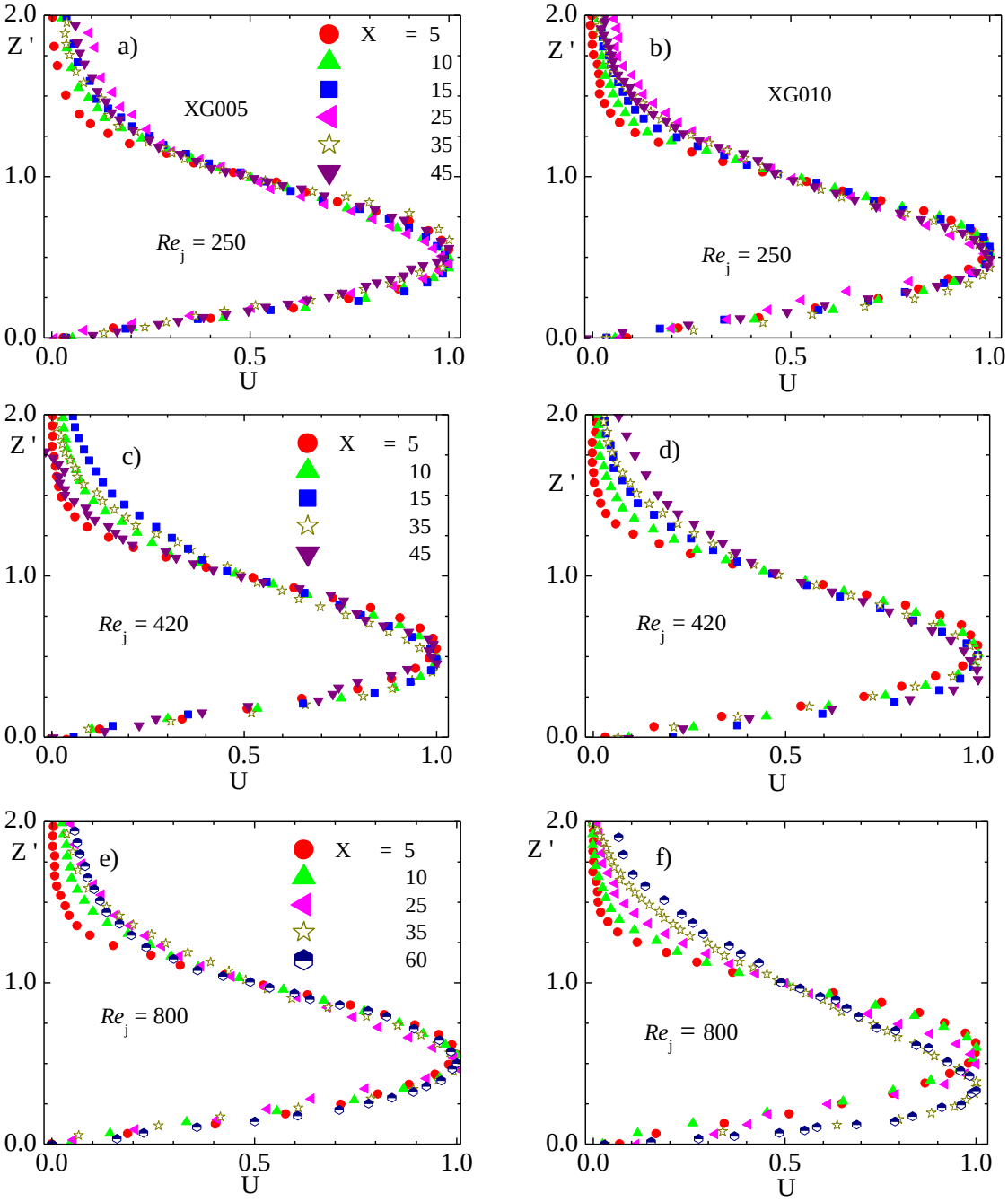

Figure 4.9: Normalised streamwise velocity profiles in transverse direction at various downstream locations for XG005 (a, c, e) and XG010 (b, d, f).

to the outer edge of the jet ($Z' \geq 1.2$) have been reported in previous 2D and 3D laminar wall jets (Bajura and Szewczyk, 1970; Cohen *et al*, 1992), and even 2D and 3D turbulent wall jets. Based on this observation, it is reasonable to assert that for the XG005 fluid at $Re_j = 250$ the flow becomes self-similar at X = 5.

Similar observations are made for the velocity profiles at $Re_j = 250$ for XG010 (Fig. 4.9b), $Re_j = 420$ for both XG005 (Fig. 4.9c) and XG010 (Fig. 4.9d), and $Re_j = 800$ for XG005 (Fig. 4.9e). However, in these figures, the location of the maximum velocity is the same for all the X locations plotted.

For XG010 at $Re_j = 800$ (Fig. 4.9f), the velocity profiles in the region $X < 25$ collapse reasonably well. The location of the maximum velocity for these profiles is at $Z' = 0.56$. The profiles in the region $35 \leq X \leq 60$ also collapsed onto each other; however, they are distinctly different from the profiles obtained upstream. The location of the maximum velocity is $Z' = 0.34$ which is closer to the bottom wall than $Z' = 0.56$. It is important to note that this region ($35 \leq X \leq 60$) corresponds to the region where $Re_j = 800$ experience a very sharp decay of U_m (Fig. 4.5b). In their work on Newtonian fluid, Tsuji *et al* (1977) reported that the velocity profiles for $Re_j = 635$ in the region $X \geq 60$ deviate from a classical 2D laminar wall profile. In fact, those profiles were in a better agreement with typical profile for a turbulent wall jet. Similarly, Bhattacharjee and Loth (2004) observed a transitional regime for $Re_j \geq 700$ for their studies on wall jet flows of Newtonian fluid.

The corresponding profiles in the spanwise direction are shown in Fig. 4.10. Although the quality of data in this plane (particularly in the region $Y' > 1.2$) is not as good as

those in the symmetry plane, it appears that these profiles also become self-similar at the axial locations where self-similarity was observed in the symmetry plane. This is true irrespective of the Reynolds number and fluid.

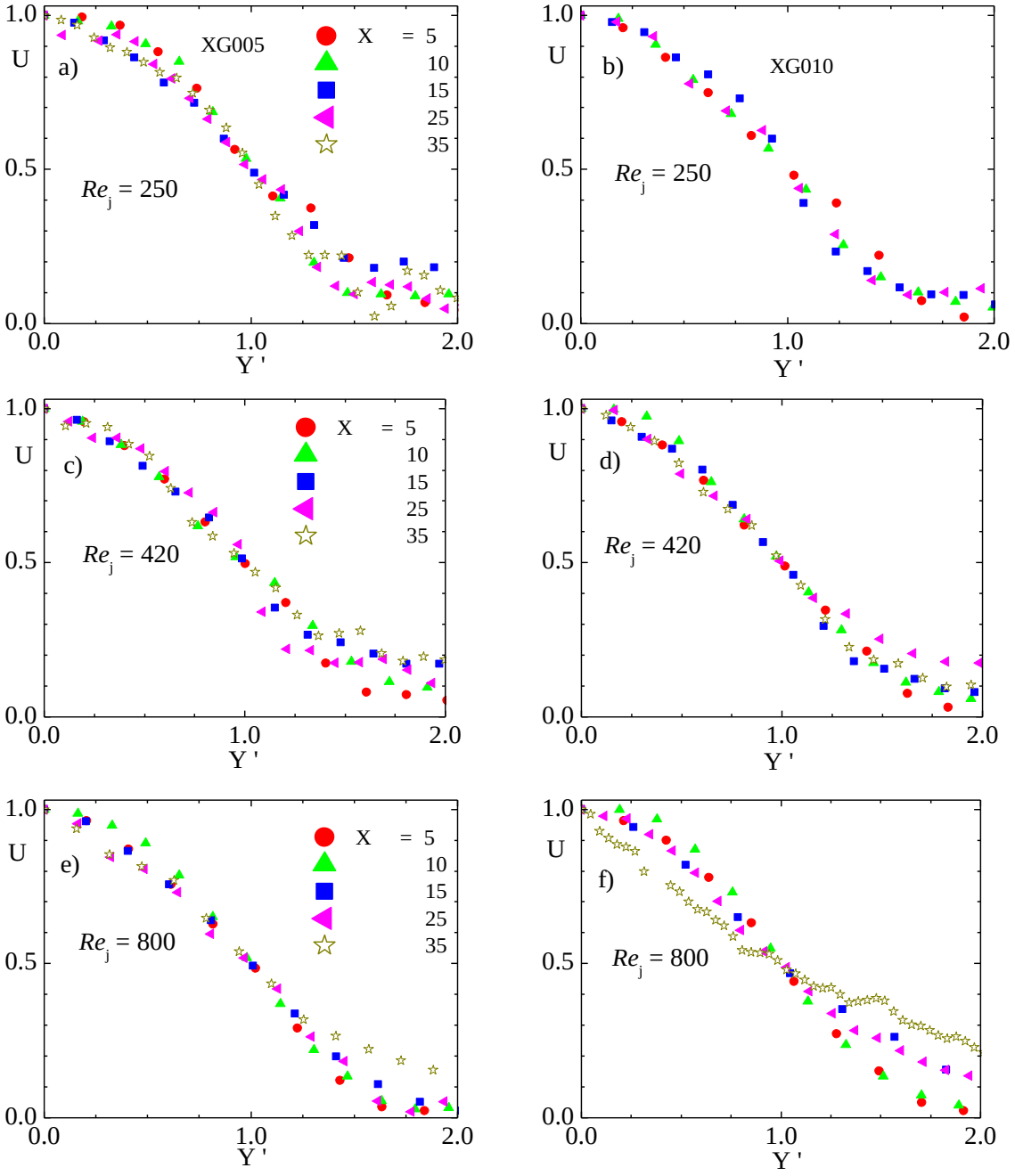

Figure 4.10: Normalised streamwise velocity profiles in spanwise direction at various downstream locations for XG005 (a, c, e) and XG010 (b, d, f).

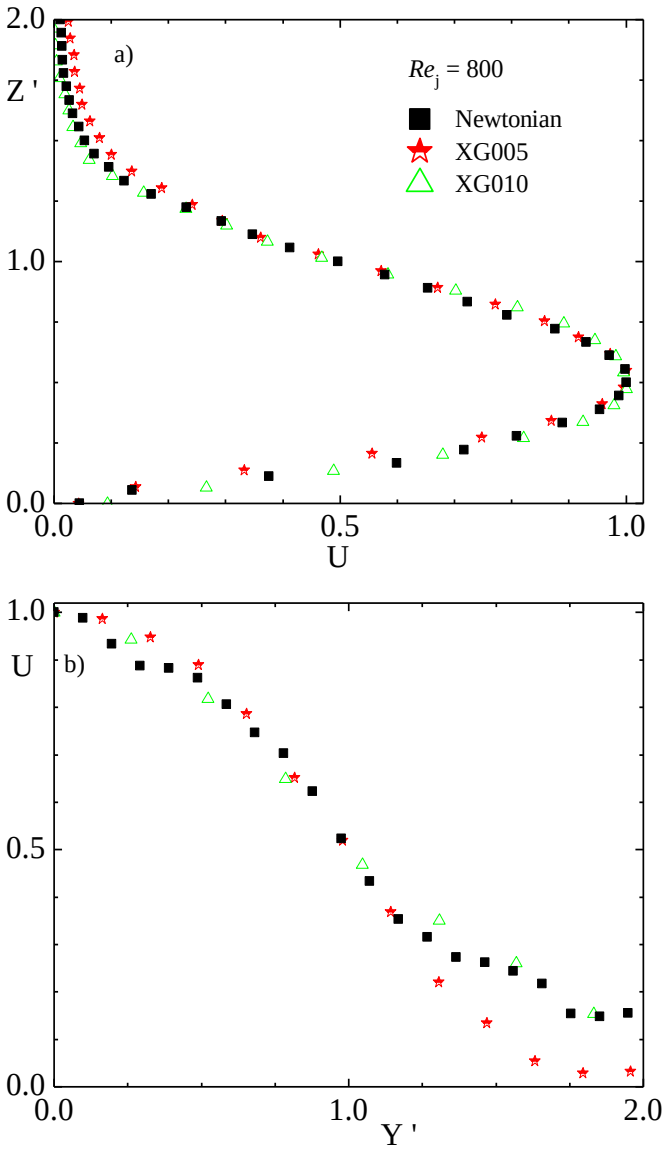

Figure 4.11: Comparison of various fluids on the similarity velocity profiles

Figure 4.11 above shows a comparison among the two non-Newtonian fluids and the Newtonian fluid at Re_j = 800. From Fig. 4.11a, it is clear that there are no marked differences among the normalised velocity profiles. Similarly, the profiles in the spanwise direction (Fig. 4.11b) showed no noticeable fluid effects especially in the region $Y' \leq 1.2$. This observation is at variance with previous numerical results for power-law fluids (Filip *et al*, 1991; Adane and Tachie, 2008a). In those previous numerical works, it

was reported that with the exception of the very near-wall region, a shear thinning fluid has higher velocities than a Newtonian fluid. It is important to note, however, that the Reynolds numbers considered in the study by Adane and Tachie (2008a) were relatively lower than those in the present experiments.

4.3 Numerical Results of Newtonian Fluid

4.3.1 Velocity Decay and Spread Rates

The decay of u_m with streamwise distance for present and previous (Adane and Tachie, 2008a) numerical results is plotted in Fig. 4.12a. The experimental data (labelled as PIV) for Re_j = 800 are also shown for comparison. Similar to the observations made for the experimental results, the local maximum velocity decreases with an increase in the downstream direction. The figure shows that agreement between experiment and computation at Re_j = 800 is limited to the early region of flow development (X < 20). Further downstream, the numerical data decayed less slowly than observed from measurement. The numerical results also show that the local maximum velocity decayed faster with decreasing inlet Reynolds number. For example, at X = 20, U_m = 0.11, 0.30, 0.38 and 0.61 for Re_j = 155, 310, 420 and 800, respectively. It should be noted that, at X = 17, the U_m is almost zero for Re_j = 77.

The Reynolds number dependence of the velocity decay can be explained by the variation of the local momentum flux (M_x) with streamwise distance. In the present study, the local momentum flux was computed from the following expression:

$$M_x = \rho \int_{Ax} u^2 dzdy \tag{4.1}$$

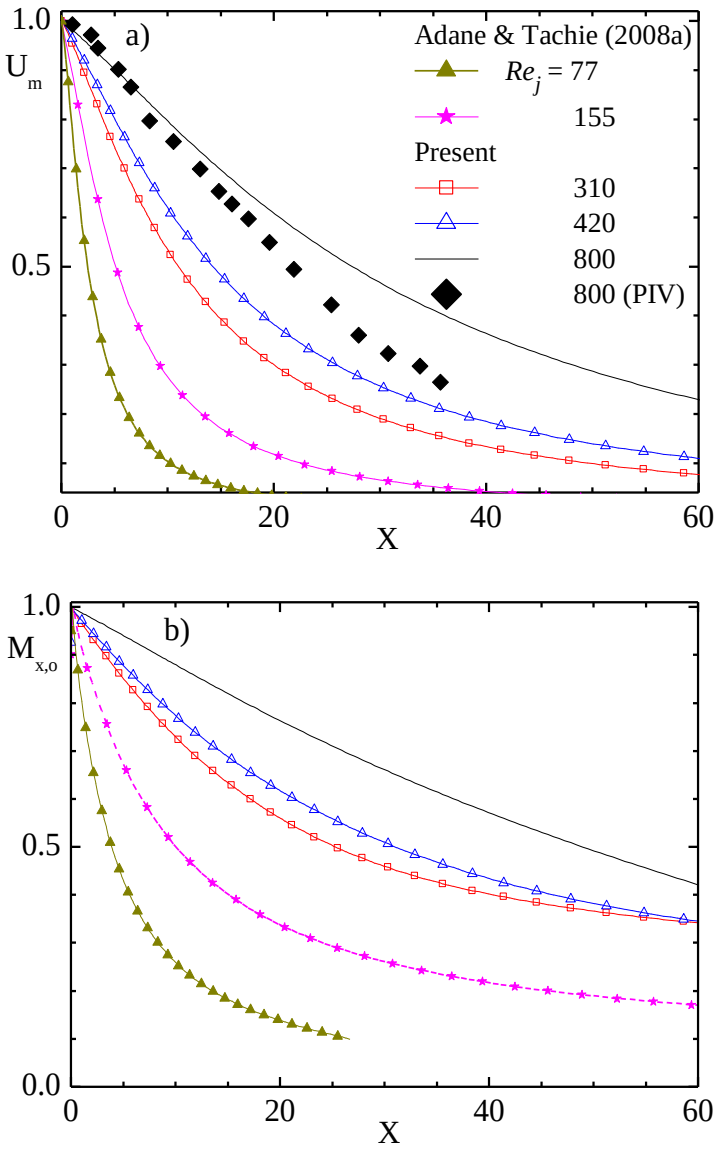

Figure 4.12: Comparison of results at various Re_j on variation of: a) maximum velocity decay, U_m and b) local momentum flux, $M_{x,o}$.

where A_x is the jet cross-sectional area in the *y*-*z* plane at a specific X location. Figure 4.12b shows the variation of the ratio $M_{x,o} = M_x / M_o$ (where M_o is the momentum flux at the inlet plane) with X. The values of M_o are 7.80×10^{-7}, 3.15×10^{-6}, 1.48×10^{-5}, 2.45×10^{-5} and 1.00×10^{-4} kg•m/s^2, respectively, for Re_j = 77, 155, 310, 420, and 800. The results show that, indeed, the momentum flux at a lower Reynolds number decayed faster

for a lower Reynolds number than a relatively higher Reynolds number. At X = 20, for example, $M_{x,0}$ = 0.14, 0.33, 0.56, 0.62 and 0.76, respectively, for Re_j = 77, 155, 310, 420 and 800.

The plots of jet half-widths obtained from both experiments and computations are shown in Fig. 4.13. It can be seen from Fig. 4.13a that there exists a good agreement between the experimental and numerical results at Re_j = 800 in the region X ≤ 22 for $Z_{0.5}$. Downstream of this region, the slower decay of maximum velocity observed from the numerical results produced a lower spread than the measured values. The figure also demonstrates clearly that the jet spreads fastest at Re_j = 77 and slowest at Re_j = 800. The differences in the spread rates will be quantified in Fig. 4.14. In the spanwise direction, the experiment and computation show similar values in the region X < 30 (Fig. 4.13b). As expected, the values of $Y_{0.5}$ from computation are significantly lower than those from measurement in the region X > 30.

The variation of the spread rates ($S_z = dz_{0.5}/dx$, $S_y = dy_{0.5}/dx$) with X for the various Re_j is shown in Fig. 4.14. In these plots, the present numerical results and the results from Adane and Tachie (2008a) and Craft and Launder (2001) (where available) are shown. The analytical results for 3D laminar wall jets presented by Krechetnikov and Lipatov (2002) indicate that the spread rates should increase linearly with downstream distance. The data presented in Fig. 4.14a show that, for $Re_j \geq 155$, the spread rate in the symmetry plane (S_z) increases sharply from the exit followed by a linear variation with X. Clearly, the onset of the linear region for S_z depends strongly on Re_j. For example, the linear region begins at X = 54, 35, and 17, respectively, for Re_j = 310, 420 and 800. It should

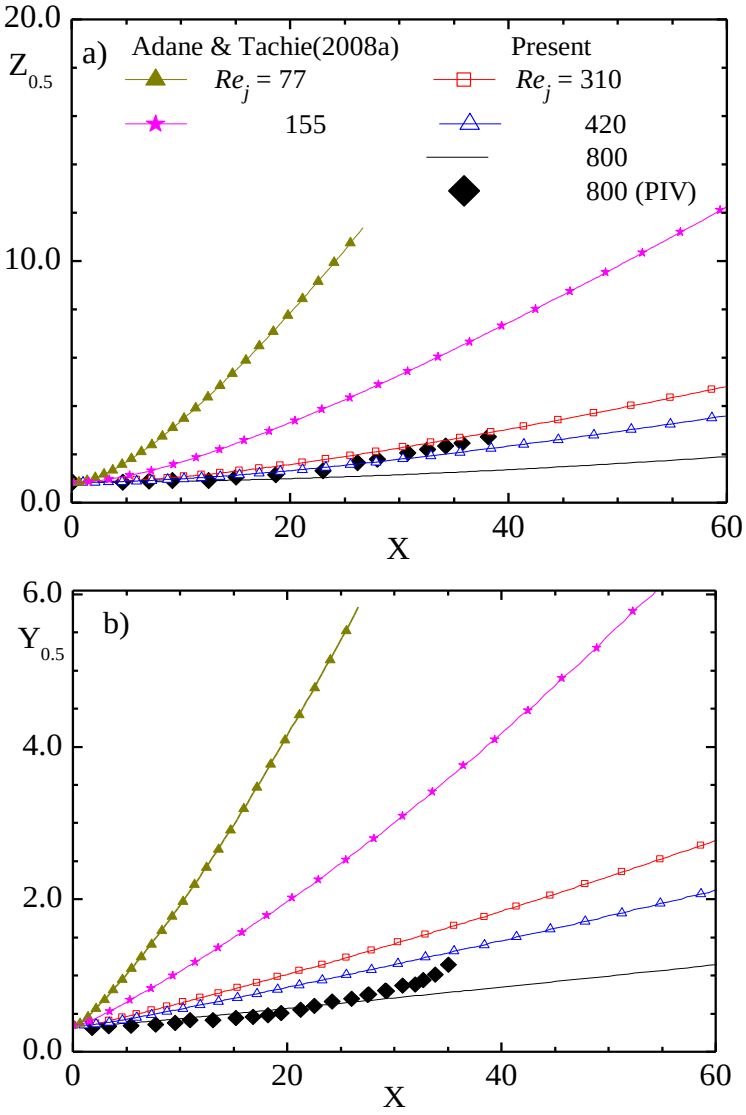

Figure 4.13: Comparison of results at various Re_j on variation of: a) transverse jet half-width, $Z_{0.5}$ and b) spanwise jet half-width, $Y_{0.5}$ with downstream distance.

be noted that the S_z data presented by Craft and Launder (2001) also indicate a linear region for X > 69 and these values are in closer agreement with those obtained at Re_j = 155 by Adane and Tachie (2008a). Figure 4.14b demonstrates that results for Re_j = 155, 310 and those from Craft and Launder (2001) also increase linearly. At higher Re_j values (420 and 800), the spanwise spread rate S_y becomes nearly constant beyond X = 7.

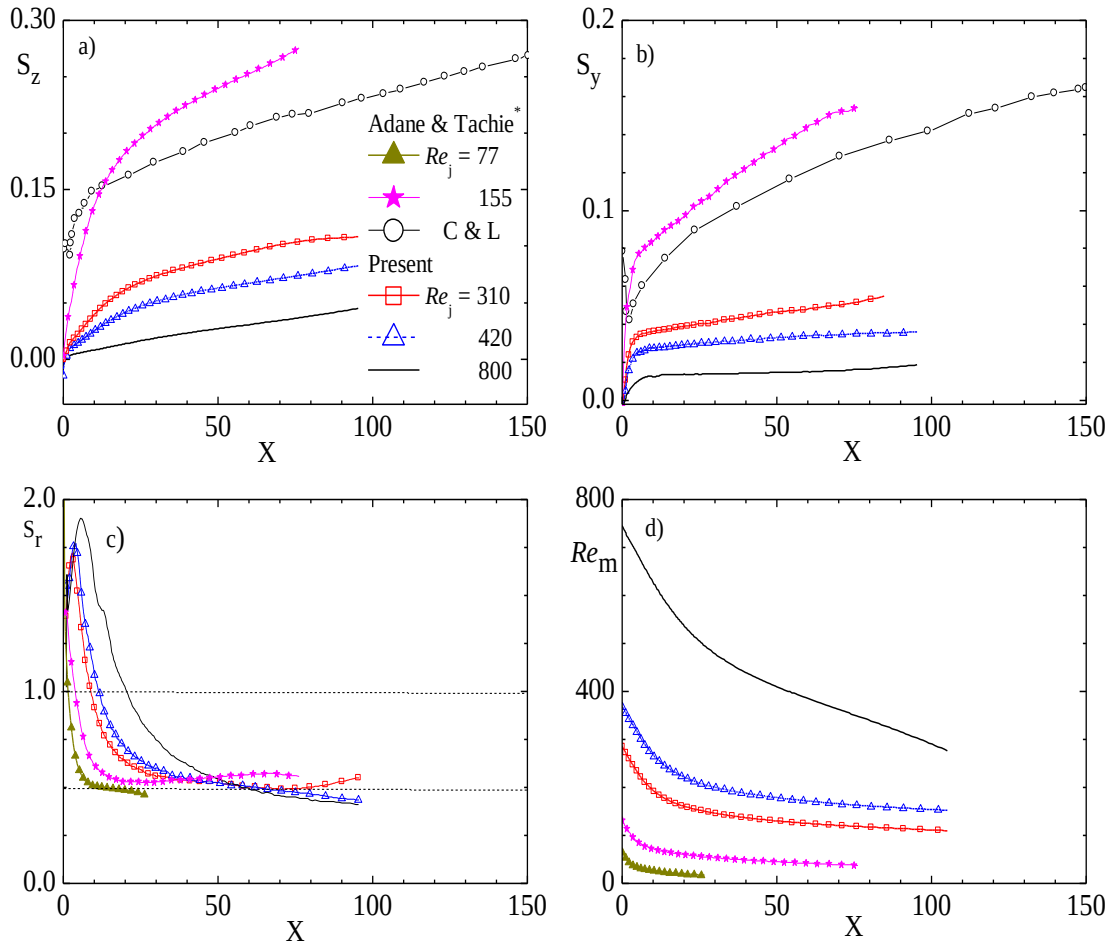

Figure 4.14: Variation of the spread rates at various Re_j: a) transverse, S_z, b) spanwise, S_y, c) spread rate ratio, S_r and d) local Reynolds number, Re_m in downstream direction.
Note: Adane & Tachie* is Adane and Tachie (2008a), and C&L is Craft and Launder (2001).

Unlike the 3D laminar wall jets, the spread in both the spanwise and transverse directions in 3D turbulent wall jets in the self-similar region varies linearly with X. It has been reported that for 3D turbulent wall jets, the spread rate in the spanwise direction is approximately 4 to 6 times the corresponding rate in the transverse direction. For example, the review article by Launder and Rodi (1981) showed that the ratio S_r (= S_y / S_z) is approximately 4.9 while the more recent measurements reported by Hall and Ewing

(2007) and Law and Herlina (2002) indicate S_r in the range 5.0 to 5.5. Furthermore, S_r = 1.07 – 6.29 were reported in the numerical study by Craft and Launder (2001). Figure 4.14c shows that, for the 3D laminar jet, the ratio S_r increases sharply to a peak during the early state of flow development, followed by a gradually decrease to values less than unity in the region $X \geq 6$ for $Re_j = 155$, $X \geq 11$ for $Re_j = 310$ and 420, and $X \geq 20$ for 800. These results imply that the anisotropic of the spread rate reported in turbulent wall jets are also observed in 3D laminar wall jets. As observed in turbulent wall jets, the S_r values are higher than unity in the early stage of flow development that is characterised by higher streamwise vortices but the degree of anisotropy is not as high as in the turbulent wall jet. That is, in this region, the values of S_r for the laminar wall jet are lower than those reported in turbulent wall jet but they do increase with increasing Reynolds number. These observations would indicate that the spreading mechanism for the 3D laminar jet may be different from the mechanism responsible for 3D turbulent wall jets. In fact, Craft and Launder (2001) concluded that for 3D laminar wall jet, there is no significant streamwise vorticity so that viscous effects may be principally responsible for the spreading mechanism.

As observed in Figs. 4.12 and 4.13, the local maximum velocity u_m decays with X while $z_{0.5}$ increases with increasing X. The variation of the local Reynolds number based on u_m and $z_{0.5}$, i.e., Re_m (= $u_m\ z_{0.5}\ /\ \nu$) with downstream distance, X is shown in Fig. 4.14d. Irrespective of the inlet Reynolds number, the local Reynolds number decreases with increasing X. This would indicate that the maximum local velocity, U_m decays faster with X than $Z_{0.5}$ increases with X.

Following the analysis of Craft and Launder (2001), the dependence of the spread rates (S_z, S_y) with Re_m is presented in Fig. 4.15. Similar to the observation made by Craft and Launder (2001), both S_z and S_y increase nearly linearly with decreasing Re_m. It is important to note that the spread rates are not only a function of the local Reynolds number, Re_m but they also vary with the jet inlet Reynolds number, Re_j.

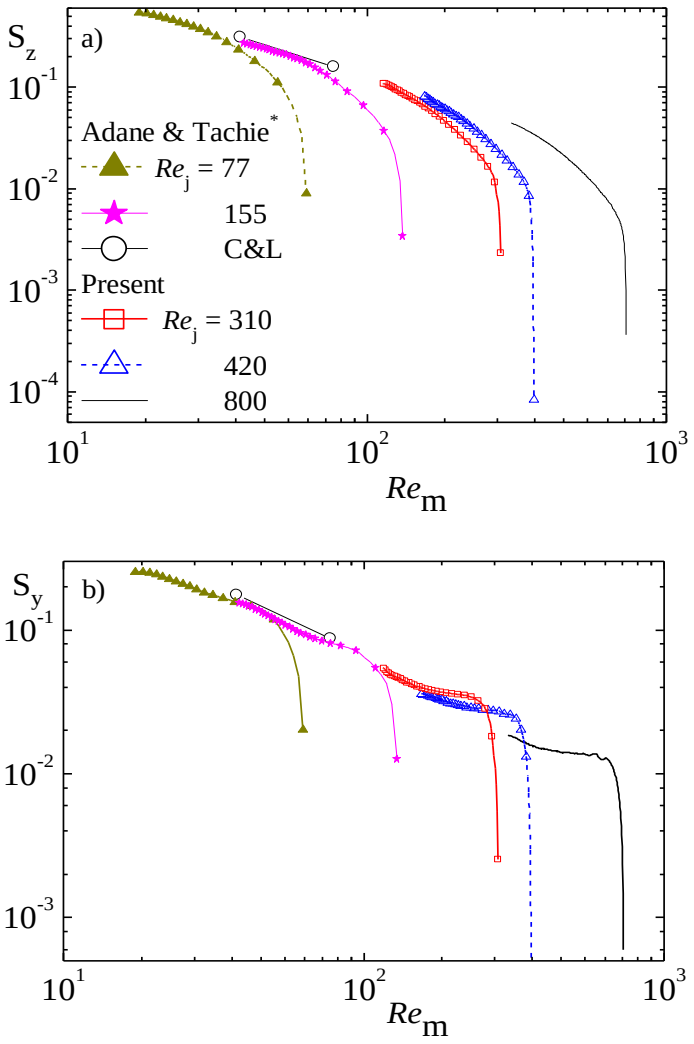

Figure 4.15: Variation of the **s**pread rates at various Re_j: a) transverse, S_z and b) spanwise, S_y with local Reynolds number, Re_m.
Note: Adane & Tachie* is Adane and Tachie (2008a), and C&L is Craft and Launder (2001).

4.3.2 Skin Friction Coefficient

The wall shear stress distribution is presented in Figs. 4.16-4.18 using the skin friction coefficient. The skin friction can be defined based on the exit velocity (Eqn. 4.2a) as was done by Glauert (1956) and Isaa (2006) or by the local maximum velocity (Eqn. 4.2b).

$$C_{fj} = 2\tau_w / \rho u_j^2 \tag{4.2a}$$

$$C_{fm} = 2\tau_w / \rho u_m^2 \tag{4.2b}$$

where $\tau_w = \mu\, du/dz|_{z=0}$

The skin friction coefficient, C_{fj} in the symmetry plane for various Re_j is presented in Fig. 4.16a. Irrespective of Re_j, C_{fj} decreases with increasing downstream distance. The present data (Fig. 4.16a) show that, in the early region of flow development, C_{fj} decreases with increasing Re_j. However, C_{fj} values at a lower Re_j decreases more rapidly than at a higher Re_j so that in region X > 20, the C_{fj} values decreases consistently with deceasing Re_j. A similar trend was observed in previous 2D studies (Glauert, 1956; Isaa, 2006). The variation of C_{fm} with X is plotted in Fig. 4.16b. Whilst C_{fm} is nearly independent of X at Re_j = 800, it increases with X at lower Re_j values.

In contrast to the significant Re_j effects observed in Fig. 4.16b, Fig. 4.17 shows that C_{fm} varies uniquely with the local Reynolds number Re_m but independent of the jet inlet Reynolds number, Re_j.

In addition to the symmetry plane (Y = 0), the skin friction coefficient, C_{fj} was also evaluated at selected spanwise locations (Y = 0.5, 1, 2 and 3). These values are plotted in Fig. 4.18a, 4.18b and 4.18c for Re_j = 310, 420 and 800, respectively. In general, the C_{fj}

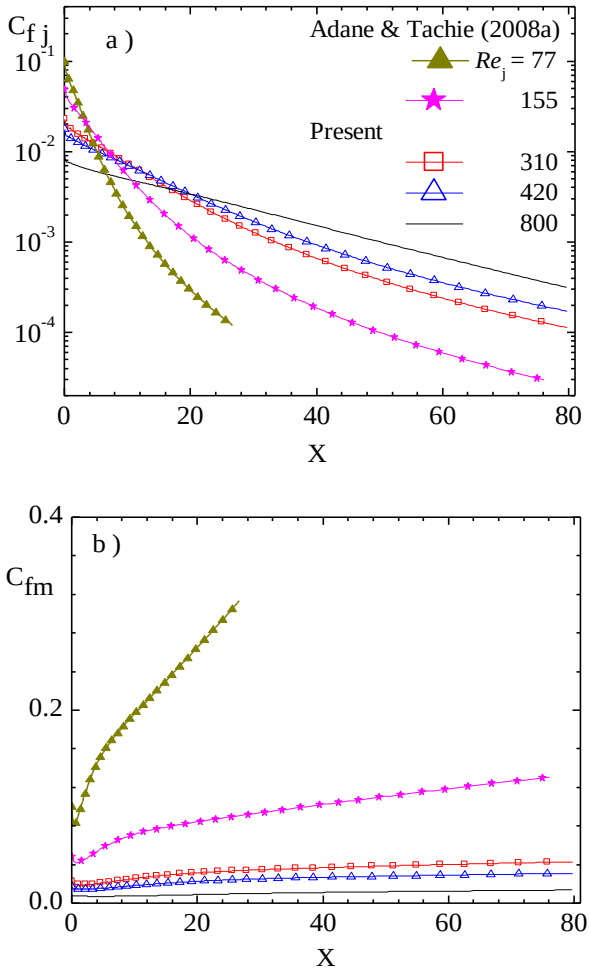

Figure 4.16: Variation of skin friction coefficients with downstream distance at various Reynolds numbers using: a) Eqn. 4.2a and b) Eqn. 4.2b.

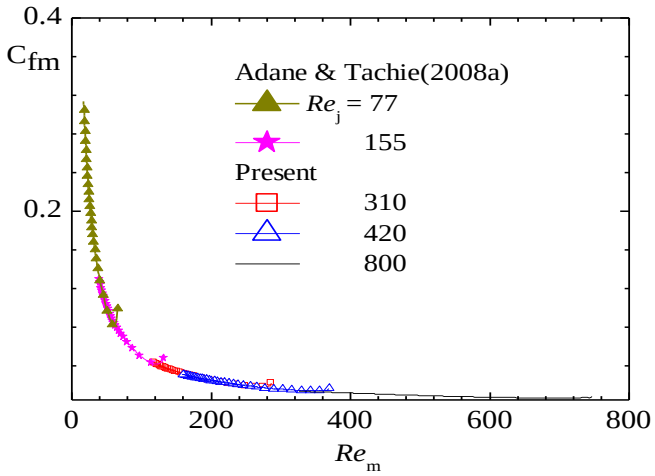

Figure 4.17: Variation of skin friction coefficients (Eqn. 4.2b) with local Reynolds numbers at various Reynolds numbers, Re_j.

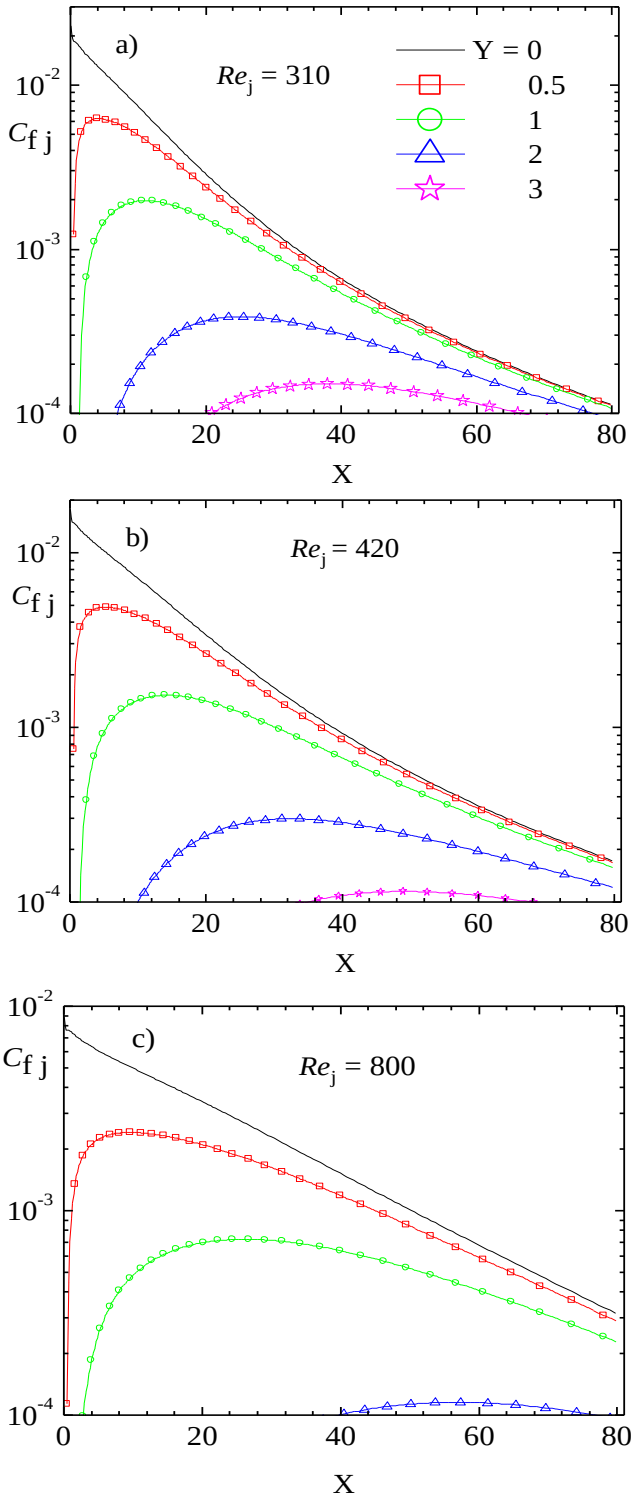

Figure 4.18: Variation of skin friction coefficients with downstream distance in the spanwise direction.

values decrease with increasing distance from the symmetry plane. The peak values of C_{fj} at Y = 0.5 and Y = 1 are approximately 27 and 9 percent, respectively of the maximum C_{fj} value at Y= 0, irrespective of Re_j. At larger Y values, the peak values for C_{fj} as a percent of the maximum value at Y = 0 for Re_j = 310 and 420 are relatively higher than the corresponding value for Re_j = 800. It should be noted that the peak value of C_{fj} at Y = 3 is more than two orders of magnitude lower than the corresponding maximum value at Y = 0. In addition, the streamwise location of the peak value increases with spanwise location and also depends on Re_j. For example, at Y = 1 and 2 for Re_j = 310, the locations of the peak values are X ~ 10 and 25. Meanwhile the corresponding values for Re_j = 800 are 26 and 57.

4.3.3 Velocity Profiles

Figure 4.19a shows a comparison between the present experimental and numerical results for the streamwise velocity profiles in the similarity region. The specific profile shown was obtained at X = 10. There are no noticeable differences between the numerical results and measured values in the symmetry plane (Fig. 4.19a). Figure 4.19(b) compares the numerical results for the present and previous numerical results (Adane and Tachie, 2008a; Craft and Launder, 2001) for streamwise velocity profile. There is no distinction among the profiles at various Re_j indicating that there is no Reynolds number dependence. The data from Adane and Tachie (2008a) and Craft and Launder (2001) also compare very well with the present results.

It is apparent from Fig. 4.20 that the numerical results showed a good agreement with measurements except in the region Y ' $\geq$ 1.0 where the measured values are

comparatively lower. Similar to the observation made in Fig. 4.19b there is no difference among the profiles at various Re_j as well as data from previous studies.

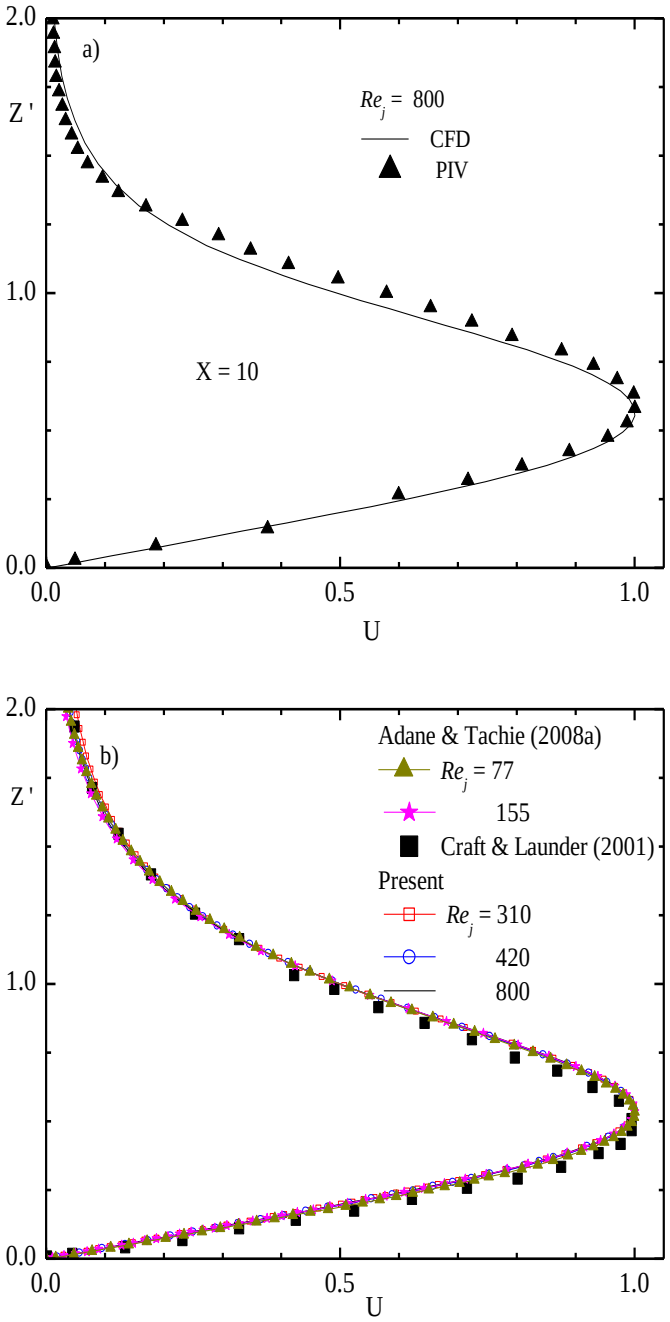

Figure 4.19: Comparison of present and previous results on the similarity velocity profiles in the transverse direction at symmetry plane, $y = 0$.

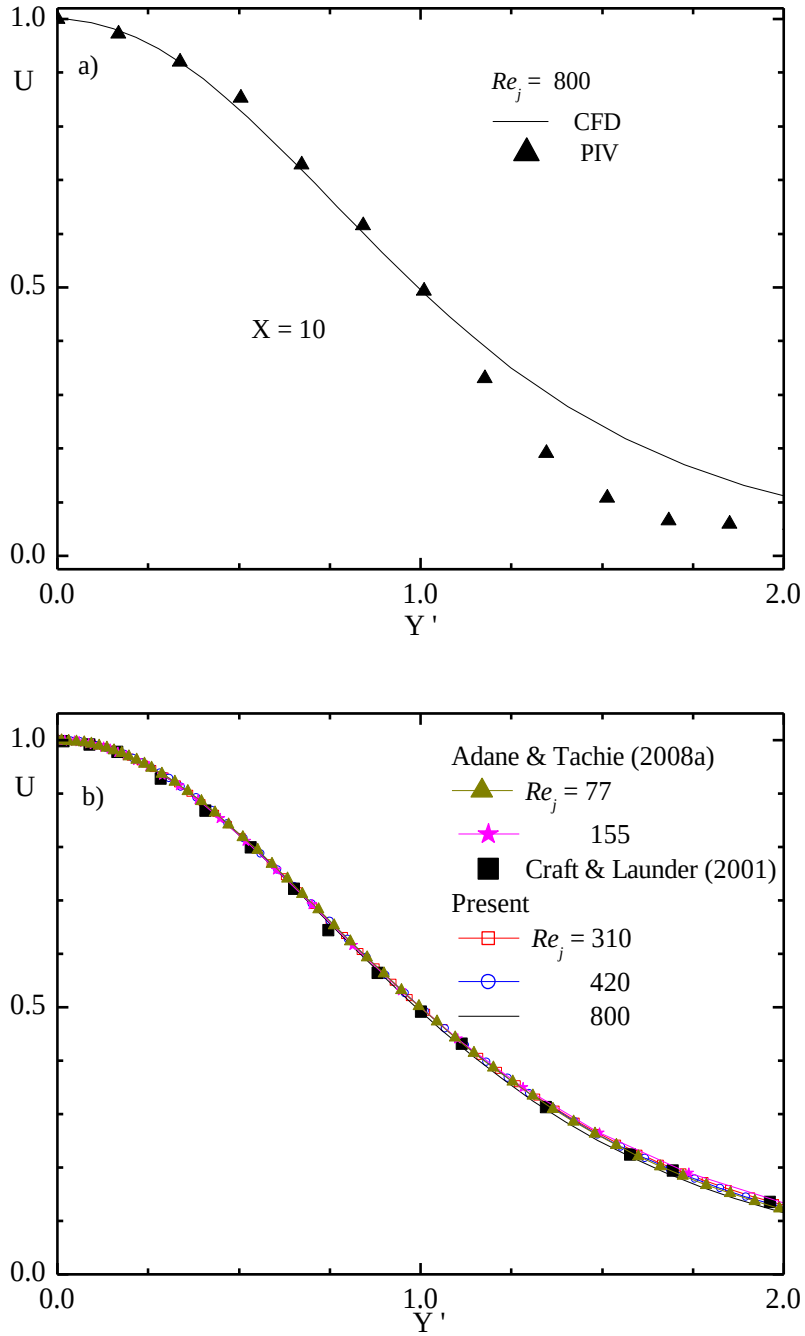

Figure 4.20: Comparison of present and previous results on the similarity velocity profiles in the spanwise direction at $z_m = 0$.

Figure 4.21 shows contour of the streamwise velocity, U, together with the normalised secondary flow velocities (V, W) in the *z-y* plane at X = 5, 30, and 60. The axes of each plot are normalised by *d*, i.e. Y = *y/d* and Z = *z/d*. The rationale for Fig. 4.21 is to qualitatively visualise the ambient fluid entrainment as the jet evolved. In each plot, contour values between 0.1 and 1 are shown with an increment of 0.1. Here, only results for Re_j = 310 and 800 results are presented. The shape of the iso-contour levels are nearly elliptical with their centres shifted away from the wall as U decreases with increasing X for Re_j = 310 (Fig. 4.21(a, c, e)). This observation is consistent with those made by Craft and Launder (2001). Similar observation is also made for Re_j = 800 in Fig. 4.21(b, d, f), however, the decrease of U_m with increasing X is less distinct. The velocity vector plots indicate that there is an entrainment of ambient fluid into the jet. With the same scale used, the vectors at Re_j = 310 show a higher entrainment, an observation that is consistent with the higher spread rate observed at a lower Reynolds number.

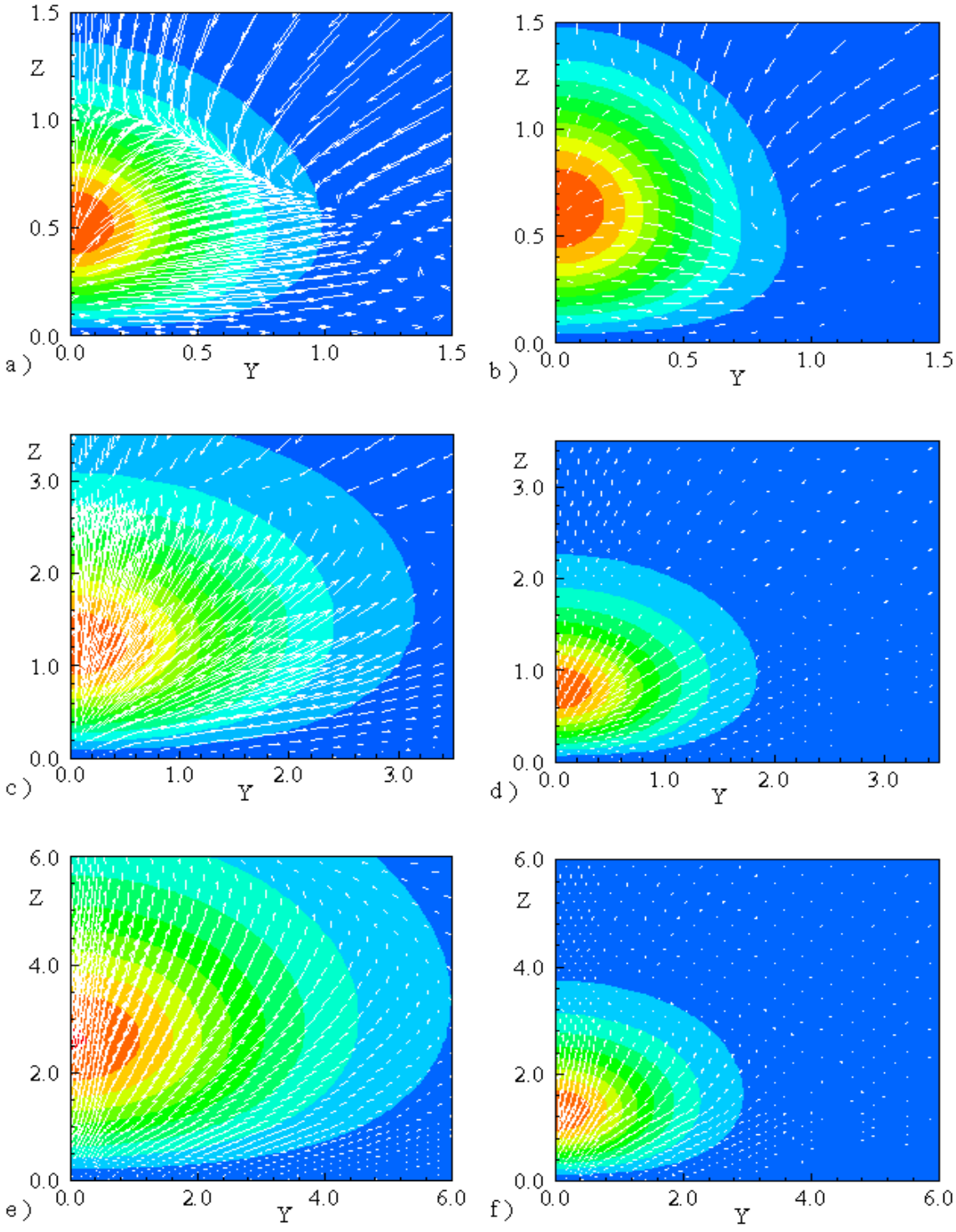

Figure 4.21: Streamwise velocity (U) contours and secondary flow vectors (W, V): Re_j = 310 (a, c, e) and 800 (b, d, f) for X = 5, 30 and 60. Note: first row is X = 5 whereas last row is for X = 60. Each contour level is 0.1 with maximum and minimum value of 1.0 and 0.1, respectively.

4.4 Numerical Results of Non-Newtonian Fluids

4.4.1 Velocity Decay, Spread Rates and Skin Friction Coefficient

4.4.1.1 Effect of initial Reynolds number

The decay of u_m with streamwise distance for the numerical results is shown in Fig. 4.22. For XG005 fluid, Fig. 4.22a shows that the agreement between experiment and computation at Re_j = 800 is limited to the early region of flow development (X < 15). Further downstream, the numerical results decayed more rapidly than observed from measurement. Similar observation is also made for XG010 fluid (Fig. 4.22b). In this case, however, a reasonable agreement was observed in the regions: X < 6 and 30 ≤ X ≤ 55. It should be recalled from Section 4.3.1 that, the experimental and numerical results presented for the Newtonian fluid also revealed a limited region of agreement (X < 20). Further downstream it was observed that the experimental data decayed faster than the numerical values (Section 4.3), a trend that is opposite to the results for the non-Newtonian fluids.

The results presented in Fig. 4.22 show that, irrespective of the fluid, the local maximum velocity decayed faster with decreasing initial Reynolds number. For example, for XG005 fluid at X = 20, U_m = 0.01, 0.20 and 0.53 for Re_j = 250, 420 and 800, respectively. This trend is consistent with those reported in previous sections (Sections 4.2 and 4.3) and previous numerical works for power-law fluids (Adane and Tachie, 2008a).

The plots of transverse jet half-width ($Z_{0.5} = z_{0.5} / d$) obtained from both experiments and computations are shown in Fig. 4.23. It can be seen from Fig. 4.23a that there exists a

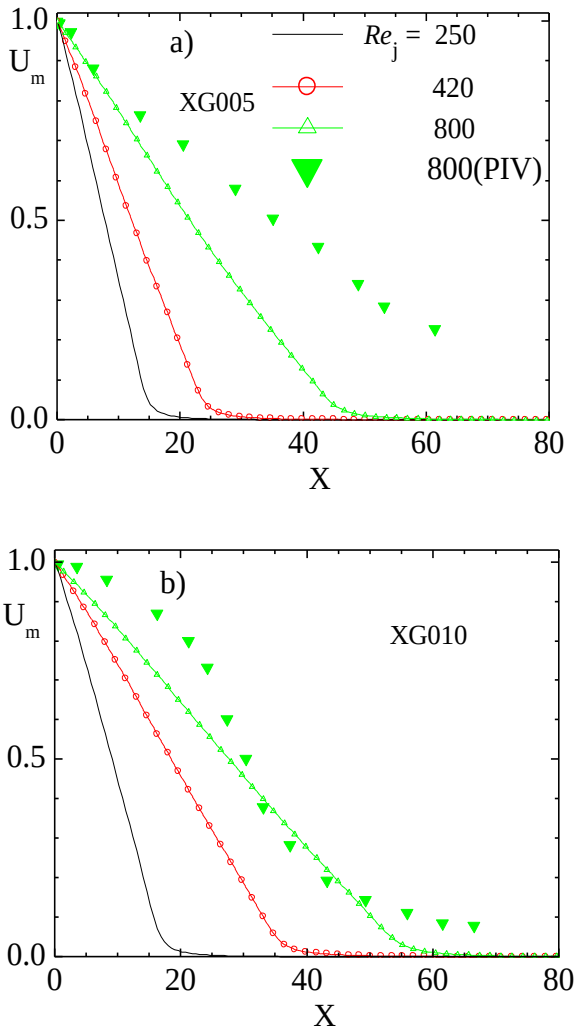

Figure 4.22: Comparison of results at various Re_j on variation of maximum velocity decay, U_m in downstream direction for: a) XG005 and b) XG010.

good agreement between the experimental and numerical results at Re_j = 800 in the region X ≤ 20 for XG005 fluid. Downstream of this region, the faster decay of maximum velocity observed from the numerical results (Fig. 4.22a) produced a higher spread than the measured values. Similarly, for XG010, the agreement between both results is excellent up to X = 45. The figure also demonstrates clearly that the jet spreads fastest at Re_j = 250 and slowest at Re_j = 800, irrespective of the fluid. The differences in the spread

rates will be quantified later in Fig. 4.25. In the spanwise direction (not shown here), a similar observation was made.

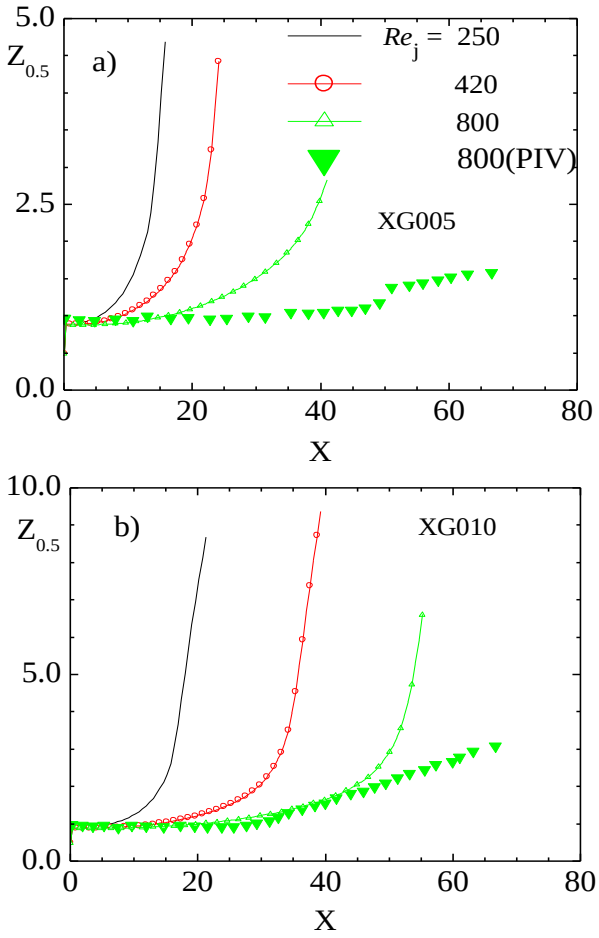

Figure 4.23: Comparison of results at various Re_j on variation of transverse jet half-width, $Z_{0.5}$ in downstream direction for: a) XG005 and b) XG010.

Following similar analysis in Section 4.3.1, the Reynolds number dependence of the velocity decay and its corresponding growth of transverse jet half-widths can be explained by the variation of the local momentum flux, M_x with streamwise distance. Figure 4.24 shows the variation of the ratio $M_{x,o} = M_x/M_o$ (where M_o is the momentum flux at the inlet plane) with X. It should be noted that the values of M_o are 8.91 x 10^{-5}, 1.59 x 10^{-4} and 3.44 x 10^{-4} kg•m/s^2, respectively, for Re_j = 250, 420, and 800 for XG005.

The corresponding values for XG010 are 3.97 x 10^{-4}, 9.62 x 10^{-4} and 1.60 x 10^{-3} kg•m/s^2, respectively. The results show that, irrespective of the specific fluid, the momentum flux at a lower Reynolds number decayed faster than at a relatively higher Reynolds number. At X = 20, for example, $M_{x,0}$ = 0.01, 0.24 and 0.61 for Re_j = 250, 420 and 800 , respectively, for XG005. The subsequent discussion on the effects of initial Reynolds number on the spread rates, skin friction coefficient, and velocity profiles will only be presented for XG005 fluid since the trends are the same for both non-Newtonian fluids (XG005 and XG010).

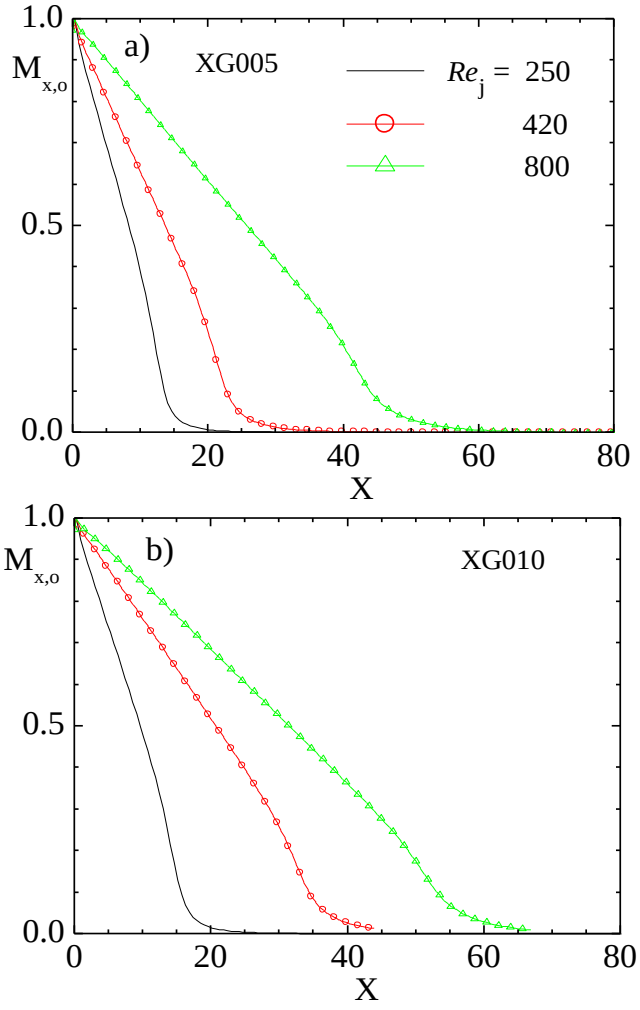

Figure 4.24: Comparison of results at various Re_j on variation of local momentum flux in downstream direction for XG005 (a) and XG010 (b).

The variation of the spread rates (S_z, S_y) with X for the various Re_j is plotted in Fig. 4.25(a, b). For the Newtonian fluid, it was observed that the spread rates increase nearly linearly with downstream distance. The data presented in Fig. 4.25a show that, for the non-Newtonian fluids, the spread rate in the symmetry plane (S_z) increases exponentially with X. In addition, the spread rates (S_z) depend strongly on the initial Reynolds number. The Reynolds number dependence observed for the spread rate was also observed for the Newtonian fluid. The spanwise spread rate, S_y (Fig. 4.25b) also varies exponentially with X except in the region X < 5, where the variation is nearly linear.

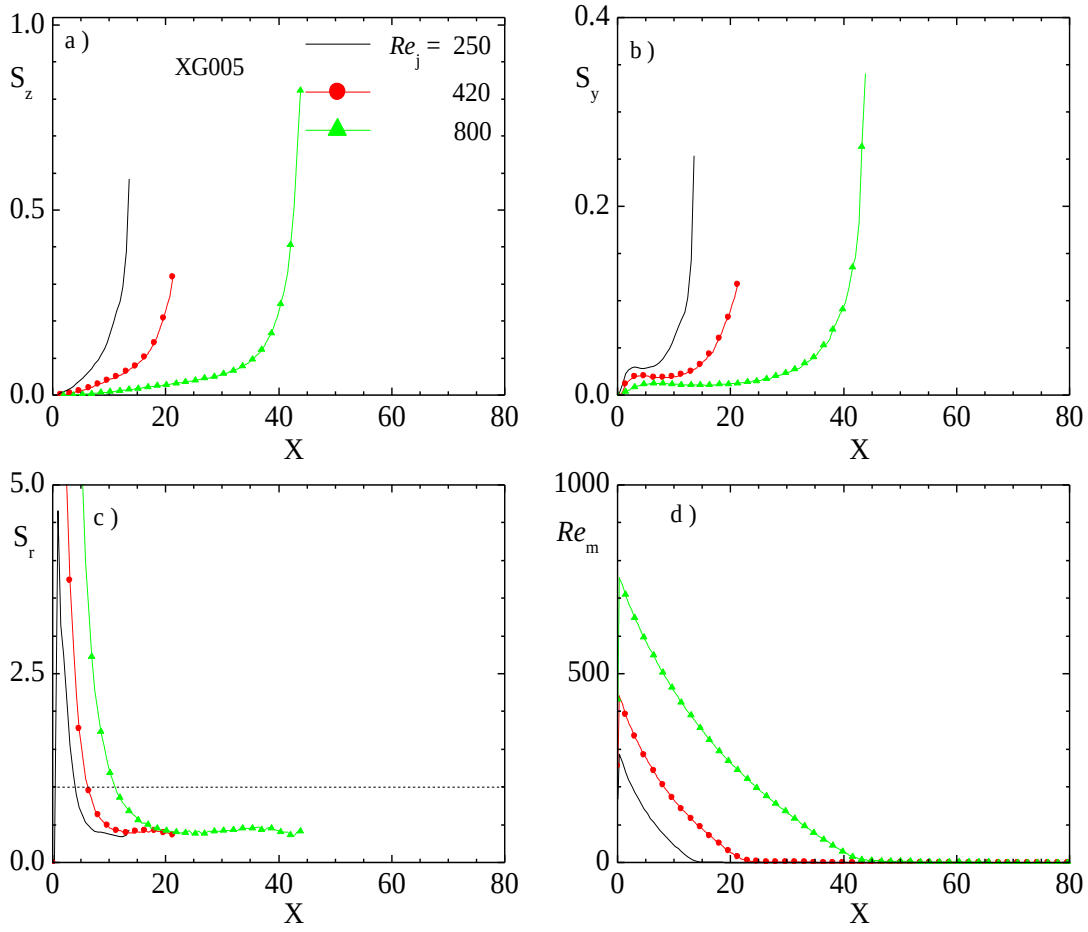

Figure 4.25: Variation of the spread rates at various Re_j: a) transverse, S_z, b) spanwise, S_y, c) spread rate ratio and d) local Reynolds number, Re_m in downstream direction.

The spread rate ratios, S_r (= S_y / S_z) are plotted in Fig. 4.25c to demonstrate the anisotropic behaviour of the spread rates. In the regions (X ≤ 5 for Re_j = 250, X ≤ 8 for Re_j = 420, and X ≤ 12 for 800), S_r > 1 which implies that the jet spreads more in the spanwise direction than in the transverse direction. Downstream of these regions, the spread is still anisotropic; however, S_r values are significantly less than unity. As indicated in the Section 4.3.1, the higher values of S_r (S_r > 1) are due to the presence of an elevated streamwise vorticity. As will be shown subsequently, the regions where S_r > 1 for the present non-Newtonian fluid are indeed characterised by a high level of streamwise vorticity.

As observed in Fig. 4.23, u_m decays with X while $z_{0.5}$ increases with increasing X. For a Newtonian fluid, it was observed that the local Reynolds number (Re_m) also decreases with increasing downstream distance. The variation of the local Reynolds number (Re_m = $\rho u_m z_{0.5} / \mu_{0.5}$, where $\mu_{0.5}$ is the apparent viscosity evaluated at $z_{0.5}$) with X for the various test cases were also evaluated for the non-Newtonian fluids (Fig. 4.25d). Unlike the Newtonian fluid for which the viscosity is constant, it was observed that the values of $\mu_{0.5}$ increases consistently with X for each of the two non-Newtonian fluid and the various Reynolds numbers. It is clear from Fig. 4.25d that the increase in $z_{0.5}$ with X is not large enough to offset the decay of u_m and the increase of $\mu_{0.5}$ with X. Although this trend is similar to the observation made for the Newtonian fluid, it was found that Re_m decays more rapidly for the non-Newtonian fluids than that for the Newtonian fluid.

The variation of the spread rates (S_z, S_y) with the local Reynolds number (Re_m) is presented in Fig. 4.26. Both S_z and S_y increase nearly linearly with decreasing Re_m

except in the early region of the flow (which corresponds to higher value of Re_m in Fig. 4.26). Similar to results for the Newtonian fluid, the spread rates are independent of Re_m in the linear region. It is important to note that the spread rates in the early region depends on the initial Reynolds number, and the extent of the linear region also increases with initial Reynolds number.

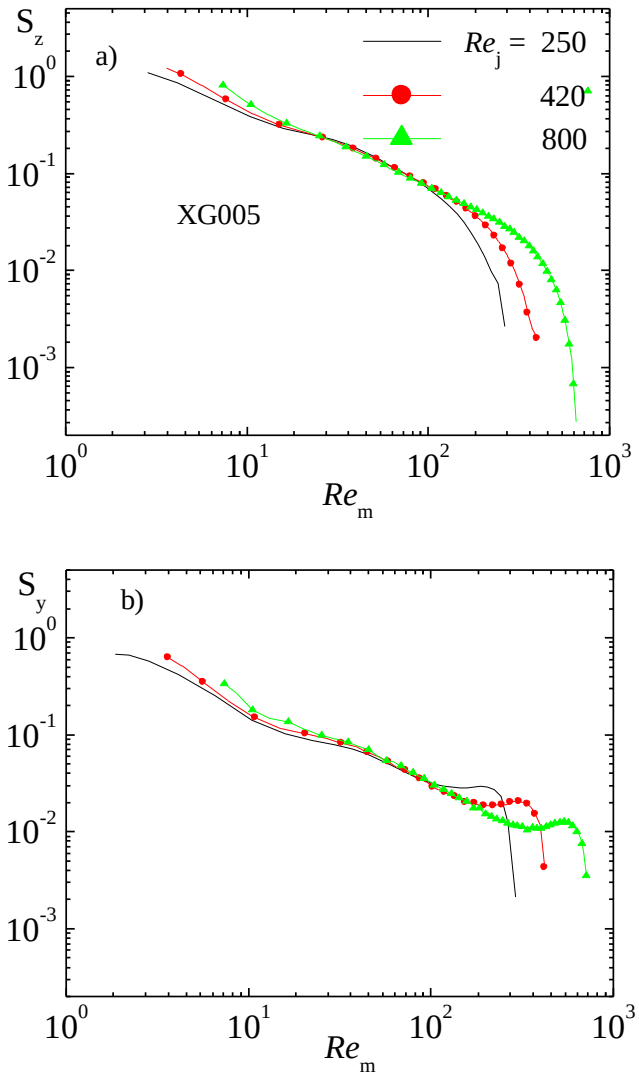

Figure 4.26: Variation of the spread rates at various Re_j: a) transverse, S_z and b) spanwise, S_y with local Reynolds number, Re_m.

.

The wall shear stress distribution is presented in Figs. 4.27-4.29 using the skin friction coefficient. The skin friction is defined based on the exit velocity (Eqn. 4.2a) or by the local maximum velocity (Eqn. 4.2b). It should be remarked that viscosity in Eqn. (4.2) was the local value and is not constant. The skin friction coefficient, C_{fj} evaluated in the symmetry plane (Y = 0) for the various Re_j for XG005 is presented in Fig. 4.27a. Irrespective of Re_j, C_{fj} decreases with increasing downstream distance. The data show that, in the early region of flow development, C_{fj} decreases with increasing Re_j. However, C_{fj} values at the lower Re_j decrease more rapidly than at a higher Re_j so that in

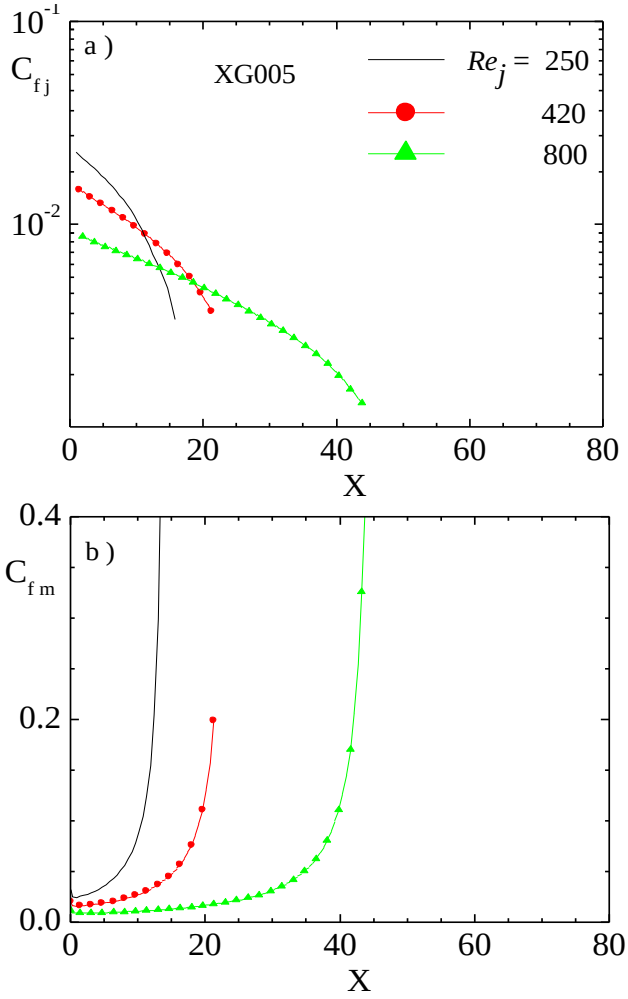

Figure 4.27: Variation of skin friction coefficients with downstream distance at various Reynolds number using: a) Eqn. 4.2a and b) Eqn. 4.2b.

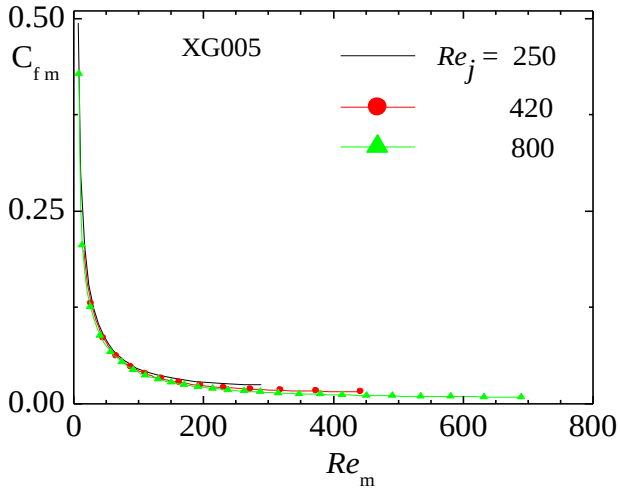

Figure 4.28: Variation of skin friction coefficients (Eqn. 4.2b) with local Reynolds number at various initial Reynolds number, Re_j.

the region X > 12, the C_{fj} values decreased consistently with deceasing Re_j. This trend is similar to that observed for Newtonian fluids. It can be observed from Fig. 4.27b that C_{fm} increases with X irrespective of Re_j value. The implication is that the decay of friction velocity is slower than the decay of u_m. In contrast to the significant Re_j effects observed in Fig. 4.27, Fig. 4.28 shows that C_{fm} varies uniquely with the local Reynolds number Re_m but independent of the jet Reynolds number, Re_j.

The skin friction coefficient, C_{fj} was also evaluated at selected spanwise locations (Y = 0.5, 1, 2 and 3) in addition to those at symmetry plane (Y = 0). These values are plotted in Fig. 4.29a, 4.29b and 4.29c for Re_j = 250, 420 and 800, respectively. In each of these plots, the variation can be demarcated into two regions (denoted by dash lines): region I: X ≤ 20, X ≤ 26 and X ≤ 46, respectively, for Re_j = 250, 420 and 800 and region II: X > 20, X > 26 and X > 46, for Re_j = 250, 420 and 800, respectively. In region I, the C_{fj} values decrease with increasing distance from the symmetry plane. Irrespective of the Re_j, the shape of C_{fj} for the non-Newtonian fluids is more 'plug-like' instead of the

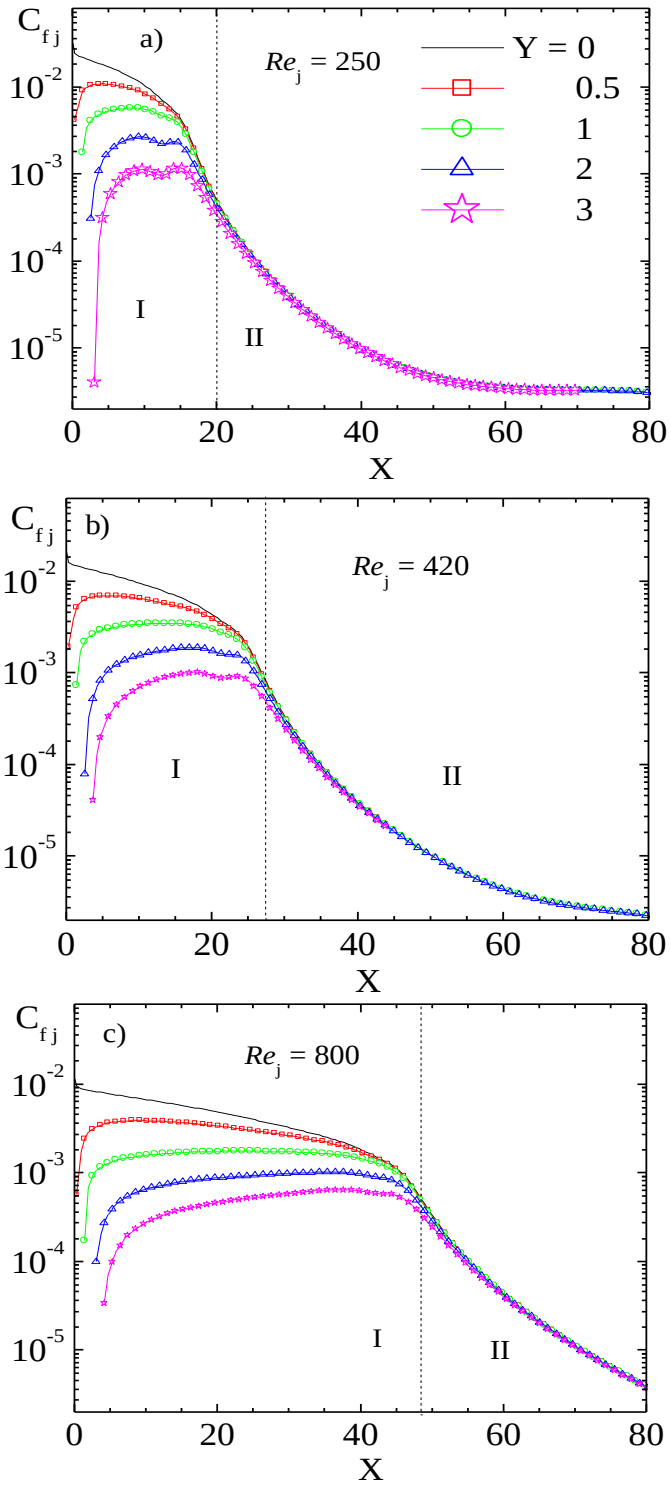

Figure 4.29: Variation of skin friction coefficients (Eqn. 4.2a) with downstream distance in the spanwise direction.

concave shape reported for Newtonian fluid. In fact, as Re_j increases the profile becomes more flat or 'plug-like'. In region II, however, the C_{fj} values consistently decrease with X but are independent of spanwise location. It is noteworthy that at X = 20, X = 26 and X = 46, respectively, for Re_j = 250, 420 and 800, the U_m values are only 0.007, 0.019 and 0.028, respectively. Thus at downstream locations where the local maximum velocity is less than 3% of the exit velocity, the skin friction is independent of spanwise direction.

4.4.1.2 Effect of concentration

Figures 4.30 and 4.31 show the effect of concentration of the xanthan gum on the decay of U_m and $M_{x,o}$. In these plots, Newtonian fluid results from Section 4.3 are also shown for comparison. In the regions: X < 5 and X < 10 for Re_j = 420 (Fig. 4.30a) and 800 (Fig. 4.30b), respectively, the velocity decay shows no dependence on the specific fluid. Further downstream, the velocity of the non-Newtonian fluids decays more rapidly than that of the Newtonian fluid, irrespective of Re_j. These results are similar to previous results for power-law fluids (Adane and Tachie, 2008a). It should be noted that in the region $5 \leq X \leq 10$ for Re_j = 420 (Fig. 4.30a) there is no distinction between the results for XG005 and the Newtonian fluid. A comparison of the two shear-thinning fluids clearly demonstrates that the dimensionless maximum velocity decays most slowly for XG010 fluid. This is true for both Re_j = 420 and 800.

Although the dimensionless momentum flux, $M_{x,0}$ (Fig. 4.31) also decays with X for all Re_j and fluid types, the specific effects of the fluid on $M_{x,0}$ are different from those observed for U_m. For instance, the values of $M_{x,0}$ for the Newtonian fluid decayed slowest whereas XG005 decays faster. This is true for both of the Reynolds numbers. At

X = 20, for example, $M_{x,0}$ = 0.63, 0.21 and 0.53, for the Newtonian fluid, XG005 and XG010, respectively.

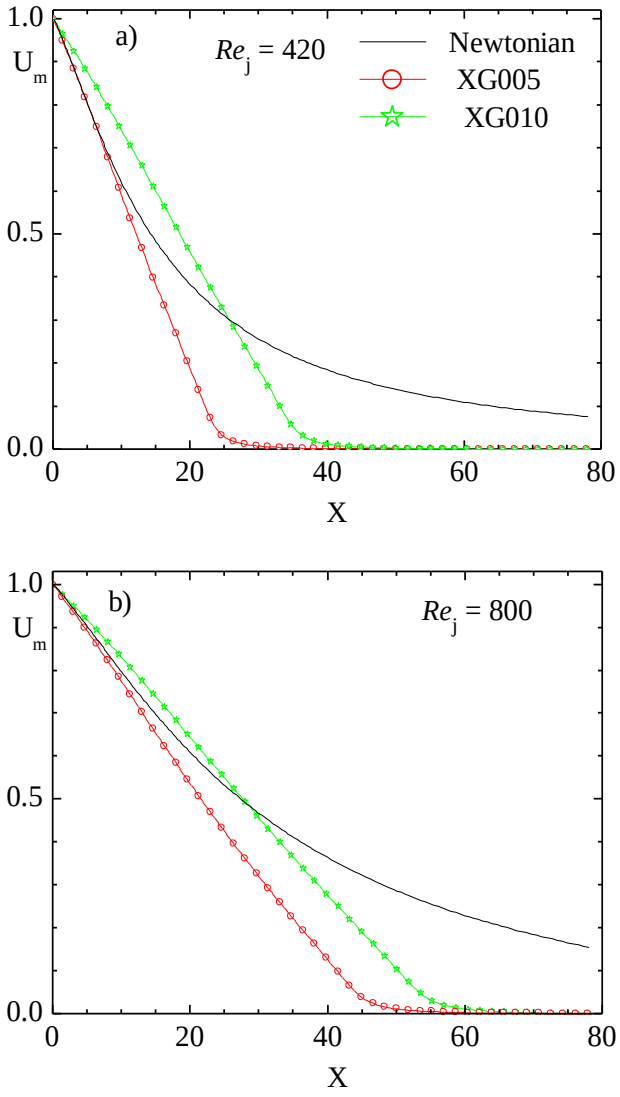

Figure 4.30: Comparison of results at various fluids on variation of maximum velocity decay, U_m for Re_j = 420 (a) and 800 (b).

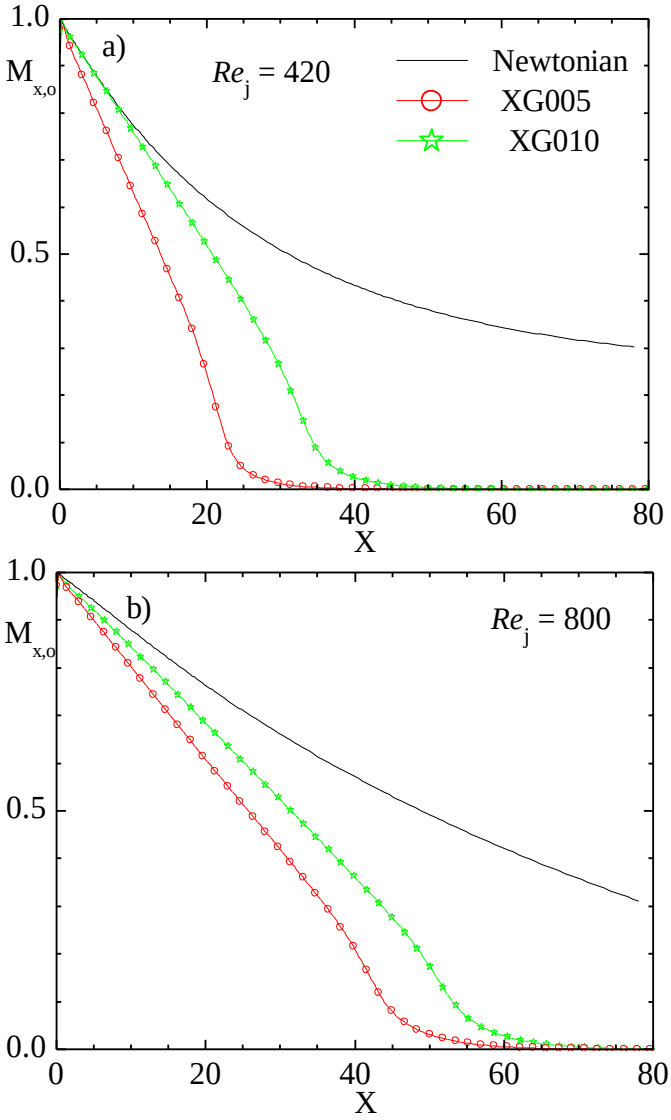

Figure 4.31: Comparison of results at various fluids on variation of local momentum flux, $M_{x,o}$ for Re_j = 420 (a) and 800 (b).

Figure 4.32 compares the spread rates (S_z, S_y) for all the three fluids at two Reynolds numbers. For Re_j = 420 in the region X < 5, there is no significant difference among the fluids for the transverse spread rate (Fig. 4.32a). In the region 5 < X < 16, the XG005 spread fastest whereas XG010 spread slowest. Meanwhile, downstream of this region (X > 16), the non-Newtonian fluids spread faster than the Newtonian fluid. In Fig. 4.32b, there is a noticeable difference among the plots for the higher Reynolds number in the

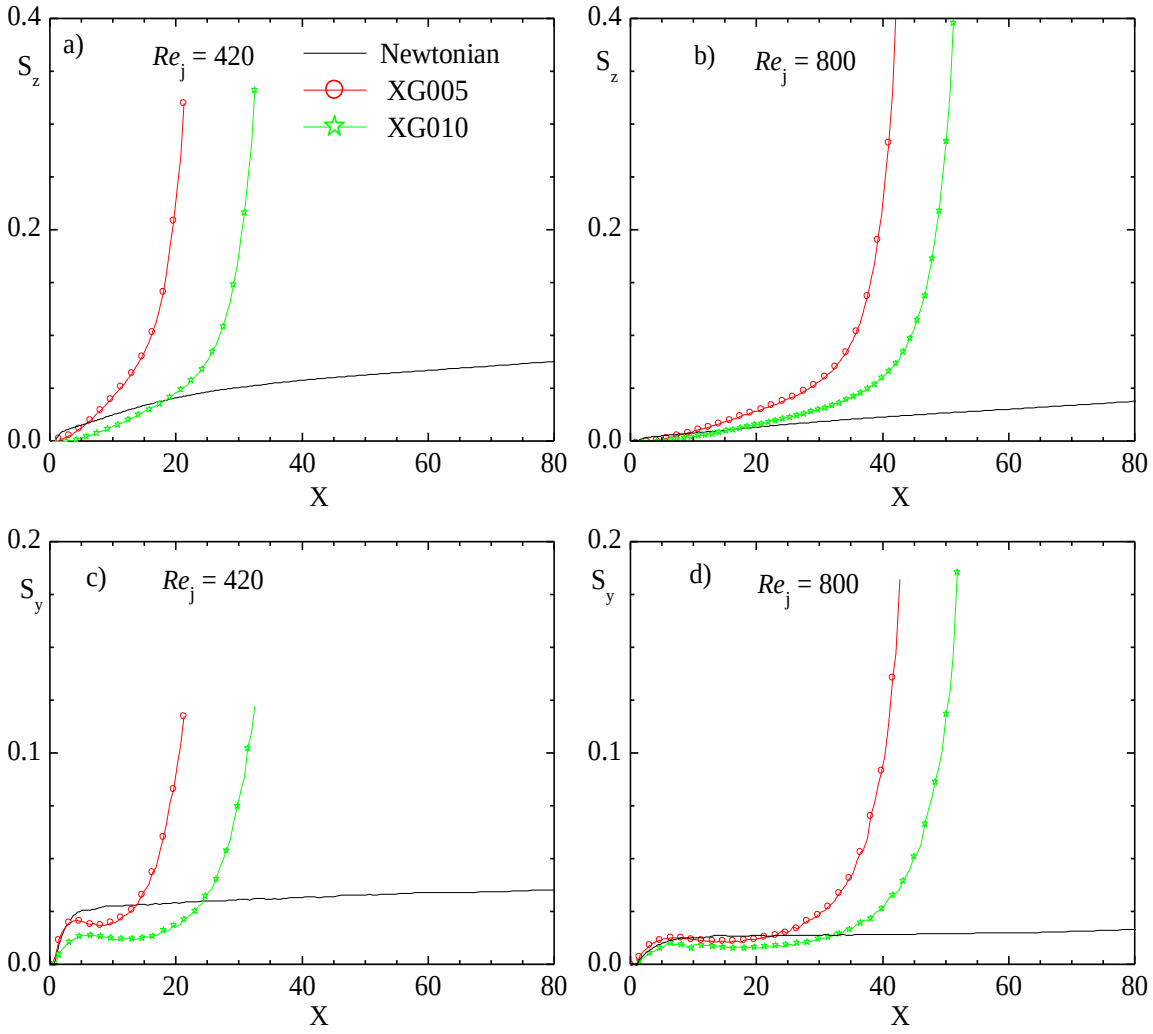

Figure 4.32: Comparison of results at various fluids on variation of spread rates transverse, S_z (a, b) and spanwise, S_y (a, b) in downstream direction for Re_j = 420 (a, c) and 800 (b, d).

region $X < 21$. It is clear that in the region $X \geq 21$, the S_z values for the Newtonian fluid are lower than those for the non-Newtonian fluids. Whilst there is no difference between the spread rate in the spanwise direction (S_y) for XG005 and the Newtonian fluid in the region $X < 5$, their S_y values are higher than those of XG010. On the contrary, the general observation from Fig. 4.32c is that the non- Newtonian fluids spread slower in the region $5 < X < 20$ than the Newtonian fluid. Further downstream, an opposite trend was

observed. Similarly, in the region X > 30 (Fig. 4.32d), the non-Newtonian fluids spread faster than the Newtonian fluid whereas no fluid dependence was observed in the region $X \leq 30$. It should be pointed out that in the regions where the non-Newtonian fluids spread faster than Newtonian fluid the variation of both spread rates with X is almost linear for the Newtonian fluid but exponential for the non-Newtonian fluids. Furthermore, between the two non-Newtonian fluids, XG005 spreads more rapidly than XG010 irrespective of Re_j. This observation is consistent with the observation made for the decay of U_m in Fig. 4.30, that is, one would expect a faster decay of U_m to result in a more rapid spread of the jet.

The spread rate ratios (Fig. 4.33) also depend strongly on the specific fluid in the early stage of the flow developments ($X \leq 8$ and $X \leq 12$, respectively for Re_j = 420 and 800). The peak value for XG010 for Re_j = 420, for example, is about 10 times the corresponding value for the Newtonian fluid. Beyond these regions, however, the spread rate ratios for both non-Newtonian fluids are lower than the corresponding values for the Newtonian fluid. The relatively lower values for the non-Newtonian fluids indicate that the streamwise vortices which are responsible for the higher spread of the jet in spanwise direction ($S_r > 1$) were significantly diffused by viscosity in the downstream region. The vorticity distribution which will be discussed later will be used to support this assertion.

Figure 4.34 clearly demonstrates that, the variation of the spread rates with the local Reynolds number is only fluid dependent in the region $Re_m > 380$ and 270, respectively for S_z and S_y. Outside this region, the variation of the spread rates with Re_m shows no difference between XG005 and XG010 although these values are distinctively lower than

those of the Newtonian fluid. The variation of the local skin friction coefficient, C_{fm} with the local Reynolds number is also independent of the fluid (Fig. 4.35).

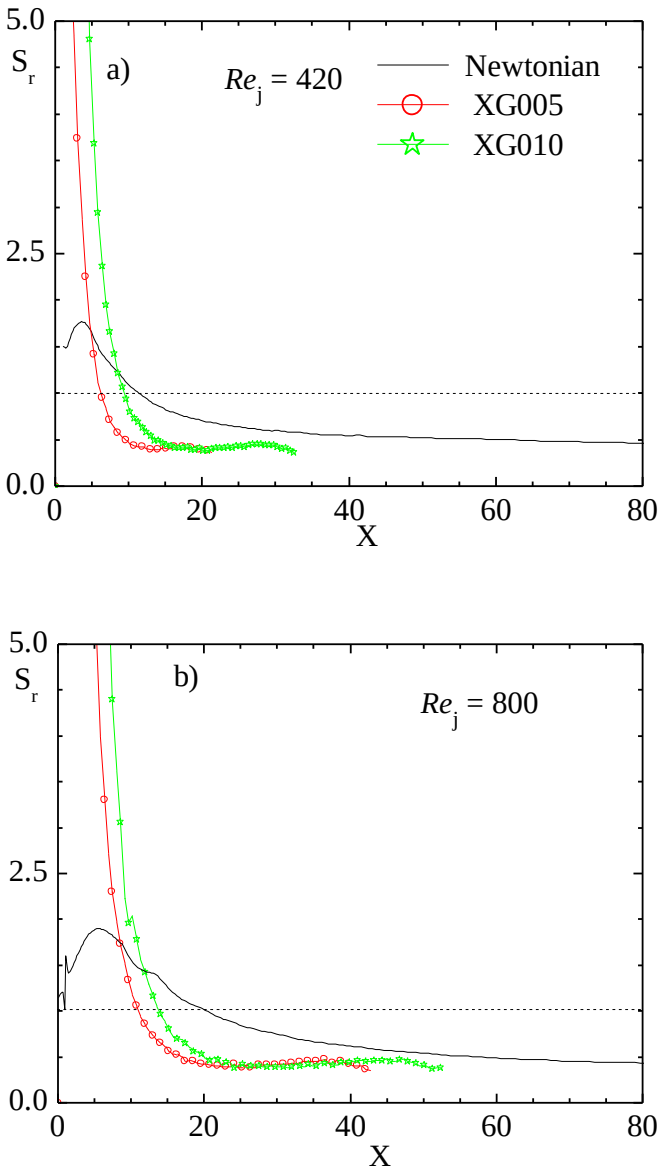

Figure 4.33: Comparison of results at various fluids on variation of spread rate ratio in downstream direction for Re_j = 420 (a) and 800 (b).

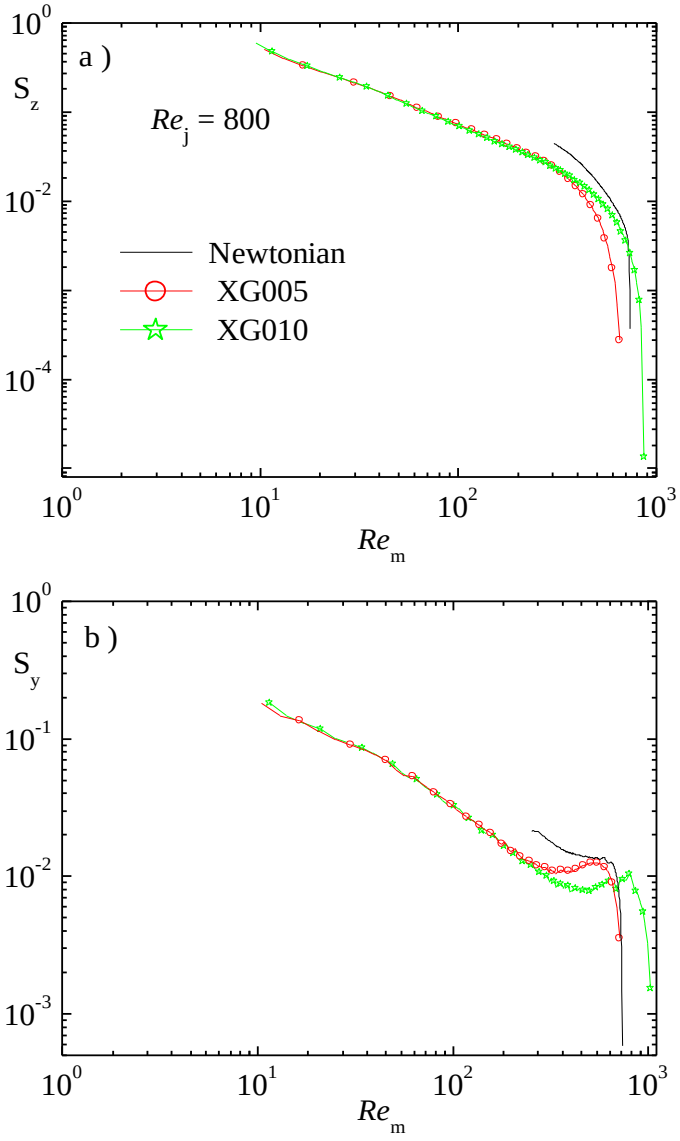

Figure 4.34: Comparison of results at various fluids on variation of spread rates: a) transverse, S_z and b) spanwise, S_y with Re_m for Re_j = 800.

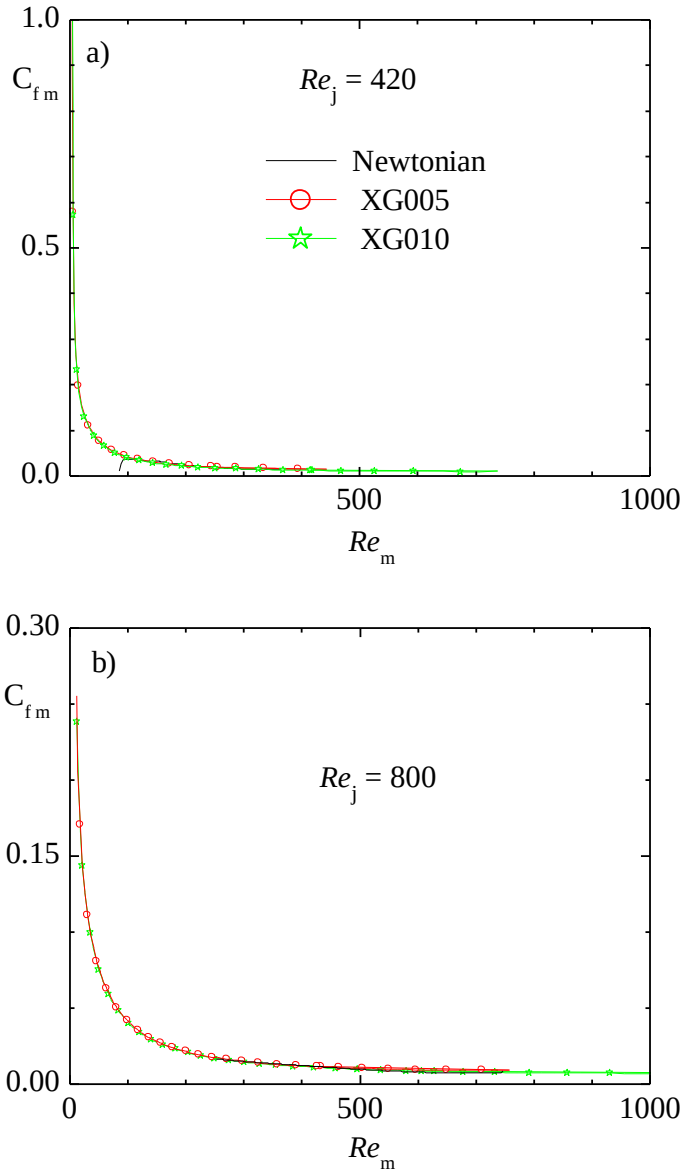

Figure 4.35: Comparison of variation of local skin friction coefficient with local Reynolds number, Re_m for various fluids at Re_j = 420 (a) and 800 (b).

4.4.2 Velocity Profiles

4.4.2.1 Similarity consideration

As mentioned in the previous section, the discussion will only focus on XG005 since these results are qualitatively similar to those obtained for XG010. Figure 4.36 shows profiles of the streamwise velocity, U, in the symmetry plane at various normalised streamwise locations ($5 \leq X \leq 60$). For $Re_j = 250$ and the axial locations shown in Fig. 4.36a, it is observed that the location of the maximum velocity ($Z' = 0.52$) for profiles at $5 \leq X \leq 10$ is somewhat higher than $Z' = 0.42$ for $X > 15$. The measurements reported in Section 4.2 also showed that the maximum velocity occurred at $Z' = 0.56$ for profiles in the range $5 \leq X \leq 25$ and $Z' = 0.46$ for $X > 25$. The velocity profiles can be divided into the following three regions: Region I ($Z' \leq 0.5$) which corresponds to the distance from the wall to the location of u_m. This region is usually referred to as the inner region. In this region, all the velocity profiles collapsed remarkably well onto a single curve. Region II ($0.5 < Z' \leq 1.0$) corresponds to distance between the location of u_m to the location of $z_{0.5}$. In this region, the profiles obtained at $X > 15$ are below those at $5 \leq X \leq 10$ and the normalised velocities generally decrease with X. In the outermost region (Region III) which corresponds to $Z' > 1.0$, there is a noticeable difference among the profiles and with the exception of $X = 20$, the normalised velocities increase with X. It should be noted that at this particular Reynolds number, the local maximum velocity at $X = 20$ is only 0.71% of the exit velocity.

Similar observations are also made in Fig. 4.36(b, c) for $Re_j = 420$ and 800. For these Reynolds numbers, the location of the maximum velocity was approximately the same

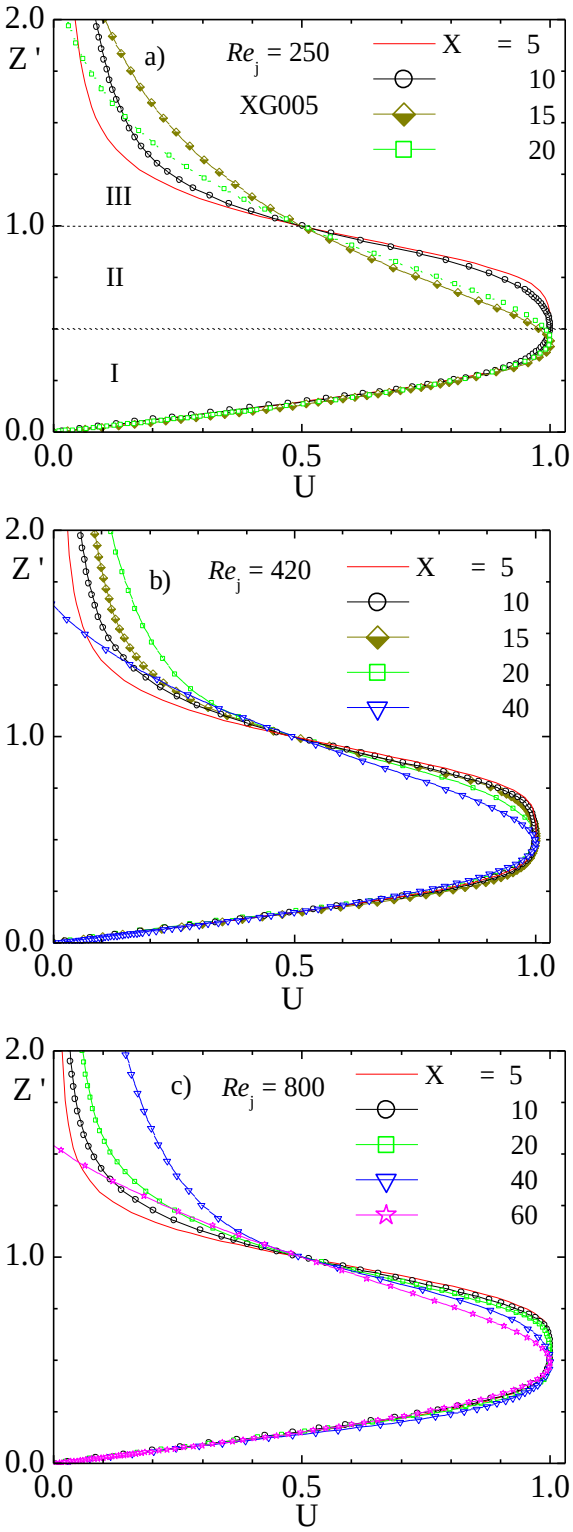

Figure 4.36: Normalised streamwise velocity profiles at various downstream locations for XG005 in the transverse direction.

(Z ' = 0.53) for all the X locations plotted. A comparison of Fig. 4.36a and Fig. 4.36(b, c) suggests that the discrepancies among the profiles in region II diminishes with Re_j. For region III, unlike Re_j = 250 where the profile at X = 20 deviates from those at X < 20, it is apparent from Fig. 4.36(b, c) that the profile at X = 40 for Re_j = 420 and X = 60 for Re_j = 800 are different from those closer to the jet exit.

The corresponding profiles in the spanwise direction and along z_m are shown in Fig. 4.37. These profiles can also be subdivided into two regions: region I (Y ' $\leq$ 1.0) and region II (Y ' > 1.0) which correspond to region II and region III, respectively. The trends observed in Figs. 4.36 and 4.37 are quite different from those made in the experiments (Section 4.2). For the measured data, the discrepancy among the velocity profiles only occurs in the region Z ' > 1.2 for the transverse direction and Y ' > 1.2 for the spanwise direction.

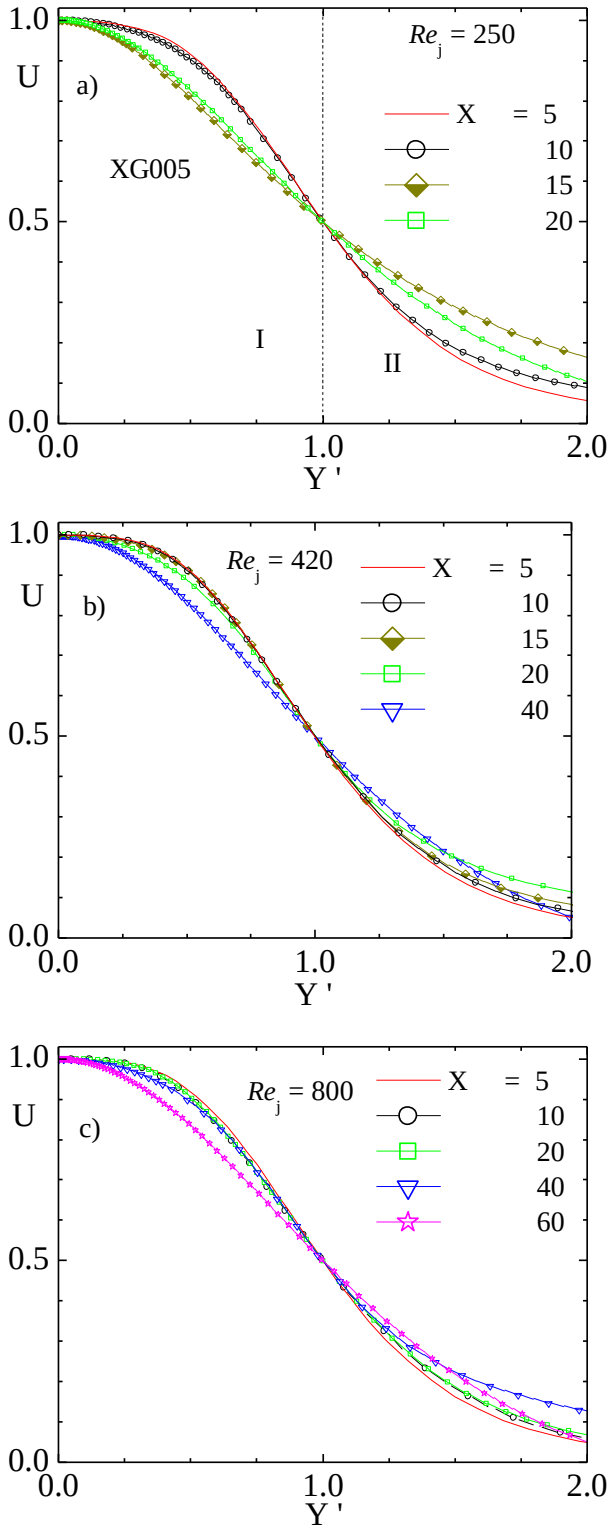

Figure 4.37: Normalised streamwise velocity profiles at various downstream locations for XG005 spanwise direction.

The normalised secondary velocity profiles at various X locations are shown in Figs. 4.38 and 4.39. Figure 4.38 shows the transverse velocity profiles ($W_u = w/u_m$) in the symmetry plane whereas Fig. 4.39 presents plots of the spanwise velocity profiles ($V_u = v/u_m$) along a line parallel to the wall passing through z_m. As expected, W_u profiles increase from zero to a maximum value and decrease in the outer region irrespective of the Reynolds number. For $Re_j = 250$, irrespective of the X location, the peak values (W_u) occur at the same location, Z ' = 0.75 which is higher than Z ' = 0.52 and 0.42, respectively, for U profiles in $5 \leq X \leq 10$ and $X > 15$ (Fig. 4.36a). The location of the peak value is comparable to Z ' $\approx$ 0.75 – 0.82 reported for power-law non-Newtonian fluids (Adane and Tachie, 2008a). Figure 4.38a also shows that the transverse velocity increases significantly with downstream distance, X. For example, the peak value of W_u at X = 10 is 0.09 compare with 0.64 at X = 20. The trends for $Re_j = 420$ and 800 are similar to those observed for $Re_j = 250$. Although the location for the peak value of W_u is independent of Reynolds number, W_u values are strongly influenced by Reynolds number. For instance, at X = 20 the peak values of W_u are 0.64, 0.13 and 0.01, respectively for $Re_j = 250$, 420 and 800.

In general, similar observations are also made for the spanwise velocity (V_u) profiles shown in Fig. 4.39. Unlike *w* profiles where the maximum value occurs at Z ' = 0.75, here, for all the three Reynolds numbers v_m occur at the same location of Y ' ~ 0.9.

It is noteworthy that for each Re_j value, *v* values are lower than *w* for each X location. This implies that the entrainment of the ambient fluid in the transverse direction is higher than that in the spanwise direction which is consistent with the larger spread of the jet in

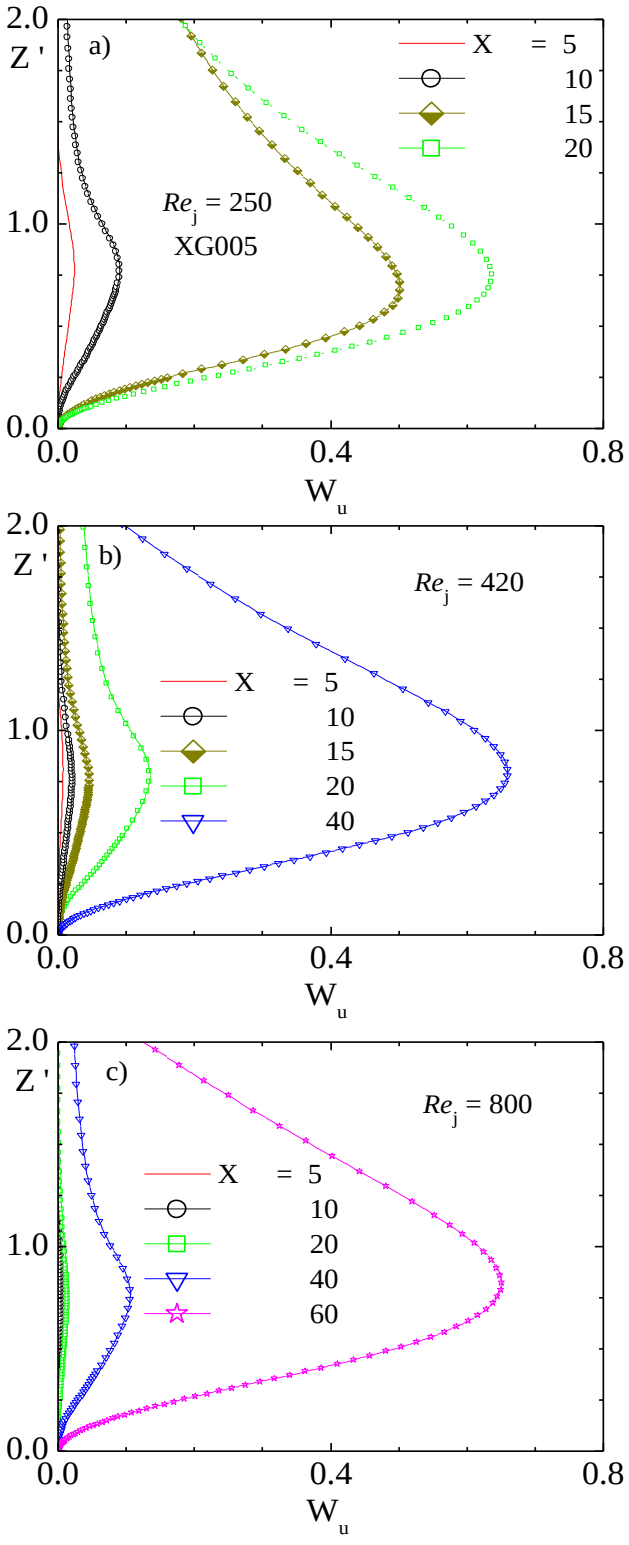

Figure 4.38: Normalised traverse velocity (W_u) profiles at various downstream locations for XG005.

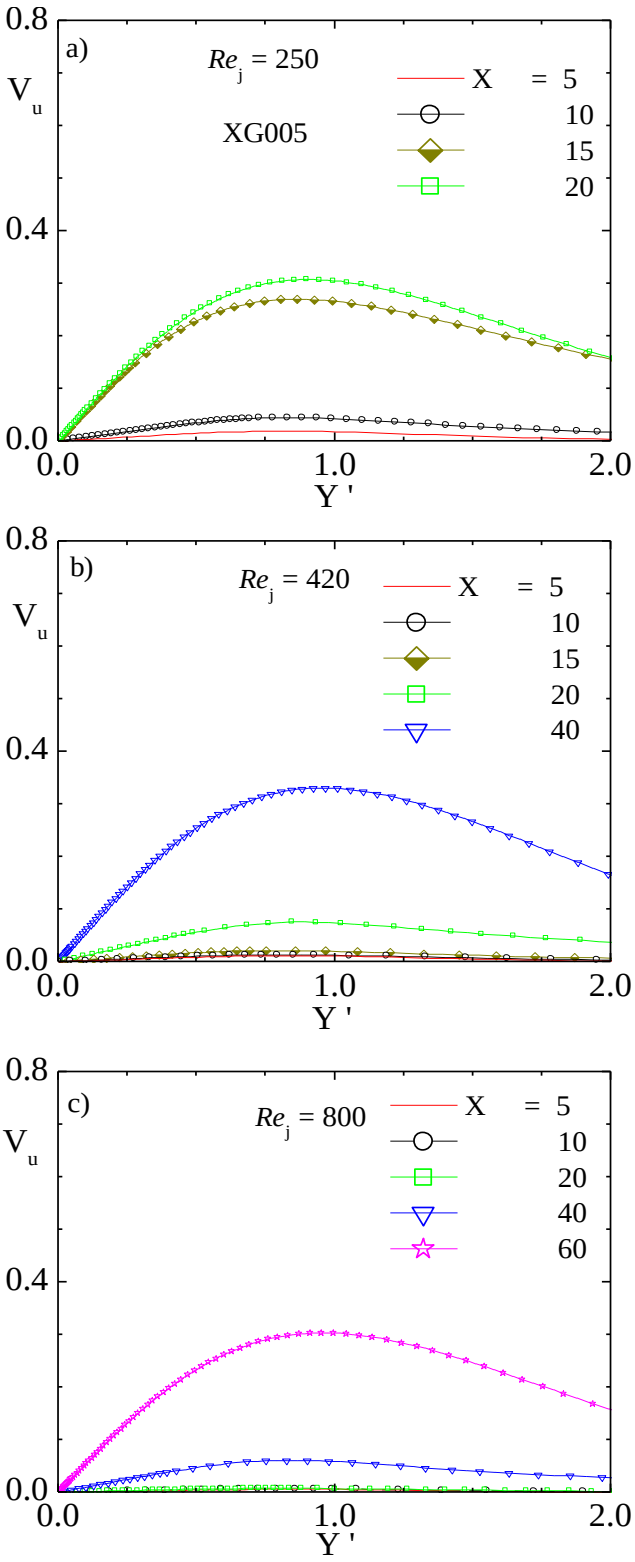

Figure 4.39: Normalised spanwise velocity (V_u) profiles at various downstream locations for XG005.

the transverse direction observed in Fig. 4.25. It is also noticed from Figs. 4.38 and 4.39 that, the scaling employed fails to collapse the secondary velocities into a single curve.

Figures 4.40 and 4.41 show the profiles of v and w normalised by their respective local maximum values (v_m and w_m). Figure 4.40 shows that although this normalisation does not completely collapse all the profiles in the symmetry plane, the agreement among the various profiles at $X \geq 5$ (for $Re_j = 250$), $X \geq 10$ (for $Re_j = 420$) and $X \geq 20$ (for $Re_j = 800$) in the region $Z' < 1$ is very good. Similarly, the V profiles (Fig. 4.41) in the region $Y' < 1$ at all axial locations shown collapsed reasonably well.

4.4.2.2 Effect of initial Reynolds number

Based on the results presented in Figs. 4.36 and 4.37, it was decided to use the profiles at X = 10 for the three Reynolds numbers to study any effects of Reynolds number (Fig. 4.42). The measured profiles at X = 10 at $Re_j = 800$ are also shown in Fig. 4.42 for comparison. The experimental data collapsed remarkably well onto the corresponding numerical results ($Re_j = 800$) except in the outermost part of the spanwise profile (Fig. 4.42b). The inner region of the profiles in the symmetry plane for the three Reynolds numbers (Fig. 4.42a) are in excellent agreement. In fact, with the exception of some minor discrepancies in the outer edge of the symmetry plane, the profiles in both the transverse and spanwise directions are nearly independent of Reynolds number.

4.4.2.3 Effect of concentration

The velocity profiles for the two non-Newtonian fluids (XG005 and XG010) and those for the reference Newtonian fluid are compared in Figs. 4.43 and 4.44. The profiles for

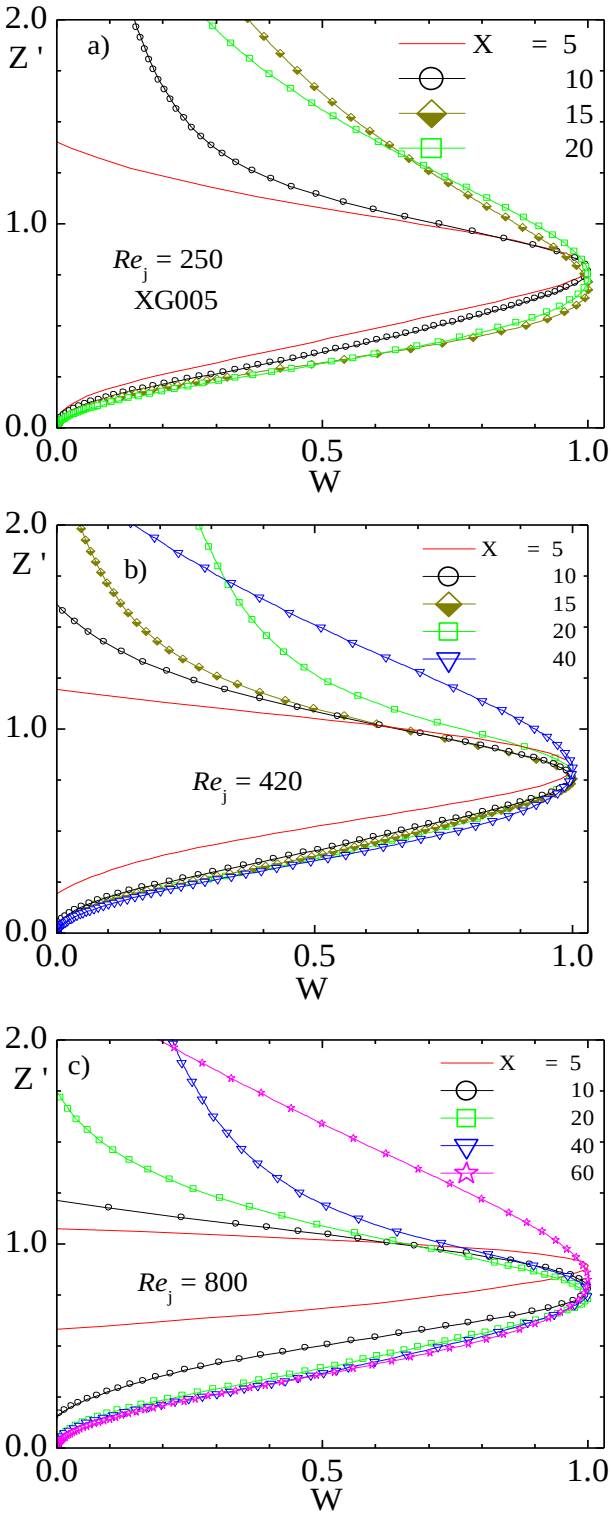

Figure 4.40: Normalised transverse velocity (W) profiles at various downstream locations for XG005.

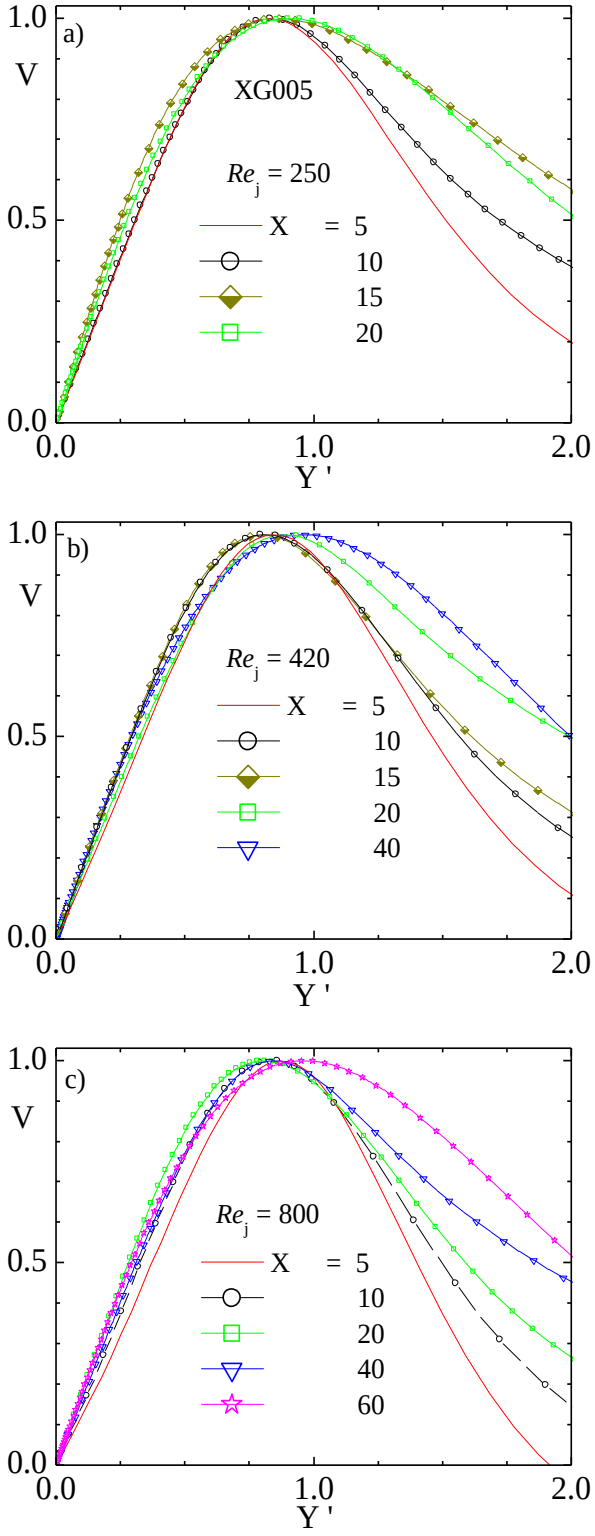

Figure 4.41: Normalised spanwise velocity (V) profiles at various downstream locations for XG005.

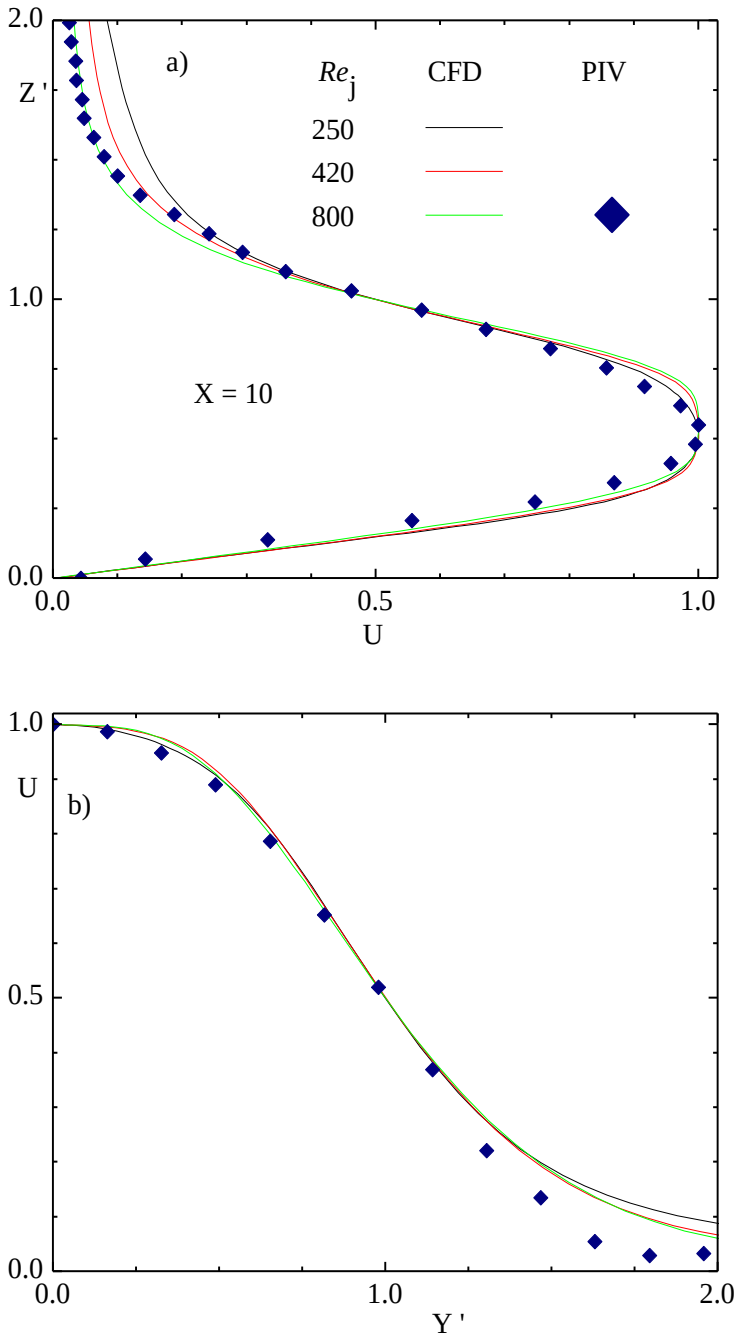

Figure 4.42: Comparison at various Re_j and previous experimental results on the similarity velocity profiles.

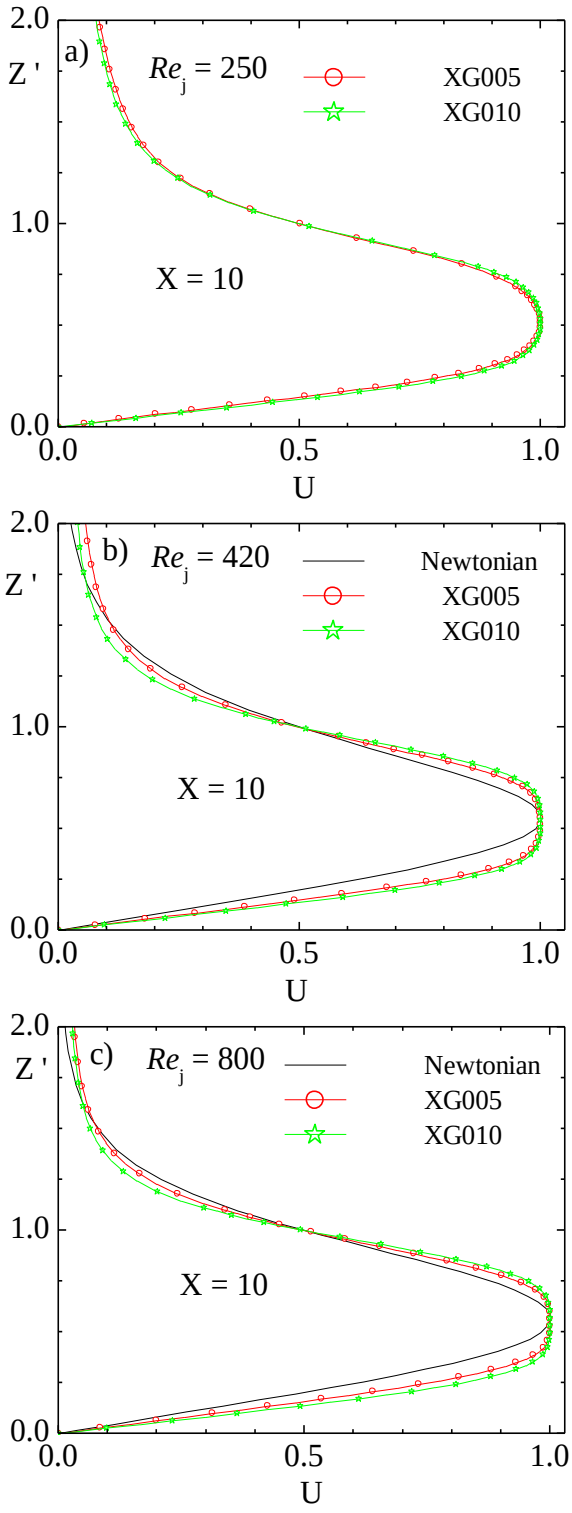

Figure 4.43: Comparison at various fluids on the similarity velocity profiles in transverse direction at $y = 0$.

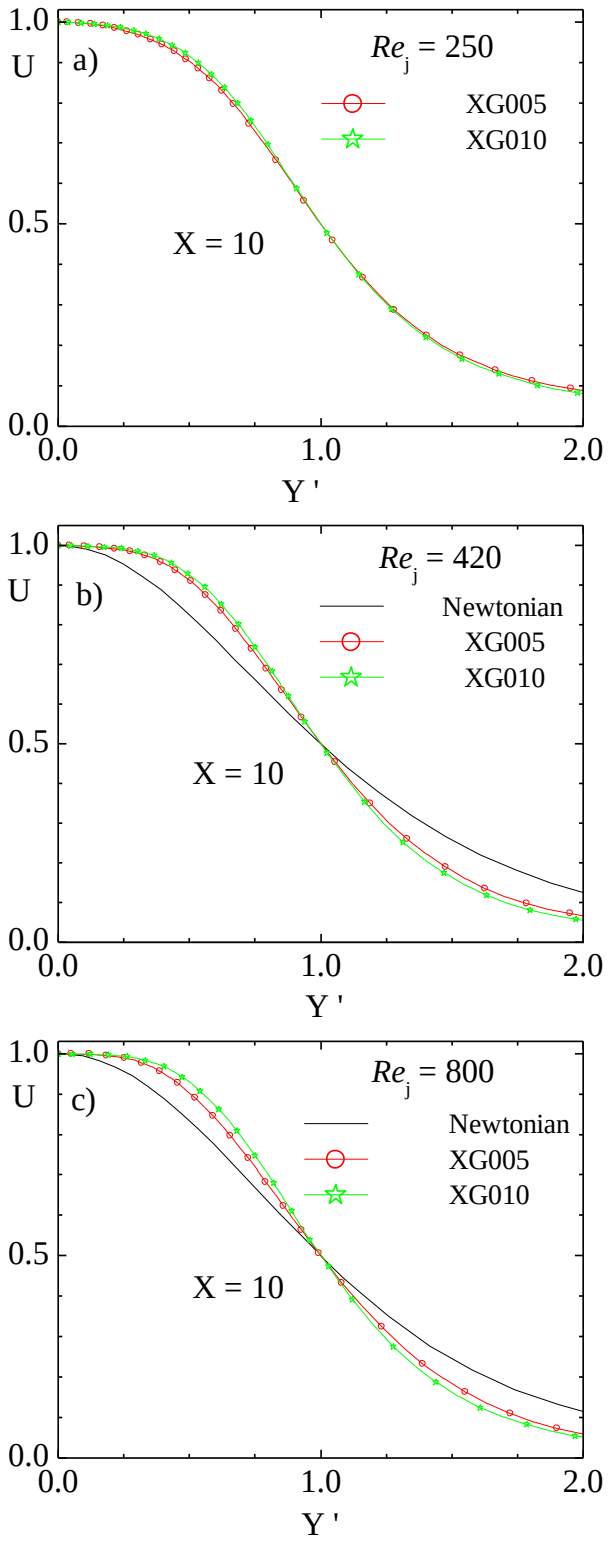

Figure 4.44: Comparison at various fluids on the similarity velocity profiles in spanwise direction at z_m.

the non-Newtonian fluid are in good agreement in both the transverse and spanwise directions. There is, however, a significant difference between the profiles for the Newtonian fluid and those for the non-Newtonian fluids. In the symmetry plane, for example, the normalised velocity for the Newtonian fluid in the inner region ($Z' < 0.5$) is relatively lower than the corresponding values for the non-Newtonian fluids. Previous results for 2-D laminar wall jet on a curve surface (Filip *et al*, 1991) and 3D-laminar wall jets (Adane and Tachie, 2008a) also showed that the velocity for a shear-thinning fluid is relatively higher than that for a Newtonian fluid. Significant differences are also observed between the Newtonian and non-Newtonian fluids in the spanwise direction (Fig. 4.44). In this case, the values of U for the Newtonian fluid are lower than the corresponding values for the non-Newtonian fluids in the region $Y' \leq 1.0$ and vice-versa in the outermost region ($Y' > 1.0$).

4.5 Vorticity Distributions

In this section, the distributions of the streamwise vorticity for both the Newtonian and non-Newtonian fluids are presented and discussed. The vorticity is computed from the velocity field using a central-differencing scheme.

4.5.1 Effect of Initial Reynolds Number

Figure 4.45 shows contours of the normalised streamwise vorticity, Ω_x ($1000\omega_x\, d / u_j$) in the *z-y* plane at X = 5, 30 and 60 for Re_j = 310 and 800 for the Newtonian fluid. The rational is to assess the level of the streamwise vortex as the flow evolves downstream. Irrespective of Re_j, Ω_x decreases with increasing X. The decrease is more dramatic at Re_j = 310 than at Re_j = 800. At X = 30, the maximum value of Ω_x is only 5% of that at X = 5

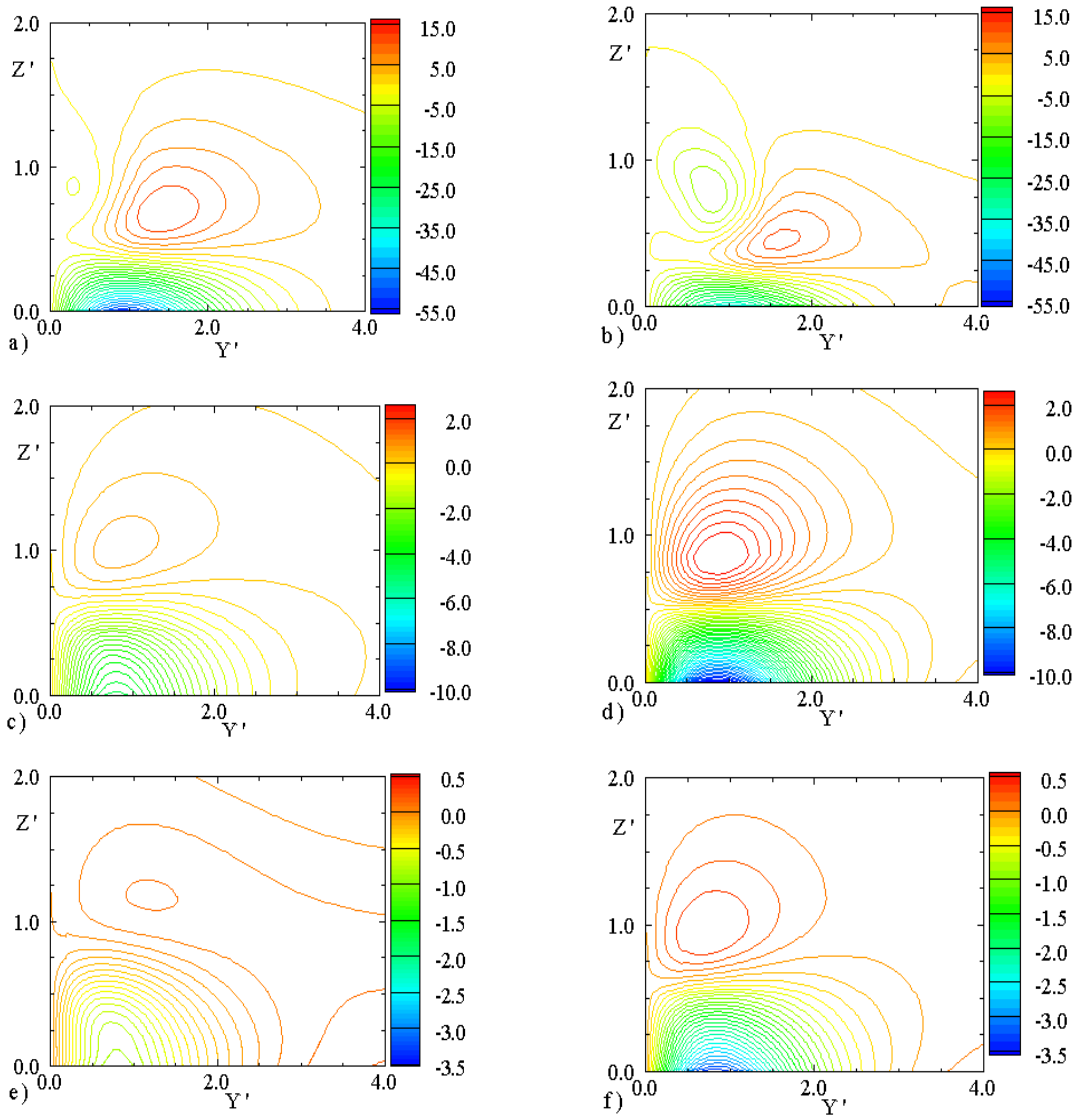

Figure 4.45: Streamwise vorticity contours at Re_j = 310 (a, c, e) and 800 (b, d, f) for X = 5, 30 and 60, respectively for the Newtonian fluid.

for Re_j = 310. Meanwhile, for Re_j = 800, the maximum value of Ω_x at X = 30 is 25% of the corresponding value at X = 5. At X = 5, the contours at Re_j = 800 (Fig. 4.45b) show a strong emergence of secondary vortex in the outer region. As the flow evolves downstream, this secondary vortex decreases while the primary vortex increases. At X = 30, the secondary vortex has disappeared and the centre of primary vortex is now at Y ' =

0.9 (Fig. 4.45d). The strong secondary vortex formation observed at X = 5 (Fig. 4.45b) indicates that the flow at Re_j = 800 generated a significant amount of streamwise vortices at the early stages of its evolution after which the velocity does not change as rapidly (see Figs. 4.12 and 4.21) as it does at Re_j = 310.

Figure 4.46 shows contour of the normalised streamwise vorticity, Ω_x in the *z-y* plane at X = 5 and 20 for Re_j = 250, 420 and 800 for XG005. Irrespective of Re_j, Ω_x decreases with increasing X. The decrease is more dramatic at Re_j = 250 than at Re_j = 800. At X = 20, the peak positive value of Ω_x is only 0.06% of the corresponding value at X = 5 for Re_j = 250. The corresponding percentage change of the peak negative value is 1.2%. On the other hand, for Re_j = 800, the peak positive and negative values of Ω_x at X = 20 are 15% and 40.4%, respectively of the corresponding values at X = 5. Figure 4.46(a, c, e) shows strong secondary vortex formation at X = 5 especially for Re_j = 420 and 800. Due to the strong interaction of the jet and the ambient fluid, these vortices were diffused by viscosity such that at X = 20 for Re_j = 250 and 420, the vortices no longer exist. The trend observed in Figs. 4.45 and 4.46 is consistent with the earlier observations made for the rapid decay of the velocity and fast spread of the jet in both transverse and spanwise directions for the lower Re_j. In fact, Fig. 4.46 also supports the notion that the higher spread rate ratios ($S_r > 1$) in Fig. 4.14 is due to streamwise vorticity.

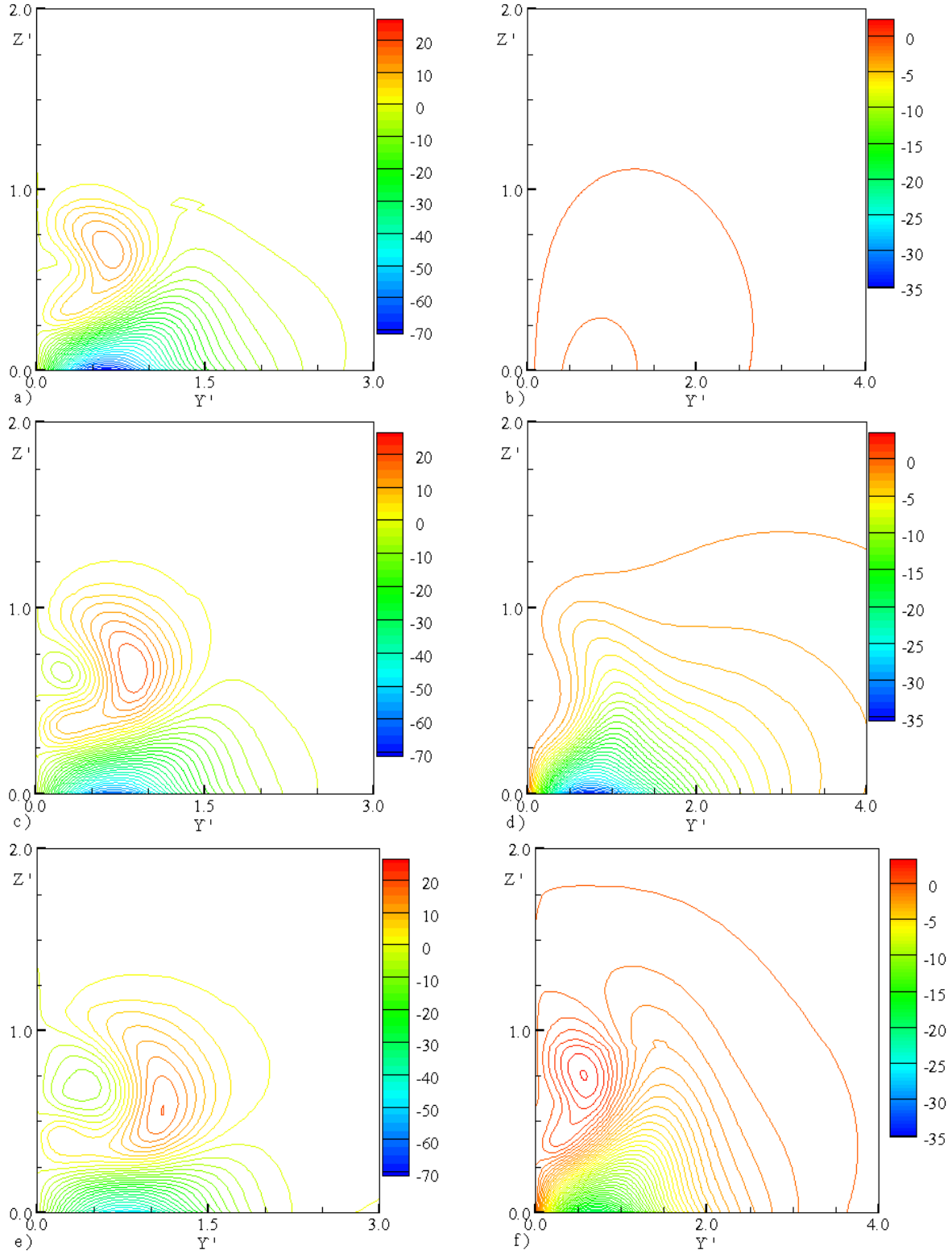

Figure 4.46: Streamwise vorticity contours at Re_j = 250 (a, b), 420 (c, d) and 800 (e, f) for X = 5 and 20, respectively for XG005 fluid.

4.5.2 Effect of Concentration

Figure 4.47 shows the Ω_x contours for all the three fluids in the *z-y* plane at X = 5, 20 and 40. Irrespective of fluid, Ω_x decreases with increasing X. At X = 5, there was no significant difference between the values of Ω_x for the two non-Newtonian fluids. The peak positive and negative values of Ω_x for the non-Newtonian fluid are 1.6 and 1.26, respectively times the corresponding values of Newtonian fluid. Meanwhile, at X = 40 the peak positive value of Ω_x for the Newtonian fluid is approximately ten times the corresponding peak positive Ω_x values for XG005 and XG010. These higher positive Ω_x values for the Newtonian fluid are vividly shown on the contour (Fig. 4.47g). Furthermore, the diffusion of the streamwise vortex in the outer region for the two shear-thinning fluids (XG005 and XG010) is clearly demonstrated by the contours of those fluids (Fig. 4.47(h, i)). This trend is consistent with the earlier observations made for the spread rates in Figs. 4.33 and 4.34.

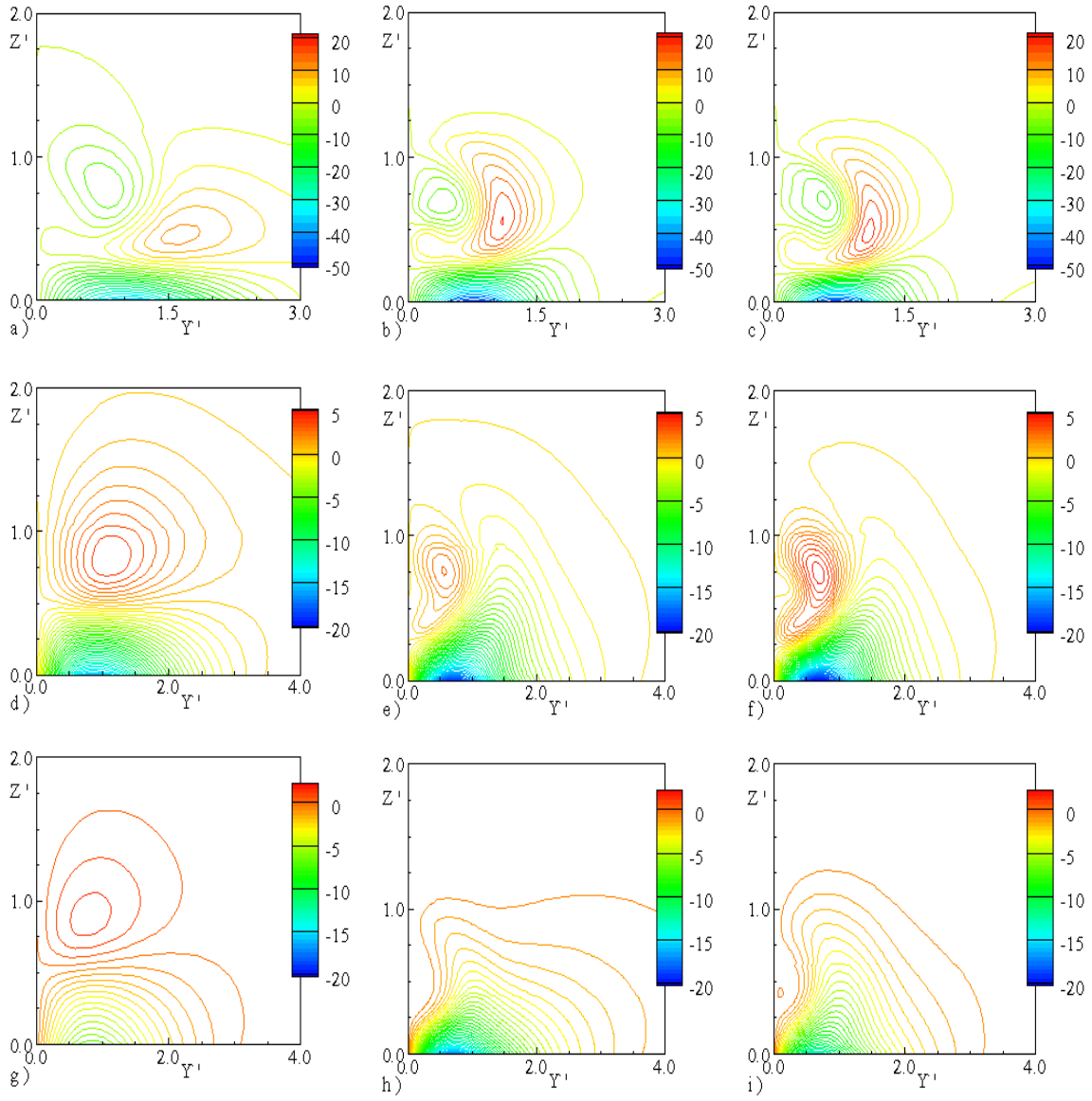

Figure 4.47: Streamwise vorticity contours at Re_j = 800 for various fluids: Newtonian (a, d, g), XG005 (b, e, h) and XG010 (c, f, i) for X = 5, 20 and 40, respectively.

Chapter 5

SUMMARY, CONCLUSIONS AND FUTURE WORK

This chapter provides a summary and the major conclusions of this thesis. Some important recommendations for future work are also presented.

5.1 Summary and Conclusions

5.1.1 Summary

An experimental research program was undertaken to study the characteristics of three-dimensional laminar wall jet flows of both Newtonian and shear-thinning non-Newtonian fluids. Water was used as the Newtonian fluid whereas the non-Newtonian fluids were prepared from two concentrations of xanthan gum (0.005 *wt*% and 0.01 *wt*%). A planar particle image velocimetry technique (PIV) was used to conduct the velocity measurements. The measurements were performed in various streamwise-transverse and streamwise-spanwise planes at various initial Reynolds numbers ($250 \leq Re_j \leq 800$). From these measurements, the wall jet characteristics including the maximum velocity decay, jet half-widths and velocities profiles were obtained to study the effects of Reynolds number and fluid type on the characteristics of the wall jet flows.

Numerical method was also employed to compute the three-dimensional laminar wall jet flows of both Newtonian and shear-thinning non-Newtonian fluids. The experimental data obtained in this study were used to validate the numerical results. Additional quantities such as spread rates, momentum flux, skin friction coefficient and streamwise vortex that could not be measured in the experiments were also evaluated from the computation.

5.1.2 Concluding Remarks

The measurements for the Newtonian fluid showed that, irrespective of the initial Reynolds number, the maximum velocity decayed whereas the jet half-widths increase with downstream distance. The decay of the maximum velocity was nearly independent of Reynolds number. However, the jet half-widths in the spanwise and transverse direction decrease with increasing initial Reynolds number. It was observed that the growth of the jet half-widths is anisotropic in nature. The substantially larger growth in the transverse direction than in spanwise direction was attributed to the dominance of viscous diffusion. The wall jet flow achieved a self-similar condition irrespective of the Reynolds number. Whilst the velocity profiles in the self-similar region were independent of Reynolds number, the onset of the self-similar condition depends on Reynolds number. For example, the streamwise locations of the onset of similarity condition were 5d and 2d, respectively, for the lower (Re_j = 310) and higher (Re_j = 800) Reynolds numbers.

With exception of the highest Reynolds number (Re_j = 800) for the higher concentration of xanthan gum (XG010) fluid, the measured results for the non-Newtonian fluids were qualitatively similar to those made for the Newtonian fluids. The only difference is that, for these non-Newtonian fluids the decay of maximum velocity was faster at the lower Reynolds number (Re_j = 250) and slower at the higher Reynolds number (Re_j = 800).

In contrast, the growth of the jet half-widths for the XG010 fluid at Re_j = 800 was significantly higher in the spanwise direction than in the transverse direction. An observation that is similar to previous results for three-dimensional turbulent wall jets.

Furthermore, the velocity profiles in the downstream locations (>30*d*) resembled those of a typical turbulent wall jet.

The measured results showed that, the decay of the maximum velocity and the spread of the jets in both spanwise and transverse directions were faster for the Newtonian fluid than for the non-Newtonian fluids. Meanwhile, the normalised velocity profiles showed no dependence on the specific fluid.

Although the experimental results are more limited in scope in comparison to the numerical results, they provide the basis for validating the numerical results. For the Newtonian fluid, a good agreement between the experimental and numerical results was observed for velocity profiles, and for the maximum velocity and jet half-widths in the early region of jet development. In the downstream region ($x > 30d$), values of the maximum velocity were higher and the jet half-widths were lower for the numerical results than the corresponding measured results. The numerical results showed that the initial momentum is expended more quickly at a lower Reynolds number; and as a result, the velocity decay more rapidly at a lower Reynolds number than at a higher Reynolds number.

The spread rates and skin friction coefficient from the numerical results showed a strong dependence on the initial Reynolds number. The variation of the transverse spread rate with streamwise distance can be divided into two regions: (i) an initial region where the spread rate increases sharply from the exit and (ii) a final region where transverse spread rate increases nearly linearly with streamwise distance, irrespective of the initial Reynolds number. The demarcation between these regions depends strongly on the

initial Reynolds number. The variation of the spanwise spread rate with streamwise distance at higher Reynolds numbers (Re_j = 420 and 800) becomes nearly constant beyond 7*d*. Also, in the downstream region, both spread rates increase nearly linear with decreasing local Reynolds number and this variation is independent of the initial Reynolds number. In the early region of flow development, the jet spreads more in the spanwise direction than in the transverse direction whereas in the downstream region the converse is true. This observation was true for all the Reynolds numbers studied. This anisotropic behaviour in the early stage of flow development was attributed to the presence of streamwise vorticity whereas that in the downstream region was due to viscous diffusion.

For a given initial Reynolds number, the skin friction coefficient obtained with the jet maximum velocity decreases with downstream distance and also as one moves away from the symmetry plane. On the contrary, the local skin friction coefficient is a unique function of the local Reynolds number but independent of the initial Reynolds number.

The general conclusions from numerical results on non-Newtonian fluids are not different from those made for Newtonian fluid. At the later stage of flow development, the numerical results for the non-Newtonian fluids are lower than the corresponding measured values. Unlike the measured values where the observations for higher Reynolds number for higher concentration of xanthan gum are different from the other flow conditions, the numerical results showed no significant differences. Numerical results for the non-Newtonian fluids showed that, irrespective of initial Reynolds number, the spread rates vary exponentially with streamwise distance. The results also

demonstrate that the streamwise velocity profiles in the outermost region of the flow never collapsed into a single curve.

The results from various concentrations of xanthan gum showed that the maximum velocity decay, the spread rates, and velocity profiles depend on the specific fluid. In the downstream region, the variation of the spread rates with the local Reynolds number is independent of the fluid. The spread rate ratios for the non-Newtonian fluids are significantly higher than that of Newtonian fluid in the early stages of the flow whereas in the downstream region the reverse is true. Finally, the local skin friction coefficient is a unique function of the local Reynolds number but independent of the fluid.

5.2 Recommendations for Future Work

Based on the above concluding remarks and the current understanding of the three-dimensional laminar wall jet flows, the following recommendations are suggested for future research. An experimental study at higher Reynolds numbers than in the present study would provide a physical understanding of the transition process from 3D laminar wall jets to the 3D turbulent wall jets. Such results will also be useful for validating future numerical results. Moreover, the complex nature of the 3D laminar wall jet flows would require measurements of the three components of the velocity field in order to completely validate numerical results.

The effect of higher concentrations of xanthan gum and a wide range of non-Newtonian fluids should be studied. Furthermore, extension of the viscosity definition by incorporating fluid behaviours such as relaxation time, elasticity, elongation and yield will provide additional insight into the fluid effect on wall jet characteristics.

BIBLIOGRAPHY

Acosta, J. M., Numerical algorithms for three dimensional computational fluid dynamic problems, PhD Thesis, Universitat Politècnica de Catalunya, Barcelona, Spain, 135-141, 2001.

Acrivos, A., Shah, M, J., and Petersen, E.E., Momentum and heat transfer in laminar boundary-layer flows of non-Newtonian fluids past external surfaces, *AICHE Journal*, **6**, 312-317, 1960.

Adane, K. K.[a] and Tachie, M. F., Numerical Investigation of Three-Dimensional Laminar Wall Jet of Newtonian and Non-Newtonian Fluids, *AIAA Journal*, **46** (11), 2868-2880, 2008.

Adane, K. K.[b] and Tachie, M. F., Numerical analysis of three-dimensional laminar wall jet flow of power-law fluids, *16th Annual Conference of the CFD Society of Canada*, Saskatoon, SK, Canada, 8 - 10 June, 2008.

Adeyinka, O. B. and Naterer, G. F. Experimental uncertainty of measured entropy production with pulsed laser PIV and planar laser induced fluorescence, *International Journal of Heat and Mass Transfer*, **48,** 1450–1461, 2005.

Adrian, R. J., Particle-imaging techniques for experimental fluid, *Annual Review Fluid Mechanics*, **23**, 261-304, 1991.

Alexandrou, A., Principles of fluid mechanics, 1st *ed*., Prentice Hall, 2001.

Arzate, A., Réglat, O., and Tanguy, P. A., Determination of in-line process viscosity using static mixers, *Flow Measurement and Instrumentation*, **15**, 77–85, 2004.

Bachmann, C., Hugo, G., Rosenberg, G., Deutsch, S., Fontaine, A., and Tarbell, J. M., Fluid dynamics of a pediatric ventricular assist device, *Artificial Organs*, **24**(5), 362–

372, 2000.

Bajura, R. A. and Szewczyk, A. A., Experimental investigation of a laminar two-dimensional plane wall jet, *The Physics of Fluids*, **13** (7), 1653-1664, 1970.

Barnes, H. A., Hutton, J. F., and Walters, K., An introduction to rheology, *Rheology Series 3*, Elsevier, New York, 1989.

Bhattacharjee, P. and Loth, E., Simulations of laminar and transitional cold wall jets, *International Journal of Heat and Fluid Flow*, **25**, 32–43, 2004.

Bibeau, L. E., *Personal communication*, Department of Mechanical and Manufacturing Engineering, University of Manitoba, Winnipeg, Canada, 2007.

Bird, R. B., Armstrong, R. C., and Hassager, O., Dynamics of polymeric liquids in fluid mechanics, *2nd ed.*, **1**, Wiley, New York, 1987.

Bittorf, K. J. and Kresta, S. M., Three-dimensional wall jets: axial flow in a stirred tank, *AIChE Journal*, **47** (6), 1277 – 1284, 2004.

Carreau, P. J., Rheological equations from molecular network theories, *Journal of Rheology*, **16** (1), 99-127, 1972.

Cavasada, A. S., Pinho, F. T., Some characteristics of stirred vessel flows of dilute polymer solutions powered by a hyperboloid impeller, *The Canadian Journal of Chemical Engineering*, **82**, 289-302, 2004.

Chen, C., Flachskampf, F.A., Anconina, J., Weyman, A. E., and Thomas, J. D., Three-dimensional shape of wall jets and free jets: implication for quantitation of valvular regurgitation by color doppler imaging, *Journal of the American College of Cardiology*, **15** (2), 89A, 1990.

Chhabra, R. P. and Richardson, J. F., Non-Newtonian flow in the process industries:

Fundamentals and engineering applications, *Butterworth-Heinemann*, 130, 1999.

Chhabra, R. P. and Uhlherr, P. H. T., Creeping motion of spheres through shear-thinning elastic fluids described by the Carreau viscosity equation, *Rheological Acta*, **19**, 187-195, 1980.

Cohen, J., Amitay, M., and Bayly, B. J., Laminar-turbulent transition of wall-jet flows subjected to blowing and suction, *Physics of Fluids A*, **4**, 283–289, 1992.

Coleman, H. W. and Steele W. G., Engineering application of experimental uncertainty analysis, *AIAA Journal*, **33**, 1888-1896, 1995.

Craft, T. J. and Launder, B. E., On the spreading mechanism of the three-dimensional turbulent wall jet, *Journal of Fluid Mechanics*, **435**, 305-326, 2001.

Cross, M. M., Rheology of non-Newtonian fluids: A new flow equation for pseudoplastic systems, *Journal of Colloid Science*, **20** (5), 417-437, 1965.

Cullen, D. K., Vukasinovic, J., Glezer, A., and LaPlaca, M. C., Microfluidic engineered high cell density three-dimensional neural cultures, *Journal of Neural Engineering*, **4**, 159–172, 2007.

Curd, E. F., Possible applications of wall jets in controlling air contaminants, *Annals of Occupational Hygiene*, **24** (1), 133-146, 1981.

Dai, L., Zhang, Z., Winyard, P. G., Gaffney, K., Jones, H., Blake, D. R., and Morris, C. J., A modified form of low-density lipoprotein with increased electronegative charge is present in rheumatoid arthritis synovial fluid, *Free Radical Biology & Medicine*, **22** (4), 705–710, 1997.

Daugan, S., Talini, L., Herzhaft, B., Peysson, Y., and Allain, C., Sedimentation of suspensions in shear-thinning fluids, *Oil & Gas Science and Technology–Rev. IFP*, **59** (1), 71-80, 2004.

de Vicente, J., Stokes, J. R., and Spikes, H. A., Soft lubrication of model hydrocolloids, *Food Hydrocolloids*, **20**, 483–491, 2006.

Denier, J. P. and Dabrowski, P. P., On the boundary-layer equations for power-law fluids, *Proceedings of the Royal Society of London, Series A-Mathematical Physical and Engineering Sciences*, **460** (2051), 3143-3158, 2004.

Denier, J. P. and Hewitt, R. E., Asymptotic matching constraints for a boundary-layer flow of a power-law fluid, *Journal of Fluid Mechanics*, **518**, 261–279, 2004.

Dressler, D. M, An experimental investigation of Newtonian and non-Newtonian spray interaction with a moving surface, MSc. Thesis, Department of Mechanical Engineering, The Faculty of Graduate Studies, The University of British Columbia, Vancouver, BC, Canada, 2006.

Escudier, M. P., and Smith, S., Turbulent flow of Newtonian and shear-thinning liquids through a sudden axisymmetric expansion, *Experiments in Fluids*, Springer-Verlag, **27**, 427-434, 1999.

Escudier, M. P., Gouldson, I. W., and Jones, D. M., Taylor vortices in Newtonian and shear-thinning liquids, *Proceedings: Mathematical and Physical Sciences*, **449** (1935), 155-176, 1995.

Escudier, M. P., Gouldson, I. W., Pereira, A. S., Pinho, F. T., and Poole, R. J., On the reproducibility of the rheology of shear-thinning liquids, *Journal of Non-Newtonian Fluid Mechanics*, **97**, 99–124, 2001.

Ferziger, J. H. and Perić, M., Computational methods for fluid dynamics, *3rd ed.*, Springer-Verlag, Berlin, Chapters 3-8, 2002.

Figliola, R. S. and Beasley, D. E., Theory and design for mechanical measurements, *3rd ed.*, 2000, John Wiley & Sons, New York.

Filip, P., Kolar, V., and Hajek, R., Similarity prediction of wall jets past axisymmetric bodies for power-law fluids, *Acta Mechanica*, **88**, 167-173, 1991.

Forliti, D. J., Strykowski, P. J. and Debatin, K., Bias and Precision of Digital Particle Image Velocimetry, *Experiments in Fluids*, **28**, 436-447, 2000.

Gervang, B. and Larsen, P. S., Secondary flows in straight ducts of rectangular cross section, *Journal of Non-Newtonian Fluid Mechanics*, **39** (3), 217-237, 1991.

Glauert, M. B., The wall jet, *Journal of Fluid Mechanics*, **1**, 625-643, 1956.

Goldstein, R. J. and Kried, D. K., Measurement of laminar flow development in a square duct using a laser dropper flowmeter, *Journal of Applied Mechanics*, **34**, 813-818, 1967.

Gorla, R. S. R. and Jeng, D. R., "Laminar plane wall jet", *Proc. of the 12th Midwestern Mechanics Conference: Developments in Mechanics*, **6** (8), 137-151, 1971.

Gorla, R. S. R., Laminar wall jet of a non-Newtonian fluid over a curved surface, *Journal of Applied Mechanics*, **51**, 440-443, 1984.

Gui, L.[a], Longo, J. and Stern, F., Towing tank PIV measurement system, data and uncertainty assessment for DTMB model 5512, *Experiments in Fluids*, **31**, 336-346, 2001.

Gui, L.[b], Longo, J. and Stern, F., Biases of PIV measurement of turbulent flow and the masked correlation-based interrogation algorithm, *Experiments in Fluids*, **30**, 27-35,

2001.

Gutfinger, C. and Shinnar, R., Velocity distributions in two-dimensional laminar liquid-to-liquid jets in power-law fluids, *AIChE Journal*, **10** (5), 631-639, 1964.

Hall, J. W. and Ewing, D., The asymmetry of the large-scale structures in turbulent three-dimensional wall jets exiting long rectangular channels, *Journal of Fluids Engineering*, **129**, 929-941, 2007.

Hari, M. V., A method to analyse the wall jet flow, *Aeronautical Journal*, 512-515, 1973.

Hartnett, J. P. and Kostic, M., Heat transfer to Newtonian and non-Newtonian fluids in rectangular ducts, *Advances in Heat Transfer*, **19**, 247-356, 1989.

Hsiao, F. B. and Sheu, S. S., Experimental studies on flow transition of a plane wall jet, *Aeronautical Journal*, **100**, 373–380, 1996.

Issa, J. S., Numerical computation of the heat transfer and fluid mechanics in the laminar wall jet and comparison to the self-similar solutions, *Proc. of IMECE04, ASME Intern. Mechanical Eng. Congress & Exposition*, **375** (3), 191-197, USA, 2004.

Issa, J. S., Scaling of convective heat transfer in laminar and turbulent wall jets with effects of freestream flow and forcing, PhD Thesis, The University of Arizona, 2006.

Itagaki, M., Kadowaki, J., and Watanabe, K., Analysis of active dissolution of copper in acidic solution by EQCM/wall jet split ring disk electrode, *Electrochemistry*, **68**, 684–688, 2000.

Kanna, P. R. and Das, M. K., Conjugate forced convection heat transfer from a flat plate by laminar plane wall jet flow, *International Journal of Heat and Mass Transfer*, **48**, 2896–2910, 2005.

Keane, R. D. and Adrian, R. J., "Optimization of particle image velocimetry, Part1:

doubled pulsed system, *Measurement Sci. & Tech*., **1**(11), 1202-1215, 1990.

Khosla, P. K. and Rubin, S. G., A diagonally dominant second-order accurate implicit scheme, *Computers and Fluids*, **2**, 207–209, 1974.

Koseff, J. R. and Street, R. L., The lid-driven cavity flow: a synthesis of qualitative and quantitative observations, *Journal of Fluid Engineering*, **106**, 385-398, 1984.

Krechetnikov, R. and Lipatov, I., Hidden invariances in problems of two-dimensional and three-dimensional wall jets for Newtonian and non-Newtonian fluids, *SIAM Journal of Applied Mathematics*, **62** (6), 1837–1855, 2002.

Launder, B. E. and Rodi, W., The turbulent wall jet measurements and modelling, *Annual Review of Fluid Mechanics*, **15**, 429–459, 1983.

Launder, B. E. and Rodi, W., The turbulent wall jet, *Progress Aerospace Science*, **19**, 81-128, 1981.

Law, A. W-K. and Herlina, An experimental study on turbulent circular wall jets, *Journal of Hydraulic Engineering*, **128**, 161-174, 2002.

Li, L., Dressler, D. M., Green, S. I., and Davy, M. H., An experimental study of non-Newtonian atomization, *ILASS Americas 18th Annual Conference on Liquid Atomization and Spray Systems*, Session 2A/1, Irvine, CA, May 2005.

Lilek, Z; Muzaferija, S., and Peric, M., Efficiency and accuracy aspects of a full-multigrid simple algorithm for three-dimensional flows, *Numerical Heat Transfer, Part B, Fundamentals*, **31** (1), 23–42, 1997.

Lima, J. A., Pereira, L. M., Macêdo, E. N., Chaves, C. L. and Quaresma, J. N. N., Hybrid solution for the laminar flow of power-law fluids inside rectangular ducts, *Computational Mechanics*, 26, 490-496, 2000.

Lindner, A., Bonn, D. and Meunier, J., Viscous fingering in a shear-thinning fluid, *Physics of Fluids*, **12** (2), 256-261, 2000.

Lo, D. C., Murugesan, K. and Young, D. L., Numerical solution of three-dimensional velocity–vorticity Navier–Stokes equations by finite difference method, *International Journal for Numerical Methods in Fluids*, **47**, 1469–1487, 2005.

Macosko, C. W., Rheology: principles, measurements, and applications, *Wiley-VCH*, 1994.

Mautner, T., Application of the synthetic jet concept to low Reynolds number biosensor microfluidic flows for enhanced mixing: a numerical study using the lattice Boltzmann method, *Biosensors and Bioelectronics*, **19**, 1409–1419, 2004.

Mei, R., Adrian, R. J. and Hanratty, T. J., Particle dispersion in isotropic turbulence under Stokes drag and Basset force with gravitational settling, *Journal of Fluid Mechanics*, **225**, 481–495, 1991.

Meyer, L. E., Fuller, G.G., Clark, R. C., and Kulicke, W.M., Investigation of xanthan gum solution behaviour under shear flow using rheooptical techniques, *Macromolecules*, **26**, 504-611, 1993.

Neofytou, P., A 3rd order upwind finite volume method for generalised Newtonian fluid flows, *Advances in Engineering Software*, **36**, 664–680, 2005.

Oliveira, P. J., Pinho, F. T. and Pinto, G. A., Numerical simulation of non-linear elastic flows with a general collocated finite-volume method, *Journal of Non-Newtonian Fluid Mechanics*, **79**, 1-43, 1998.

Ormiston, S. J., Computational methods for thermofluids, *Supplementary Course Notes* V5.0, 2006.

Patankar, S. V., Numerical heat transfer and fluid flow, Taylor & Francis, 1980.

Patankar, S., and Spalding, D., A calculation procedure for heat, mass and momentum transfer in three-dimensional parabolic flows, *International Journal of Heat and Mass Transfer*, **15**, 1787-1806, 1972.

Perić, M., Kessler, R., and Scheuerer, G., Comparison of finite-volume numerical methods with staggered and colocated grids, *Computers and Fluids*, **16** (4), 389-403, 1988.

Peters, F., Ruppel, C., Javili, A., and Kunkel, T., The two-dimensional laminar wall jet velocity measurements compared with similarity Theory, *Forsch Ingenieurwes*, **72**, 19–28, 2008.

Pinho, F. T., The finite-volume method applied to computational rheology: II-fundamentals for stress-explicit fluids, *e-rheo.pt*, **1**, 63-100, 2001.

Prasad, A. K., Adrian, R. J., Landreth, C. C. and Offutt P. W., Effect of resolution on the speed and accuracy of particle image velocimetry interrogation, *Experiments in Fluids*, **13**, 105-116, 1992.

Quintana, D. L., Amitay, M., Ortega, A., and Wygnanski, I. J., Heat transfer in the forced laminar wall jet, *Journal of Heat Transfer*, **119**, 451–459, 1997.

Raffel, M., Willert, C. E., and Kompenhaus, J, Particle image velocimetry: a practical guide, Springer Verlag., 1998.

Rhie, C. M. and Chow, W. L., Numerical study of the turbulent flow part an airfoil with trailing edge separation, *AIAA Journal*, **21**, 1525-1532, 1983.

Roth, R. J., An investigation of flow acceleration and electromagnetic absorption phenomena induced by paraelectric and peristaltic electrohydrodynamic effects of

the one atmosphere uniform glow discharge plasma, *Final Report*, University of Tennessee Plasma Sciences Laboratory (http://plasma.ece.utk.edu), Nov. 30, 2003.

Saad, B., Bee-Leng, Y., and Saleh, M. I., A wall jet flow-through detector for the sensing of quinine and paraquat ions, *Laboratory Robotics and Automation*, **12**, 133–137, 2000.

Scarano, F. and Riethmuller, M., Iterative multigrid approach in PIV image processing with discrete window offset, *Experiment of Fluids*, **26**, 513-523, 1999.

Schechter, R. S., On the steady flow of a non-Newtonian fluid in cylinder ducts, *AIChE Journal*, **7**, 445-448, 1961.

Schowalter, W. R, The application of boundary layer theory to power-law pseudoplastic fluids: similar solutions, *AICHE Journal*, **6** (1), 24-28, 1960.

Settles, G. S., Miller, J. D., Hartranft, T. J., and Brandt, A. D., Visualization and collection of overspray from airless spray painting, *Proceedings of the 8th International Symposium on Flow Visualization*, Paper No. 138, Sept. 1-4, Sorrento, Italy, 1998.

Shankar, P. N. and Deshpande, M. D., Fluid mechanics in the driven cavity, *Annual Review Fluid Mechanics*, **32**, 93–136, 2000.

Simison, S., Pellicano, A., Brust, M., and Schiffrin, D. J., Detection of near-wall hydrodynamic effects by electrochemiluminescence, *Journal of Electroanalytical Chemistry*, **470,** 89–94, 1999.

Sisko, A. W., The flow of lubricating greases, *Industrial & Engineering Chemistry*, **50**, 1789-1792, 1958.

Smolka, L. B. and Belmonte, A., Charge screening effects on filament dynamics in

xanthan gum solutions, *Journal of Non-Newtonian Fluid Mech.*, **137**, 103–109, 2006.

Spelt, P. D. M., Selerland, T., Lawrence, C. J. and Lee, P. D., Flows of inelastic non-Newtonian fluids through arrays of aligned cylinders, Part 1: Creeping Flows, *Journal of Engineering Mathematics*, **51**, 57-80, 2005.

Steffe, J. F., Rheological methods in food process engineering, *2nd ed.*, Freeman Press, East Lansing, USA, 1996.

Stern, F., Muste, M., Berninati, L. M. and Eichinnger, W.E., Summary of experimental Uncertainty Assessment Methodology with Example, *IIHR Technical Report* no. **406**, The University of Iowa, Iowa City, I.A, 1999.

Stokes, J. R., Swirling flow of viscoelastic fluids, PhD Thesis, University of Melbourne, Australia, 1998.

Stone, H. L., Iterative solution of implicit approximations of multi-dimensional partial differential equations, SIAM *Journal on Numerical Analysis*, **5**, 530-558, 1968.

Sun Microsystems, Fortran 95 programming and user guides, 2005.

Tanner, R. I., Engineering rheology, Oxford University Press, 1985.

Tetervin, N., Laminar flow of a slightly viscous incompressible fluid that issues from a slit and passes over a flat plate, NACA TN, No. 1644, 1948.

Torrestiana, B., Galindo, E., and Brito, E., Diffusion of sucrose in xanthan gum solutions**,** *Bioprocess Engineering*, **4**, 265-273, 1989.

Tsuji, Y., Morikawa, Y., Nagatani, T., and Sakou, M., The stability of a two-dimensional wall jet, *The Aeronautical Quarterly*, **28**, 235-246, 1977.

Van Doormaal, J. P. and Raithby, G. D., Enhancements of the SIMPLE method for predicting incompressible fluid flows, *Numerical Heat Transfer*, **7**, 147-163, 1984.

Wang, C. and Sun, M., Separation control on a thick airfoil with multiple slots blowing at small speeds, *Acta Mechanics*, **143**, 215–227, 2000.

Weinstein, H. G., Stone, H. L., and Kwan, T. V., Iterative procedure for solution of systems of parabolic and elliptic equations in three dimensions, *Industrial & Engineering Chemistry Fundamentals*, **8** (2), 281-287, 1969.

Westerweel, J., Draad, A. A., Th. Van der Hoeven, J. G., and Oord van, J., Measurement of fully developed turbulent pipe flow with digital particle image velocimetry, *Experiment of Fluids*, **20**, 165–177, 1996.

Willert, C. E. and Gharib, M., Digital particle image velocimetry, *Experiment of Fluids*, **10**, 181-193, 1991.

Wu, J. and Thompson, M. C., Non-Newtonian shear-thinning flows past a flat plate, *Journal of Non-Newtonian Fluid Mechanics*, **66**, 127-144, 1996.

Yasuda, K., Armstrong, R. C., and Cohen, R. E., Shear flow properties of concentrated solutions of linear and star branched polystyrenes, *Rheologica Acta*, **20** (2), 163- 178, 1981.

Zirnsak, M. A. and Boger, D. V., Axisymmetric entry flow of semi-dilute xanthan gum solutions: prediction and experiment I, *Journal of Non-Newtonian Fluid Mechanics*, **79**, 105-136, 1998.

APPENDIX A

PARTICLE IMAGE VELOCIMETRY AND MEASUREMENT ERRORS

In this appendix, a detail description of the particle image velocimetry (PIV) system used in the present study is provided. In addition, a detailed analysis of measurement errors analysis and uncertainties is also provided.

A.1 Principles of Particle Image Velocimetry

Particle image velocimetry (PIV) is a non-intrusive optical measurement technique that provides simultaneous whole-field instantaneous velocity measurements. The PIV is well suited for estimating velocity gradients and derived quantities such as vorticity. Due to these attractive features, the PIV has been applied in many areas of fluid mechanics and aerodynamics research in the recent past. There are two types of PIV: the standard PIV (planar) and the stereo PIV. The standard PIV can measure only two velocity components whereas the stereo PIV can measure all the three velocity components. In this section, the basic principle of the standard PIV is outlined and its various components are described.

A.1.1 Planar PIV

As shown in Fig. A.1, a typical PIV system consists of a pulsed light source (laser) to illuminate the flow area of interest, a film or CCD camera to record the illuminated particles, a synchronizer to control the camera and laser, and a computer with suitable software to record, store and post-process the recorded images.

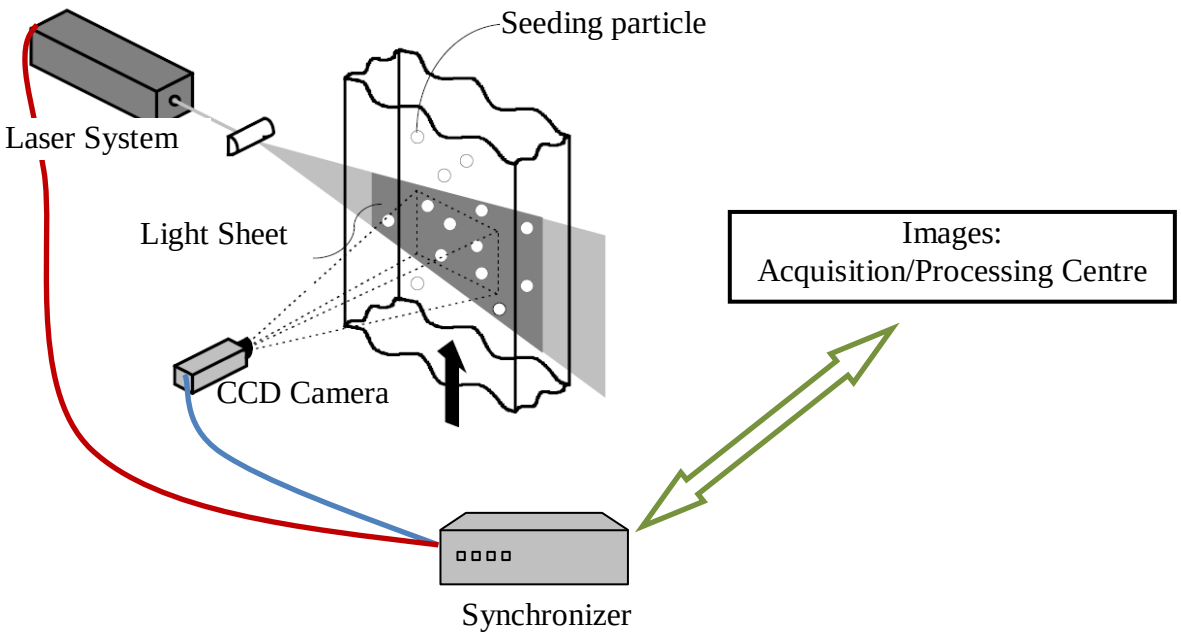

Figure A.1: A typical experimental set-up of PIV system

The principle of PIV involves a flow field seeded with small particles. These seeding particles which are assumed to faithfully follow the fluid motion are then illuminated by two pulses of laser sheet separated by a time delay, Δt. The light scattered by the seeding particles is recorded and two successive images are captured. The images are divided into a grid of small so-called interrogation areas. The principle of PIV also assumes that there is a uniform displacement within an interrogation area. A correlation algorithm is applied to statistically determine the displacement vector (Δs) of particles between the first and the second illuminations for each interrogation area. The velocity, V, for a particular interrogation area is obtained from the expression $V = \Delta s/\Delta t$. The correlation for each interrogation area over the two image frames captured is repeated to obtain the

velocity vector map over the whole target area. The description of the basic components of a PIV is presented in detail in the subsequent sections.

A.1.2 Light Source

For PIV measurements, a pulse laser is required to freeze the motion of the particles during image capturing. The fact that the whole-field is illuminated and the camera captures the side-wards scattered light by the particles makes a high power laser necessary. The commonly used lasers for PIV measurements are frequency doubled neodymium-yttrium-aluminum-garnet (Nd:YAG) lasers. This is because these lasers provide monochromatic light with high intensity illumination. Laser-emitted light is passed through a lens system to create a plane sheet of light.

A.1.3 Seeding Particles

As mentioned in prior sections, the main feature of the particles is to be able to follow the fluid faithfully without disturbing the flow. The particles should also be large enough to scatter sufficient light for them to be detected by the camera. The particles must also be good at scattering light to ensure that they are visible to the CCD sensor (Willert and Gharib, 1991). In addition, the seeding particles should be distributed homogeneously (Westerweel *et al*, 1996). Furthermore, the selection of the seeding particles should take into account the particle size and shape, the refractive index, and the wavelength of radiation. These factors affect the particles light scattering. A variety of seeding particles are commercially available ranging from few microns to hundreds of microns. Some of the widely used particles are polyamide seeding particles, silver-coated hollow glass spheres, hollow glass spheres, polystyrene latex and fluorescent polymer particles.

In PIV measurements, it is the velocity of the particle (but not the fluid velocity) that is measured. Therefore, it is essential that the particles have certain hydrodynamic properties to ensure that they faithfully follow the flow. It is always desirable that the particles have negligible settling velocity. The settling velocity can be estimated from Stokes drag law for flow around a sphere under gravity and is given by (Mei *et al*, 1991),

$$v_s = \frac{(\rho_p - \rho_f) g d_p^2}{18 \mu_f}, \tag{A.1}$$

where, ρ_p is the particle density, ρ_f is the working fluid density, g is the acceleration due to gravity, d_p is the diameter of the particle and μ_f is the viscosity of the fluid. Hence, the settling velocity can be minimized by using small particles and/or particles whose density is similar to that of the working fluid.

Another key parameter of PIV measurements is the response time. Response time is used to characterise the ability of a particle to follow the flow. It is a measure of the tendency of the particles to attain velocity equilibrium with the fluid. Assuming a Stokes' flow, the particle response time, t_r, is given by Raffel *et al*. (1998) as follows:

$$t_r = \rho_p \frac{d_p^2}{18 \mu_f}. \tag{A.2}$$

where all the variables have the same meaning as in Eqn. (A.1).

A.1.4 Recording Medium

The most commonly used recording device for PIV is the CCD camera. This camera has several advantages over the photographic film cameras. Some of these advantages are higher frame rates and possibility of on-line image analysis. However, photographic film

cameras provide higher resolution. An important component of a CCD camera is the CCD sensor. The CCD sensor consists of an array of detectors called pixels. The CCD camera employed in PIV studies generally uses high-performance progressive scan interline CCD chips. The chip consists of an array of photosensitive cells and an equal number of storage cells. The first image is acquired after triggering the first laser pulse which is immediately transferred from the photosensitive cells to the storage cells. Later, when the second laser pulse is triggered, the photosensitive cells are available to store the second image. In this case, the storage cells contain the first image and the photosensitive cells contain the second image. Then both images are transferred sequentially from the camera to the computer for storage. This allows the exposure interval Δt to be reduced to less than 1 microsecond.

A.1.5 Methods of Correlation in PIV

The two sequential digital images are sub-divided into smaller regions called interrogation areas. The images at the first and second frames are correlated to obtain an average displacement vector for each of the interrogation areas which would then produce a vector map of average displacements for all the interrogation areas. The most commonly used correlation methods are auto-correlation and cross-correlation.

For an auto-correlation method, the particles in an interrogation area are correlated with themselves. This produces correlation function with characteristic central peak (the self-correlation peak) and other two displacement peaks. The distance between the central peak and either of the displacement peaks corresponds to the average particle displacement in the interrogation area. One of the setbacks of this method is the presence

of the self-correlation peak which can lead to the particle displacements less than 2-3 pixels not being detected. This setback can reduce the dynamic range of the auto-correlation technique. Another major drawback is 180-degree directional ambiguity of the correlation method.

In cross-correlation, the particles in two different interrogation areas belonging to two different images at the first and second frames are correlated. The advantage of this method is that the order of the image recording is known and therefore directional ambiguity is no more an issue. With the cross-correlation method, two sequential images of the flow field with a specific time between them are considered as two spatial signals. The spatial shift may be represented by using a linear digital signal image process as shown in Fig. A.2. In Fig. A.2, the function f (m, n) describes the light intensity within the interrogation area at time, t whereas the intensity recorded at time Δt later is described by the function g (m, n). The function f (m, n) is considered as the input signal and g (m, n) is the output of the transfer function s (m, n) in the presence of noise function d (m, n). The capitalised functions, F (u, v) and G (u, v) shown in Fig. A.2 represent the Fourier transforms of the respective functions, and u, v are the coordinates of the spatial frequency domain. The major challenge of this method is the estimation of the spatial shift function s (m, n) on the basis of known functional values of f (m, n) and g (m, n) in the presence of noise function d (m, n). The spatial shift function s (m, n) is commonly determined by using the statistical technique of spatial cross-correlation. A detailed description of this technique and the computational implementation are given in Willert and Gharib (1991) and Raffel *et al* (1998).

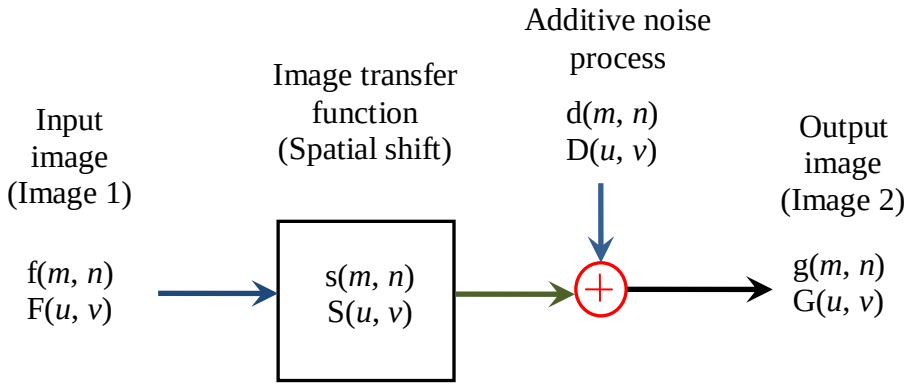

Figure A.2: Image displacement function

The adaptive-correlation algorithm is an advanced version of the cross-correlation method. This iterative method relies on knowledge of the actual velocity spatial distribution. This velocity spatial distribution which is unknown a *priori*, is also the objective of the measurement procedure itself. The adaptive-correlation involves an initial guessed offset value which is used to introduce an offset from the first window (the interrogation area in the image frame from the first laser pulse) to the second window. The result of each single interrogation is used as an input to evaluate the interrogation parameters for the subsequent iteration. The iteration is stopped by a convergence criterion. One of the attractive features of adaptive correlation is that the signal strength is raised due to the capture of in-plane dropout. In-plane dropout occurs because during the time between the two light pulses some of the particles leave the interrogation area and are lost. This loss of particles reduces signal strength and the number of successful vectors that can be obtained. In adaptive-correlation algorithm, there is also a possibility of interrogation area refinement because an adaptive window offset may be applied, again producing a successful signal.

A.1.6 Optimisation of PIV Measurements

It is imperative that a PIV system be optimised for high accuracy results. This is because a PIV system involves a combination of laser energy, camera magnification, and light sheet dimension which might affect the accuracy of results from a PIV system. Even under ideal experimental conditions, a PIV vector map may contain spurious vectors. These spurious vectors emanate from interrogation spots where signal-to-noise ratio is less than unity. That is, a noise peak is higher than the signal peak. Keane and Adrian (1990) investigated the detection probability (i.e., the percentage of valid vectors). To improve the signal-to-noise ratio, it was recommended that the interrogation areas be large enough to accommodate a sufficient number of particles, but small enough so that one vector describes the flow. Raffel *et al* (1998) point out that the selection of the particle size should be such that the particle image size is approximately two pixels when imaged by the digital camera. The particle image diameter, d_{image} , is given by:

$$d_{image} \approx [d_p^2 M^2 + (2.44(1+M)f_{\#})\lambda] \qquad \text{(A.3)}$$

where d_p is particle diameter, $f_{\#}$ is the *f*-number of the lens, λ is the wavelength of the laser light, and M is the magnification factor of the camera. Raffel *et al* (1998) suggested that when the image diameter becomes too small there is insufficient information to make effective use of sub pixel interpolation. This is because there is likelihood of biasing data towards integer pixel values. Sub pixel interpolation is used to increase the resolution or accuracy when detecting the position of the correlation peak which makes it possible to determine displacements with an accuracy of a fraction of a pixel.

The seeding density is dependent on the type of correlation method used. For the two-frame cross-correlation method, for example, Willert and Gharib (1991) showed that to obtain a high valid detection probability the number of particles should be at least 6 in an interrogation area. Using very high particle image densities, large particle image diameters, and small interrogation cell sizes will reduce the error due to gradients. The movement of the particles can only be tracked as long as they remain within the same interrogation area during both exposures. In addition, the particles should not traverse more than one-fourth of the side length of the interrogation areas between exposures to keep the number of particles that leave the interrogation area low.

The thickness of a laser sheet, Δ_z, is usually chosen to be smaller than the depth-of-field of the recording system, δ_z. Consequently, all particles illuminated by the light sheet produce in-focus images, reducing background noise in the image field (Adrian 1991). The depth-of-field of the lens is given by,

$$\delta_z = 4(1+M^{-1})^2 f_{\#}^2 \lambda \qquad \text{(A.4)}$$

It should be noted that for a given magnification, a large depth-of-field can only be obtained at the cost of increasing the $f_{\#}$ implying that a smaller fraction of the light scattered by the particles will reach the sensor.

A.2 Error Analysis in PIV

Measurement is the act of assigning a value to some physical variables. The relative closeness of agreement between an experimentally determined value of a quantity and its true value indicates the accuracy of the measurement. The difference between the experimentally determined value and the true value is the measurement error. Generally,

the true values of measured quantities are not known and therefore, estimation of the error must be made. This estimate is called an uncertainty. Coleman and Steele (1995) presented a detailed uncertainty assessment methodology. Stern *et al* (1999) provided comprehensive guidelines for the application of uncertainty assessment methodology into the test process and documentation of results. In general, the total error is composed of two components: a precision component and a bias component. Coleman and Steele (1995) defined the precision error as that due to the scatter of the data, whereas the bias error is the systematic error. Gui *et al* (2001a) quantified both bias and precision uncertainties in PIV measurements and their contributions to the total measurement uncertainty for a turbulent flow. Recently, Adeyinka and Naterer (2005) followed Gui *et al* (2001a) procedure to obtained similar analysis for laminar flows. According to previous studies such as Forliti *et al* (2000) a Gaussian peak-fitting algorithm is found to have the lowest bias and precision errors. They reported that the evaluation bias and gradient of the evaluation bias can both be minimised effectively by using Gaussian digital masks on the interrogation window, and this can in turn reduce measurement uncertainty. Therefore in the subsequent sections, details analysis of the errors inherent in the present PIV is given.

A.2.1 Measurement Error

The sources of error in PIV measurements include: bad selection of time between image pairs, sub-pixel displacement bias, insufficient sample size, effect of velocity gradients, and spatial resolution. Through careful selection of experimental conditions such as time between image pairs, certain errors can be minimised. Peak locking, which is an artifact

of sub-pixel particle displacement being biased toward integer values, is a major contributor to the bias error. A number of steps were taken during image acquisition and image processing to reduce peak locking in the present study. The particle image diameter, d_p was estimated to be 1.89-1.99 pixels, 1.91-2.01 pixels and 1.89-1.93 pixels for Newtonian fluid, XG005 and XG010 experiments, respectively. These values are close to the value of 2.0 pixels recommended by Raffel *et al* (1998) to minimise peak locking. The histograms (Fig. A.3) show no discernible peak locking effects which imply that the contribution to the bias error is minimal. The large sample size (700 for water and 750 for XG instantaneous images) also reduces the precision error.

The effect of velocity gradient on bias errors that occurs in flows with large velocity gradients is also a concern. The velocity gradients tend to broaden the displacement peak and reduce the amplitude. The error associated with the velocity gradient is typical of all boundary layer flows. Keane and Adrian (1992) suggested that for the cross-correlation technique, to achieve an acceptable valid detection probability of 95%, the acceptable gradients should follow the expression:

$$M u_z \Delta t < 0.03 \qquad \text{(A.5)}$$

where, M is the magnification factor, $u_z = 0.5\,(\partial u/\partial z)$, and Δt is the time between the two laser pulses. Sample values with corresponding inputs for various fluids are shown in Table A.1. From Table A.1 and other test locations (not shown), the condition expressed in the Eqn. (A.5) is easily satisfied.

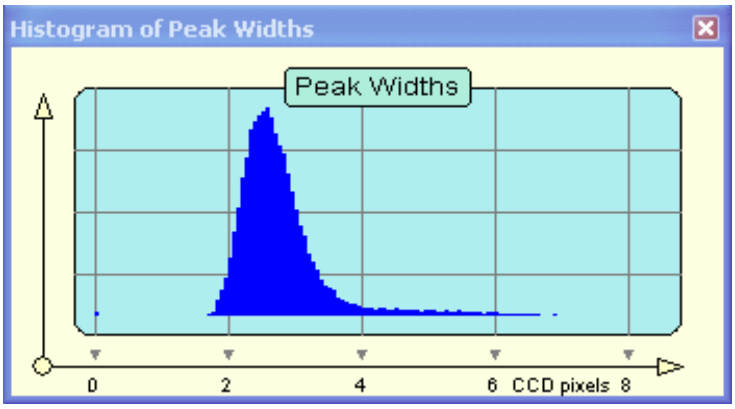

(a)

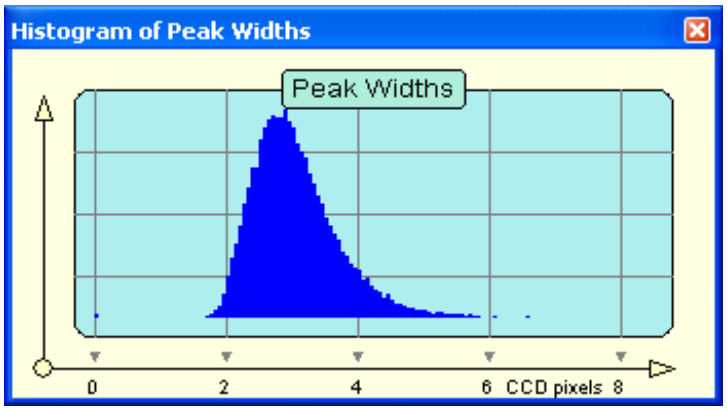

(b)

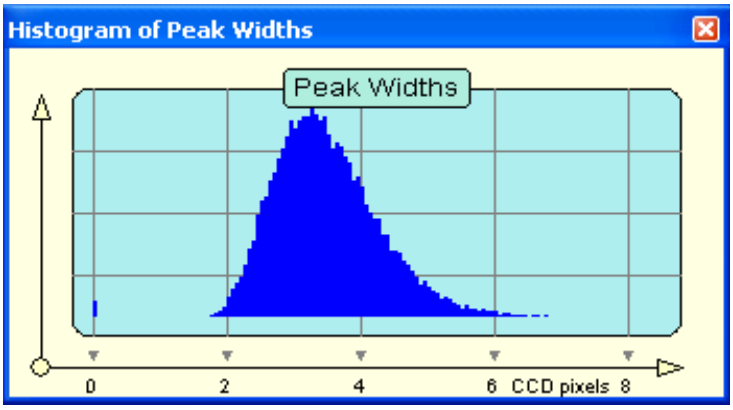

(c)

Figure A.3: Sample histogram of some measurement planes: (a) Newtonian fluid, (b) XG005 and (c) XG010.

Table A.1: Sample values from Eqn. A.5

	M	u_z (s^{-1})	Δt (s)	$M\, u_z \Delta t$
Newtonian fluid	1.620E-01	1.048	1.500E-03	2.550E-04
XG005	1.620E-01	0.963	8.900E-04	1.390E-04
XG010	1.620E-01	0.955	3.700E-04	5.730E-05

It is necessary to keep the interrogation area size as small as possible in order to capture the flow dynamics in the inner region especially for the present studies where the jet thickness is around 0.5 times the pipe diameter. This spatial resolution is critical in the calculation of the vorticity. On the other hand, the dynamic range of the measured velocity values increases with larger interrogation area sizes which implies that larger interrogation area sizes are desirable to achieving a larger velocity dynamic range. The above conflicting interests require a compromise between spatial resolution and velocity dynamic range. The dynamic range in a PIV measurement based on a pixel displacement level is the displacement divided by the sub-pixel accuracy. The sub-pixel accuracy is a function of many parameters, for which most are beyond the PIV system itself and therefore often unknown. As a rule-of-thumb 0.1 pixel accuracy is a realistic value (Scarano and Riethmuller, 1999). In the present measurements, it was ensured that particle displacement was less than one-quarter of the size of the interrogation area as recommended by many researchers (Willert and Gharib, 1991). For a typical PIV recording in the symmetry plane (*x*-*z* plane), the maximum displacement was 4 pixels so that the velocity dynamic range is of the order of 4/0.1 = 40. For the spanwise plane (*x*-*y*

plane), the corresponding maximum displacement was 8 pixels which gave the velocity dynamic range of the order of 8/0.1 = 80.

A.2.2 Error Estimation

The uncertainty analysis of the present measurement follows the American Institute of Aeronautics and Astronautics standard derived and explained by Coleman & Steele (1995). These uncertainties include particle response to fluid motion, light sheet positioning, light pulse timing, and the error arising from the peak-finding algorithm to determine the average particle displacement (Forliti *et al*, 2000). A complete uncertainty analysis of the PIV measurement involves identifying and quantifying both the bias and the precision errors in each part of the measurement chain. The total error or measurement uncertainty, $\varepsilon(\%)$ in a measured quantity is a percentage of the sum of the bias component (B) and precision component (P). In the following sections, details on how these errors were obtained for the present study are presented.

A.2.2.1 Biased error

The average fluid velocity, u for an interrogation area at any instant is reduced by Eqn. (A.6) (Gui *et al*, 2001a; Adeyinka and Naterer, 2005).

$$u = \frac{\Delta s L_o}{\Delta t L_i} \tag{A.6}$$

where Δt (s) is the time interval between laser pulses, Δs (pixel) is the particle displacement from the correlation algorithm, L_o (mm) is the width of the camera view in the object plane, and L_i (pixel) is the width of the digital image. The bias limit (B) of the

measured velocity is determined with a root-sum-square (RSS) of the elementary bias limit (B_χ), and they are related through the sensitivity coefficients, θ_χ which is given as:

$$B = \theta_{L_0}^2 B_{L_0}^2 + \theta_{L_I}^2 B_{L_I}^2 + \theta_{\Delta s}^2 B_{\Delta s}^2 + \theta_{\Delta t}^2 B_{\Delta t}^2, \quad \text{(A.7)}$$

where the sensitivity coefficients, θ_χ are defined as

$$\theta_\chi = \frac{\partial u}{\partial \chi}, \quad \chi = (L_0,\ L_I, \Delta t, \Delta s) \quad \text{(A.8)}$$

The classification of bias error, ε_b (= B / u) sources and contribution to the bias limits are provided in Tables A.2 and A.3, respectively for Newtonian fluid and xanthan gum based fluids. Also shown in the tables are the manufacturer's specifications of the elementary bias limits for Δt and Δs. The bias limit for L_0 is obtained from a calibration procedure.

Table A.2: Bias limits of the velocity for Newtonian fluid (water).

χ	**Magnitude**	B_χ	κ_χ	$B_\chi\kappa_\chi$	$B_\chi\kappa_\chi / \Sigma(B_\chi\kappa_\chi)$	$(B_\chi \kappa_\chi)^2$
***L*o (m)**	9.000E-02	5.000E-04	1.302E+00	6.510E-04	6.145E-01	4.239E-07
L_i (m)	2.048E+03	5.000E-01	-5.722E-05	2.861E-05	2.700E-02	8.185E-10
***t* (s)**	1.500E-03	1.000E-07	-7.813E+01	7.813E-06	7.374E-03	6.104E-11
***s* (pix)**	4.000E+00	1.270E-02	2.930E-02	3.721E-04	3.512E-01	1.384E-07
***θ* (m/s)**				1.060E-03		
$\Sigma\theta^2$						5.632E-07
B_u	7.505E-04					
***u* (m/s)**	1.025E-01					
ε_b (%)	0.732					

Table A.3: Bias limits of the velocity for non-Newtonian fluids (XG005 and XG010)

χ	**Magnitude**	B_χ	κ_χ	$B_\chi\kappa_\chi$	$B_\chi\kappa_\chi$ / $\Sigma(B_\chi\kappa_\chi)$	$(B_\chi\kappa_\chi)^2$
***L*o (m)**	9.000E-02	5.000E-04	5.279E+00	2.639E-03	6.009E-01	6.966E-06
L_i (m)	2.048E+03	5.000E-01	-2.320E-04	1.160E-04	2.641E-02	1.345E-08
***t* (s)**	3.700E-04	1.000E-07	-1.284E+03	1.284E-04	2.923E-02	1.649E-08
***s* (pix)**	4.000E+00	1.270E-02	1.188E-01	1.508E-03	3.434E-01	2.275E-06
***θ* (m/s)**				4.392E-03		
$\Sigma\theta^2$						9.271E-06
B_u	3.045E-03					
***u* (m/s)**	4.095E-01					
ε_b (%)	0.744					

A.2.2.2 Precision error

The precision limit, P of a measured velocity, *u* is given as:

$$P = \frac{2\sigma}{\sqrt{M}} \tag{A.9}$$

where 2 was taken as the confidence coefficient for a 95% confidence level for *M* sample readings (Figliola and Beasley, 2000), and σ is the standard deviation of the variable, *u* for sample of *M* readings. In the present study, *M* = *N* (Gui *et al*, 2001b) which is the same as the number of the instantaneous images. The standard deviation, σ is therefore defined as:

$$\sigma = \sqrt{\frac{1}{N-1}\sum_{n=1}^{N}(u_n - \bar{u})^2} \tag{A.10}$$

where $\bar{u}$ is the mean given by Eqn. (A.11).

$$\bar{u} = \frac{1}{N}\sum_{n=1}^{N} u_n \quad . \tag{A.11}$$

The corresponding precision limits contributions to the total uncertainty are given in Table A.5.

Table A.5: Precision errors

	$\bar{u}$(m/s)	N	σ(m/s)	P(m/s)	ε_p (%)
Water	1.025E-01	700	1.573E-02	1.189E-03	1.16
XG	1.00E-01	750	3.50E-02	2.556E-03	2.56

A.1.2.3 Total error

The total error or measurement uncertainty, ε(%) is obtained as follows:

$$\varepsilon = \varepsilon_p + \varepsilon_b \tag{A.12}$$

The standard deviation of the measured dataset was estimated in the near-wall region and at z_m. Since the requirement of maximum seeding particle displacement was met, it can be assumed that the sample standard deviation is not too different from those presented in Table A.5. On the basis of this assumption, the measurement uncertainties at 95% confidence level in velocities are estimated to be ± 1.9% and 3.2% of the local velocity, respectively for Newtonian (water) fluid and non-Newtonian (xanthan gum) fluids. Close to the plane wall, uncertainties in velocities are estimated to be ± 2.7% and ± 3.5, respectively for Newtonian (water) fluid and non-Newtonian (xanthan gum) fluids.

APPENDIX B

NUMERICAL TECHNIQUES

This appendix provides detail descriptions of the numerical techniques employed to compute the 3D laminar wall jet flow of both Newtonian and shear-thinning inelastic non-Newtonian fluids. More specifically, the mathematical models, boundary conditions, grid generation, discretisation methods, and numerical procedure are discussed.

B.1 Description of the Governing Equations

A schematic of the 3D wall jet flow domain used in the present computation is shown in Fig. 3.4. Figure 1.1 defines the Cartesian coordinate system adopted. The origin of the coordinate system coincides with the intersection of the pipe exit (x = 0), the bottom wall (z = 0) and channel mid-span or plane of symmetry (y = 0). It is assumed that the fluid flow is incompressible with negligible buoyancy and body forces. Both Newtonian and non-Newtonian are considered. The standard governing equations and the constitutive relation for the non-Newtonian fluid may be written in Cartesian form as:

Mass Conservation Equation:

$$\frac{\partial(\rho U)}{\partial x}+\frac{\partial(\rho V)}{\partial y}+\frac{\partial(\rho W)}{\partial z}=0 \qquad \text{(B.1)}$$

Momentum Conservation Equations:

$$\frac{\partial(\rho U)}{\partial t}+\frac{\partial(\rho UU)}{\partial x}+\frac{\partial(\rho VU)}{\partial y}+\frac{\partial(\rho WU)}{\partial z}=\frac{\partial}{\partial x}\left(\mu\frac{\partial U}{\partial x}\right)+\frac{\partial}{\partial y}\left(\mu\frac{\partial U}{\partial y}\right)+\frac{\partial}{\partial z}\left(\mu\frac{\partial U}{\partial z}\right)-\frac{\partial P}{\partial x} \qquad \text{(B.2)}$$

$$\frac{\partial(\rho V)}{\partial t}+\frac{\partial(\rho UV)}{\partial x}+\frac{\partial(\rho VV)}{\partial y}+\frac{\partial(\rho WV)}{\partial z}=\frac{\partial}{\partial x}\left(\mu\frac{\partial V}{\partial x}\right)+\frac{\partial}{\partial y}\left(\mu\frac{\partial V}{\partial y}\right)+\frac{\partial}{\partial z}\left(\mu\frac{\partial V}{\partial z}\right)-\frac{\partial P}{\partial y} \qquad \text{(B.3)}$$

$$\frac{\partial(\rho W)}{\partial t}+\frac{\partial(\rho UW)}{\partial x}+\frac{\partial(\rho VW)}{\partial y}+\frac{\partial(\rho WW)}{\partial z}=\frac{\partial}{\partial x}\left(\mu\frac{\partial W}{\partial x}\right)+\frac{\partial}{\partial y}\left(\mu\frac{\partial W}{\partial y}\right)+\frac{\partial}{\partial z}\left(\mu\frac{\partial W}{\partial z}\right)-\frac{\partial P}{\partial z} \tag{B.4}$$

Constitutive equation is given in Eqn. 2.2 (Carreau model):

$$\mu(\Lambda)=\mu_{\infty}+(\mu_0-\mu_{\infty})\left[1+(\theta\Lambda)^2\right]^{n-1/2} \tag{B.5}$$

where *U*, *V*, and *W* are velocities in *x*, *y*, and *z* directions, respectively, *P* is pressure, Λ is shear rate which is calculated from the second invariant of the shear rate tensor (Π_{2D}), and other variables have their usual meanings. The shear rate and second invariant of the shear rate tensor are related through:

$$\Lambda=[0.5\Pi_{2D}]^{1/2}$$

$$\therefore\ \Lambda=\left[2\left\{\left(\frac{\partial U}{\partial x}\right)^2+\left(\frac{\partial V}{\partial y}\right)^2+\left(\frac{\partial W}{\partial z}\right)^2\right\}+\left(\frac{\partial U}{\partial y}+\frac{\partial V}{\partial x}\right)^2+\left(\frac{\partial U}{\partial z}+\frac{\partial W}{\partial x}\right)^2+\left(\frac{\partial V}{\partial z}+\frac{\partial W}{\partial y}\right)^2\right]^{1/2} \tag{B.6}$$

Here, detail is only given for a Carreau constitutive relation since the shear rate expression is the same for all power-law based models. The coupled nonlinear partial differential equations (Eqns. B.1-B.5) will be integrated over a volume using a finite volume method (FVM). The colocated variable storage on an orthogonal grid is used.

B.2 Grid Generation

The governing differential equations are discretised by subdividing the computational domain into a set of control volumes called a grid. These sub-domains should conform to the computational domain boundaries. The grid can be structured or unstructured. In this work, a structured orthogonal grid is used. This consists of quadrilateral control volumes which can be expanded or contracted across the domain. The specific locations of all the coordinate points of the grid are controlled by an expansion factor.

A single block structured computational mesh representing the entire domain shown in Fig. 3.4 was created by assigning nodal distributions, N_x, N_y, and N_z in the *x*, *y*, and *z* directions, respectively. In general, the distribution of the nodes in respective directions is implemented geometrically with uniformly spaced control volumes being a special case. Figure B.1 shows a typical distribution and the nomenclature employed. The expression for a generic length, $L \in (143d, 35.5d, 43d)$ is given by Ormiston (2006) as:

$$L = \Delta l_1 \left[\frac{1-\beta^N}{1-\beta}\right] \tag{B.7}$$

where β ($\neq 1$) is the expansion ratio, and N is the number of spacings which is typically the same as number of nodes or control volumes. Equation (B.7) is based on the premise that N and β are known. In the present work, however, L, N, and Δl_1 are known whereas β is unknown. This is because the experimental domain was used for computations.

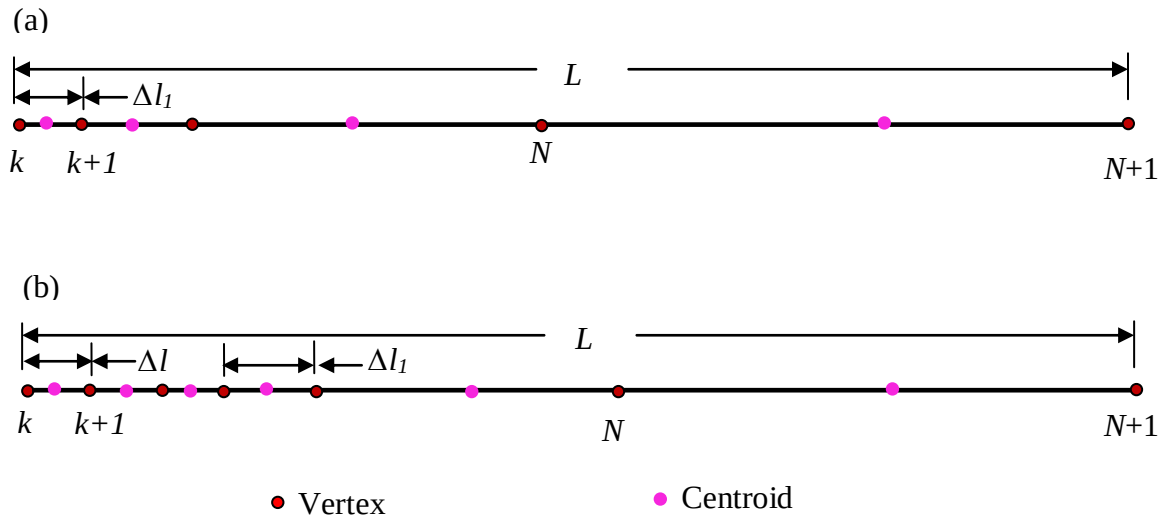

Figure B.1: Typical region nomenclature: (a) single node (b) multiple node distributions.

A uniform grid-points distribution was used near the wall up to the pipe boundary. This enabled the inlet velocity profile to fall exactly on the pipe boundary. In addition, Δl_1

which is a percentage of Δl (Fig. B.1b) was used as a first nodal point from the pipe boundary. This value allowed a smooth transition between the pipe boundary and the region after. The value of β was therefore obtained iteratively using Newton-Raphson root search. The update of β at iteration m+1 is given by Ormiston (2006) as:

$$\beta^{m+1} = \beta^{m} - \frac{\mathrm{F}(\beta^{m})}{\mathrm{F}'(\beta^{m})} \tag{B.8}$$

where

$$\mathrm{F}'(\beta^{m}) = N\beta^{N-1} - \frac{\mathrm{L}}{\Delta l_1} \qquad \text{and} \qquad \mathrm{F}(\beta^{m}) = \beta^{N-1} - \left(\frac{\mathrm{L}}{\Delta l_1}\right)(\beta - 1) - 1 \tag{B.9}$$

The generated values from Eqn. (B.7) are the vertices of the control volumes (CVs). The respective coordinate points are stored in one-dimensional array due to the simple shape of the flow geometry. For a colocated FVM, the centroid of the CVs are required, and therefore needed to be computed. Here, *X*, *Y*, and *Z* which corresponded to streamwise, spanwise, and transverse coordinates, respectively (Fig. 1.1), contained the values of the vertices whereas the centroid locations were stored in X_C, Y_C, and Z_C, respectively. The centroid coordinates were obtained by averaging the neighbouring vertices. A typical coordinate point and its centroid were given, for example, *X* and X_C, in Eqn. (B.10). The centroid points at the boundaries are assumed to be the same as the boundary vertices, that is, X_C (*N*+1) is the same as *X* (*N*).

$$X(k) = \Delta l_1 \left[\frac{1-\beta^{k-1}}{1-\beta}\right]_{k\epsilon(1,\ \ N+1)} \text{ and } X_C(k) = 0.5\,(X(k) + X(k+1)) \tag{B.10}$$

B.3 Numerical Modelling

B.3.1 Introduction

The discretisation of the governing equations and the constitutive relation mentioned in

Section B.1 is discussed here. The treatment of the various boundary conditions is also presented.

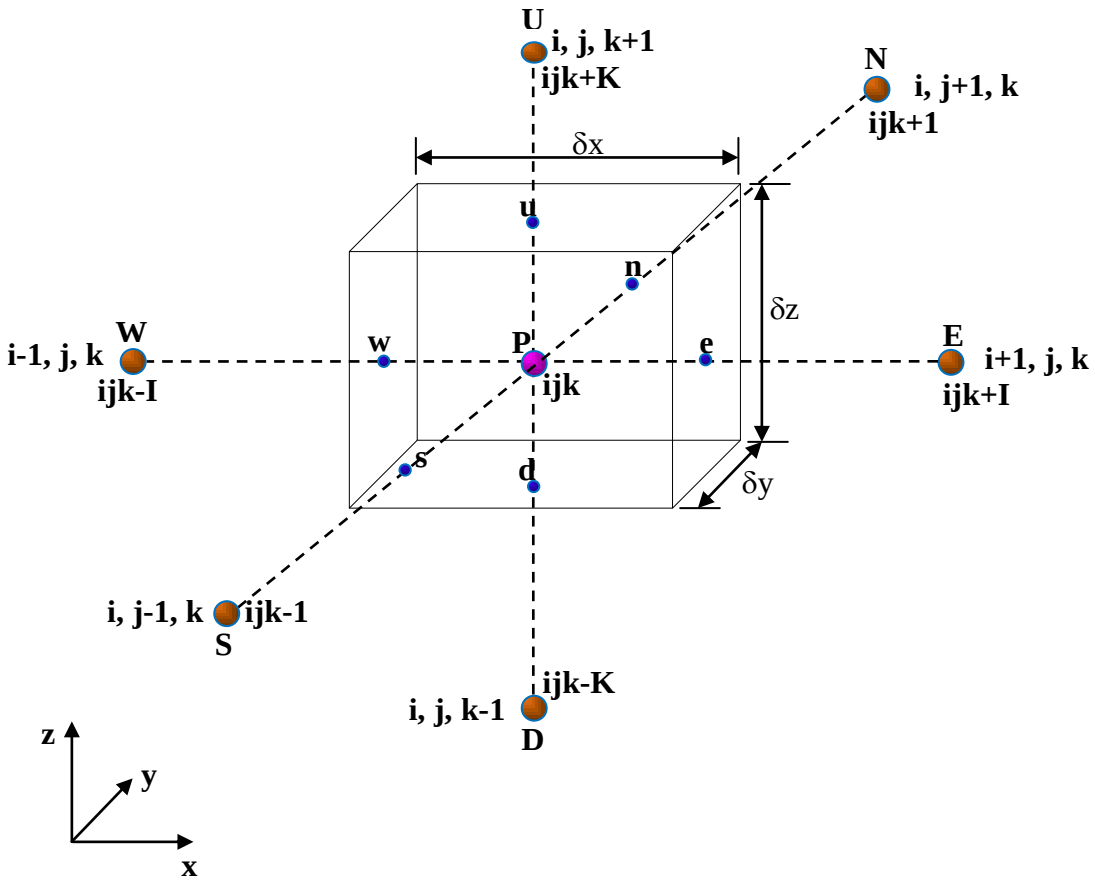

Figure B.2: Schematic of a typical control with notations

A typical control volume (CV) over which the governing equations are integrated is shown in Fig. B.2 above. One of the attractive features of colocated grid arrangement is that the same CV is used for all the variables *U*, *V*, *W*, *P*, and μ. The discretised values of the nodal velocities (*U*, *V*, *W*), pressure (*P*) and apparent viscosity (μ) are located in the centre of the CV. Using seven stencils computational molecule, the central CV is represented by its node, P, where the fluid and flow quantities are stored. The six neighbouring nodes are denoted by compass notation: W, E, S, N, D, and U for west,

east, south, north, down, and up cells, respectively. The faces of the control volume, P adjacent to a given neighbour cell W, E, S, N, D, and U are denoted by w, e, s, n, d, and u, respectively (Fig. B.2). The cell areas of the CV and indices in Fig. B.2 are:

$A_e = \delta y \delta z$; $A_n = \delta x \delta z$; $A_u = \delta y \delta x$

ijk = i, j, k; $I = N_x + 2$; $J = N_y + 2$; $K = N_z + 2$; ije = I × J

B.3.2 Algebraic Equation of the Governing Equations

The practical impossibility of analytically solving the governing equations requires a numerical solution which needs to transform them into algebraic equations. The algebraic equations require approximations to evaluate integrals and perform interpolations of the governing equations over the CV. The mass conservation and general form of momentum equations for a dependent variable, Φ which is *U*, *V*, or *W* in the integral form reads:

$$\underbrace{\int_{\forall} \frac{\partial}{\partial x}(\rho U)d\forall}_{I} + \underbrace{\int_{\forall} \frac{\partial}{\partial y}(\rho V)d\forall}_{II} + \underbrace{\int_{\forall} \frac{\partial}{\partial z}(\rho W)d\forall}_{III} = 0 \tag{B.11}$$

$$\underbrace{\frac{\partial}{\partial t}\int_{\forall}(\rho\Phi)d\forall}_{I} + \underbrace{\int_{\forall} \frac{\partial}{\partial x}(\rho U\Phi)d\forall}_{II} + \underbrace{\int_{\forall} \frac{\partial}{\partial y}(\rho V\Phi)d\forall}_{III} + \underbrace{\int_{\forall} \frac{\partial}{\partial z}(\rho W\Phi)d\forall}_{VI} = \underbrace{\int_{\forall} \frac{\partial}{\partial x}\left(\mu \frac{\partial \Phi}{\partial x}\right)d\forall}_{V}$$
$$+ \underbrace{\int_{\forall} \frac{\partial}{\partial y}\left(\mu \frac{\partial \Phi}{\partial y}\right)d\forall}_{VI} + \underbrace{\int_{\forall} \frac{\partial}{\partial z}\left(\mu \frac{\partial \Phi}{\partial z}\right)d\forall}_{VII} + \underbrace{\int_{\forall} S_{\Phi} d\forall}_{VIII} \tag{B.12}$$

where S_Φ is the source term which is pressure gradient in the present case.

Integrating Eqn. (B.11) over the CV shown in Fig. B.2, the first term (*I*) in the *x*-direction mass flow becomes

$$\int_{\forall} \frac{\partial}{\partial x}(\rho U)d\forall = A_e \rho U_e - A_w \rho U_w \tag{B.13}$$

Similarly, the mass flows in both *y*- and *z*- directions are given as:

$$\int_{\forall} \frac{\partial}{\partial y}(\rho V) d\forall = A_n \rho V_n - A_s \rho V_s \tag{B.14}$$

$$\int_{\forall} \frac{\partial}{\partial z}(\rho W) d\forall = A_u \rho W_u - A_d \rho W_d \tag{B.15}$$

Combining Eqns. (B.13-15) gives the following algebraic equation:

$$\dot{m}_e + \dot{m}_n + \dot{m}_u - \dot{m}_w - \dot{m}_s - \dot{m}_d = 0 \tag{B.16}$$

where:

$$\dot{m}_e = A_e \rho U_e ; \quad \dot{m}_w = A_w \rho U_w ; \quad \dot{m}_n = A_n \rho V_n \qquad \dot{m}_n = A_n \rho V_n \qquad \dot{m}_u = A_u \rho W_u ; \quad \dot{m}_d = A_d \rho W_d$$

The generic momentum conservation equation (B.12) was grouped into unsteady (*I*), convective (*II, III, IV*), diffusion (*V, VI, VII*) and source or sink (*VIII*) terms. The details will only be given in the CV face "e".

Convective flux (*II, III, IV*):

$$F_e = \int_{\forall} \frac{\partial}{\partial x}(\rho U \Phi) d\forall \Big|_e = \dot{m}_e \Phi_e \tag{B.17}$$

The value of Φ_e at the cell face centre, which represents the mean value over the whole face is expressed through the neighbouring nodal values Φ_P and Φ_E. The deferred correction approach proposed by Khosla and Rubin (1974) which is described in detail in Ferziger and Peric (2002) is implemented by blending the central difference scheme (CDS) and upwind differencing scheme (UDS) to obtain the value of F_e. The main advantages of deferred correction are stability, simplicity, and computer-memory saving. Deferred correction approach tends to promote numerical stability as it ensures that the coefficient matrix from CDS algebraic equation systems is diagonal dominant (Ferziger and Perić, 2002). Therefore, Eqn. (B.17) becomes:

$$F_e = F_e^{UDS} + \beta(F_e^{CDS} - F_e^{UDS})^{old} \tag{B.18}$$

where $F_e^{UDS} = \dot{m}_e \Phi_e^{UDS}$, $F_e^{CDS} = \dot{m}_e \Phi_e^{CDS}$, $\dot{m}_e \Phi_e^{UDS} = \|\dot{m}_e, 0\| \Phi_P - \|-\dot{m}_e, 0\| \Phi_E$, and blending factor, $\beta \in (0, 1)$. $\|\cdot\,\cdot\|$ denotes the maximum of the two values. The "old" term is evaluated from the previous iteration. At convergence the UDS contributions will cancel out leaving the CDS solution. Another attractive feature of this procedure was that it usually converges at an approximate rate as a pure upwind approximation. The use of the blending factor can also remove oscillations associated with CDS on the coarse grids. To take advantage of this blending factor without a compromise of accuracy, it was used locally where the grids were considered coarse. The general interpolation equation used in the present work is given in Eqn. (B.19) for "e".

$$\Phi_e = r_e \Phi_E + (1 - r_e)\Phi_P; \; r_e = (x_e - x_P)/(x_E - x_P) \tag{B.19}$$

Therefore, the CDS value at "e" is:

$$\Phi_e^{CDS} = r_e \Phi_E + (1 - r_e)\Phi_P; \; r_e = (x_e - x_P)/(x_E - x_P)$$

Diffusive flux (*V, VI, VII*):

$$D_e = \int_{\forall} \frac{\partial}{\partial x}\left(\mu \frac{\partial \Phi}{\partial x}\right) d\forall \Big|_e = \int_A \frac{\partial}{\partial x}\left(\mu \frac{\partial \Phi}{\partial x}\right) dx dA \Big|_e = \mu_e A_e \left.\frac{\partial \Phi}{\partial x}\right|_e \tag{B.20}$$

$$\left.\frac{\partial \Phi}{\partial x}\right|_e \approx \frac{\Phi_E - \Phi_P}{(\delta x)_{PE}}$$

$$D_e = \frac{\mu_e A_e}{(\delta x)_{PE}} (\Phi_E - \Phi_P) \tag{B.21}$$

Source term (*VIII*):

$$S_P^{\Phi} = \int_{\forall} S_{\Phi} d\forall \approx S_{\Phi} \forall_P \tag{B.22}$$

For momentum equation, Eqn. (B.22) which represents the pressure gradient becomes:

$$S_P^e = \int_{\forall} -\frac{\partial P}{\partial x} dx dA \approx -P_e A_e \tag{B.23}$$

Similarly, the corresponding expressions for other five faces (w, n, s, u, and d) of the CV are:

$$F_w = F_w^{UDS} + \beta(F_w^{CDS} - F_w^{UDS})^{old} \quad D_w = \frac{\mu_w A_w}{(\delta x)_{WP}}(\Phi_P - \Phi_W) \text{ and } S_P^w \approx P_w A_w \tag{B.24}$$

$$F_n = F_n^{UDS} + \beta(F_n^{CDS} - F_n^{UDS})^{old} \quad D_n = \frac{\mu_n A_n}{(\delta y)_{PN}}(\Phi_N - \Phi_P) \text{ and } S_P^n \approx -P_n A_n \tag{B.25}$$

$$F_s = F_s^{UDS} + \beta(F_s^{CDS} - F_s^{UDS})^{old} \quad D_s = \frac{\mu_s A_s}{(\delta y)_{SP}}(\Phi_P - \Phi_S) \text{ and } S_P^s \approx P_s A_s \tag{B.26}$$

$$F_u = F_u^{UDS} + \beta(F_u^{CDS} - F_u^{UDS})^{old} \quad D_u = \frac{\mu_u A_u}{(\delta z)_{PU}}(\Phi_U - \Phi_P) \text{ and } S_P^u \approx -P_u A_u \tag{B.27}$$

$$F_d = F_d^{UDS} + \beta(F_d^{CDS} - F_d^{UDS})^{old} \quad D_d = \frac{\mu_d A_d}{(\delta z)_{DP}}(\Phi_P - \Phi_D) \text{ and } S_P^d \approx P_d A_d \tag{B.28}$$

Unsteady or inertia term (*I*):

$$F_t^{\Phi,3t} = \rho \int_{\forall} \frac{\partial \Phi}{\partial t} d\forall \approx \rho \forall_p \left[\frac{3\Phi_P - 4\Phi_P^{\circ} + \Phi_P^{\circ\circ}}{2\delta t} \right] \tag{B.29a}$$

$$F_t^{\Phi,1t} = \rho \int_{\forall} \frac{\partial \Phi}{\partial t} d\forall \approx \rho \forall_p \left[\frac{\Phi_P - \Phi_P^{\circ}}{\delta t} \right] \tag{B.29b}$$

where in Eqns. B.29(a, b) both three time level and implicit Euler methods are used respectively. Φ_P° and $\Phi_P^{\circ\circ}$ are Φ at cell P at the first and second previous time level, respectively, whereas δt is the time step and all other variables have their usual meaning. The present methods are fully implicit, that is, all variables without a time level superscript are assumed to pertain to the new time-level. In addition, it is easily noticed that, the backward difference scheme, implicit Euler method (Eqn. B.29b) is a first order.

Meanwhile, the quadratic backward approximation in time (three time level, Eqn. B.29a) is second order accurate. Using deferred correction approach for these two methods, the unsteady term becomes:

$$F_t^{\Phi} = F_t^{\Phi,1t} + \beta_t (F_t^{\Phi,3t} - F_t^{\Phi,1t}) \tag{B.30}$$

Substituting Eqns. B.29 (a, b) in B.30 and after a little algebra becomes:

$$F_t^{\Phi} = \frac{\rho \forall_p}{\delta t}\left[1 + 0.5\beta_t\right]\Phi_P - \frac{\rho \forall_p}{\delta t}\left[(1+\beta_t)\Phi_P^{\circ} - 0.5\beta_t \Phi_P^{\circ\circ}\right] \tag{B.31}$$

In Eqn. (B.31), a blending factor has been implemented with a value of "1" corresponding to three time level method and "0" means Euler implicit method. The three time level was easier to implement than other second order schemes such as Crank-Nicolson. It is also less prone to producing oscillatory solutions on the premises that δt is small. It can easily be inferred from Eqn. (B.31) that, the coefficient of first previous time level is always positive whereas the second previous level is always negative. This means that with large time steps the scheme may produce oscillatory solutions. Another problem with this scheme is its unconditional stability. Ferziger and Peric (2002) recommended that blending a small amount of Euler implicit will help prevent the oscillatory nature of the solution despite its first order. Since one is after a steady state solution, this Euler implicit scheme will ensure stability and allow the use of large time steps. The contribution of the "old" time levels were added to the source term.

Combining Eqns. (B.18, B.20, B.23-28, and B.31), the general algebraic equation is then given as:

$$C_P^* \Phi_P = C_W \Phi_W + C_E \Phi_E + C_S \Phi_S + C_N \Phi_N + C_D \Phi_D + C_U \Phi_U + b_P^{\Phi} \tag{B.32}$$

where

$$C_E = \|-\dot{m}_e, 0\| + \frac{\mu_e A_e}{(\delta x)_{PE}} \qquad C_W = \|\dot{m}_w, 0\| + \frac{\mu_w A_w}{(\delta x)_{WP}}$$

$$C_N = \|-\dot{m}_n, 0\| + \frac{\mu_n A_n}{(\delta y)_{PN}} \qquad C_S = \|\dot{m}_s, 0\| + \frac{\mu_s A_s}{(\delta y)_{SP}}$$

$$C_U = \|-\dot{m}_u, 0\| + \frac{\mu_u A_u}{(\delta z)_{PU}} \qquad C_D = \|\dot{m}_d, 0\| + \frac{\mu_d A_d}{(\delta z)_{DP}}$$

$$C_P^* = \sum C_f = C_W + C_E + C_S + C_N + C_D + C_U + \frac{\rho \forall_p}{\delta t}\left[1 + 0.5\beta_t\right] \qquad b_P^{\Phi} = S_P^{\Phi} + F_{nk}^{old}$$

The value of F_{nk}^{old} is the explicit part of the convective terms as a result of deferred-correction approach. It should be noted also that the CV centred around node P has $\dot{m}_w$ equals to $-\dot{m}_e$ for CV centred around node W. Similar relationship holds for $\dot{m}_s$ and $\dot{m}_n$, and $\dot{m}_d$ and $\dot{m}_u$. Usually, an under-relaxation parameter, κ is incorporated into Eqn. (B.32) to account for the nonlinear nature of the equation systems and stability of the solver (Patankar, 1980). While this is a requirement for large time step or steady solution, for the unsteady or smaller time step, it is not necessary (Ferziger and Perić, 2002). The under-relaxation parameter can be different or the same for each momentum equation. The algebraic equation for each momentum equation can therefore be written as:

$$C_P^U U_P = C_W U_W + C_E U_E + C_S U_S + C_N U_N + C_D U_D + C_U U_U + b_P^U \tag{B.33}$$

$$C_P^V V_P = C_W V_W + C_E V_E + C_S V_S + C_N V_N + C_D V_D + C_U V_U + b_P^V \tag{B.34}$$

$$C_P^W W_P = C_W W_W + C_E W_E + C_S W_S + C_N W_N + C_D W_D + C_U W_U + b_P^W \tag{B.35}$$

where

$$C_P^U = C_P^* / \kappa_U \qquad C_P^V = C_P^* / \kappa_V \qquad C_P^W = C_P^* / \kappa_W$$

$$b_P^U = \beta\left[\sum(\dot{m}U)_{nk}^{CDS} - \sum(\dot{m}U)_{nk}^{UDS}\right]^{old} - (P_e A_e - P_w A_w) + \frac{\rho\forall_p}{\delta t}\left[(1+\beta_t)U_P^{\circ} - 0.5\beta_t U_P^{\circ\circ}\right] + (1-\kappa_U)C_P^U U_P^{old}$$

$$b_P^V = \beta\left[\sum(\dot{m}V)_{nk}^{CDS} - \sum(\dot{m}V)_{nk}^{UDS}\right]^{old} - (P_n A_n - P_s A_s) + \frac{\rho\forall_p}{\delta t}\left[(1+\beta_t)V_P^{\circ} - 0.5\beta_t V_P^{\circ\circ}\right] + (1-\kappa_V)C_P^V V_P^{old}$$

$$b_P^W = \beta\left[\sum(\dot{m}W)_{nk}^{CDS} - \sum(\dot{m}W)_{nk}^{UDS}\right]^{old} - (P_u A_u - P_d A_d) + \frac{\rho\forall_p}{\delta t}\left[(1+\beta_t)W_P^{\circ} - 0.5\beta_t W_P^{\circ\circ}\right] + (1-\kappa_W)C_P^W W_P^{old}$$

The central difference scheme is used to evaluate the terms in constitutive relation (Eqn. B.6) at the centroid of the neighbouring nodes of node P in respective direction and they are given as:

$$\frac{\partial\Phi}{\partial x} \approx \frac{\Phi_E - \Phi_W}{(\delta x)_{WE}} \qquad \frac{\partial\Phi}{\partial y} \approx \frac{\Phi_N - \Phi_S}{(\delta y)_{NS}} \qquad \frac{\partial\Phi}{\partial z} \approx \frac{\Phi_U - \Phi_D}{(\delta z)_{UD}} \tag{B.36}$$

The variables used to evaluate the viscosity are “old”, i.e. the values from the last iteration. This means that the apparent viscosity is evaluated explicitly. This procedure has also been implemented in previous studies such as Spelt *et al* (2005). The face value of the viscosity was obtained using CDS similar to that used for the convective terms in Eqn. (B.19). Both power-law (Eqn. 2.1) and Carreau (Eqn. 2.3) models were implemented. The unbounded nature of the power-law model was accounted for by setting both “small” and “large” limits of the apparent viscosity to avoid any singularity in the solver. The Newtonian fluid is a special case of the power-law based fluid. The viscosity is the same over the domain and specific CV.

4.3.3 Boundary Conditions

In general, boundary conditions are prescribed for velocity, pressure, stresses (apparent

viscosity), or any dependent variables in the governing equations. In this study, two types of boundary conditions were implemented. The first was the Dirichlet condition, where the value of a variable is specified at the boundary; and the second was the Neumann condition, where the value of a variable gradient was specified at the boundary. The implementation of these boundary conditions to the discretised equations (Eqns. B.33– B.35) will be discussed in details in this section.

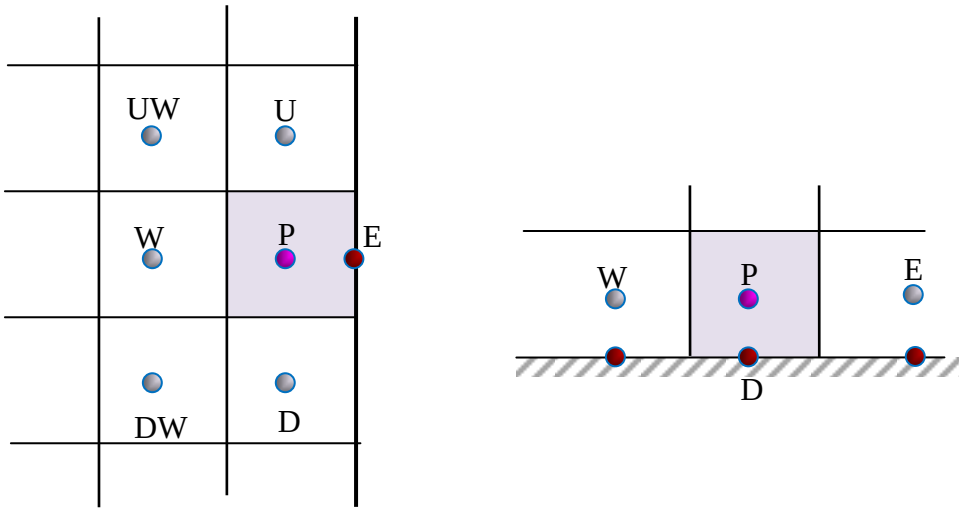

(a) East: i = ie+1 (b) Down-Wall: k = 1

Figure B.3: East and wall (Down) boundaries computational molecule

Figure B.3 above shows a typical boundary of the computational domain which has the "east" plane as an illustration. For the Dirichlet condition, discrete values of the variable, Φ were specified at the boundary. Both the face and nodal values at the boundaries were considered to be the same since the half-width control volume is used. For example, specifying the values of U at the east plane (U_E), the coefficient C_E was evaluated at the boundary (see Fig. B.3), and $C_E U_E$ was added to the source term whereas C_E is set to zero. However, if the pressure value was specified, the velocity normal to the plane (see Fig. B.3), U_E was obtained by mass balanced for each cell (Eqn. B.37) and they were

corrected. It is important to note that at a boundary, either velocity or pressure is specified but not both variables. In general, if the pressure is not prescribed, the boundary values of the pressure are obtained by extrapolation from the nearest two interior nodes. The expression used, for example, for the east plane is given in Eqn. (B.38).

$$U_{ie+1} = \frac{\sum_f \dot{m}_f}{A_{ie+1}} \; ; f = \text{w, n, s, u, d} \tag{B.37}$$

$$p_{ijk} = p_{ijk-J} + (p_{ijk-J} - p_{ijk-2J}) \times (1 - r_{ie-1}) \tag{B.38}$$

The Neumann boundary condition usually requires the specification of the normal velocity gradient for a fluid flow problem. In the east plane (Fig.B.3), for example, the Neumann boundary condition is given as:

$$\frac{dU}{dx} = \Omega_b^{sp} \tag{B.39}$$

If $\Omega_b^{sp} = 0$ the above expression using first-order approximation becomes

$$U_E^{ie+1} = U_P \tag{B.40}$$

Equation B.40 was implemented by adding the coefficient C_E to C_P and setting the C_E values at the east plane to zero. These expressions hold for the other five planes, however, the respective coefficient and direction were used.

Normally, at the wall the no-slip boundary condition is applied. However, this condition indicates that only the normal viscous stress is zero at the wall (but the shear stress is nonzero). For FVM, Ferziger and Peric (2002) recommends the implementation of these shear stresses in addition to the no-slip condition. From Fig. B.3, as an example, using

one-sided approximation for $\partial U/\partial z$, the nonzero viscous term becomes:

$$D^U = \int_{S_d} \mu \frac{\partial U}{\partial z} dA = \frac{\mu_d A_d}{(\delta z)_{PD}} (U_P - U_D) = \Im (U_P - U_D) \tag{B.41}$$

Similarly, the *V* component becomes:

$$D^V = \int_{S_d} \mu \frac{\partial V}{\partial z} dA = \Im (V_P - V_D) \tag{B.42}$$

These viscous forces D^U and D^V are accounted for in the algebraic equation by adding $\Im$ to both C_P and source terms as follows:

$$C_P^U = C_P^U + \Im \qquad b_P^U = b_P^U + \Im$$

$$C_P^V = C_P^V + \Im \qquad b_P^V = b_P^V + \Im \tag{B.43}$$

Similar expressions were obtained for all the wall boundary conditions. To account for entrainment, tangential velocity gradient (free slip) boundary condition is usually imposed on either of the north or top boundary plane (Fig. 3.4). For a free slip boundary condition, the boundary tangential velocity components are calculated by extrapolation from interior cells. This is equivalent to $d(u, v)/dz = 0$. Here, the first-order extrapolation similar to that used for pressures is used (Eqn. B.38).

Another boundary type that will be used in this work is symmetry plane. Unlike the wall condition (Fig. B.3b) where the normal stress is zero, for symmetry condition the shear stress is zero ($\partial U/\partial z$ and $\partial V/\partial z$). The symmetry version of Eqns. (B.41-B.43) is given in Equation B.44.

$$D^W = \int_{S_d} \mu \frac{\partial W}{\partial z} dA = \frac{\mu_d A_d}{(\delta z)_{PD}} (W_P - W_D) = \Im (W_P - W_D) \tag{B.44}$$

$$C_P^W = C_P^W + \Im$$

The velocity components at symmetry boundary were taken as the immediate interior nodal value.

For the non-Newtonian fluids, the apparent viscosity values at boundaries are not known. Following a similar procedure used by Oliveira *et al* (1998), basically three approaches were attempted. The first attempt was to obtain the boundary value using linear extrapolation, similar to that for the pressure (Eqn. B.38). This proved to be highly unstable. The second approach was to implement velocity boundary values into the constitutive model (Eqns. B.5-B.6). This allowed the boundary viscosity to change depending on the nonzero local velocity gradients. The last attempt was to use first-order approximation (Eqns. B.40) for the apparent viscosity, $\partial\mu / \partial x_i = 0$, $x_i \in (x, y, z)$. That is, the boundary value was set to the nearest cell centre value. None of these last two attempts did have stability problem. The insignificant difference between results did not warrant the considerable computational time used by the second approach. Therefore, in the present work the apparent viscosity values at boundaries were obtained by the first-order approximation ($\partial\mu / \partial x_i = 0$) using Eqn. (B.40).

B.4 Numerical Solution Procedure

This section describes the solution procedure for the linearised algebraic equations. The coupling of the pressure and velocity fields is presented in detail. The solver used to obtain the solution of the algebraic equation is also described.

B.4.1 Pressure-Velocity Coupling

The governing momentum equations (B.1-B.3) have contribution from the pressure gradient. However, there is no independent equation for the pressure field. Mostly, a

pressure field is constructed such that the continuity equation is satisfied. The most commonly used methods for the pressure-velocity coupling algorithms are the semi-implicit method for pressure-linked equation (SIMPLE) by Patankar and Spalding (1972) and semi-implicit method for pressure-linked equations consistent (SIMPLEC) by Van Doormal and Raithby (1984). Unlike SIMPLE which is often used on a staggered grid, SIMPLEC is more robust and efficient. The basic principle of these algorithms is that the momentum conservation is used to solve for guessed velocities and then in order to conserve mass, a pressure-correction equation which is based on continuity is used to correct the velocities. In view of the advantages of SIMPLEC algorithm, it was adopted in the present work to solve pressure-velocity coupling equation.

As indicated in the previous paragraph, the solutions to the momentum equations did not necessarily produce a mass-conserving velocity fields since the *x*-, *y*- and *z*-momentum equations do not enforce continuity. There is therefore the need to correct the velocity solution by using continuity equation. The "new" solution of *U*, *V* and *W* that conserved mass is given as:

$$U = U^* + U^c \qquad V = V^* + V^c \qquad W = W^* + W^c \tag{B.45}$$

where the "*" values are the guessed solution of the momentum equations and "c" values indicate the correction values added to obtained a mass-conserving field. It is worth noting that these guessed values were obtained by initially guessed pressure field. Now, focusing on *U* velocity field as an illustration, the correction value becomes:

$$U^c = U - U^* \tag{B.46}$$

Equation B.33 for control volume (CV) P which is the final solution field can be recast into the following form:

$$U_P = \frac{\sum_P C_{nk} U_{nk} + b_P}{C_P^U} - \frac{\forall_P}{C_P^U} \left. \frac{\partial P}{\partial x} \right|_P \tag{B.47}$$

The source term, b_P in Eqn. (B.47) does not include the pressure gradient. The analogy equation for the guessed solution field is given as:

$$U_P^* = \frac{\sum_P C_{nk} U_{nk}^* + b_P}{C_P^U} - \frac{\forall_P}{C_P^U} \left. \frac{\partial P^*}{\partial x} \right|_P \tag{B.48}$$

Substituting Eqns. (B.47 and B.48) into Eqn. (B.46), the correction velocity becomes:

$$U_P^c = \frac{\sum_P C_{nk} U_{nk}^c}{C_P^U} - \frac{\forall_P}{C_P^U} \left. \frac{\partial P^c}{\partial x} \right|_P \tag{B.49}$$

where P^c is the corrected pressure value. Similarly, the corrected velocities at the CV faces are obtained using Eqn. (B.49), and for the east-face 'e', it becomes:

$$U_e^c = \frac{\sum_e C_{nk} U_{nk}^c}{C_{Pe}^U} - \frac{\forall_e}{C_{Pe}^U} \left. \frac{\partial P^c}{\partial x} \right|_e \tag{B.50}$$

Rearranging Eqn. (B.49) by multiplying through by C_P^U and subtracting $\sum_P C_{nk} U_P^c$ from both sides gives:

$$\left(C_P^U - \sum_P C_{nk} \right) U_P^c = \sum_P C_{nk} (U_{nk}^c - U_P^c) - \forall_P \left. \frac{\partial P^c}{\partial x} \right|_P \tag{B.51}$$

The SIMPLEC is based on the premise that the first term on the right-hand side of Eqn. (B.51) is to be neglected so that

$$U_P^c = - \frac{\forall_P}{C_P^U - \sum_P C_{nk}} \left. \frac{\partial P^c}{\partial x} \right|_P \tag{B.52}$$

The corresponding east-face of CV is given as:

$$U_e^c = -\frac{\forall_e}{C_{Pe}^U - \sum_e C_{nk}} \left.\frac{\partial P^c}{\partial x}\right|_e \tag{B.53}$$

The volume centred around a cell face is defined as:

$$\forall_e = (x_E - x_P)A_e = (\delta x)_e A_e \tag{B.54}$$

Substituting Eqn. (B.53) into B.46 using the corresponding expressions for *V* and *W*, and central difference approximation for the gradient terms, Eqn. (B.1) becomes:

$$\begin{aligned} C_E^P\left(P_E^c - P_P^c\right) + C_N^P\left(P_N^c - P_P^c\right) + C_U^P\left(P_U^c - P_P^c\right) + C_W^P\left(P_W^c - P_P^c\right) + \\ C_S^P\left(P_S^c - P_P^c\right) + C_D^P\left(P_D^c - P_P^c\right) + b_m^P = 0 \end{aligned} \tag{B.55}$$

Rearranging the above equation gives:

$$C_P^P P_P^c = C_E^P P_E^c + C_N^P P_N^c + C_U^P P_U^c + C_W^P P_W^c + C_S^P P_S^c + C_D^P P_D^c + b_m^P \tag{B.56}$$

where

$$b_m^P = \dot{m}_e^* + \dot{m}_n^* + \dot{m}_u^* - \dot{m}_w^* - \dot{m}_s^* - \dot{m}_d^* \tag{B.57}$$

$$C_E^P = -\rho A_e \Pi_e; \qquad C_N^P = -\rho A_n \Pi_n; \qquad C_U^P = -\rho A_u \Pi_u$$

$$C_W^P = -\rho A_w \Pi_w; \qquad C_S^P = -\rho A_s \Pi_s; \qquad C_D^P = -\rho A_d \Pi_d$$

$$C_P^P = C_E^P + C_N^P + C_U^P + C_W^P + C_S^P + C_D^P = \sum_{nk} C_{nk}^P \qquad \Pi_f = \frac{A_f}{\left(C_P^\Phi - \sum_{nk} C_{nk}\right)_f}$$

f = e, w, n, s, u, and d

Here, all the cell face values are interpolated using Eqn. (B.19). However, CV cell face mass fluxes in Eqn. (B.57) deserved special attention in order to avoid oscillatory solutions and slow convergence of the solution algorithm associated with the colocated finite volume approach. This problem usually results from the so-called checkerboard pressure field. To overcome this problem, a compact central-difference approximation

which was first developed by Rhie and Chow (1983) is employed for the cell-face velocities. Using the "e" cell face as an example, *U* value is given as:

$$U_e^* = \widetilde{U}_e^* - \frac{\forall_e}{(c_P^{\Phi} - \sum_{nk} c_{nk})_e}\left[\left(\frac{\partial P^*}{\partial x}\right)_e + \widetilde{\left(\frac{\partial P^*}{\partial x}\right)_e}\right] \quad \text{(B.58a)}$$

$$\left(\frac{\partial P^*}{\partial x}\right)_e = P_e^* - P_w^* \quad \text{(B.58b)}$$

In Eqn. (B.58a), the overbar denotes values obtained by a linear interpolation scheme. That is, the pressure gradient is temporary stored, and the corresponding face value is obtained from neighbouring nodal values using Eqn. (B.19). Equation (B.19) is also used to obtain the face pressures in Eqn. (B.58b). All the mass fluxes in Eqn. (B.57) were computed using respective velocity from Eqn. (B.58). The pressure correction, P^c is therefore obtained from Eqn. (B.56), whereas the final pressure values are computed from the guessed or previous iteration pressure values, P^* and P^c through:

$$P = P^c + P^* \quad \text{(B.59)}$$

The boundary conditions of the pressure-correction equation are on the premise that the boundary velocities are prescribed except those boundaries where pressure values are specified. This condition is equivalent to specifying a Neumann boundary condition (zero gradient) for the pressure correction. The velocities on pressure prescribed boundaries are, however, corrected.

B.4.2 Solutions of the Algebraic Equations

Each of the four algebraic systems of equations, (B.30-B.32 and B.56) has a dominant variable. However, this variable also occurs in some of the other equations. These equations can be solved either by coupled or segregation approach. For the coupled approach, all the algebraic equations are considered part of a single system and the

variables are solved simultaneously. For the segregation approach, on the other hand, the solution of the dominant variable is obtained from its equation on the basis that the other variables are known. Iterations are performed through the equations until the solution that satisfies all the equations is obtained. Although there is no advantage in terms of accuracy, the coupled approach tends to be costly especially when the problem is three-dimensional. The segregation approach is therefore employed in the present work.

The resulting algebraic Eqns. (B.30-B.32 and B.56) for nodal velocities and pressure correction, respectively, were solved using a 3D version of the strongly implicit procedure (SIP) solver (Stone, 1968). The SIP solver is an iterative procedure which is based on incomplete lower-upper (LU) decomposition method. This procedure has been described in detailed by Weinstein *et al* (1969), and Ferziger and Peric (2002). A brief summary and notation will be given here.

The general algebraic equation can be cast into the form:

$$M\Phi = Q \tag{B.60}$$

where the matrix M consists of the coefficients, Φ is U, V, W, or P, and Q is the sum of known values. The matrix M is sparse, and therefore it would be advantageous to store its elements in one-dimensional array. The indexing shown in Fig. B.2 will be used. The SIP method involves factorisation of the matrix M into К and Л, such that the modified matrix КЛ is a good approximation to M. Obviously, this factorisation is not exact; however, КЛ can be used as a substitute of M for the iterative method. The iterative equation is given as:

$$K\Lambda\psi^{l+1} = \delta^{l} \tag{B.61}$$

where δ^{l} (= $Q - M\,\Phi^{l}$) is a non-zero residual, ψ^{l+1} (= $\Phi^{l+1} - \Phi^{l}$) is the correction or update at $(l+1)^{th}$ step iteration, and the lower and upper triangular matrices are К and Л, respectively. Equation (B.61) can be modified by multiplying both sides by $К^{-1}$ which leads to:

$$Л\psi^{l+1} = K^{-1}\delta^{l} = \mathrm{B} \tag{B.62a}$$

$$Л\psi^{l+1} = B \quad \text{and} \quad \delta^{l} = K\mathrm{B} \tag{B.62b}$$

The computation of Eqn. (B.62a) is performed sequentially beginning at the southwest corner of the grid. The procedure involves two "sweeps": the first sweep computes the residual and B by incremental order of ijk, Eqns. (B.62b and B.63a), and the second sweep calculates corrections, ψ and Φ in decreasing order of ijk using Eqns. (B.63b and B.64).

$$\mathrm{B}^{ijk} = (\delta^{ijk} - K_{tD}^{ijk} B^{ijk-ije} - K_{tW}^{ijk} B^{ijk-J} - K_{tS}^{ijk} B^{ijk-1}) / K_{tP}^{ijk} \tag{B.63a}$$

$$\psi^{ijk} = B^{ijk} - Л_{tU}^{ijk}\psi^{ijk+ije} - Л_{tE}^{ijk}\psi^{ijk+J} - Л_{tN}^{ijk}\psi^{ijk+1} \tag{B.63b}$$

$$\Phi^{l+1} = \Phi^{l} + \psi^{l+1} \tag{B.64}$$

The triangulation matrices for Eqn. (B.63) are given as:

$$K_{tD}^{ijk} = \frac{C_{D}^{ijk}}{1+\alpha\left(Л_{tN}^{ijk-ije} + Л_{tE}^{ijk-ije}\right)}; \qquad K_{tW}^{ijk} = \frac{C_{W}^{ijk}}{1+\alpha\left(Л_{tN}^{ijk-J} + Л_{tU}^{ijk-J}\right)};$$

$$K_{tS}^{ijk} = \frac{C_{S}^{ijk}}{1+\alpha\left(Л_{tE}^{ijk-1} + Л_{tU}^{ijk-1}\right)}$$

$$\mathrm{H}_{P}^{ijk} = C_{P}^{ijk} - \alpha\left(K_{tD}^{ijk} Л_{tN}^{ijk-ije} + K_{tW}^{ijk} Л_{tN}^{ijk-J}\right) - \alpha\left(K_{tD}^{ijk} Л_{tE}^{ijk-ije} + K_{tS}^{ijk} Л_{tE}^{ijk-1}\right) - \alpha\left(K_{tW}^{ijk} U_{tU}^{ijk-J} + K_{tW}^{ijk} Л_{tU}^{ijk-1}\right) - K_{tD}^{ijk} Л_{tU}^{ijk-ije} - K_{tW}^{ijk} Л_{tE}^{ijk-J} - K_{tS}^{ijk} Л_{tN}^{ijk-1}$$

$$Л_{tU}^{ijk} = \frac{C_{U}^{ijk} - \alpha\left(K_{W}^{ijk} Л_{tU}^{ijk-J} + K_{W}^{ijk} Л_{tU}^{ijk-1}\right)}{\mathrm{H}_{P}^{ijk}}$$

$$Л_{tE}^{ijk} = \frac{C_E^{ijk} - \alpha\left(K_D^{ijk} Л_{tE}^{ijk-ije} + K_S^{ijk} Л_{tE}^{ijk-1}\right)}{\mathrm{H}_P^{ijk}}$$

$$Л_{tN}^{ijk} = \frac{C_N^{ijk} - \alpha\left(K_D^{ijk} Л_{tN}^{ijk-ije} + K_W^{ijk} Л_{tN}^{ijk-J}\right)}{\mathrm{H}_P^{ijk}}$$

where α is SIP parameter and is usually less than unity for the purpose of stability. This parameter can be varied from iteration to iteration, which requires updated values of Л and K matrices for respective values of α. The SIP parameter will be fixed and elements of the matrices K and Л are calculated once prior to the first iteration in the present study. Ferziger and Peric (2002) found that it is usually more efficient in general to keep α constant.

Below is a brief description of the solution procedure:

1. Read in all input data
2. Generate grid
3. Initialise solution fields and set boundary conditions
4. Calculate the viscosity if the fluid is non-Newtonian
5. Calculate the coefficients of the three momentum equations
6. Add all the source terms: the pressure gradient terms from P^* and deferred-correction terms
7. Absorb the boundary conditions, implement the wall and symmetry boundary conditions, and update the source terms
8. Solve momentum equations for the guessed velocities, U^*, V^*, and W^*
9. Calculate the pressure correction source terms and coefficients
10. Solve for the pressure correction field

11. Correct mass fluxes, nodal velocities, and pressure field using the new pressure field
12. Repeat step 4 through 11 until the convergence criteria are satisfied
13. Calculate post-process quantities such as vorticity

In the subsequent sections, step 12 which is the iterative loop for the algebraic equations or SIMPLEC iteration will be denoted "outer" and the SIP iteration will be called "inner". In the procedure outlined above, for the first iteration the viscosity field may take the value at zero shear-rate since the velocity fields are nearly zero. However, for a power-law fluid this will pose a problem due to its unbounded nature. The remedy to this problem therefore is that, the apparent viscosity field is initialised by a constant value for the first iteration after which the calculations proceed with the true variation of the viscosity (Pinho, 2001).

B.4.3 Convergence Criteria

The convergence criterion which limits the number of solver iterations for individual algebraic equation is based on a residual reduction. This residual reduction is implemented differently for both inner (SIP) and outer loops. For the outer loop, similar to definition used by Perić *et al* (1988), residual reduction is the sum of absolute values of residuals (the L_1 norm) over all control volumes normalised by inlet mass or momentum for pressure-correction or momentum equations, respectively. It is given as:

$$\xi^{\Phi} = \frac{\left\| \sum_{P} C_{nk}^{\Phi} \Phi_{nk} + b_P^{\Phi} - C_P^{\Phi} \Phi_P \right\|_1}{\Re_o} \tag{B.65}$$

where $\Phi \in (U, V, W, \text{or } P)$, $\Re_o$ is sum of mass or momentum flux for all CVs at the inlet,

$\|\cdot\|_1$ is L_1 norm, and all other variables have their usual meanings. The solver is terminated or ceases iterating when this reduction residual is less than a specified value, ξ_{sp}.

The inner iteration, however, has $\Re_o$ being defined as L_1 norm of its first iteration. This is because the variables need to be updated in outer iterations, and therefore a solution to a tighter tolerance will yield no advantage. The SIP iterations are typically stopped if the residual level drops by a factor of five for velocity components and ten for pressure-correction equation. This inner iteration is performed for each outer iteration. A convergence criterion for each equation was set to a maximum value of 10^{-4}. Whilst this criterion required less computing time for Newtonian fluid, the converse is true when the degree of shear-thinning is intense, say for $n < 0.4$. In fact, the required number of iterations or computing time can be as much as two to three times those for the equivalent Newtonian fluid simulation. The code that implements the numerical model was checked thoroughly for internal consistency. Section 3.4 (Chapter 3) documents all the test cases performed.